Damped Modes in Plasma Microturbulence: Saturation, Regulation, and Energy Partition

By

Kiritkumar D. Makwana

A dissertation submitted in partial fulfillment of

the requirements for the degree of

Doctor of Philosophy

(Physics)

at the

UNIVERSITY OF WISCONSIN-MADISON

2013

Date of final oral examination: 07/19/2013

The dissertation is approved by the following members of the Final Oral Committee:

Paul W. Terry, Professor, Physics

Cary Forest, Professor, Physics

Stas Boldyrev, Associate Professor, Physics

Chris Hegna, Professor, Engineering Physics

Carl Sovinec, Professor, Engineering Physics

M. J. Pueschel, Research Associate, Physics

To my parents,

Hansaben and Dhirubhai

Abstract

Understanding plasma turbulence has always been a key component of plasma physics research. Plasma microturbulence at the scale of the ion gyroradius and smaller is considered to be the primary cause of loss of confinement in tokamaks. Thus, understanding microturbulence and its saturation mechanism is very critical for nuclear fusion.

Over the last decade, a new saturation mechanism of microturbulence has been discovered, namely saturation by damped modes. Damped modes are stable roots of the plasma dispersion relation. We look at various aspects of this saturation mechanism in a variety of fluid as well as kinetic turbulence models. Energy diagnostics are defined and implemented for each model in order to study damped modes. These models describe vastly different fusion plasmas, but all of them show saturation by damped modes. Damped modes dissipate energy at almost the same rate as the energy injection rate of the unstable modes. The peak of this dissipation lies within the low wavenumber range where the instability also peaks, distinguishing it from the traditional viscous dissipation mechanism at large wavenumbers. Damped modes are typically found to be important in saturation when their damping rate is not much stronger than the instability growth rate. A simple criterion is defined to identify parameter regimes in which damped modes are important for saturation. It is also shown that quasilinear flux estimates may be unreliable when damped modes are active in saturation.

The regulation of ion temperature gradient driven (ITG) turbulence by zonal flows is a very important phenomenon in plasma fusion. Until now it has been explained using the zonal flow-drift wave shearing paradigm: zonal flow shearing enhances energy transfer from large scale drift waves to smaller, dissipative scales. However, we show that the zonal flows help transfer a majority of the energy injected by the unstable modes to the damped modes, leading to saturation. In order to show this, several new energy transfer diagnostics are developed, both in a simple fluid model as well as in a fully comprehensive, gyrokinetic model. Although the transfer to damped modes simultaneously excites smaller scales, a significant fraction of the injected energy is dissipated by damped modes in the large-scale, unstable region. This transfer occurs via three-wave interactions that include a zonal flow, an unstable mode and a damped mode.

These interactions dominate due to their coupling coefficients, a strong zonal flow amplitude and frequency matching. Frequency matching analysis shows that the nonlinear frequency sum of such a triplet interaction is the smallest, leading to the largest correlation time and enhanced energy transfer.

Gyrokinetic models have a slew of damped modes that is analyzed using proper orthogonal decomposition (POD) modes and linear eigenmodes. A metric is devised to identify which of these modes are well-resolved. The damping rate turns out to be a useful organizing property of these modes. Spectra of energy and amplitude attenuation rates of damped modes are calculated, showing regions of equipartition and power law behavior. It is found that energy is transferred to damped modes simultaneously, in a parallel manner, over a large range of scales in phase space. This can lead to a simplified and deeper understanding of how energy is partitioned among the damped modes in gyrokinetics.

Acknowledgments

This thesis is the culmination of a six year journey filled with learning. First I will thank Prof. Paul Terry under whose guidance most of this work was done. He has always been willing to help and I have a learned a lot about research from him. Thanks to professors Chris Hegna, Stas Boldyrev, Carl Sovinec, and Cary Forest for serving on my defense committee and teaching interesting courses.

Thanks to M. J. Pueschel and David Hatch for teaching most of what I know about gyrokinetics. Thanks to Dan for participating in the plasma discussion group. Conversations with Juhyung, Derek, Kurt, and Varun about plasma physics were enlightening. I also enjoyed working with Abdul during my first summer in Madison. The department staff, especially Jim and Dale, were very helpful. Thanks to Kerry Kresse for maintaining such a wonderful library where I have enjoyed studying and sleeping.

I really enjoyed my stay in Madison with Pradeep, Edwin, Rishabh, Anba, Ankur, and Lakshman. Thanks to Suraj for all the amazing dinners and Bozidar for all the concerts. Thanks to Danny for all the conversations and advice about physics and life in general. Thanks to Tobi for all the fun and physics during spring of 2009. It was also fun working with the 2009 holiday colloquium team. Also thanks to Steve, Jun, Deja, Viren, Paritosh, Anand, and Saurabh Maiti for cheering me up during different phases of this journey.

I am indebted to my friends and teachers from India who have helped me through all these years. I was fortunate to learn physics from professors Kasi and AP in school. I learned physics in IIT from Venky and Prarit. Big thanks to Ghodke, PJ, and Prarit for the friendship in IIT as well as for the most amazing trips of my life in USA. Also thanks to Sethi, Santosh, Bhushan, Sougato, and Pari for their support.

Thanks to Vinit, Divyani, Sheetal, and Ketan. Special thanks to the little ones; Tirth, Urvi, and Pratham; for all the amusement and laughs. Finally, my deepest thanks to my parents for supporting me in every decision of my life. I will end by thanking all the other people who have helped me reach where I am, but whom I have forgotten.

Contents

List of Figures

List of Tables

Chapter 1

Introduction

1.1 Turbulence

Turbulence is often regarded as the most important unsolved problem of classical physics, most notably by the renowned physicist Richard Feynman [1]. We have a sense of turbulence from our day to day experiences. Right from the motion of water flowing out of a faucet with high speed, up to the choppy rides experienced on airplanes, these are all examples of turbulence. We associate turbulence with chaotic, seemingly random motion in fluids and gases. It is associated with patterns of flow changing rapidly, compared to human space and time scales.

Humans have been trying to comprehend turbulence for at least five hundred years. In a famous sketch, Leonardo da Vinci portrayed the motion of water flowing across obstacles and falling down in a pool. His sketches, shown in Fig. 1.1, bring out the essence of turbulence. The flow is random and chaotic, containing structures of disparate scales. It is very difficult to predict what the flow at a particular point would be at a particular time in future.

It is impossible to give an exact mathematical definition for the term turbulence. However, we can attribute the following characteristics to it [2],

- randomness and irreversibility
- excitation of fluctuations over a broad range of scales

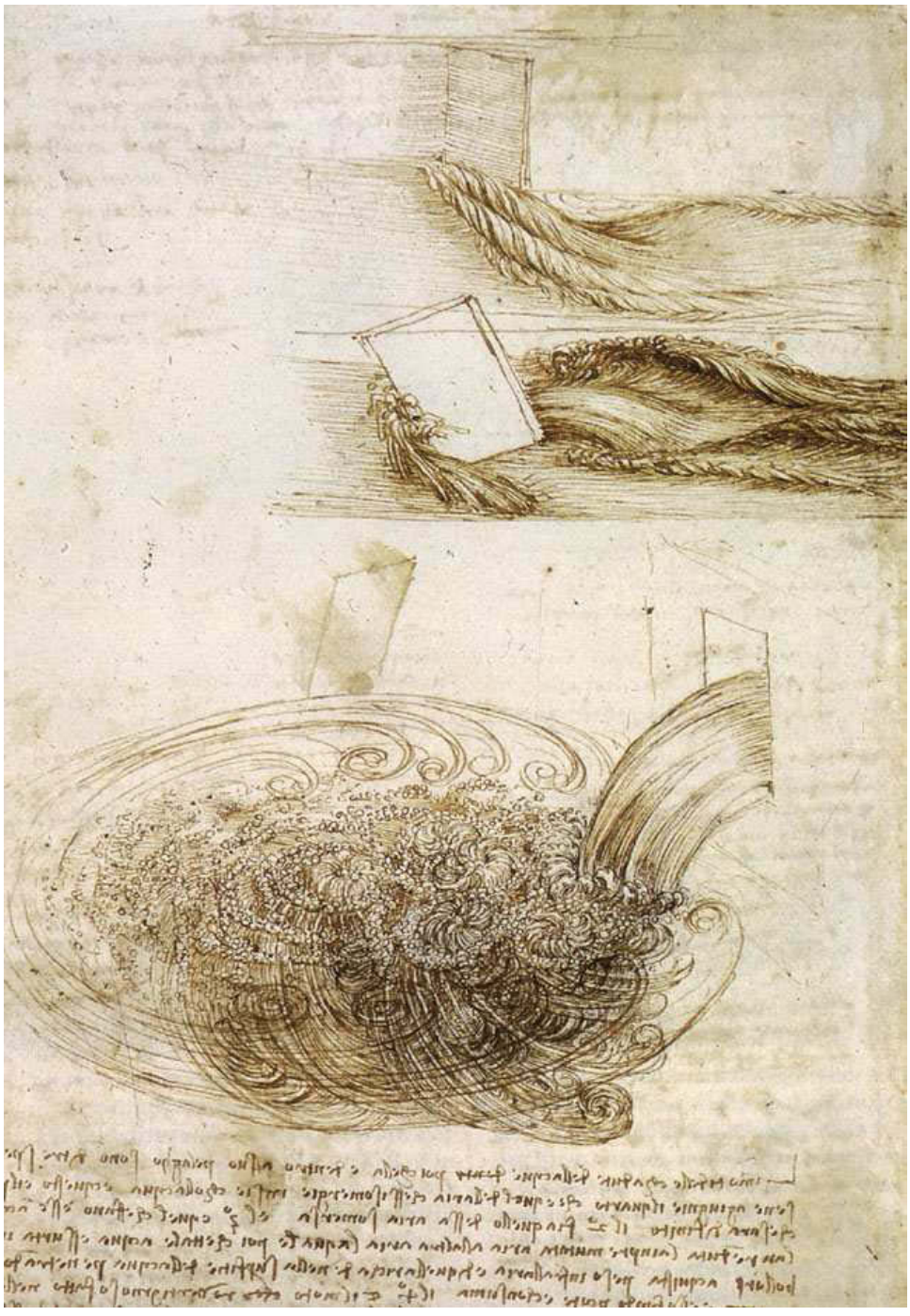

Figure 1.1: Sketches of turbulence by Leonardo da Vinci. Taken from the webpage :- http://www.cora.nwra.com/~werne/eos/images/eddy-davinci.jpg

- exchange of energy between fluctuations excited over the range of scales.

The randomness and irreversibility is related to the chaotic nature of turbulence. Even infinitesimal changes in initial conditions lead to drastic changes in the flow profile as time goes on. The large range of scales excited in turbulence gives rise to self similarity. Large eddies drive smaller eddies, which drive even smaller eddies, and so on, producing a self-similar cascade. Moreover, these eddies of different scales are constantly exchanging energy amongst themselves, leading to a very complex behavior.

The mathematical discussion of turbulence almost always starts with the Navier-Stokes equation for an incompressible flow [3], which is,

$$\frac{\partial \mathbf{v}}{\partial t} + \mathbf{v} \cdot \nabla \mathbf{v} = -\frac{\nabla p}{\rho} + \nu \nabla^2 \mathbf{v}. \tag{1.1}$$

It is an equation that describes the time evolution of the velocity field $\mathbf{v}$ of a fluid in terms of the density ρ, pressure p and the kinematic viscosity ν. The Reynolds number is closely associated with this equation and is defined as $Re \equiv vL/\nu$, where v is the velocity at system length scale L. Re is basically the ratio of the nonlinear term in the Navier-Stokes equation to the viscous term, defined for velocity fluctuations at the system scale. When this number is large (practically when $\gtrsim 10^6$) the flow is turbulent.

Fully analytical treatment of turbulent flow is thought to be impossible. However, one of the major goals of turbulence research, either analytical or numerical, has always been to identify simple conceptual principles which can guide our thinking about turbulence. Probably the most famous, unifying, and simplifying principle in turbulence is Kolmogorov's $5/3^{\text{rd}}$ law [4], [5], shown in Fig. 1.2, which plots the energy spectrum as a function of wavenumber. This law applies to high Reynolds number, three-dimensional, hydrodynamic turbulence. The turbulence is driven by stirring at a large scale k_0. The energy injected is transferred from the large eddy to smaller eddies by a local interaction in wavenumber space, i.e., large eddies break into smaller eddies which are not vastly different in scale from the original eddy. This process is self-similar over a range of scales, known as the inertial range. Ultimately the energy reaches the Kolmogorov scale,

k_{D}. Beyond this scale, viscosity overcomes the self similar energy transfer process and converts it into heat. The energy spectrum was predicted to fall off as $-5/3^{\mathrm{rd}}$ power of wavenumber by Kolmogorov [6], and this has been verified to great precision in experiment [7]. Thus, in 3D,

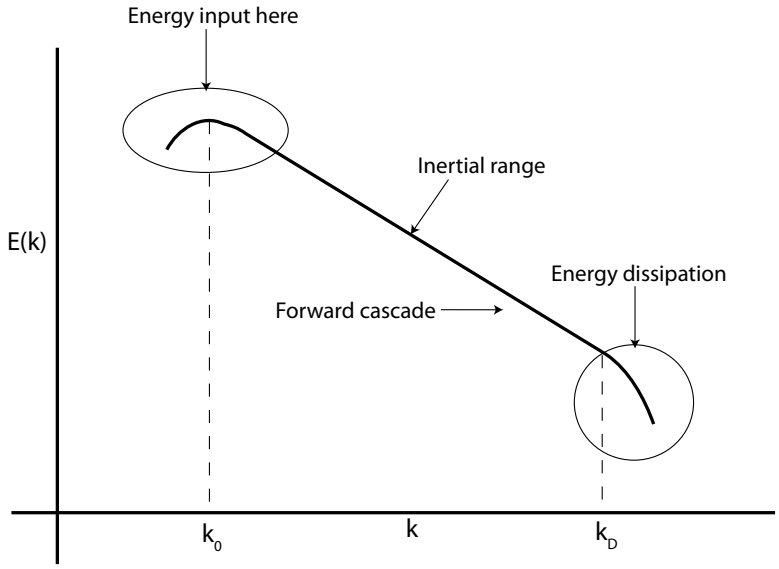

Figure 1.2: Cartoon of spectrum in three dimensional hydrodynamic turbulence. Energy is injected at large scale k_0 and dissipated beyond the Kolmogorov scale k_D. It cascades in the forward direction in the inertial range.

homogeneous, hydrodynamic turbulence, energy which is injected by stirring is conservatively transferred through the inertial range and eventually converted into heat in the dissipation range. That is how the system achieves saturation - a steady level of energy - by balancing the energy injection with energy dissipation bridged by a large inertial range. Most of this thesis involves work about how saturation can occur in plasma turbulence and how it can differ from the saturation just described for hydrodynamic turbulence. We restrict ourselves to plasma microturbulence which is the turbulence most relevant for fusion devices.

1.2 Plasma microturbulence and nuclear fusion

A large amount of research in plasma turbulence has been motivated by nuclear fusion. Nuclear fusion is the process that powers our Sun and all the other stars in the universe. Harnessing

the power of nuclear fusion for the peaceful purpose of meeting mankind's energy needs has always been the holy grail of fusion research [8]. It is increasingly becoming clear that the world is facing an energy crisis with the depleting fossil fuels and the damage done by such fuels to the environment in terms of pollution and global warming. There is mounting evidence that man-made global warming is real [9]. Also, at present, oil, natural gas, and coal are the primary sources of energy all around the world. Although estimates vary, more or less it is clear that oil supplies will last another 50 years, natural gas for 60 years, and coal for another 150 years [9]. In order to maintain the pace of progress and the standard of living of the last three centuries, we have to find a clean, sustainable alternative to fossil fuels [10].

There are several alternative sources of energy; namely, solar, wind, geothermal, nuclear fission and nuclear fusion. Solar and wind power are very promising but it is not proven that they can provide the baseload power that is required round the clock. Nuclear fission depends on heavy radioactive elements which are limited and which also raise concerns of public safety and nuclear proliferation. Under such circumstances, nuclear fusion is a very attractive option for energy production. Fusion has two major advantages [11]. Firstly, the primary fuel used in fusion is Deuterium, which is abundantly available in ocean water, so much so that it is practically limitless. Secondly, fusion does not generate polluting byproducts which harm the environment or cause global warming. It does produce radioactive elements but they represent short lived isotopes at much lower concentrations than the radioactive byproducts of nuclear fission. Fusion also does not depend on the weather, unlike solar and wind power.

Fusion research began in the 1950's with the goal of producing net energy out of fusion reactions and ultimately developing power plants. It was realized early on that very high temperatures (several hundred million °C) would be required in order to fuse two repelling, positively charged nuclei [12]. Lawson derived the criterion determining fusion yield as a function of the triple product of temperature, density and confinement time. The challenge of fusion always has been to achieve a high enough triple product to get net energy gain. There are two major approaches taken to do this - inertial confinement fusion and magnetic confinement fusion. In inertial confinement fusion, intense beams of lasers or particles implode a spherical fuel pellet

producing high temperatures and the inertia of the reacting fuel is expected to keep it confined for a long enough time with a high enough density so that the Lawson criterion for fusion gain is satisfied. The second approach is magnetic confinement fusion. In this approach the plasma is heated by driving a current through it and then by injecting radiation or particles. The plasma is enclosed in some kind of a magnetic bottle, which is expected to keep it confined for a long enough time at high enough density to achieve fusion.

In either of these approaches, the triple product has continuously improved with time, indicating the progress fusion research has made over all these decades as seen in Fig. 1.3. However, in neither of them has the Lawson criterion been met until now. Two big facilities, the National Ignition Facility (NIF) in USA and the International Thermonuclear Experimental Reactor (ITER) in France, have the possibility of breaking this barrier. The NIF has taken the inertial confinement approach while ITER has taken the magnetic confinement approach. In this thesis we deal with plasma turbulence which is relevant to the magnetic confinement approach.

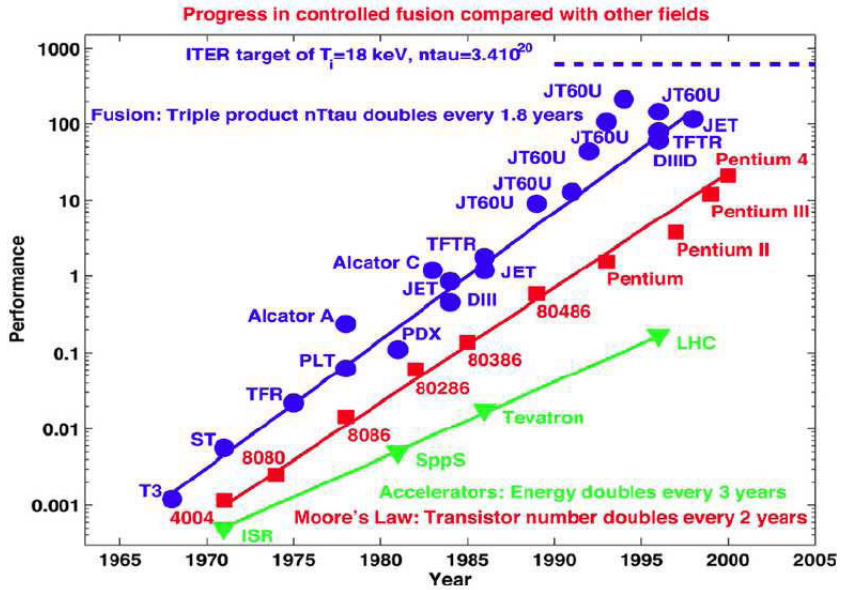

Figure 1.3: The fusion triple product in tokamaks has improved at a rate faster than Moore's law for transistors in a microprocessor chip or the rate of energy increase in particle accelerators. Taken from Ref. [13].

Plasma physics and plasma turbulence have become extremely important in understanding

and controlling magnetically confined plasmas. Since the start of fusion research in the 1950's, a large variety of magnetic configurations were tried to confine plasmas. All of these earlier configurations showed violent large scale instabilities that would cool down the plasma abruptly. These were macro scale magnetohydrodynamic (MHD) instabilities. The most preferred magnetic configuration for confinement is called a tokamak. The first tokamak was built in USSR in 1958, and called the T1 tokamak [14]. Tokamaks have a strong toroidal magnetic field generated by coils around the donut shaped vessel. In addition, a transformer is used to generate a strong electric field in the toroidal direction, driving a plasma current. This current produces a weaker poloidal magnetic field which, when superimposed with the external toroidal field, gives a helical field around the torus. New heating schemes, like the neutral beam injection, were also devised to reach higher temperatures. Several new theoretical concepts were developed to understand the macro-instabilities in the framework of MHD. The introduction of divertors lead to the discovery of the H-mode [8]. With the help of all these measures, tokamaks were able to mitigate the violent instabilities that had plagued earlier devices and obtain record levels of plasma temperature.

However, tokamaks were still not able to reach break-even where they could produce more energy than what was put in. An anomalous mechanism of heat transport was thought to be responsible for this. Classically, we can consider transport as a diffusion process. The particles suffer collisions with a characteristic collision time τ_c. A collision allows the particle to step across the magnetic field line with a step length equal to its Larmor radius, ρ. This gives a diffusion coefficient of $D \sim \rho^2/\tau_c$. This gives a confinement time of $\tau \sim (a/\rho)^2\tau_c$, where a is the plasma radius [15]. This estimate works for plasmas which are cold such that collisional effects dominate. However as confinement in tokamaks improved and plasmas became less collisional, this estimate turned out to be considerably inadequate compared to experimentally measured confinement. Neoclassical theory was developed to explain this transport. Neoclassical theory still relies on Coulomb collisions for transport but takes into account effects of complicated geometry on particle trajectories and drifts leading, in some cases, to enhanced transport [16]. Toroidal geometry can lead to particle trapping, giving rise to trapped orbits with a larger step size, leading to larger diffusion rates.

As tokamaks became even hotter and more collisionless due to external heating, the neoclassical transport estimates also fell short of experimental observations [17]. Such high levels of transport are often called "anomalous transport in tokamaks". It is widely believed that this transport is caused by turbulent fluctuations in the plasma [17]. If these fluctuations are totally random, we do not expect them to cause net transport. However, there are collective modes in the plasma which can correlate two fluctuations (electrostatic potential and temperature, for example) and, depending on the phase relationship between the two, cause transport of particles and heat. Several such collective modes of the plasma have been discovered, and it is believed that we now should be able to explain the anomalous transport using these modes. These collective modes are called "drift waves" because their phase velocity is typically the diamagnetic drift velocity, which is in turn driven by equilibrium gradients in the plasma [18]. As a simple example we can consider fluctuations in the electrostatic potential ($\delta\phi$) and plasma temperature (δT). This is shown schematically in Fig. 1.4. The x and y axis represent the radial and poloidal directions in a tokamak slab with a temperature gradient pointing in the $-x$ direction. A collective mode of electrostatic potential and temperature fluctuations is shown traveling in the y direction, with a phase difference of 90° between the two. The potential fluctuations gives rise to electric field fluctuations ($\delta\mathbf{E}$) as shown in the figure. Combined with the equilibrium magnetic field $\mathbf{B}_0$, this will give rise to $\mathbf{E}\times\mathbf{B}$ advection of the background temperature profile. If the two fluctuations had been in phase, then this $\mathbf{E}\times\mathbf{B}$ advection would have led to the drift wave simply propagating in the $+y$ direction. However, in the case shown, we can see that this advection will bring hotter plasma into regions of high temperature and colder plasma into low temperature regions, thus reinforcing the fluctuations and giving rise to an instability.

Ultimately some nonlinear effect will saturate the growth of these fields. In the saturated state, the heat flux transported out of the tokamak, Q, will be proportional to the correlation of temperature and potential fluctuations, $Q \sim \langle \delta T \delta v_{E\times B} \rangle$. This heat flux has a direct bearing on the confinement time and is responsible for the loss of confinement. Thus, the performance of a fusion device is directly related to these small scale fluctuations and their correlations. With this knowledge, it becomes extremely important to understand the saturation mechanism of

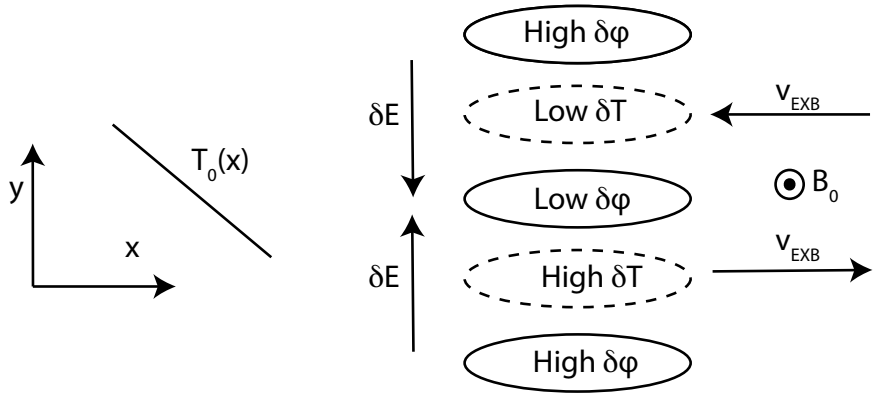

Figure 1.4: A cartoon showing the physical mechanism of instability in drift waves.

such fluctuations and maybe come up with schemes to reduce the heat loss due to them. Such fluctuations are collectively referred to as plasma microturbulence because the scale of these is very small, of the order of the ion or even the electron gyroradius. This thesis deals with such turbulent fluctuations and the mechanism by which they saturate at a steady level. A key goal of research in this field is to be able to accurately model this microturbulence in a real world plasma and to be able to predict the transport and confinement properties of such a plasma [19]. Obviously, this will be a big boost to ITER, as we would be able to predict how ITER will behave and tell us what steps we will need to take in order to ensure that it accomplishes its mission!

1.3 Damped modes in plasma microturbulence

As explained above, the saturation mechanism of plasma microturbulence directly determines the transport and hence the confinement of plasma. We have seen in Sec. 1.1 that 3D hydrodynamic turbulence saturates by viscous dissipation beyond the Kolmogorov scale. What is the situation in plasmas? In MHD turbulence it is thought that a similar process occurs wherein viscosity and resistivity at small scales dissipate the kinetic and magnetic energy into heat [20]. Very little attention has been paid to this question in microturbulence as most of the focus has been on calculating the heat flux and transport, whichever way the turbulence saturates. Implicitly it has been assumed that a similar mechanism of small scale dissipation should be at work in microturbulence as well. However, there are significant qualitative differences between plasma

microturbulence and hydrodynamic turbulence. Firstly, there is no large, intermediate, inertial range observed in microturbulence. Indeed, poorly resolved simulations, with hardly a decade of scales resolved, show well converged saturation levels and transport rates that do not change as the resolution is increased. Secondly, unlike hydrodynamic and MHD turbulence in homogeneous media, which are driven by external stirring, microturbulence in tokamaks is typically driven by instabilities which arise in fusion devices because the plasma is never in a stable equilibrium. There are always gradients in a confined system and they drive such instabilities.

Plasma instabilities are expressed as roots of the linear dispersion relation. The plasma dispersion relation expresses the linear frequency as a function of wavenumber and the most unstable mode is only one of the several possible roots it admits! In homogeneous fluid models, the number of roots at a given wavenumber is equal to the number of independent fields in the model. The different roots can be thought of as different manifolds spanning the wavenumber space (see Fig. 1.2 in Ref. [21]). The unstable manifold is the one which contains the most unstable mode. The other manifolds are subdominant manifolds and for all the models discussed in this thesis, most of the subdominant manifolds will be damped, i.e., they have a negative imaginary part of the frequency. We will interchangeably use the words "damped" and "stable" to describe modes with a negative growth rate in this thesis.

The damped modes are usually ignored in any analysis since, naively, one expects them to damp away exponentially with time. However, recently it has been found that such damped modes are important energy sinks in the saturation of many types of instability-driven plasma turbulence [22–28]. They are found to be important in both fluid models [22–24; 28] as well as kinetic models [25–27]. Several features of the damped modes are striking. Nonlinearity, in the form of three-wave coupling, drives all damped modes available to the system [23]. In two-field fluid models, the dispersion relation is quadratic. There is one damped mode and one unstable mode, both of which are functions of wavenumber from large to small scales [29]. In gyrokinetics there are in principle an infinite number of damped modes spanning the directions of inhomogeneity in phase space. Under numerical discretization the number becomes finite but very large [$\mathcal{O}(10^4)$ for typical resolutions] [27]. In fluid models the mode damping is because of

a different phase relationship between the fluctuating quantities than required for an instability. For example, in Fig. 1.4, if the phase difference between density and temperature fluctuations is changed by 180°, then the mode will become damped. In kinetic models, the damping mechanism arises from either velocity space resonances (Landau damping) or particle-particle collisions. Whether the number of damped modes is one or many, certain aspects of the saturation are qualitatively the same. Damped modes damp energy at all wavenumbers available, not just at large wavenumbers (small scales). In fact, in many models their damping peaks at the same low wavenumbers where instability exists, typically in the large scale range where the turbulent spectrum peaks [26]. Also, damped modes dissipate energy at a rate that is comparable to the rate of energy injection by the instability. All this previous work and the present thesis show that damped modes play a dominant role in the saturation of plasma microturbulence.

This thesis investigates several aspects of saturation by damped modes in plasma microturbulence. We begin in Chap. 2 with a survey of nine different two-field fluid models of turbulence. These models describe a wide range of plasmas in fusion devices. The goal is to demonstrate that saturation by damped modes is a ubiquitous phenomenon and also to identify some unifying principles of such a saturation mechanism. We numerically solve these models, decompose the solutions into the unstable and damped eigenmodes, and define energy diagnostics for analysis of saturation. In all the models we are able to find parameter regimes in which damped modes play a significant role in saturation by damping away majority of the energy injected by linear instability. An analytical criterion based on model parameters is derived which correctly predicts these regimes. We find the striking result that damped modes are mostly excited when the gradient drive is strong. We also look at the effect of damped modes on quasilinear heat flux calculations and show that the quasilinear estimates might not be reliable when damped modes saturate the turbulence. In Chap. 3 we look at the specific example of zonal flow regulated ion temperature gradient driven (ITG) turbulence, again using a two-field fluid model. A well known and very important phenomenon in plasma microturbulence is the regulation of ITG turbulence by self-generated zonal flows. This phenomenon has long been attributed to the shearing effect of zonal flows on drift wave eddies, breaking them into smaller eddies and increasing coupling to

dissipative scales. In this chapter it is shown that zonal flow assisted energy transfer to stable modes, which has been ignored till now, is actually a key effect in this turbulence. Nonlinear energy transfer diagnostics are heavily used to show this, also providing a base for the more comprehensive diagnostics utilized in Chap. 4. We find that three-wave interactions that include a zonal flow, an unstable mode and a stable mode are much stronger than other interactions. These interactions dominate because of their coupling coefficients, the zonal flow amplitude and frequency matching.

In Chap. 4 we look at regulation of ITG turbulence by zonal flows using a much more comprehensive, state-of-the-art gyrokinetic model. This model adds a whole new level of complexity in the analysis of this problem by introducing thousands of damped modes, but also yields new and richer insights into it. Proper orthogonal decomposition (POD) modes are utilized to analyze the damped mode spectrum. After defining gyrokinetic nonlinear transfer functions we are able to calculate how much energy is dissipated by damped modes within the region of low, unstable wavenumbers. It is seen that a large fraction of the injected energy is dissipated by such modes, thus establishing the importance of zonal flow assisted energy transfer to stable modes in regulation of ITG turbulence. We also look at the concept of frequency matching in more detail. In Chap. 5 we analyze energy partitioning among damped modes in gyrokinetics. We look at some of the effects of hyper-diffusivity and higher k_x connected modes on the damped mode energetics. As stated earlier, a key goal of turbulence research is to identify key conceptual principles that can guide our thinking about the problem. With this in mind, we calculate the energy dissipation and amplitude attenuation rate spectra for POD and linear modes. They seem to show favorable scaling behavior. Calculations also show that energy is transferred in parallel to all the damped modes simultaneously in gyrokinetics. It is hoped that these developments will lead to a simplified picture of damped modes in plasma microturbulence. Finally, we conclude in Chap. 6 with a summary and directions for future research.

Chapter 2

Damped modes in two-field fluid models

Fluid models of plasma turbulence treat the plasma as a fluid. Fluid equations can be derived from a more fundamental kinetic description [30]. A typical example of such fluid equations is a two field model for ion/electron temperature gradient (ITG/ETG) driven turbulence [31]. These equations look as follows

$$\frac{\partial p}{\partial t} + (1+\eta)\frac{\partial \phi}{\partial y} + \chi \nabla_\perp^4 p = -\{\phi, p\}, \tag{2.1}$$

$$(1-\nabla_\perp^2)\frac{\partial \phi}{\partial t} + \frac{\partial \phi}{\partial y} - \varepsilon \frac{\partial p}{\partial y} - \nu(\nabla_\perp^2)\phi = \{\phi, \nabla_\perp^2 \phi\}. \tag{2.2}$$

These equations describe the time evolution of two fluid fields - the ion pressure p and the electrostatic potential ϕ. The system they describe is in two dimensional slab geometry. The gradient in this two dimensional $x-y$ plane is represented by $\nabla_\perp$. The radial direction is taken as x and the poloidal direction as y. There is a gradient in the equilibrium density and temperature in the radial (x) direction. There is also an equilibrium magnetic field B_0 in the z direction, perpendicular to the $x-y$ plane. Symbols ν and χ are coefficients of collisional dissipation, η is the ratio of density to temperature gradient scale length and ε is the ratio of density gradient scale length to magnetic field variation scale length. The curly brackets represent the Poisson bracket, $\{f, g\} \equiv \hat{z} \cdot (\nabla f \times \nabla g)$. The spatial coordinates are normalized to ρ where ρ represents electron gyro radius in ETG and ion sound gyro radius in ITG. Time is normalized to L_{ref}/u_{ref} where L_{ref} is the density gradient scale length and u_{ref} is electron thermal speed, v_{Te}, for ETG

and ion sound speed, c_s, for ITG.

These equations are derived from a three field fluid model of ITG [32]. They are derived in a sheared slab geometry from the ion continuity equation, parallel ion dynamics and pressure evolution equation. The perpendicular velocity is taken to be the $\mathbf{E}\times\mathbf{B}$ velocity and ion diamagnetic drift velocity to zeroth order, and the polarization drift velocity in first order. Quasineutrality and adiabatic electron response are assumed ($\tilde{n}_i = \tilde{n}_e = e\Phi/T_e$). If we restrict ourselves to fluctuations with $k_z = k_{||} = 0$ then we get the reduced two field model above.

2.1 Model equations

There are several other two-field fluid models of plasma turbulence that can be found in the literature. Nine such models have been identified and analyzed. These models represent a wide range of physical mechanisms for instability, turbulent mode coupling and parameter regimes. They were all devised in order to explain a certain aspect of physics in plasma confinement devices such as tokamaks. As such, they range in their applicability from hot to cold temperatures, from trapped to untapped particles, from electrostatic to electromagnetic physics, from core to edge plasmas and so on. The models describe trapped electron mode turbulence, local Hasegawa-Wakatani turbulence, two-dimensional turbulence driven by the Rayleigh-Taylor instability, local electrostatic resistive g-mode turbulence, ion temperature gradient turbulence, microtearing mode turbulence, a variant of microtearing turbulence with temperature fluctuations, a thermally driven edge drift wave, and an edge drift wave driven by ionization and charge exchange processes. Each of these models will be described in detail later. However, all these models can be expressed in the following form,

$$\frac{\partial F_1}{\partial t} + Z_{11}F_1 + Z_{12}F_2 = N_1, \tag{2.3}$$

$$\frac{\partial F_2}{\partial t} + Z_{21}F_1 + Z_{22}F_2 = N_2. \tag{2.4}$$

Equations (2.3-2.4) are expressed in Fourier space, with all the quantities a function of wavenumber k. In this chapter, we use k to denote the Fourier wavenumber, it should be clear from context whether it denotes the vector or its scalar magnitude. F_1 and F_2 are the time dependent coefficients of the two fields in a Fourier decomposition of the two fields in x and y assuming periodic boundary conditions on the slab. In Fourier representation the linear operators just become matrices whose elements are represented by Z_{11}, Z_{12}, Z_{21} and Z_{22}. The nonlinear terms become a convolution sum over the Fourier wavenumber which are represented by N_1 and N_2. With the exception of the thermal microtearing model, their general form is as follows,

$$N_1 = \sum_{k'} [A_1(k,k')F_2(k')F_1(k-k') + B_1(k,k')F_2(k')F_2(k-k')], \tag{2.5}$$

$$N_2 = \sum_{k'} [A_2(k,k')F_2(k')F_2(k-k') + B_2(k,k')F_2(k')F_1(k-k')]. \tag{2.6}$$

Here $A_{1,2}(k,k')$ and $B_{1,2}(k,k')$ are the nonlinear, three-wave coupling coefficients between wavenumbers k, k' and $k-k'$.

As an example, we can express the fields in the ITG model as a Fourier decomposition, $p = \sum_k p_k e^{ikr}$ and $\phi = \sum_k \phi_k e^{ikr}$. Substituting these expressions into equations (2.1-2.2), we get,

$$\frac{\partial p_k}{\partial t} + ik_y(1+\eta)\phi_k + \chi k^4 p_k = -\frac{1}{2}\sum_{k'}(k' \times \hat{z} \cdot k)[\phi_{k'} p_{k-k'} - \phi_{k-k'} p_{k'}], \tag{2.7}$$

$$[1+k^2]\frac{\partial \phi_k}{\partial t} + ik_y\phi_k - ik_y\epsilon p_k + \nu k^2 \phi_k = -\frac{1}{2}\sum_{k'}(k' \times \hat{z} \cdot k)[(k-k')^2 - k'^2]\phi_{k'}\phi_{k-k'}. \tag{2.8}$$

Comparing equations (2.3-2.4) with equations (2.7-2.8) respectively, we can identify F_1 with p_k and F_2 with ϕ_k respectively. Similarly, the linear coupling coefficients become $Z_{11} = \chi k^4$, $Z_{12} = ik_y(1+\eta)$, $Z_{21} = -ik_y\varepsilon/(1+k^2)$ and $Z_{22} = (ik_y + \nu k^2)/(1+k^2)$. The nonlinear coupling coefficients become $A_1 = -(\mathbf{k}' \times \hat{\mathbf{z}} \cdot \mathbf{k})$, $B_1(k,k') = B_2(k,k') = 0$ and $A_2 = -(\mathbf{k}' \times \hat{\mathbf{z}} \cdot \mathbf{k})[(k-k')^2 - k'^2]/[2(1+k^2)]$. One should note that the nonlinear term is symmetric under the interchange of k' with $k-k'$. This symmetrization has been applied to obtain the form of nonlinearities in Eqs. (2.7-2.8).

The details of all the nine models surveyed, including their equations are described later on. Right now let us assume that $i\omega_{1,2}$ are the eigenvalues of the linear coupling coefficient matrix Z and $R_{1,2}$ are the eigenvectors, i.e.,

$$\begin{bmatrix} Z_{11} & Z_{12} \\ Z_{21} & Z_{22} \end{bmatrix} \begin{bmatrix} R_{1,2} \\ 1 \end{bmatrix} = i\omega_{1,2} \begin{bmatrix} R_{1,2} \\ 1 \end{bmatrix}. \tag{2.9}$$

The eigenvalues are nothing but the eigenfrequencies of this problem. If the imaginary part of ω is positive then it is an unstable mode otherwise it is a stable mode. For the two field models that we consider, one always gets an eigenfrequency which is unstable for some range of wavenumbers and this branch of eigenvalues is called the unstable mode. The other branch of eigenvalues is always damped and is called the stable branch. We will interchangeably use the terms "stable mode" and "damped mode". We choose to label the unstable root as ω_1 and the stable root as ω_2. The dispersion relation (eigenvalue equation) is $\omega^2 + i\omega(Z_{11} + Z_{22}) + (Z_{12}Z_{21} - Z_{11}Z_{22}) = 0$. This relation can be easily solved to obtain the growth/damping rates of the two modes,

$$\gamma_{1,2} = -\frac{\mathrm{Re}(Z_{11} + Z_{22})}{2} \pm \frac{1}{2}[(Z_{11} - Z_{22})^2 + 4Z_{12}Z_{21}]^{1/2} \tag{2.10}$$

$$= -\frac{b_r}{2} \pm \frac{\rho^{1/2}}{2} cos\left[\frac{\phi}{2}\right], \tag{2.11}$$

where,

$$b_r = \mathrm{Re}(Z_{11} + Z_{22}), \qquad \rho = |4Z_{12}Z_{21} + (Z_{11} - Z_{22})^2|, \tag{2.12}$$

$$\phi = \tan^{-1}\left[\frac{\mathrm{Im}[4Z_{12}Z_{21} + (Z_{11} - Z_{22})^2]}{\mathrm{Re}[4Z_{12}Z_{21} + (Z_{11} - Z_{22})^2]}\right]. \tag{2.13}$$

The eigenvectors are

$$R_{1,2}(k) = \frac{i\omega_{1,2}(k) - Z_{22}}{Z_{21}}, \tag{2.14}$$

where $\omega_j = \omega_{jr} + i\gamma_j$ and $j = 1, 2$. The expression for γ_j is given in Eq. 2.10 and the real part

of frequency, ω_{jr}, is given by,

$$\omega_{1,2r} = \frac{\mathrm{Im}(Z_{11} + Z_{22})}{2} \pm \frac{\rho^{1/2}}{2} \sin\Big[\frac{\phi}{2}\Big]. \tag{2.15}$$

We can express the two fields $F_{1,2}$ as a linear combination of the eigenvectors,

$$\begin{bmatrix} F_1 \\ F_2 \end{bmatrix} = \beta_1 \begin{bmatrix} R_1 \\ 1 \end{bmatrix} + \beta_2 \begin{bmatrix} R_2 \\ 1 \end{bmatrix}, \tag{2.16}$$

where β_1 and β_2 are the amplitudes of the unstable and stable modes respectively. This linear combination can be substituted into Eqs. (2.3-2.4) and can be inverted to obtain the time evolution equations of the eigenmode amplitudes $\beta_{1,2}$.

$$\frac{\partial\beta_1(k)}{\partial t} + i\omega_1(k)\beta_1(k) = \sum_{k'} \Big[C_1(k,k')\beta_1(k')\beta_1(k'') + C_2(k,k')\beta_1(k')\beta_2(k'')$$

$$+C_3(k,k')\beta_1(k'')\beta_2(k') + C_4(k,k')\beta_2(k')\beta_2(k'')\Big], \tag{2.17}$$

$$\frac{\partial\beta_2(k)}{\partial t} + i\omega_2(k)\beta_2(k) = \sum_{k'} \Big[D_1(k,k')\beta_1(k')\beta_1(k'') + D_2(k,k')\beta_1(k')\beta_2(k'')$$

$$+D_3(k,k')\beta_1(k'')\beta_2(k') + D_4(k,k')\beta_2(k')\beta_2(k'')\Big], \tag{2.18}$$

where,

$$C_1 = C_3 = (A_1R_1'' + B_1 - R_2A_2 - R_2B_2R_1'')/(R_1 - R_2), \tag{2.19}$$

$$C_2 = C_4 = (A_1R_2'' + B_1 - R_2A_2 - R_2B_2R_2'')/(R_1 - R_2), \tag{2.20}$$

$$D_1 = D_3 = (-A_1R_1'' - B_1 + R_1A_2 + R_1B_2R_1'')/(R_1 - R_2), \tag{2.21}$$

$$D_2 = D_4 = (-A_1R_2'' - B_1 + R_1A_2 + R_1B_2R_2'')/(R_1 - R_2). \tag{2.22}$$

Here it is understood that all the C's, D's, A's and B's are functions of wavenumbers k and k'. The symbols $R_{1,2} \equiv R_{1,2}(k)$ and $R''_{1,2} \equiv R_{1,2}(k-k')$.

2.2 Threshold criterion for stable mode excitation - P_t

In a simplified sense, ignoring the Fourier wavenumber dependencies, Eqs. (2.17-2.18) can be written in the following way [23],

$$\dot{x}_1 = \gamma_1 x_1 + C_1 x_1^2 + C_2 x_1 x_2 + \cdots , \tag{2.23}$$

$$\dot{x}_2 = -\gamma_2 x_2 + D_1 x_1^2 + \cdots . \tag{2.24}$$

Here x_1 is likened to β_1 and x_2 is like β_2. Similarly C_1 in Eq. 2.23 is like $C_1(k, k')$ in Eq. 2.17 and C_2 in Eq. 2.23 can be thought of as the combination $C_2 + C_3$ in Eq. 2.17. D_1 in Eq. 2.24 is like D_1 in Eq. 2.18, and γ_1 and $-\gamma_2$ are the growth and damping rates respectively. In Ref. [23] it is shown that excitation of stable modes to an amplitude comparable to that of unstable modes depends on the criterion,

$$P_t \equiv \frac{D_1 C_2}{C_1^2} \frac{1}{(2 - \gamma_2/\gamma_1)}. \tag{2.25}$$

If P_t is of the order or larger than unity then stable modes are excited and play an important role in saturation. It is derived by taking a ratio of the third term in Eq. (2.23) to its second term at a time when the first term is balanced by the second term. P_t is proportional to the product of nonlinear coupling coefficients D_1 and C_2, which control the nonlinear energy transfer from the unstable mode to the damped mode. It is natural that the role of damped modes in saturation is directly proportional to these two coupling coefficients. It is inversely proportional to C_1^2 because the larger this coefficient is, the more efficient it is for energy to nonlinearly cascade along the unstable branch to high-k dissipative modes, instead of cascading to the damped modes. It is also important that $|\gamma_2|$ not be much larger than $|\gamma_1|$ because if this is the case, then the nonlinear energy transfer to damped modes will not be able to overcome their strong linear damping. This is expressed by the $(2 - \gamma_2/\gamma_1)$ factor in the denominator of P_t. All the quantities in P_t depend upon wavenumbers k and $k - k'$, hence it is evaluated for a range of wavenumbers and should only be used as an order of magnitude estimate.

Because the coupling coefficients C_1, C_2, C_3, and D_1 are formed from similar linear combi-

nations of A_j and B_j, frequently $D_1(C_2+C_3)/C_1^2 \approx 1$. When true, P_t is most sensitive to the growth rate ratio γ_2/γ_1. If $|\gamma_2| \gg |\gamma_1|$ then $P_t \ll 1$. This implies that if the damped eigenmode is heavily damped then its amplitude in saturation is very small. If $|\gamma_2| \sim |\gamma_1|$, the growth rates are optimal for strong excitation, and γ_2 is a significant energy sink for saturation. From the properties of quadratic dispersion relations, a necessary and sufficient condition for modes with growth rates with opposite signs is $|b_r| < \rho^{1/2}|\cos(\phi/2)|$. When $|b_r| \ll \rho^{1/2}|\cos(\phi/2)|$ growth and damping rates are comparable. All models, except drift thermal turbulence and ionization driven turbulence, have $b_r > 0$. With instability for $(-b_r + \rho^{1/2}|\cos(\phi/2)|)/2 > 0$, it is always possible for the system to be sufficiently close to threshold of instability so that $|\gamma_2| = (b_r + \rho^{1/2}|\cos(\phi/2)|)/2 \gg (-b_r + \rho^{1/2}|\cos(\phi/2)|)/2 = \gamma_1$. This means that sufficiently near threshold of instability, damped eigenmode effects are weak for two-field systems. For three-field systems it is possible to have conjugate paired eigenmodes with a third neutral mode, such that growth and damping rates are matched near threshold [24].

There can be some situations in which $D_1(C_2+C_3)/C_1^2$ can be vastly different from unity. The factors C_1, C_2, C_3 and D_1 have almost identical expressions except for variation in the eigenvectors R_1 and R_2. This combination can be different from unity only when R_1 or R_2 assumes values that are greatly different from unity, in combination with either A_j or B_j vanishing. Furthermore, this combination is averaged over k', smoothing the wavenumber dependencies of R_1 and R_2, leaving the parametric dependencies to govern when these quantities are large or small. For the sake of discussion assume that the coefficients A_j and B_j, if not zero identically, are all the same order of magnitude. There are four cases, two each for A-type and B-type nonlinearities. A-type nonlinearities arise from $\mathbf{E} \times \mathbf{B}$ advection of field F_1 and vorticity. For A-type nonlinearities, $D_1(C_2+C_3)/C_1^2$ goes like $(A_1R_2 - A_2R_2)(A_1R_1 - A_2R_1)/(A_1R_1 - A_2R_2)^2$. This is akin to a reduced mass $R_1R_2/(R_1-R_2)^2$, which yields $D_1(C_2+C_3)/C_1^2 \ll 1$ whenever R_1/R_2 is much greater than or much less than unity. B-type nonlinearities arise from parallel advection along magnetic field lines that are bent by magnetic fluctuations. For B-type nonlinearities, $D_1(C_2+C_3)/C_1^2$ reduces crudely to $(B_1 - B_2R_1^2)/(B_1 - B_2R_1R_2)$, which too can be much larger or much smaller than unity for exceptional values of R_j. The four cases are summarized

as follows: Case 1) $B_j = 0$, $R_2 \gg R_1$; Case 2) $B_j = 0$, $R_1 \gg R_2$; Case 3) $A_j = 0$, $R_1 \gg 1$, $R_1 \gg R_2$; Case 4) $A_j = 0$, $R_1 R_2 \gg 1$, $R_2 \gg R_1$. In the next few sections we will discuss the models individually and describe which, if any, of these situations arise in them.

To verify the predictions of P_t, we look at the energy in saturation. The energy can be defined as proportional to $\sum_k |F_1(k)|^2 + K(k)|F_2(k)|^2$, where K is a real function of wavenumber and model parameters. This K is chosen such that the energy is conserved by the nonlinearities. Eigenmode decomposition (Eq. 2.16) gives energy proportional to $\sum_k \{(|R_1|^2+K)|\beta_1|^2+(|R_2|^2+K)|\beta_2|^2+[2Re(R_1^* R_2\langle\beta_1^*\beta_2\rangle+2KRe\langle\beta_1^*\beta_2\rangle]\}$. The first term is the energy in the unstable modes, the second term is the energy in damped modes and the last term is a mixed term containing both damped and growing mode amplitudes. The mixed term arises from non-orthogonal eigenmodes and can be large and either positive or negative. In analyzing the models we compare the saturation energies of damped and growing modes, and the energy injection and damping rates from the growing and stable modes to evaluate the relative importance of damped modes.

Next we look at each model individually including its dispersion relation, P_t parameter and the excitation of damped modes. Then we study the energetics in more detail along with damped mode effects on quasilinear heat fluxes.

2.3 Survey of 2 field fluid models

2.3.1 Trapped electron mode turbulence (TEM)

TEM turbulence is a core fluctuation in tokamaks requiring that the collisional detrapping rate be less than the bounce frequency. The equations are,

$$\frac{\partial n}{\partial t} + \nu(n-\phi) + \nu_D(1+\alpha\eta_e)\frac{\partial \phi}{\partial y} = \nabla\phi \times \hat{z}\cdot\nabla n, \tag{2.26}$$

$$\frac{\partial}{\partial t}(1-\nabla^2-\epsilon^{1/2})\phi - \epsilon^{1/2}\nu(n-\phi) + \nu_D[1-\epsilon^{1/2}(1+\alpha\eta_e)]\frac{\partial\phi}{\partial y} = -\nabla\phi\times\hat{z}\cdot\nabla\nabla^2\phi. \tag{2.27}$$

Upon Fourier transformation, this two-field reduction of TEM turbulence [22] has $F_1 = n_k = \epsilon^{-1/2} n_{tr} + \phi_k$, where n_{tr} is the density of trapped electrons, F_2 is the electrostatic potential

ϕ_k, and ϵ is the inverse aspect ratio of the flux surface of interest. The nonlinearities are electrostatic with $A_1 = -\mathbf{k}' \times \hat{\mathbf{z}} \cdot \mathbf{k}$ arising from $\mathbf{E} \times \mathbf{B}$ advection of the density and $A_2 = -(\mathbf{k}' \times \hat{\mathbf{z}} \cdot \mathbf{k})[(k-k')^2 - k'^2]/2(1+k^2-\epsilon^{1/2})$ arising from advection of the vorticity (k is normalized to the ion sound gyroradius ρ_s). The linear coupling coefficients are $Z_{11} = \nu$, $Z_{12} = -\nu + ik_y v_D \hat{\alpha}$, $Z_{21} = -\epsilon^{1/2}\nu/(1+k^2-\epsilon^{1/2})$, and $Z_{22} = [\epsilon^{1/2}\nu + ik_y v_D(1-\epsilon^{1/2}\hat{\alpha})]/(1+k^2-\epsilon^{1/2})$, where ν is the detrapping rate, v_D is the diamagnetic frequency, and $\hat{\alpha}$ is a parameter of order unity proportional to the electron density gradient drive. The eigenfrequencies are given by

$$\omega = \frac{k_y v_D(1-\hat{\alpha}\epsilon^{1/2}) - i\nu(1+k^2)}{2(1+k^2-\epsilon^{1/2})} \pm \left\{ \frac{\left[k_y v_D(1-\hat{\alpha}\epsilon^{1/2}) - i\nu(1+k^2)\right]^2}{4\left[1+k^2-\epsilon^{1/2}\right]^2} + \frac{ik_y v_D \nu}{(1+k^2-\epsilon^{1/2})} \right\}^{1/2}. \tag{2.28}$$

The growth rates are comparable and of opposite sign if $\rho^{1/2}|\cos(\phi/2)| \gg b_r$, which translates to $k_y v_D \gg \nu$. This defines the weakly collisional regime, sometimes referred to as "collisionless". In this limit $\mathrm{Im}Z_{12} \approx \mathrm{Im}Z_{22} \gg \mathrm{Re}Z_{11}$, $\mathrm{Re}Z_{12}$, $\mathrm{Re}Z_{21}$, and $\mathrm{Re}Z_{22}$. On the other hand, if $\nu \gg k_y v_D$ (dissipative regime), the damped mode has a damping rate proportional to ν, while the growth rate of the unstable mode is much smaller (proportional to $k_y^2 v_D^2/\nu$). In this case, no imaginary part of Z_{ij} is larger than a real part. As a result, $(2-\gamma_2/\gamma_1)^{-1}$ is of order unity in the weakly collisional case, and much smaller than unity in the dissipative case.

It remains to determine the ratio of coupling coefficients, $D_1(C_2+C_3)/C_1^2$, in the two limits. In the weakly collisional limit the eigenvector components go as $R_1 \sim \mathrm{O}(1)$, $R_2 \sim \mathrm{O}(k_y v_D/\nu) \gg 1$. With $R_2 \gg R_1$, the ratio of nonlinear coupling coefficients in P_t can assume values that are greater than unity. For turbulence whose spectrum is contained within a long wavelength range $A_2 \ll A_1$. Furthermore, weak dispersion ($k^2 \ll 1$) leads to a situation in which $D_1/C_1 \sim \mathrm{O}(1)$, and $(C_2+C_3)/C_1 \sim \mathrm{O}(k_y^2 v_D^2/\nu^2)$. Thus, P_t is larger than unity, and the damped eigenmode is expected to saturate the linear instability. For a spectrum contained within a short wavelength range where $A_2 \approx A_1$, $A_2 R_2$ dominates C_1, C_2, and C_3, while the lowest order term of R_1 governs D_1. The result is $(C_2+C_3)/C_1 \sim \mathrm{O}(1)$, $D_1/C_1 \sim \mathrm{O}(\nu/k_y v_D)$. Now $P_t < 1$, and damped eigenmodes play a weaker role in saturation.

In the dissipative limit the eigenvector coefficients are $R_1 \sim \mathrm{O}(1)$, $R_2 \sim \mathrm{O}(1)$, leading to

$(C_2 + C_3)/C_1 \sim \nu/k_y v_D \gg 1$ and $D_1/C_1 \sim 1$ in the long wavelength limit. The nonlinear transfer to the damped eigenmode is strong, but the damping rate is so large that $(2-\gamma_2/\gamma_1)^{-1} \sim k_y^2 v_D^2/\nu^2$, making P_t small in spite of the strong coupling. The damped eigenmode is therefore expected to have a small amplitude in saturation relative to the growing eigenmode. In the short wavelength range, the nonlinear coupling is weaker.

Numerical evaluation of P_t in the weakly collisional limit and in an intermediate wavenumber range gives values of P_t that are slightly below unity. Specifically, $P_t = 0.39$ and 0.38, for (k_x, k_y)=(0.5,0.6) and (0.2,-0.5) respectively. Here we have averaged P_t over k' as for all other models in this chapter. For longer wavelengths, P_t is larger. Energy evolution in the weakly collisional regime for intermediate wavenumbers has been shown in Fig. 2 of Ref. [22], and the figure confirms that the damped eigenmode reaches a level in saturation that is similar to that of the growing mode. In contrast, numerical evaluation of P_t in the dissipative limit yields values of 0.0058 and 0.048 for (k_x, k_y)=(0.4,0.6) and (0.2,0.5) respectively. In this case the damped eigenmode energy is five orders of magnitude lower than the energy of the growing eigenmode.

More germane to the question of saturation is the rate of energy dissipation by the damped eigenmode compared to energy injection rate by the instability. These two rates are estimated as $\sum_k \gamma_1(k)(|R_1|^2 + K)|\beta_1|^2$ and $|\sum_k \gamma_2(k)(|R_2|^2 + K)|\beta_2|^2|$ respectively, where $K = 1 + k^2 - \epsilon^{1/2}$. We show a direct comparison between these two rates in Fig. 2.1(a), which plots the ratio of these two energy rates versus ν/v_D. It is seen that these two rates are comparable over the weakly collisional regime. As collisions begin to dominate, the rate of energy dissipated by the damped eigenmode becomes smaller relative to the energy injection rate. The same data are plotted as a function of $-\gamma_2/\gamma_1$ in Fig. 2.1(b). Here we find the striking result that the energy rates remain in balance even as $-\gamma_2/\gamma_1$ increases to values of more than 100. This indicates that even when the damped eigenmode amplitude drops off as $|\gamma_2|$ increases well above γ_1, the drop off is offset by the increasing damping rate, keeping the dissipation rate in balance with energy injection rate. The damped mode not only achieves a significant level in the weakly collisional case, but it provides the primary energy sink for saturation.

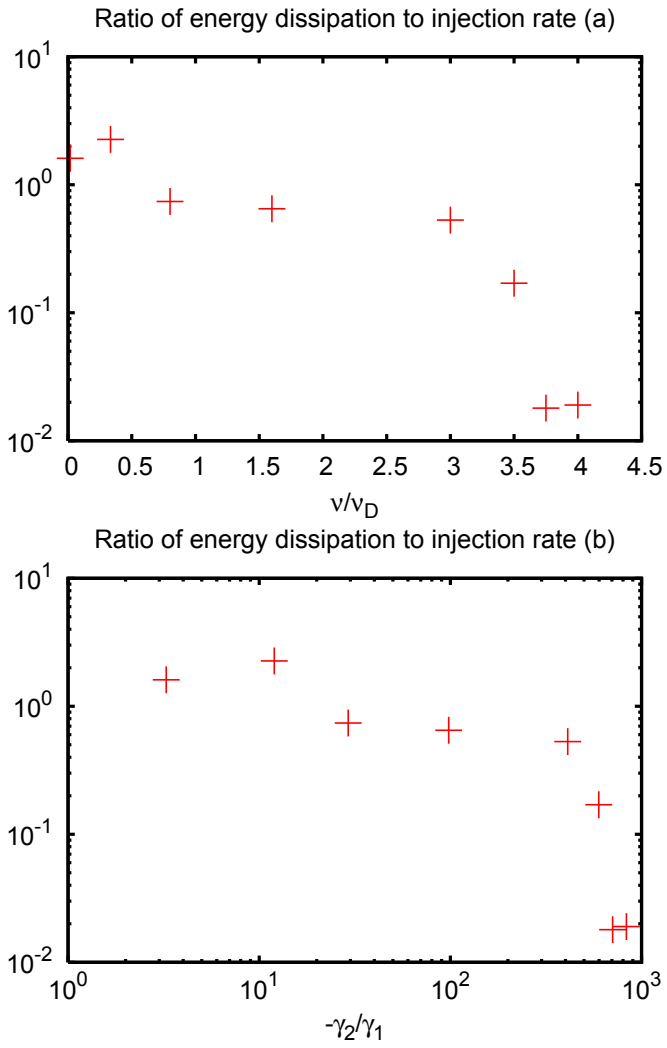

Figure 2.1: Ratio of energy dissipation by damped modes to energy injection by unstable modes in TEM. (a) as a function of ν/ν_D and (b) as a function of $-\gamma_2/\gamma_1$, calculated at the most unstable wavenumber.

2.3.2 Local Hasegawa-Wakatani turbulence

The Hasegawa-Wakatani (HW) model applies when the detrapping collision rate exceeds the bounce frequency [33]. Like the 2 field ITG, its equations are also derived from the momentum and density continuity equation of ions. However, due to the high collisionality, the electron fluid is assumed to be isothermal. This closes the equations by relating the current density to ion density and electrostatic potential via quasineutrality and force balance of electric field with electron pressure gradient and collisional resistive force. The larger collisionality relative to TEM makes this model relevant towards the edge of hot tokamaks, or in colder plasmas [34]. This model has been widely studied [33–35], but damped eigenmodes have not been considered. The fluctuation fields are the passing electron density (n) for F_1 and electrostatic potential (ϕ) for F_2. Like the TEM model, the nonlinearities are electrostatic density advection in the density equation and advection of vorticity in the vorticity equation. The equations are

$$\frac{\partial n}{\partial t} + v_D \frac{\partial \phi}{\partial y} + \frac{k_z^2 V_e^2}{\nu_e}(n-\phi) - D\nabla_\perp^2 n = \nabla\phi \times \hat{z} \cdot \nabla n, \tag{2.29}$$

$$\frac{\partial}{\partial t}\nabla_\perp^2 \phi + \frac{k_z^2 V_e^2}{\nu_e}(n-\phi) + \nu_{in}\nabla_\perp^2\phi - \mu_{ii}\nabla_\perp^4\phi = \nabla\phi \times \hat{z} \cdot \nabla\nabla^2\phi. \tag{2.30}$$

After Fourier transforming, the linear coupling coefficients are $Z_{11} = k_z^2 V_e^2/\nu_e + Dk^2$, $Z_{12} = -k_z^2 V_e^2/\nu_e + ik_y v_D$, $Z_{21} = -k_z^2 V_e^2/\nu_e k^2$, and $Z_{22} = k_z^2 V_e^2/\nu_e k^2 + \nu_{in} + \mu_{ii}k^2$, where V_e is the electron thermal velocity, ν_e is the electron collision rate, D is a collisional diffusivity of electron density, $k^2 = k_x^2 + k_y^2$ here and in the rest of the chapter, v_D is the ion diamagnetic drift velocity in normalized units, i.e., $(-1/n_0)(\mathrm{d}n_0/\mathrm{d}x)$, ν_{in} is an ion neutral drag, and μ_{ii} is an ion-ion viscosity. In the three dimensional model k_z is a Fourier wavenumber, but in two dimensions we treat it as an input parameter. This will apply in all the models of this chapter where k_z appears. This model also has A type nonlinearities with $A_1 = -\mathbf{k}' \times \hat{\mathbf{z}} \cdot \mathbf{k}$ and $A_2 = -(\mathbf{k}' \times \hat{\mathbf{z}} \cdot \mathbf{k})[(k-k')^2 - k'^2]/2k^2$.

Writing $k_z^2 V_e^2/\nu_e = \Omega_{||}$, the eigenfrequencies are

$$\omega = -\frac{i}{2}\Big[\Omega_{||}\Big(1+\frac{1}{k^2}\Big) + Dk^2 + \nu_{in} + \mu_{ii}k^2\Big] \pm \frac{i}{2}\Bigg\{\Big[\Omega_{||}\Big(1-\frac{1}{k^2}\Big) + Dk^2 - \nu_{in} - \mu_{ii}k^2\Big]^2 + (4\Omega_{||}/k^2)(\Omega_{||} - ik_y v_D)\Bigg\}^{1/2}. \quad (2.31)$$

This dispersion leads to a nearly conjugate pair of eigenmodes if $k_y v_D \gg \Omega_{||}$, Dk^2, ν_{in}, and μ_{ii},

$$\omega_{1,2} = \pm i\frac{(1-i)}{\sqrt{2}}\Big(\frac{k_y v_D \Omega_{||}}{k^2}\Big)^{1/2} + \mathrm{O}(\Omega_{||}). \quad (2.32)$$

The condition $\Omega_{||} \ll k_y v_D$ can be rewritten using Eq. (2.32) to replace $k_y v_D$ by $\omega^2 k^2/\Omega_{||}$, yielding $k_z^2 V_e^2/\nu_e\omega \ll k \approx 1$. The factor on the left of the inequality is known as the adiabatic parameter, and the inequality defines the hydrodynamic regime of HW. We find that the hydrodynamic regime has growing and damped eigenmodes with $-\gamma_2 \sim \gamma_1$. The conjugate pairing makes R_1 and R_2 comparable, leading to comparable coupling coefficients C_j and D_1. The parameter P_t is therefore expected to be order unity, and the damped eigenmode is predicted to reach a significant level. Numerical evaluation of P_t yields values of 7.9 and 0.2 for (k_x, k_y)=(0.3,1.1) and (-0.1,0.2) respectively. In this regime $\mathrm{Im}Z_{12} \gg \mathrm{Re}Z_{11}$, $\mathrm{Re}Z_{12}$, $\mathrm{Re}Z_{21}$, $\mathrm{Re}Z_{22}$.

The limit $k_y\nu_D \lesssim \Omega_{||}$ is known as the adiabatic limit. Here $\mathrm{Im}Z_{12}$ is smaller than $\mathrm{Re}Z_{11}$, $\mathrm{Re}Z_{12}$, $\mathrm{Re}Z_{21}$, $\mathrm{Re}Z_{22}$. When $|Dk^2 - \nu_{in} - \mu_{ii}k^2|$ is either much larger or much smaller than $|1 - 1/k^2|\Omega_{||}$ both eigenmodes are damped. Otherwise there is an unstable mode whose growth rate is much smaller than the damping rate. Numerical evaluation of P_t yields values of 0.04 and 0.03 for (k_x, k_y)=(0.1,-0.6) and (-0.3,0.5) respectively.

Numerical simulation shows that the damped mode energy is comparable to the growing mode energy in the hydrodynamic regime and much smaller in the adiabatic regime, consistent with the calculated values of P_t in the two regimes. Dissipation rates behave in a like fashion as seen in Fig. 2.2. The damped eigenmode decay rate is nearly as large as the growing mode growth rate in the hydrodynamic regime and becomes much smaller as $k_z^2 V_e^2/\nu_e\omega$ becomes large.

In the local approximation, $\nabla_{||} \to ik_z = constant$, the HW and TEM models are very similar.

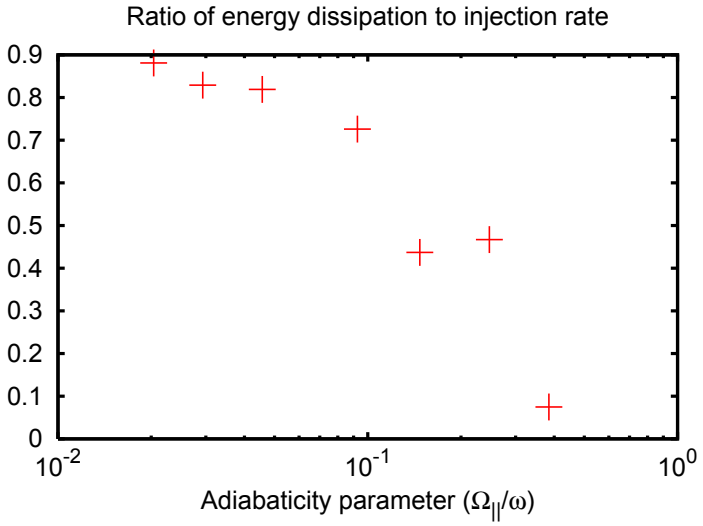

Figure 2.2: As the adiabaticity parameter is made smaller the damped modes play an increasingly important role in saturation as evidenced by the increasing of fraction of energy injected being dissipated by them.

Both models have terms in both equations proportional to the difference of density and potential. The constant of proportionality is the adiabatic parameter (multiplied by ω) in HW and $\nu/k_y v_D$ in TEM. In both systems, when the constant of proportionality is large, n and ϕ must be nearly equal to maintain a balance with any other term in the equations. With $n \approx \phi$ the dynamics is reducible to a single field and dominated by a single eigenmode. When the parameter is small, n and ϕ are independent and two eigenmodes are present at finite amplitude. Both constants of proportionality directly relate to the linear coupling rule and P_t. It is well known that adiabatic and hydrodynamic regimes are different. It is seen here that a crucial aspect of this difference is damped eigenmode dissipation, which saturates the turbulence in the hydrodynamic regime.

2.3.3 Drift thermal turbulence

This system models fluctuations in the tokamak scrape-off layer driven by atomic physics [36]. The fields F_1 and F_2 are electron temperature (T) and electrostatic potential (ϕ) respectively.

The two-field equations are

$$\frac{\partial T}{\partial t} - \gamma_T T + \frac{2}{3}\alpha\chi\nabla_\parallel^2(\phi - \alpha T) - \chi_\perp \nabla^2 T - \chi_\parallel \nabla_\parallel^2 T + v_{*T}\frac{\partial \phi}{\partial y} = \nabla\phi \times \hat{z} \cdot \nabla T, \tag{2.33}$$

$$\frac{\partial}{\partial t}\nabla^2\phi + \chi\nabla_\parallel^2(\phi - \alpha T) = \nabla\phi \times \hat{z} \cdot \nabla\nabla^2\phi. \tag{2.34}$$

The nonlinearities are advection of temperature and vorticity, making them electrostatic A-type nonlinearities. After Fourier transforming, the linear coupling coefficients are $Z_{11} = -\gamma_T + (2/3)\alpha^2\chi k_z^2 + \chi_\perp k^2 + \chi_\parallel k_z^2$, $Z_{12} = -(2/3)\alpha\chi k_z^2 + ik_y v_{*T}$, $Z_{21} = -\chi\alpha k_z^2/k^2$ and $Z_{22} = \chi k_z^2/k^2$, where χ is the electron parallel resistive diffusivity, $\chi_\perp$ and $\chi_\parallel$ are perpendicular and parallel thermal conductivities, $\alpha = 1.71$ is a constant, γ_T represents the effect of radiative cooling, and v_{*T} is a diamagnetic velocity associated with temperature advection [36]. This model also has A type nonlinearities with $A_1 = -\mathbf{k}' \times \hat{\mathbf{z}} \cdot \mathbf{k}$ and $A_2 = -(\mathbf{k}' \times \hat{\mathbf{z}} \cdot \mathbf{k})[(k - k')^2 - k'^2]/2k^2$. Radiative cooling makes a negative contribution to $\mathrm{Re}Z_{11}$, allowing instability from negative dissipation. This model can also have instability through the diamagnetic frequency $k_y v_{*T}$, which appears in $\mathrm{Im}Z_{12}$. If $k_y v_{*T}$ is large, $\mathrm{Im}Z_{12}$ is larger than the other components of Z_{ij}.

Simplifying notation with $\gamma_c \equiv \gamma_T - (2/3)\alpha^2\chi k_z^2 - \chi_\perp k^2 - \chi_\parallel k_z^2$, the eigenfrequencies are

$$\omega_{1,2} = \frac{i}{2}\left(\gamma_c - \frac{\chi k_z^2}{k^2}\right) \pm \frac{i}{2}\left\{\left(\gamma_c + \frac{\chi k_z^2}{k^2}\right)^2 - 4\frac{\chi k_z^2 \alpha}{k^2}\left(ik_y v_{*T} - \frac{2}{3}\alpha\chi k_z^2\right)\right\}^{1/2}. \tag{2.35}$$

When $(4\chi k_z^2\alpha/k^2)(ik_y v_{*T} - 2\alpha\chi k_z^2/3)$ inside the radical is smaller than the other term $(\gamma_c + \chi k_z^2/k^2)^2$, the growth rate is $\gamma_1 \approx \gamma_c$ and the damping rate is $\gamma_2 \approx -\chi k_z^2/k^2$. This is the regime of the radiative cooling drive associated with negative $\mathrm{Re}Z_{11}$. While the eigenvectors have $|R_1| \gg |R_2|$, this doesn't affect the factor $D_1(C_2 + C_3)/C_1^2$, which stays close to unity. If $\gamma_c \gg \chi k_z^2/k^2$ the growth is stronger than damping, and $P_t \sim 1$ is expected. Numerical evaluation gives $P_t = 0.72$ and 0.70 for $(k_x, k_y) = (0.6, 0.4)$ and (-0.2,0.9) respectively, indicating damped modes are significant. If $\gamma_c \ll \chi k_z^2/k^2$ the damping becomes very strong and we should get $P_t \ll 1$. Numerically, P_t is 0.001 and 0.002 for $(k_x, k_y) = (0.5, -0.1)$ and $(0.0, 0.5)$.

Large diamagnetic frequency makes $(4\chi k_z^2\alpha/k^2)(ik_y v_{*T} - 2\alpha\chi k_z^2/3) \gg (\gamma_c + \chi k_z^2/k^2)^2$, re-

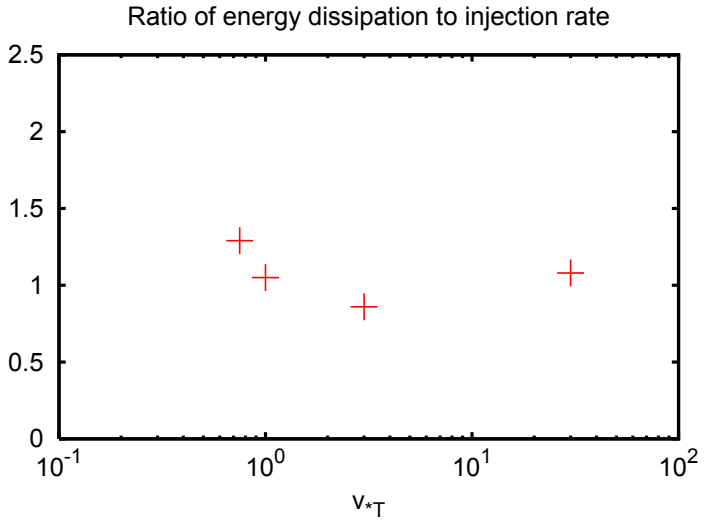

Figure 2.3: Ratio of time averaged dissipation rate of damped modes to energy injection rate by unstable modes, as a function of the diamagnetic velocity v_{*T}.

sulting in almost equal growth and damping rates $\gamma_{1,2} \approx \pm(\chi k_z^2 \alpha k_y v_{*T}/2k^2)^{1/2}$, assuming $k_y v_{*T} \gg \alpha\chi k_z^2$. With matched growth and damping rates, $|R_1| \sim |R_2|$, leading to $P_t = 1.6$ and 0.51 for $(k_x, k_y) = (0.6, 0.3)$ and $(-0.1, -0.4)$ respectively. Energy dissipation and injection rates are compared in Fig. 2.3. Their ratio is of order unity for a large range of diamagnetic velocities, which shows that damped modes saturate turbulence over a wide parameter range. For several points on this plot the damping rate of the damped mode, which is proportional to $|\beta_2|^2$, is larger than the energy input rate of the instability (proportional to $|\beta_1|^2$). The difference arises because the nonorthogonality of the eigenmodes produces additional energy change through terms that are proportional to $\beta_1\beta_2^*$ and its complex conjugate. This change in the present case slightly enhances the energy injection rate, requiring the larger damping rate. The eigenmode cross correlation terms are shown explicitly in Eqs. (2.61) and (2.63).

2.3.4 Ionization driven turbulence

Similar to the previous model, ionization driven turbulence describes fluctuations driven by atomic physics in the scrape-off layer of tokamaks [37]. The two fields of this model are ion parallel velocity ($v_\parallel$) for F_1 and electrostatic potential (ϕ) for F_2. The nonlinearities are advection

of parallel flow and a nonlinearity in the F_2 equation that combines advection of electron density and vorticity [38]. These are A-type nonlinearities. The equations are

$$\frac{\partial v_\parallel}{\partial t} + (\gamma_{cx} - \mu\nabla_\parallel^2)v_\parallel + v_{*v}\frac{\partial \phi}{\partial y} + c_s\nabla_\parallel\phi = \rho_s c_s \nabla\phi \times \hat{z}\cdot\nabla v_\parallel, \tag{2.36}$$

$$\frac{\partial}{\partial t}(1-\rho_s^2\nabla_\perp^2)\phi + c_s\nabla_\parallel v_\parallel + v_{*\phi}\frac{\partial\phi}{\partial y} - \left(\gamma_I + D\frac{\partial^2}{\partial y^2}\right)\phi = \\ -\rho_s^3 c_s \nabla\phi\times\hat{z}\cdot\nabla\nabla_\perp^2\phi - L_n D\nabla\frac{\partial\phi}{\partial y}\times\hat{z}\cdot\nabla\phi. \tag{2.37}$$

After Fourier transforming, the linear coupling coefficients are $Z_{11} = \gamma_{cx} + \mu k_z^2$, $Z_{12} = i(k_y v_{*v} + k_z c_s)$, $Z_{21} = ik_z c_s/(1+k^2\rho_s^2)$, and $Z_{22} = -(\gamma_I - Dk_y^2)/(1+k^2\rho_s^2) + ik_y v_{*\phi}/(1+k^2\rho_s^2)$, where γ_I and γ_{cx} are the ionization and charge exchange rates, μ is a parallel viscosity, $D = 1.71 v_{*\phi}^2\eta_e/\chi_\parallel k_z^2$, η_e is the ratio of electron density gradient scale length (L_n) to temperature gradient scale length, $\chi_\parallel$ is the parallel thermal conductivity, k_z is an average parallel wavenumber, c_s is the ion sound speed, ρ_s is the ion sound gyroradius, $v_{*\phi}$ is the diamagnetic drift velocity, and v_{*v} is the diamagnetic drift velocity for parallel velocity. This model is like the drift thermal model, and different from the other models, because instability can be driven by its negative values of dissipation. Here it is $\mathrm{Re}Z_{22}$ that can be negative, representing the destabilizing effect of ionization. However, the model can also have instability associated with large diamagnetic terms. This model also has A type nonlinearities with $A_1 = -\rho_s c_s(\mathbf{k}'\times\hat{\mathbf{z}}\cdot\mathbf{k})$ and

$$A_2 = \frac{(\mathbf{k}'\times\hat{\mathbf{z}}\cdot\mathbf{k})}{(1+k^2\rho_s^2)}\left\{iL_n D k_y' - \frac{\rho_s^3 c_s}{2}[(k-k')^2 - k'^2]\right\}. \tag{2.38}$$

Defining $\gamma_c \equiv -\gamma_{cx} - \mu k_z^2 - (Dk_y^2/\hat{b}) + (\gamma_I/\hat{b})$ and $\hat{b} \equiv 1 + k^2\rho_s^2$, the eigenfrequencies are

$$\omega_{1,2} = \frac{i}{2}\left(\gamma_c - \frac{ik_y v_{*\phi}}{\hat{b}}\right) \pm \frac{i}{2}\left\{\left(\gamma_{cx} + \mu k_z^2 + \frac{\gamma_I - Dk_y^2 - ik_y v_{*\phi}}{\hat{b}}\right)^2 - 4\frac{k_z c_s}{\hat{b}}(k_y v_{*v} + k_z c_s)\right\}^{1/2}. \tag{2.39}$$

The regime of ionization drive occurs when the term $(\gamma_{cx} + \mu k_z^2 + (\gamma_I - Dk_y^2 - ik_y v_{*\phi})/\hat{b})^2$ is

much larger than the other term inside the radical. This yields a growth rate $\gamma_1 \approx (\gamma_I - Dk_y^2)/\hat{b}$ and a damping rate $\gamma_2 \approx -\gamma_{cx} - \mu k_z^2$. If $Dk_y^2 \lesssim \gamma_I$ and $\gamma_I \sim \gamma_{cx}$, the damping is very strong and $P_t(k,k')$ is around 10^{-5} for all (k,k') except $k'_y = 0$. This implies that the damped modes do not play a strong role in saturation and this has been verified in simulations. If $\gamma_I \sim \gamma_{cx} \gg Dk_y^2, \mu k_z^2$ then the damping and growth rates are comparable. However, in this case $|R_2| \gg |R_1|$ and for A-type nonlinearities this leads to $D_1(C_2 + C_3)/C_1^2 \ll 1$. As a result, P_t turns out to be similar to the case before and damped modes again do not play a role. This case is illustrated in Fig. 2.4 where the energy in damped modes is three orders of magnitude lower than the total energy. There is one more case when $\gamma_I \gg \gamma_{cx}, Dk_y^2, \mu k_z^2$. Here, the growth is very strong compared to the damping but still $|R_2| \gg |R_1|$ leading to P_t values of around 10^{-5}. Thus stable modes do not affect saturation, as verified in simulations. Comparing to drift thermal turbulence, the other negative dissipation model, we note that both have regimes where the growing and damped modes have comparable rates. However, nonlinear coupling is sufficient to excite damped eigenmodes to a significant level for drift thermal turbulence but not for ionization driven turbulence.

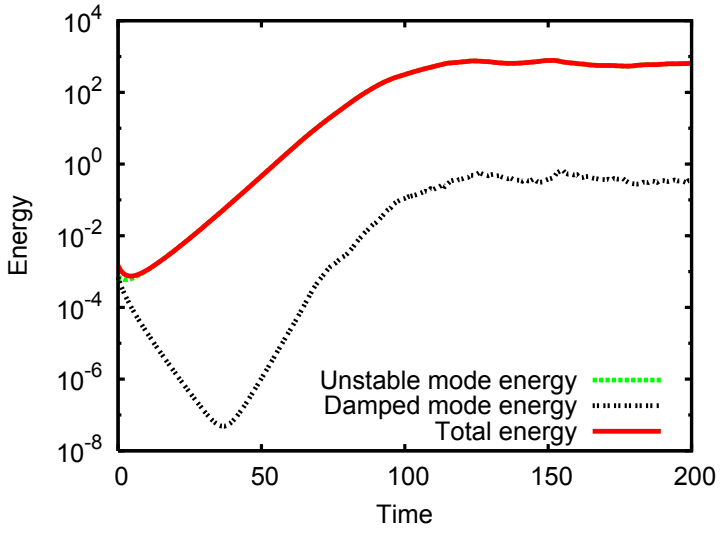

Figure 2.4: Time trace of energy in ionization driven drift wave turbulence. The energy in damped modes is three orders of magnitude less than the total energy, which lies almost exactly on top of the energy in unstable modes.

There is a regime of gradient driven instability occurring when the term $[\gamma_{cx} + \mu k_z^2 + (\gamma_I -$

$Dk_y^2 - ik_y v_{*\phi})/\hat{b}]^2$ is much smaller than the other term inside the radical. Unlike the previous models, Re$Z_{12} = 0$ and $Z_{12}Z_{21}$ is real and negative for k_y and k_z positive. This causes both modes to be damped or growing depending on the sign of γ_c. A second diamagnetic regime occurs when $k_y v_{*v}$ is the largest rate. If k_z is negative relative to k_y, there is is a pair of growing and damped eigenmodes with comparable rates. The nonlinear coefficient ratio $D_1(C_2 + C_3)/C_1^2$ is also order unity giving P_t values of order unity. Numerical evaluation gives $P_t = 0.72$ and 0.43 for $(k_x, k_y) = (0.4, -0.4)$ and (-0.1,0.2) respectively. Numerical solutions confirm that the damped and growing eigenmode energies are comparable in saturation.

This model is complicated because of its negative dissipation and two diamagnetic frequencies. In the appropriate strong gradient regime it does have significant damped eigenmode activity, like the other models. In the regime of negative dissipation instability, damped eigenmode activity hinges on nonlinear coupling strengths.

2.3.5 Local resistive interchange turbulence

The local resistive interchange instability is driven by pressure gradients and is relevant at the edge of tokamaks and stellarators. It is a three-field electromagnetic model [39] involving the poloidal flux, electrostatic potential, and total pressure, but it can be reduced to a two-field electrostatic model by neglecting the induced electric field. The electrostatic case, which we study here, has F_1 as the pressure (p), F_2 as the electrostatic potential (ϕ), and A-type nonlinearities arising from advection of pressure and vorticity. The equations are

$$\frac{\partial p}{\partial t} + \frac{\partial \phi}{\partial y}\frac{dP_0}{dr} = -\nabla\phi \times \hat{z} \cdot \nabla p, \tag{2.40}$$

$$\frac{\partial}{\partial t}\nabla_\perp^2 \phi + \frac{\nabla_\parallel^2 \phi}{\eta} + \kappa\frac{\partial p}{\partial y} = -\nabla\phi \times \hat{z} \cdot \nabla\nabla^2\phi. \tag{2.41}$$

After Fourier transforming, the linear coupling coefficients are $Z_{11} = 0$, $Z_{12} = ik_y dP_0/dr$, $Z_{21} = -i\kappa k_y/k^2$, and $Z_{22} = k_z^2/\eta k^2$, where P_0 is the equilibrium pressure, dP_0/dr is taken as a parameter, κ is the curvature, and η is the resistivity. This model has A type nonlinearities

with $A_1 = \mathbf{k}' \times \hat{\mathbf{z}} \cdot \mathbf{k}$ and $A_2 = (\mathbf{k}' \times \hat{\mathbf{z}} \cdot \mathbf{k})[(k-k')^2 - k'^2]/2k^2$. With $Z_{11} = 0$ and Z_{22} real this mode does not have negative dissipation. Like ionization driven turbulence it does have $\mathrm{Re}Z_{12} = \mathrm{Re}Z_{21} = 0$, but the product $Z_{12}Z_{21}$ is positive and real. Consequently instability is driven by the pressure gradient, which when weak gives weak instability with a heavily damped, unimportant eigenmode, and when strong gives a regime in which the damped mode is important. The latter corresponds to $(\mathrm{Im}Z_{12})(\mathrm{Im}Z_{21}) > (\mathrm{Re}Z_{22})^2$.

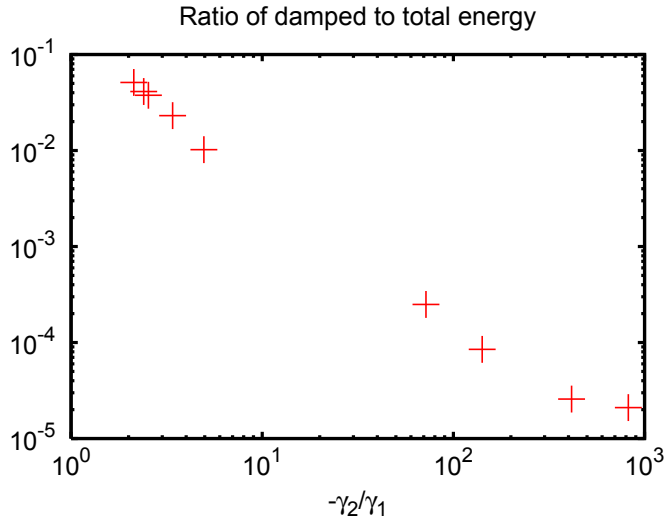

Figure 2.5: Fraction of damped mode energy in total energy in resistive interchange turbulence, as a function of $-\gamma_2/\gamma_1$ calculated at the most unstable wavenumber.

The dispersion relation is $\omega^2 + i(k_z^2/\eta k^2)\omega + \kappa(k_y^2/k^2)(dP_0/dr) = 0$ and the roots are

$$\omega_{1,2} = \frac{-i}{2}\left(\frac{k_z^2}{\eta k^2}\right) \pm \frac{i}{2}\left\{\left(\frac{k_z^2}{\eta k^2}\right)^2 + 4\frac{dP_0}{dr}\frac{\kappa k_y^2}{k^2}\right\}^{1/2}. \tag{2.42}$$

Instability requires that $\kappa(dP_0/dr) > 0$. When $\kappa(k_y^2/k^2)(dP_0/dr) \ll k_z^4/\eta^2 k^4$ then $-\gamma_2 \gg \gamma_1$. In this case $R_1 \gg R_2$ and with A-type nonlinearities this leads to $D_1(C_2 + C_3)/C_1^2 \sim 1$. Because of this, numerical evaluation of P_t gives values of 0.0003 and 0.001 for the wavenumbers (k_x, k_y) = (-0.4,-0.7) and (0.1,-0.8) respectively. In the situation when $k_z^4/\eta^2 k^4 \ll \kappa(k_y^2/k^2)(dP_0/dr)$ the

eigenfrequencies are given by

$$\omega_{1,2} \simeq \frac{-i}{2}\left(\frac{k_z^2}{\eta k^2}\right) \pm \frac{i}{2}\left(\frac{dP_o}{dr}\frac{4k_y^2\kappa}{k^2}\right)^{1/2} \pm \frac{i}{4}\frac{k_z^4/\eta^2 k^4}{[(dP_0/dr)(4k_y^2\kappa/k^2)]^{1/2}}. \tag{2.43}$$

In this case, $-\gamma_2 \sim \gamma_1$ and $|R_1| \sim |R_2|$. This gives P_t values of 2.7 and 0.6 for the wavenumbers $(k_x, k_y) = (0.4, 0.3)$ and $(-0.3, 0.1)$ respectively. Thus damped modes are expected to play a role in saturation of turbulence. Both these cases have been verified in simulations. Fig. 2.5 shows this by plotting the ratio of energy in damped modes to total energy, while in saturation, as the ratio $-\gamma_2/\gamma_1$ is increased by decreasing the driving gradient dP_0/dr. As predicted by P_t, damped mode amplitude decreases as the driving gradient is lowered, with the damped mode unimportant for large values of $-\gamma_2/\gamma_1$.

2.3.6 Rayleigh-Taylor turbulence

The Rayleigh-Taylor instability is driven by pressure gradients in regions of bad field-line curvature [40]. A two-field model for turbulence driven by this instability was studied in Ref. [41], where saturation was described in conventional terms by a cascade to small scales, aided by the shearing of zonal flows. We show here that the damped eigenmode is strongly excited and provides an energy sink in the wavenumber range of the instability. The model has equations for plasma density (n) represented by F_1 and potential (ϕ) represented by F_2, with A-type nonlinearities describing advection of density and vorticity. The equations are

$$\frac{\partial n}{\partial t} + v_g\frac{\partial n}{\partial y} + (v_n - v_g)\frac{\partial \phi}{\partial y} - D\nabla^2 n = \nabla\phi \times \hat{z} \cdot \nabla n, \tag{2.44}$$

$$\frac{\partial}{\partial t}\nabla^2\phi + v_g\frac{\partial n}{\partial y} - \mu\nabla^4\phi = \nabla\phi \times \hat{z} \cdot \nabla\nabla^2\phi. \tag{2.45}$$

After Fourier transforming, the linear coupling coefficients are $Z_{11} = Dk^2 + ik_y v_g$, $Z_{12} = ik_y(v_n - v_g)$, $Z_{21} = -ik_y v_g/k^2$, and $Z_{22} = \mu k^2$, where D is a collisional diffusion coefficient of density, μ is the viscosity, v_g is a normalized gravitational drift arising through curvature, and v_n is the diamagnetic drift. This model also has A type nonlinearities with $A_1 = -\mathbf{k}' \times \hat{\mathbf{z}} \cdot \mathbf{k}$ and

$A_2 = -(\mathbf{k}' \times \hat{\mathbf{z}} \cdot \mathbf{k})[(k-k')^2 - k'^2]/2k^2$. Like the resistive interchange model, this model has positive dissipation, $\mathrm{Re}Z_{12} = \mathrm{Re}Z_{21} = 0$, and $Z_{12}Z_{21}$ real and positive (when $v_n > v_g$). Consequently, turbulence is driven by the gravity and gradient drift terms residing in the imaginary parts of Z_{ij}.

The dispersion relation is $\omega^2 + i(Dk^2 + \mu k^2 + ik_y v_g)\omega - \mu k^2(Dk^2 + ik_y v_g) + (k_y^2/k^2)v_g(v_n - v_g) = 0$, with roots given by

$$\omega = \frac{k_y v_g - i(\mu + D)k^2}{2} \pm \frac{i}{2}\left\{ \left[(D-\mu)k^2 + ik_y v_g\right]^2 + \frac{4v_g k_y^2}{k^2}[v_n - v_g] \right\}^{1/2}. \tag{2.46}$$

When $[(D-\mu)k^2]^2$ is larger than $k_y^2 v_g^2$ and $4(k_y^2/k^2)v_g(v_n - v_g)$, both eigenmodes are damped with damping rates $\gamma_1 = -\mu k^2$ and $\gamma_2 = -Dk^2$. When $[(D-\mu)k^2]^2 \ll |4(k_y^2/k^2)v_g(v_n - v_g) - k_y^2 v_g^2|$ there is a pair of unstable and stable eigenmodes that form a conjugate pair in lowest order, with second order dissipative terms breaking the conjugate symmetry. The eigenfrequencies are

$$\omega_{1,2} \approx \frac{k_y v_g}{2} \mp \frac{v_g(D-\mu)k^2}{2\left[4v_g(v_n - v_g)/k^2 - v_g^2\right]^{1/2}} \pm i\frac{k_y}{k}\left\{ v_g\left[(v_n - v_g) - v_g k^2/4\right]\right\}^{1/2} - \frac{i}{2}(D+\mu)k^2. \tag{2.47}$$

With $-\gamma_2 \approx \gamma_1$, R_1 and R_2 are comparable, as are the coupling coefficients D_1 and C_j. We therefore expect that P_t is nearly unity and that the damped eigenmode plays a significant role in saturation. This is confirmed from numerical evaluation of P_t, which gives values of 0.55 and 0.27 for wavenumbers of $(k_x, k_y) = (0.6, -0.2)$ and (-0.1,-0.4), respectively. Fig. 2.6 shows that the damped modes sink most of the energy input by the instability when the ratio $-\gamma_2/\gamma_1$ is between 1 and 1.5. As in Fig. 2.3, nonorthogonal eigenmodes increase the dissipation rate beyond that produced by $|\beta_1|^2$, making the damping rate larger than the unstable eigenmode injection rate for some of the data points. However, unlike Fig. 2.1(b) where the energy rates remain in balance for a large range of $-\gamma_2/\gamma_1$, in this case the energy dissipation by damped modes becomes insignificant as $-\gamma_2/\gamma_1$ goes over 3.

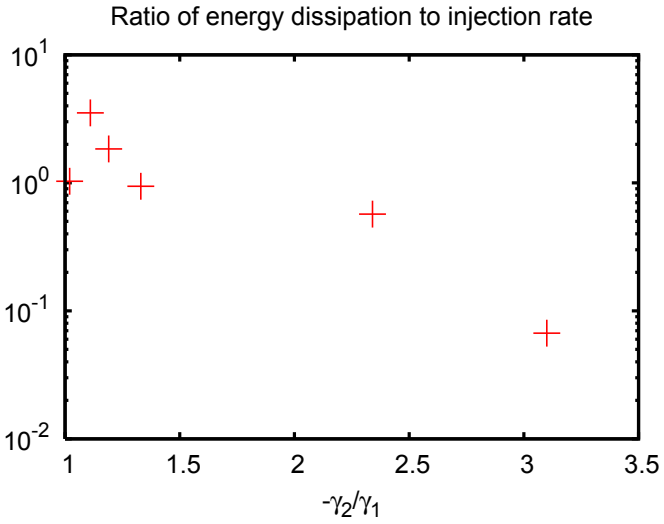

Figure 2.6: Ratio of energy dissipation by damped mode to energy injected by unstable modes in Rayleigh-Taylor turbulence.

2.3.7 Two-field ion temperature gradient turbulence

Ion temperature gradient (ITG) turbulence is driven by an electrostatic instability associated with the ion pressure gradient [31]. It plays a major role in ion confinement in tokamaks. Damped eigenmodes in ITG have been examined for a 3-field model and gyrokinetics. Because there is a two-field ITG model we briefly examine it in connection with the other types of turbulence studied here. This model is useful for tracking zonal flows. The relationship between zonal flows and saturation by damped eigenmodes will be described in the next chapter.

The equations for this model are the Eqs. (2.1-2.2). This model has ion pressure (p) for F_1 and electrostatic potential (ϕ) for F_2. The nonlinearities are type A, corresponding to advection of pressure and vorticity. The linear coupling coefficients are $Z_{11} = \chi k^4$, $Z_{12} = ik_y(1+\eta_i)$, $Z_{21} = -i\epsilon k_y/(1+k^2)$ and $Z_{22} = (\nu k^2 + ik_y)/(1+k^2)$, where χ is a coefficient of collisional hyper diffusion of pressure, $\eta_i = d(ln\ T_i)/d(ln\ n)$ is the ratio of ion density (n) gradient scale length to ion temperature (T_i) gradient scale length, ϵ is the ratio of density gradient scale length to magnetic field variation scale length, and ν is dissipation of flow active at large scales. The nonlinear coupling coefficients are $A_1 = -\mathbf{k}'\times\hat{\mathbf{z}}\cdot\mathbf{k}$ and $A_2 = -(\mathbf{k}'\times\hat{\mathbf{z}}\cdot\mathbf{k})[(k-k')^2-k'^2]/[2(1+k^2)]$. With Re$Z_{11}$ and ReZ_{22} positive the system is unstable through η_i and can be expected to have a

damped mode damping rate that is comparable to the growth rate, when the instability is above threshold.

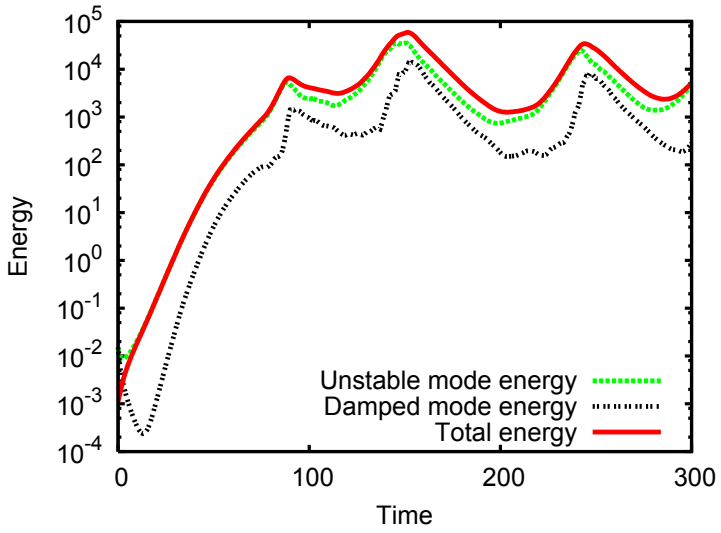

Figure 2.7: Comparison of energy in damped modes with energy in unstable modes and total energy for ITG turbulence.

The dispersion relation is $\omega^2(1+k^2)+\omega[i\chi k^4(1+k^2)-k_y+i\nu k^2]-i\chi k_y k^4-\nu\chi k^6+\epsilon k_y^2(1+\eta_i)=0$ and the roots are

$$\omega_{1,2}=-\frac{i}{2}\left(\chi k^4+\frac{\nu k^2+ik_y}{1+k^2}\right)\pm\frac{i}{2}\left\{\left(\chi k^4-\frac{\nu k^2+ik_y}{1+k^2}\right)^2+\frac{4(1+\eta_i)k_y^2\epsilon}{1+k^2}\right\}^{1/2}. \qquad (2.48)$$

If $[\chi k^4-(\nu k^2+ik_y)/(1+k^2)]^2 \gg (1+\eta_i)k_y^2\epsilon/(1+k^2)$ then both roots are damped with damping $\gamma_1 \approx -\nu k^2/(1+k^2)$ and $\gamma_2 \approx -\chi k^4$. If η_i is larger than the other parameters then we get approximately equal growth and damping rates $\gamma_{1,2} \approx \pm[(1+\eta_i)k_y^2\epsilon/(1+k^2)]^{1/2}$. In this case the eigenvectors R_1 and R_2 have nearly equal magnitude and so P_t is expected to be close to unity. Numerical calculation of P_t gives 0.35 and 0.66 for the wavenumbers $(k_x, k_y) = (0.1, 0.3)$ and $(-0.5, -0.5)$ respectively. Fig. 2.7 shows the verification of this prediction where the energy in damped modes is very close to the total energy.

2.3.8 Microtearing turbulence with time-dependent thermal force

This model was introduced to provide a minimal two-field description of magnetic turbulence in magnetically confined plasmas. Although the fluctuations have been labeled microtearing, they are two dimensional and require the time-dependent thermal force (TDTF) for instability [42]. Without the TDTF the fluctuations are stable and correspond to collisionally damped, counter propagating kinetic Alfvén waves [43]. The model has electron density (n) for F_1 and the parallel component of the magnetic vector potential (ψ) for F_2. The nonlinearites are magnetic, and of type B. They correspond to the gradient of electron pressure along the perturbed magnetic field in Ohm's law (F_2 equation) and compression of electron flow along the perturbed field in the density continuity equation (F_1 equation). The equations are

$$\frac{\partial n}{\partial t} + \frac{\partial}{\partial z}\nabla^2\psi - \mu\nabla^2 n = -\nabla\psi \times \hat{z} \cdot \nabla\nabla^2\psi, \tag{2.49}$$

$$\frac{\partial \psi}{\partial t} - \frac{\alpha\alpha'}{\nu} ik_y \frac{\partial \psi}{\partial t}\frac{dT_0}{dx} - \frac{\partial n}{\partial z} - \eta\nabla^2\psi - (1+\alpha)ik_y\psi\frac{dT_0}{dx} = -\nabla\psi \times \hat{z} \cdot \nabla n. \tag{2.50}$$

After Fourier transforming, the linear coupling coefficients are $Z_{11} = \mu k^2$, $Z_{12} = -ik_z k^2$, $Z_{21} = -ik_z/[1 - i(\alpha\alpha'/\nu_e)k_y dT_0/dx]$, and $Z_{22} = [\eta k^2 - ik_y(1+\alpha)dT_0/dx]/[1 - i(\alpha\alpha'/\nu_e)k_y dT_0/dx]$, where μ is a collisional density diffusivity, α and α' are the order-unity coefficients of the thermal and time-dependent thermal forces, ν_e is the electron collision frequency, T_0 is the electron temperature, and η is the resistivity. The electron temperature gradient $\mathrm{d}T_0/\mathrm{d}x$ is taken as a constant parameter. The B type nonlinear coupling coefficients are $B_1 = -(\mathbf{k}' \times \hat{\mathbf{z}} \cdot \mathbf{k})[(k-k')^2 - k'^2]/2$ and $B_2 = (\mathbf{k}' \times \hat{\mathbf{z}} \cdot \mathbf{k})/[1 - ik_y(\alpha\alpha'/\nu_e)(\mathrm{d}T_0/\mathrm{d}x)]$. This model has positive dissipation. Instability from the TDTF introduces imaginary components of $Z_{12}Z_{21}$ and Z_{22} and should therefore lead to growing and damped modes with comparable rates when the instability is above threshold.

The dispersion relation is given by $\omega^2(1 - ik_y\alpha_T) + i\omega[(\mu+\eta)k^2 - ik_y(\hat{\alpha} + \alpha_T\mu k^2)] - k_z^2k^2 - \mu k^2(\eta k^2 - ik_y\hat{\alpha}) = 0$. Here $\hat{\alpha} \equiv (1+\alpha)(dT_0/dx)$ and $\alpha_T \equiv (\alpha\alpha'/\nu_e)(dT_0/dx)$. The roots of this

equation are

$$\omega_{1,2} = -\frac{i}{2}\left[\mu k^2 + \frac{k_y^2\hat{\alpha}\alpha_T + \eta k^2 + i(\eta k^2 k_y \alpha_T - k_y\hat{\alpha})}{1+k_y^2\alpha_T^2}\right]$$

$$\pm\frac{i}{2}\left\{\left[\mu k^2 - \frac{k_y^2\hat{\alpha}\alpha_T + \eta k^2 + i(\eta k^2 k_y \alpha_T - k_y\hat{\alpha})}{1+k_y^2\alpha_T^2}\right]^2 - 4k_z^2k^2\left(\frac{1+ik_y\alpha_T}{1+k_y^2\alpha_T^2}\right)\right\}^{1/2}. \tag{2.51}$$

When $k_z^2k^2, k_y^2\alpha_T^2 \gg \mu k^2, \eta k^2, k_y\hat{\alpha}$ then the eigenfrequencies become

$$\omega_{1,2} \approx \mp\frac{k_z k}{(1+k_y^2\alpha_T^2)^{1/2}}\left[\frac{1+(1+k_y^2\alpha_T^2)^{1/2}}{2}\right]^{1/2} \mp \frac{ik_z k}{(1+k_y^2\alpha_T^2)^{1/2}}\left[\frac{-1+(1+k_y^2\alpha_T^2)^{1/2}}{2}\right]^{1/2}. \tag{2.52}$$

In this case $\mathrm{Im}Z_{12}$ is larger than the real part of all Z's and so the growth and damping rates are almost equal. The eigenvectors R_1 and R_2 have comparable magnitudes which should lead to P_t values of close to unity. Numerical evaluation of P_t gives 1.1 and 0.23 for wavenumbers $(k_x, k_y) = (0.6, 0.2)$ and $(-0.4, -1.0)$ respectively. We therefore expect damped modes to play a prominent part in saturation for this case. If $k_y^2\alpha_T^2 \lesssim \mu k^2, \eta k^2, k_y\hat{\alpha}$ there is no instability drive as both modes are damped.

2.3.9 Thermal microtearing turbulence

Thermal microtearing turbulence is a variant of microtearing turbulence driven by the TDTF that couples parallel component of magnetic vector potential (ψ) fluctuations to temperature (T) fluctuations [44]. The basic equations are

$$\frac{\partial T}{\partial t} - \frac{2}{3}\frac{\kappa}{n_0}\nabla_\parallel^2(T_0+T) + \frac{2}{3}(1+\alpha)\frac{T_0}{n_o}\nabla_\parallel\nabla^2\psi = 0, \tag{2.53}$$

$$\frac{\partial \psi}{\partial t} - \frac{T_0}{n_0}\nabla_\parallel n_0 - \left(1+\alpha+\frac{\alpha\alpha'}{\nu_e}\frac{\partial}{\partial t}\right)\nabla_\parallel(T_0+T) - \eta\nabla^2\psi = 0, \tag{2.54}$$

where $\nabla_\parallel = \partial/\partial z + \nabla\psi\times\hat{z}\cdot\nabla$. This model becomes quite complicated when put in the standard form of Eqs. (2.3) and (2.4). The electron temperature fluctuation T is F_1 while F_2 is a linear combination of temperature and parallel component of magnetic vector potential ψ given by $F_2 = \hat{\psi}_k \equiv [1 - i(\alpha\alpha'/\nu_e)k_y dT_0/dx]\psi - i(\alpha\alpha'/\nu_e)k_z T$. The linear coefficients are $Z_{11} = (2/3)(\kappa/n_0)k_z^2 +$

$(2/3)(\alpha\alpha'/\nu_e)k_z^2[T_\alpha + iT'_\kappa]/[1 - i(\alpha\alpha'/\nu_e)k_y dT_0/dx]$, $Z_{12} = (2/3)k_z[T'_\kappa - iT_\alpha]$, $Z_{21} = -ik_z(1 + \alpha) + i(\alpha\alpha'/\nu_e)k_z[\eta k^2 - ik_y(T_0/n_0)dn_0/dx - ik_y(1+\alpha)dT_0/dx]/[1 - i(\alpha\alpha'/\nu_e)k_y dT_0/dx]$, and $Z_{22} = [\eta k^2 - ik_y(T_0/n_0)dn_0/dx - ik_y(1+\alpha)dT_0/dx]/[1 - i(\alpha\alpha'/\nu_e)k_y dT_0/dx]$, where $T_\alpha = (1 + \alpha)(T_0/n_0)k^2$, $T'_\kappa = (\kappa/n_0)k_y dT_0/dx$, κ is the collisional parallel thermal conductivity, n_0 is the equilibrium density, and the remaining quantities are the same as those of microtearing turbulence (Sec. 2.3.8). The nonlinearities in this model are very complicated and cannot be written in the form of Eqs. (2.5-2.6). They are,

$$N_1 = \sum_{\mathbf{k}'} \frac{(\mathbf{k}' \times \hat{\mathbf{z}} \cdot \mathbf{k})(2k_z - k'_z)}{[1 - ik'_y(\alpha\alpha'/\nu_e)(\mathrm{d}T_0/\mathrm{d}x)]}[-(\alpha\alpha'/\nu_e)k'_z T_{k'} T_{k-k'} + i\hat{\psi}_{k'} T_{k-k'}] +$$
$$\sum_{\mathbf{k}'} \left\{ \left[i(\mathbf{k}' \times \hat{\mathbf{z}} \cdot \mathbf{k})(k_y - k'_y)\frac{\mathrm{d}T_0}{\mathrm{d}x} + k'_y(k_y - k'_y)\frac{\mathrm{d}^2 T_0}{\mathrm{d}x^2} - \frac{(1+\alpha)T_e}{3n_0}(\mathbf{k}' \times \hat{\mathbf{z}} \cdot \mathbf{k})[(k - k')^2 - k'^2] \right] \right.$$
$$\times \frac{1}{[1 - ik'_y(\alpha\alpha'/\nu_e)(\mathrm{d}T_0/\mathrm{d}x)]} \frac{1}{[1 - i(k_y - k'_y)(\alpha\alpha'/\nu_e)(\mathrm{d}T_0/\mathrm{d}x)]}$$
$$\left. \times \left[\left(i\frac{\alpha\alpha'}{\nu_e} k'_z T_{k'} + \hat{\psi}_{k'} \right) \left(i\frac{\alpha\alpha'}{\nu_e}(k_z - k'_z)T_{k-k'} + \hat{\psi_{k-k'}} \right) \right] \right\}, \tag{2.55}$$

$$N_2 = -(1+\alpha) \sum_{\mathbf{k}'} \frac{(\mathbf{k}' \times \hat{\mathbf{z}} \cdot \mathbf{k})}{[1 - ik'_y(\alpha\alpha'/\nu_e)(\mathrm{d}T_0/\mathrm{d}x)]}[i(\alpha\alpha'/\nu_e)k'_z T_{k'} T_{k-k'} + \hat{\psi}_{k'} T_{k-k'}]. \tag{2.56}$$

The TDTF drive appears in every linear coefficient except Z_{12}, making it difficult to infer eigenmode properties solely from inspection of Z_{ij}. The frequency expression is also sufficiently complicated that little is learned from inspection. The nonlinear coupling coefficients are also extremely complicated. Numerical evaluation shows that when k_z is an appreciable fraction of k_y and $(\alpha\alpha'/\nu_e) > (1 + \alpha)$ there is a pair of growing and damped roots with $-\gamma_2 < \gamma_1$. The eigenvector components have similar magnitude so that P_t should be of order unity. The damped eigenmode is therefore expected to play a significant role in saturation.

2.4 Energetics of damped modes

Following section 2.2 we choose to define the energy in these two field fluid models as $E = (1/2)\sum_k[|F_1(k)|^2 + K(k)|F_2(k)|^2]$. The energy evolution equation becomes, from Eqs. (2.3-2.4),

$$\frac{\mathrm{d}E}{\mathrm{d}t} = \mathrm{Re}\Big\{ \sum_k \big[-Z_{11}|F_1|^2 - Z_{12}F_1^*F_2 - Z_{21}K(k) - Z_{22}K(k)|F_2|^2\big]\Big\} + 2\mathrm{Re}\Big\{ \sum_k \big[F_1^*N_1 + K(k)N_2F_2^*\big]\Big\}. \tag{2.57}$$

The coefficient $K(k)$ is always chosen such that the nonlinear energy term, $\sum_k \mathrm{Re}\{\sum_k \big[F_1^*N_1 + K(k)N_2F_2^*\big]\}$ is zero. This implies that energy is conserved by the nonlinear terms and the only net sources and sinks of the energy are the linear terms. Hence these terms are called non-conservative terms (n.c.),

$$\left.\frac{\mathrm{d}E}{\mathrm{d}t}\right|_{\mathrm{n.c.}} = -\mathrm{Re}\Big[Z_{12}\langle F_2F_1^*\rangle\Big] - K(k)\mathrm{Re}\Big[Z_{21}\langle F_1F_2^*\rangle\Big] - \mathrm{Re}Z_{11}|F_1|^2 - K(k)\mathrm{Re}Z_{22}|F_2|^2. \tag{2.58}$$

The first two terms on the right hand side are proportional to the correlation between the two fields. This correlation also governs the transport flux. The second two terms arise from collisional dissipation of F_1 and F_2. When $\mathrm{Re}Z_{11}$ and $\mathrm{Re}Z_{22}$ are positive these terms damp fluctuation energy, and instability comes from the cross correlation. For the drift thermal and ionization drift wave models $\mathrm{Re}Z_{11}$ and $\mathrm{Re}Z_{22}$ could have negative values, in which case instability could be driven by the last two terms.

To separate the roles of unstable and stable eigenmodes we express the right hand side in terms of the eigenmode amplitudes using the eigenmode decomposition $F_1 = R_1(k)\beta_1 + R_2(k)\beta_2$ and $F_2 = \beta_1 + \beta_2$, yielding,

$$\left.\frac{dE}{dt}\right|_{\mathrm{n.c.}} = \mathcal{C}_u + \mathcal{C}_s + \mathcal{D}_u + \mathcal{D}_s. \tag{2.59}$$

Here

$$\mathcal{C}_u = -\Big[\mathrm{Re}(Z_{12}R_1^*) + K(k)\mathrm{Re}(Z_{21}R_1)\Big]|\beta_1|^2, \tag{2.60}$$

is the cross-correlation term associated with the unstable eigenmode,

$$\mathcal{C}_s = -\Big[\mathrm{Re}(Z_{12}R_2^*) + K(k)\mathrm{Re}(Z_{21}R_2)\Big]|\beta_2|^2$$

$$-\mathrm{Re}\Big[Z_{12}\Big(R_1^*\langle\beta_1^*\beta_2\rangle + R_2^*\langle\beta_1\beta_2^*\rangle\Big)\Big] - K(k)\mathrm{Re}\Big[Z_{21}\Big(R_1\langle\beta_1\beta_2^*\rangle + R_2\langle\beta_1^*\beta_2\rangle\Big)\Big], \tag{2.61}$$

is the cross-correlation term associated with stable eigenmode excitation,

$$\mathcal{D}_u = -\Big[\mathrm{Re}(Z_{11})|R_1|^2 + K(k)\mathrm{Re}(Z_{22})\Big]|\beta_1|^2, \tag{2.62}$$

is the collisional dissipation term associated with the unstable eigenmode, and

$$\mathcal{D}_s = -[\mathrm{Re}(Z_{11})|R_2|^2 + K(k)\mathrm{Re}(Z_{22})]|\beta_2|^2 - 2\mathrm{Re}Z_{11}\mathrm{Re}(R_1R_2^*\langle\beta_1\beta_2^*\rangle) - 2K(k)\mathrm{Re}Z_{22}\mathrm{Re}\langle\beta_1\beta_2^*\rangle, \tag{2.63}$$

is the collisional dissipation term associated with stable eigenmode excitation.

The conventional view of saturation does not account for damped eigenmodes, effectively assuming that $\beta_2 = 0$ and making $\mathcal{C}_s = \mathcal{D}_s = 0$. For conventional saturation $\sum_k \mathcal{C}_u = -\sum_k \mathcal{D}_u$, with $\mathcal{C}_u$ typically large and positive at large scales and $\mathcal{D}_u$ large and negative at small scales. Prior work based on selected fluid models [23],[45],[28] has shown that $\mathcal{C}_s$ is not zero, but negative and a significant fraction of $\mathcal{C}_u$. In this case, the transport flux is significantly reduced from the quasilinear value by the damped eigenmode contribution to the correlation that governs transport. When $\mathcal{C}_s$ is a significant fraction of $\mathcal{C}_u$ damped eigenmodes are said to play a role in saturation. This statement refers to saturation of the *linear instability*, which is represented by $\mathcal{C}_u$.

An important point must be made here. It is true that time irreversible dissipation is only possible by viscous and diffusive terms. However, in this work we are concerned with the removal of energy from the fluctuation spectrum by damped modes, which occurs in two ways. Through the heat flux term, damped modes remove energy out of the turbulence and put it back in the temperature gradient by driving a negative heat flux. This is not irreversible dissipation,

but it definitely does remove energy injected into the turbulence by the linear instability. This reduces the energy input rate drastically. In fact, $\mathcal{C}_s \neq 0$ can equally well be described as a finite-amplitude reduction of the instability growth rate from its linear value associated with $\mathcal{C}_u$. After subtracting this energy removed by the damped modes, a tiny fraction of the linear energy input remains. This is then removed by the viscous (irreversible) dissipation. But even the viscous dissipation terms can be split into unstable and stable mode contributions. In that also we find the stable mode contribution is significant. However, in this study we are focussing on the drastic negative heat flux (C_s) driven by the stable modes that almost completely balances the linear instability driven heat flux. By the term "energy dissipation due to damped modes" we mean both the above processes in which stable modes take part.

The difference $\mathcal{C}_u - |\mathcal{C}_s|$, which sets the reduced growth rate due to the damped eigenmode at finite amplitude, must still be saturated. This is accomplished by $\mathcal{D}_u + \mathcal{D}_s$. In gyrokinetic models for the Cyclone Base Case [46] of ITG turbulence there are a very large number of damped eigenmodes [27]. Some of these modes have values of $|\mathcal{C}_s|$ that are a significant fraction of $\mathcal{C}_u$. However, their effect is not systematic - there are positive and negative values in roughly equal measure, such that in a sum over the eigenmode spectrum, the net value of $\mathcal{C}_s$ is close to zero. In this situation the probability distribution of $\mathcal{C}_s$ peaks near zero, i.e., it has a near zero mean value, even though it is broad [25]. The transport flux, which is proportional to the mean value of $\mathcal{C}_u + \mathcal{C}_s$ is therefore not very different from the quasilinear flux (which is proportional to $\mathcal{C}_u$). In the gyrokinetic models $\mathcal{D}_s$ is both large and systematic in its effect, so that damped eigenmodes govern saturation primarily through collisional dissipation.

The situation for two-field fluid models is quite different, as depicted in Figs. 2.8 and 2.9, which give the values of $\mathcal{C}$ and $\mathcal{D}$ for Rayleigh-Taylor [$K(k) = 1$] and ion temperature gradient turbulence [$K(k) = 1 + k^2$]. In both cases the most significant damped eigenmode effect resides in the cross correlation. The damped eigenmode also contributes to the collisional dissipation at a level somewhat weaker than the contribution of the unstable eigenmode.

These results are consistent with a large reduction of the quasilinear flux. The $\mathbf{E}\times\mathbf{B}$ advection of pressure causes heat flux out of the tokamak. In such fluid models, this is calculated as

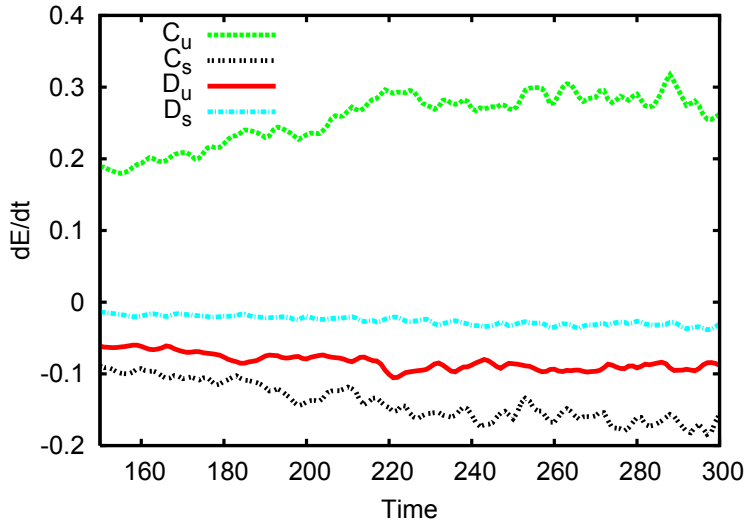

Figure 2.8: Energy dissipation and heat flux in the Rayleigh-Taylor model, breaking them up into unstable and stable mode contributions of Eq. 2.59. The damped modes most significant contribution is to drive a negative heat flux C_s, which balances a large portion of the instability drive, C_u.

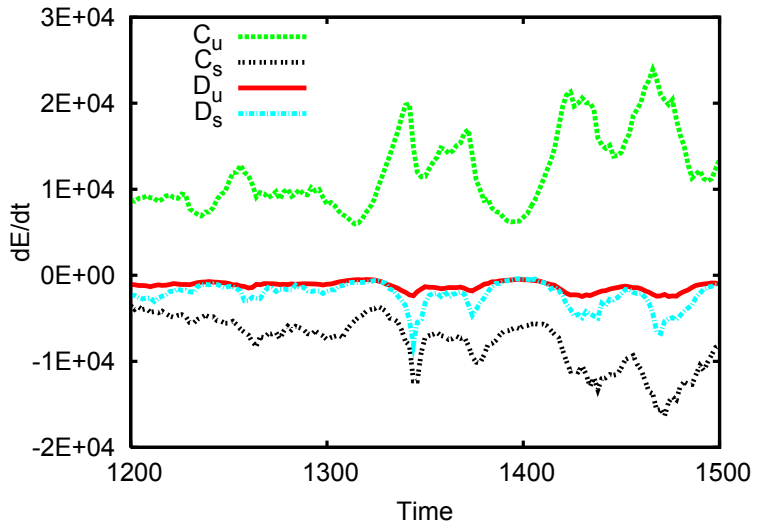

Figure 2.9: Energy dissipation and heat flux in the ITG model, breaking them up into unstable and stable mode configurations of Eq. 2.59.

$\Gamma = -\sum_k k_y \mathrm{Im}(\phi_k^* p_k)$. In order to simplify this calculation often a quasilinear approximation is made. Under this approximation, the stable modes are ignored and hence the pressure is expressed as $p_k = R_1(k)\phi_k$. This gives the quasilinear flux as $\Gamma_{\mathrm{quasilinear}} = -\sum_k k_y \mathrm{Im}(R_1)|\phi_k|^2$. These two fluxes are compared in Fig. 2.10, which shows the quasilinear and true fluxes for both the hydrodynamic and adiabatic regimes of Hasegawa-Wakatani turbulence. In the former there is a considerable reduction, consistent with strong excitation of the damped eigenmode, as the damped eigenmodes drive a strong inward, negative flux. Three-field fluid models for ITG and ETG turbulence also have a significant systematic deviation of $\mathcal{C}_s$ from zero, and a correspondingly large reduction of the flux [24].

2.5 Discussion

Nine two-field fluid models for instability-driven plasma turbulence covering different regimes of physics and parameters have been found to have commonplace regimes where damped eigenmodes saturate the linear instability. The damped eigenmodes are zeros of the dispersion relation. With the exception of TEM [22], their role as the energy sink for saturation has not been described. It is concluded, therefore, that the involvement of damped eigenmodes in saturation is not unique to a certain type of instability process or parameter regime, but a natural adjunct to instability in turbulence driven by instability. For two-field fluid reductions, the quadratic dispersion makes damped eigenmodes more prominent when the instability is well above threshold, and for strong diamagnetic frequency. When damped eigenmodes play a dominant role in saturation the energy dissipation rate of the damped eigenmode is comparable to the energy injection rate of linear instability. The saturation levels of stable and unstable eigenmodes are similar in many cases. Saturation by damped eigenmodes involves an energy sink in the energy-containing wavenumber range of the instability. Consequently, damped eigenmodes cannot be ignored in the descriptions of saturation, the steady state, or transport. This is important because damped eigenmodes are found to provide the energy sink for saturation in extensively studied systems where they were not previously identified, such as Rayleigh-Taylor, resistive interchange, and Hasegawa-Wakatani

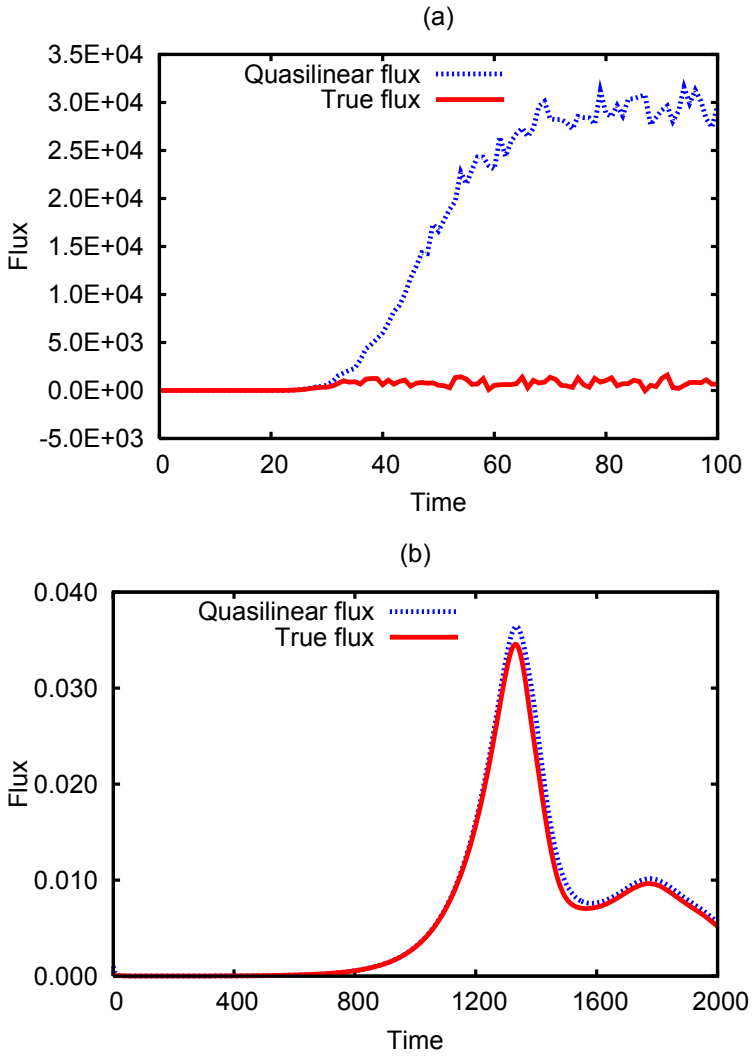

Figure 2.10: Comparison of quasilinear heat flux with the true heat flux in Hasegawa-Wakatani model. (a) is for hydrodynamic regime and (b) is for adiabatic regime.

turbulence. We note that shear flows have been included as an entity apart from the instability in representations of some of these systems [41]. However they have not been envisaged as, or play the role of the primary energy sink. The interesting interaction between shear flows and damped eigenmodes will be described in the next chapter.

A previously derived threshold parameter for saturation by damped eigenmodes, P_t, is found to be reliable for all nine models. When this parameter reaches values of a few tenths, damped eigenmodes become the dominant saturation mechanism. The parameter depends on the ratio of the damping rate to the growth rate, and indicates that when the damped eigenmode damping rate is too large, energy flowing to small scales on the unstable wavenumber manifold will instead saturate the instability according to the conventional picture of saturation. The ratio of coupling coefficients between wavenumbers on the unstable manifold and modes across the two manifolds also affects the value of P_t. This coupling ratio is often of order unity, but can be significantly different in certain cases described here. It is found that the energy dissipation rate of the damped eigenmode remains similar to the energy injection rate when the ratio of damping to growth, $|\gamma_2/\gamma_1|$ is not much greater than unity.

For all nine models, the damped eigenmode significantly changes the cross phase between the two fields from the value associated with the unstable eigenmode. This means that fluctuation energy is reabsorbed into the equilibrium gradients through the damped eigenmode in an inverse of the instability process. The transport flux is correspondingly reduced compared to the quasi-linear flux estimate. This process can be viewed as a finite-amplitude-induced reduction of the energy injected into the spectrum by the instability, however in this picture, the instability is no longer linear. The stable eigenmode also contributes to the damping arising from collisional dissipation terms. In the overall energetics this is a smaller effect than the change in energy evolution associated with the cross phase.

Chapter 3

Fluid model study of stable modes in zonal flow regulated turbulence

In the previous chapter we analyzed a variety of turbulence models, all of which showed saturation by damped modes in some parameter regime. One of the models studied was the ITG/ETG model. Now it is a well known fact that zonal flows play an important role in saturation of ITG turbulence [47]. In this chapter we look at the role played by stable modes in zonal flow regulated ITG turbulence. This is a topic of significant importance because ITG turbulence is a major player in tokamak turbulent transport. It is well known that zonal flows play an important role in regulating the transport caused by this turbulence. In fact, it has been argued that zonal flows are a critical trigger in the L to H transition of tokamaks that leads to enhanced confinement [48].

First we will give a brief overview of zonal flows and the conventional reasoning explaining the regulation of turbulence by zonal flows. Then we propose an alternate scenario wherein the stable modes play an important role in this regulation. In essence, we try to show that zonal flows provide an efficient coupling of energy from unstable to stable modes. Numerical studies are performed using a 2D fluid code similar to the one described in the previous chapter. The results show that indeed zonal flows are responsible for transfer of energy to stable modes, which causes saturation. The reasons for such a strong coupling are then provided in terms of phase matching arguments and an examination of the nonlinear coupling coefficients.

3.1 Zonal flows in ITG

Zonal flows are associated with a toroidally and poloidally symmetric, electrostatic potential perturbation in a toroidal plasma. In other words, the potential perturbation has toroidal mode number (m) and poloidal mode number (n) equal to zero, and hence is constant on magnetic flux surfaces [47]. However, it varies rapidly in the radial direction, giving rise to a radial electric field. This field produces an $\mathbf{E} \times \mathbf{B}$ flow which is mostly in the poloidal direction in tokamaks. This is the "flow" in zonal flows. A schematic representation of zonal flows is shown in Fig. 3.1. We can see a poloidal cross section of a tokamak and the shaded regions represent flux surfaces which also happen to be equipotential surfaces for zonal flow potential. There is a shear in the radial direction which produces sheared $\mathbf{E} \times \mathbf{B}$ poloidal flow, the zonal flows. These flows have been observed in both simulations and experiments [49]. They are characterized by low frequencies compared to ambient drift wave turbulence. Their wavelength in the radial direction is of the order of $10\rho_i$, where ρ_i is the ion gyroradius.

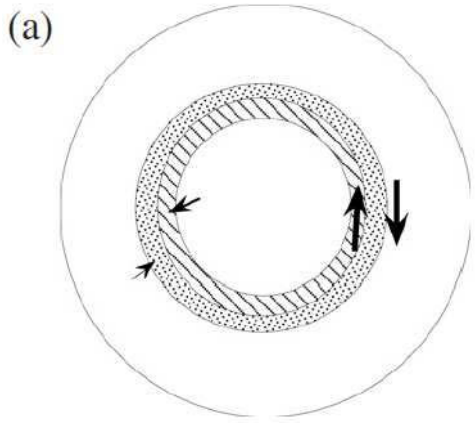

Figure 3.1: Schematic of zonal flows. The shaded regions are equipotential flux surfaces and the arrows on the right hand side indicate the direction of zonal flows. It is evident that they are sheared flows. Figure taken from Ref. [47].

Zonal flows arise self consistently in ITG turbulence as seen in simulations and also in experiments [50]. Their excitation by turbulence can be modeled by a modulational instability analysis of the drift waves of ITG [51]. A simplified derivation of this instability is given in Ref. [52]. The starting point is a Hasegawa-Mima type equation for the electrostatic potential. Then a

simplified four wave problem is considered, consisting of a pump wave k_2, two sidebands k_3 and k_4, and the zonal flow itself k_1. It is found that the zonal flow is nonlinearly unstable to the beating of the pump wave with the two sidebands, and the growth rate of the zonal flow is derived. It has been observed that the correct nonadiabatic response of electrons to zonal potential perturbations has to be taken into account to self consistently generate zonal flows [53]. The electrons can respond adiabatically to non-zonal perturbations which vary on the flux surface. However they cannot respond adiabatically to zonal perturbations which are constant on flux surfaces. In other words, zonal perturbations are not shielded by adiabatic electrons. In this way they can be thought to have "low inertia" and hence are readily excited by the modulational instability [47].

When the zonal flows are excited, the level of turbulence is drastically reduced by more than an order of magnitude as seen in numerical simulations [47], [54]. Indirect evidence from experiments [55] also indicates that zonal flows are crucial in regulating the turbulence and thus potentially play an important role in the L-H transition. In a numerical experiment, Fig. 3.2, the zonal flows are turned off artificially by removing the nonadiabatic response of electrons and the turbulence is allowed to saturate. Then the zonal flows are turned on by allowing the correct non-adiabatic response of electrons. It is observed that as the zonal flows rise, the turbulent energy decreases by an order of magnitude and so does the transport.

The conventional explanation for this phenomenon is the drift wave-zonal flow shearing paradigm. There are two ways to explain how this works. Firstly zonal flows arise due to nonlinear energy transfer from drift waves to zonal flows. This implies that zonal flows form a depository of drift wave energy. However, zonal flows themselves do not cause transport unlike drift waves. Also the zonal flows are damped by collisions and so serve as a dissipation channel. As a result, generation of zonal flows naturally leads to regulation of transport. Secondly, zonal flows, being shear flows, shear apart turbulent eddies. This tearing of turbulent eddies leads to increased coupling to dissipative scales which leads to the saturation of turbulence. This shearing effect is observed in simulations, Fig. 3.3 and Ref. [56].

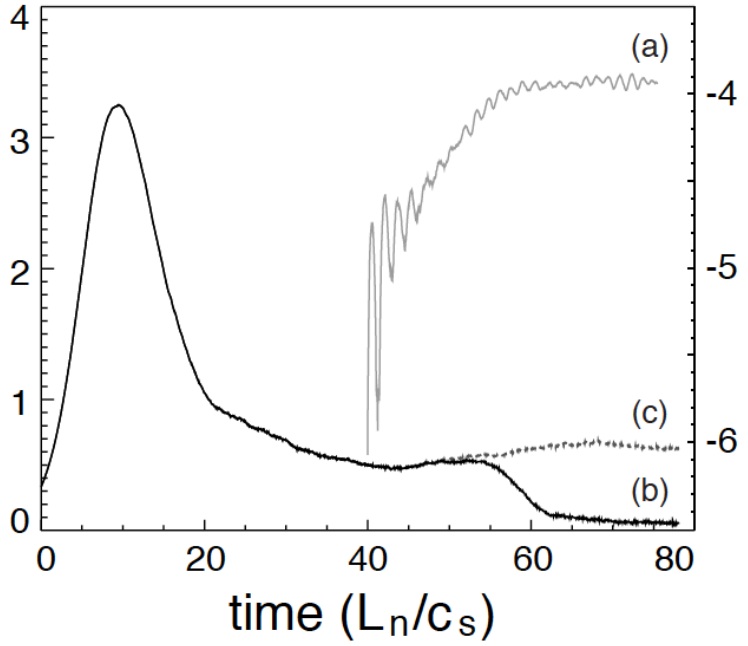

Figure 3.2: In this numerical experiment, ITG is allowed to saturate by some process in the absence of zonal flows. Then at $t \approx 40 L_n/c_s$ the zonal flows are allowed to evolve and they rise exponentially (gray curve (a)). The turbulence saturates at a lower level (solid black curve (b)) compared to if the zonal flows hadn't been allowed to be formed (dotted curve (c)). Taken from Ref. [54].

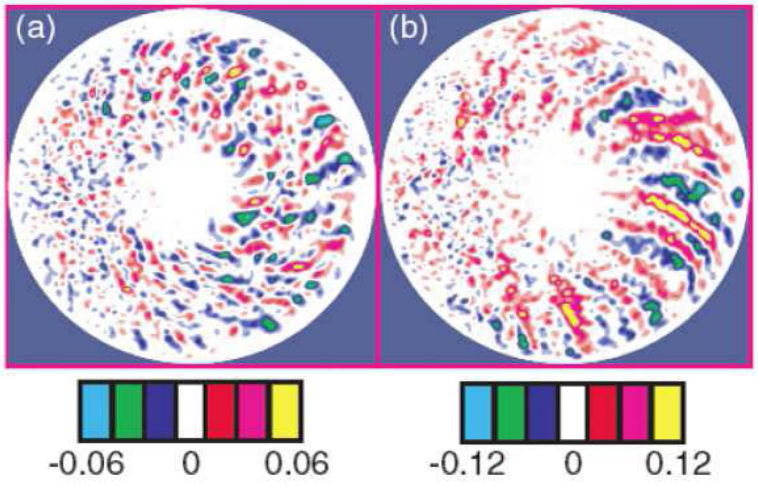

Figure 3.3: In this numerical experiment, ITG is allowed to saturate by some process in the absence of zonal flows in plot (b). We can see radially elongated turbulent eddies in the poloidal cross section of the simulated tokamak. In plot (a) the zonal flows are allowed to evolve self consistently in which case we see that the eddies are torn apart and appear with a much smaller radial extent, thus lowering the transport. Taken from Ref. [57].

3.2 Zonal flows and stable modes

From the previous section we know that zonal flows are important in saturation of ITG turbulence. However, in the previous chapter we saw that stable modes are the major saturation mechanism in ITG turbulence. How to reconcile these two seemingly disparate descriptions? A possible answer can be that zonal flows could enhance energy transfer to stable modes, which would also lead to saturation of turbulence at a lower level. This is represented in Fig. 3.4.

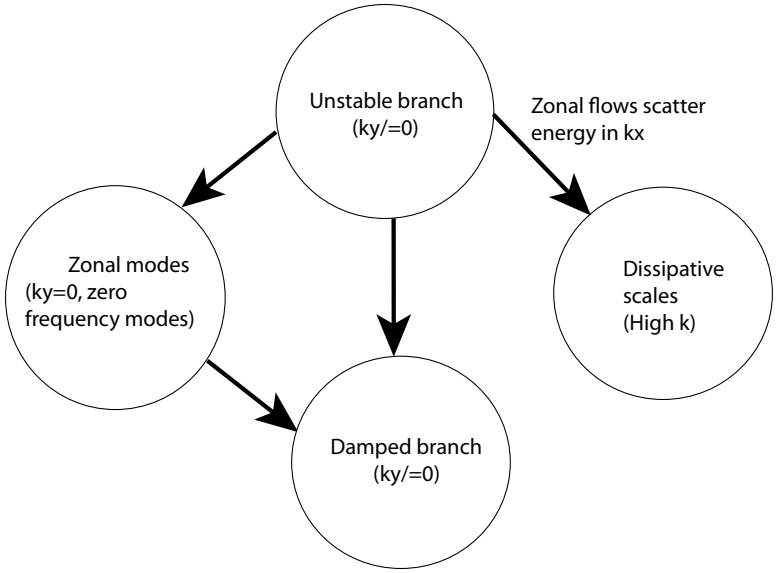

Figure 3.4: Two different ways of energy transfer. The rightmost arrow shows enhanced energy transfer to dissipative scales by zonal flow shearing. The leftmost arrows show how zonal flows can enhance energy transfer to damped modes.

In Fig. 3.4 the drift waves at low wavenumber are separated into two divisions, unstable and stable. The zonal flows are represented by zero poloidal wavenumber ($k_y = 0$) and low frequency. On the other hand,the high wavenumbers are dissipative drift waves. According to the conventional mechanism, zonal flows enhance energy transfer from the unstable modes to dissipative modes via shearing, which is represented by the right most arrow in the figure. We have already seen that unstable modes transfer a lot of energy to stable modes by three wave interactions. However, it is also possible that zonal flows can enhance energy transfer to stable modes in addition to enhancing energy transfer to small-scale, dissipative modes. This energy

can flow directly to stable modes, as shown by the center arrow, or via the zonal flows, as shown by the two leftmost arrows. This can also result in the regulation of turbulence since the stable modes are dissipative. In order to study this we first look at a simplified two field fluid model in this chapter. In the next chapter we look at the same problem using a comprehensive gyrokinetic model.

3.3 Model equations

A simple 2 field model is used which describes both ITG and ETG [31],

$$\frac{\partial p_k}{\partial t} + ik_y(1+\eta)\phi_k + \chi k^4 p_k = -\frac{1}{2}\sum_{k'}(k' \times \hat{z} \cdot k)[\phi_{k'} p_{k-k'} - \phi_{k-k'} p_{k'}], \tag{3.1}$$

$$[\delta(k_y) + k^2]\frac{\partial \phi_k}{\partial t} + ik_y\phi_k - ik_y\epsilon p_k + \nu k^2 \phi_k = -\frac{1}{2}\sum_{k'}(k' \times \hat{z} \cdot k)[(k-k')^2 - k'^2]\phi_{k'}\phi_{k-k'}. \tag{3.2}$$

These equations are almost the same as Eqs. (2.1-2.2). Here p_k and ϕ_k are Fourier amplitudes of pressure and electrostatic potential, ν and χ are coefficients of collisional dissipation, η is the ratio of density to temperature gradient scale lengths, and ϵ is the ratio of density gradient scale length to magnetic field variation scale length. In this chapter also we denote the Fourier wavenumber with k, and it should be clear from context whether it denotes the wave-vector or its scalar magnitude. The spatial coordinates are normalized to ρ and time is normalized to L_{ref}/u_{ref}. The symbol ρ represents the electron gyroradius for the electron temperature gradient (ETG) turbulence case and the ion sound gyroradius for the ion temperature gradient (ITG) turbulence case. The symbol L_{ref} represents the density gradient scale length and u_{ref} is v_{Te} (electron thermal velocity) for ETG and c_s (ion sound speed) for ITG. To set the model for ETG turbulence, $\delta = 1$ for all k_y. For ITG,

$$\delta(k_y) = \begin{cases} 1 & \text{if } k_y \neq 0 \\ 0 & \text{if } k_y = 0. \end{cases} \tag{3.3}$$

Poloidally symmetric $k_y = 0$ fluctuations are referred to as zonal fields. In this model there are two zonal fields, namely the zonal flow $v_z(k_x) = ik_x\phi_{k_y=0}$ and the zonal pressure $p_{k_y=0}$. There is a zonal flow and pressure for both the ETG and ITG cases. In the ITG case where $\delta(k_y)|_{k_y=0} = 0$, the potential equation can be rewritten as an equation for zonal flow

$$\dot{v}_z + \nu v_z = (-i/2)\sum_{k'} k'_y[(k_x - k'_x)^2 - k'^2_x]\phi_{k'}\phi_{k-k'}. \tag{3.4}$$

In the ETG case the equation for v_z is

$$\dot{v}_z + \nu k_x^2(1+k_x^2)^{-1}v_z = (-i/2)\sum_{k'} k'_y k_x^2(1+k_x^2)^{-1}[(k_x - k'_x)^2 - k'^2_x]\phi_{k'}\phi_{k-k'}. \tag{3.5}$$

For the energy containing scales $k_x \ll 1$. Looking at the rhs of Eqs. (3.4-3.5) we see that the nonlinear coupling to the zonal flow is stronger by a factor k_x^{-2} in the ITG case than in its ETG counterpart. Since transfer to $k_y = 0$ is already favored when damped eigenmodes are present [58], the zonal flow is strongly excited. In this model the zonal flow brings down the level of turbulence and reduces ion-channel transport. This is shown in Fig. 3.5, where the turbulent energy in the ITG case is almost two orders of magnitude smaller than the ETG case. The definition of energy is given in Eq. 3.15.

As in the previous chapter, we look at the linear frequencies of this model, which are,

$$\omega_{1,2} = -\frac{i}{2}\left(\chi k^4 + \frac{\nu k^2 + ik_y}{\delta + k^2}\right) \pm \frac{i}{2}\left\{\left(\chi k^4 - \frac{\nu k^2 + ik_y}{\delta + k^2}\right)^2 + \frac{4(1+\eta)k_y^2\epsilon}{\delta + k^2}\right\}^{1/2}. \tag{3.6}$$

We consider the regime of weak collisionality $\chi k^4, \nu k^2 \ll k_y\sqrt{\eta\epsilon}$, where $0 < k_y < 1$. This is a regime of robust linear instability. In this regime an expansion of the radical shows that the two eigenfrequencies are nearly complex conjugates, with the deviation proportional to the collisionalities,

$$\omega_{1,2} \approx \frac{k_y}{2(\delta + k^2)} \pm ik_y\left[\frac{(1+\eta)\epsilon}{\delta + k^2}\right]^{1/2} - \frac{i}{2}\frac{\nu k^2}{(\delta + k^2)} - \frac{i}{2}\chi k^4. \tag{3.7}$$

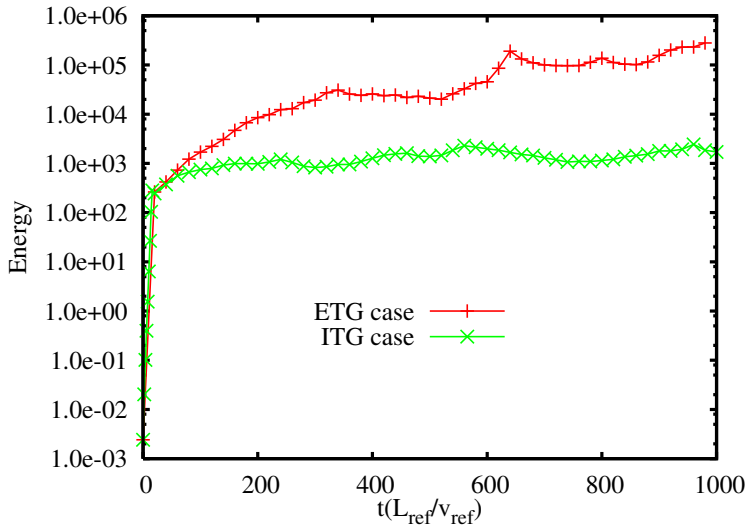

Figure 3.5: Comparison of total energy (as defined in Eq. 3.15) in ITG vs ETG. ITG saturates at a much lower level than ETG.

As a near conjugate to the unstable eigenmode ω_1, the second eigenmode ω_2 is damped. Moreover, with $|\text{Im } \omega_2| \approx |\text{Im } \omega_1|$ the damped eigenmode satisfies the condition for strong excitation, Eq. (2.25), and dissipates energy at a rate that is comparable to the energy injection rate of the instability.

For $k_y = 0$ the eigenfrequencies reduce to

$$\omega_1 = -i\nu k_x^2/(\delta + k_x^2), \tag{3.8}$$

$$\omega_2 = -i\chi k_x^4. \tag{3.9}$$

We observe from Eqs. (3.1) and (3.2) that setting $k_y = 0$ diagonalizes the linear part of the equations. Hence pressure and potential are the eigenmodes at $k_y = 0$. (Away from $k_y = 0$ the eigenmodes are linear combinations of pressure and potential, given by Eq. 3.10.) For convenience, we label the frequencies of the $k_y = 0$ flow and pressure as respectively ω_1 and ω_2, irrespective of whether $(\chi k_x^4 - \nu k_x^2/(\delta + k_x^2))$ is positive or negative. This is a labeling convention for $k_y = 0$, and does not change the results of this chapter in any way. For the ITG case the zonal flow damping rate is $-\nu$.

To track the amplitudes of the unstable and damped modes we introduce the eigenmode decomposition of Eq. 2.16,

$$\begin{pmatrix} p_k \\ \phi_k \end{pmatrix} = \beta_1(k) \begin{pmatrix} R_1(k) \\ 1 \end{pmatrix} + \beta_2(k) \begin{pmatrix} R_2(k) \\ 1 \end{pmatrix}, \tag{3.10}$$

where $[R_1(k), 1]$ and $[R_2(k), 1]$ are the eigenvectors of the unstable and stable modes, $\beta_1(k)$ and $\beta_2(k)$ are the mode amplitudes, and

$$R_{1,2} = \frac{-\omega_{1,2}(\delta + k^2) + k_y - i\nu k^2}{k_y \epsilon}. \tag{3.11}$$

Evolution equations for the amplitudes $\beta_1(k)$ and $\beta_2(k)$ are found by inverting Eq. (3.10) and taking the time derivative [23]. This procedure diagonalizes the linear coupling of the evolution equations, while mixing the nonlinearities.

It is helpful to explicitly break out the $k_y = 0$ component of the evolution from the $k_y \neq 0$ components, writing the evolution equations as two equations for $\dot{\beta}_1(k)|_{k_y \neq 0}$ and $\dot{\beta}_2(k)|_{k_y \neq 0}$ and two equations for $\dot{p}_k|_{k_y=0}$ and $\dot{\phi}_k|_{k_y=0}$. The evolution equations are

$$\dot{\beta}_l + i\omega_l \beta_l = \sum_{k'(k'_y \neq 0, k_y)} [C_{lmn} \beta'_m \beta''_n] + \sum_{k'_x} \Big\{ [C_{lFn} v'_z \beta''_n + C_{lPn} p'_z \beta''_n]|_{k'_y=0} + [C_{lmF} \beta'_m v''_z + C_{lmP} \beta'_m p''_Z]|_{k'_y=k_y} \Big\}, \tag{3.12}$$

$$\dot{v_z} + \frac{\nu k_x^2}{(\delta + k_x^2)} v_z = \sum_{k'_x} [C_{Fmn} \beta'_m \beta''_n]|_{k_y=0}, \tag{3.13}$$

$$\dot{p_z} + \chi k_x^4 p_z = \sum_{k'_x} [C_{Pmn} \beta'_m \beta''_n]|_{k_y=0}, \tag{3.14}$$

where $l, m, n = 1$ or 2 and the Einstein convention is used to imply summation over repeated indices. A shorthand notation is introduced as follows: $\beta_{1,2} = \beta_{1,2}(k)|_{k_y \neq 0}$, $\beta'_{1,2} = \beta_{1,2}(k')|_{k'_y \neq 0}$, $\beta''_{1,2} = \beta_{1,2}(k - k')|_{k'_y \neq k_y}$, $v_z = ik_x \phi_k|_{k_y=0}$, $v'_z = ik'_x \phi_{k'}|_{k'_y=0}$, $v''_z = i(k_x - k'_x)\phi_{k-k'}|_{k'_y=k_y}$, $p_z = p_k|_{k_y=0}$, $p'_z = p_{k'}|_{k'_y=0}$, and $p''_z = p_{k-k'}|_{k'_y=k_y}$. The coupling coefficients C_{lmn}, C_{lFn}, C_{lPn}, C_{lmF},

C_{lmP}, C_{Fmn} and C_{Pmn} are functions of the nonlinear coefficients of Eqs. (3.1) and (3.2) and the eigenvector components R_1 and R_2. Their precise forms are given in the Appendix A.

3.3.1 Details of the code used

The code used in the previous chapter had very limited resolution and thus is not suitable for studying nonlinear energy transfer to high wavenumber modes. Thus a new high resolution code was developed in order to study the energy transfer processes with this model. All the simulations were done on a grid of 160×160 points in (k_x, k_y), with $k_{x,min}\rho = k_{y,min}\rho = 0.04$. A $5^{\text{th}} - 6^{\text{th}}$ order Runge-Kutta scheme is utilized. The linear terms are calculated in Fourier space, whereas the nonlinear term is calculated in real space with Intel MKL FFT routines implemented for fast conversion from one space to another space. Thus, it is a pseudo spectral code which utilizes Orszag's 2/3rd anti-aliasing scheme. The code conserves energy to machine precision. The analytically derived linear growth rates are numerically verified with this code.

3.4 Energy dynamics

The energy expression for this model is

$$E = \sum_k [(\delta + k^2)|\phi_k|^2 + |p_k|^2]. \tag{3.15}$$

The rate of change of the total energy can be expressed as

$$\frac{dE}{dt} = Q_u + Q_s + Q_{us} + D + D_{zonal}, \tag{3.16}$$

where Q_u is the rate of change of energy due to unstable modes, Q_s is the rate of energy removal by stable modes, and Q_{us} is the rate of change of energy due to cross terms of unstable and stable modes. The sum of these terms is related to the turbulent heat transport flux by $Q_u + Q_s + Q_{us} = -(1 + \eta + \epsilon)Q$, where $Q = -\sum_k k_y Im(\phi_k^* p_k)$ is the heat flux. D is the high-wavenumber dissipation for nonzonal modes, and D_{zonal} is the linear energy damping rate of the

zonal modes. These terms can be derived by substituting Eqs. (3.1-3.2) in the time derivative of Eq. 3.15. They are given in the Appendix A. These quantities are plotted in Fig. 3.6 for the ETG case. We see that Q_u is large and positive. It is balanced by a large and negative Q_s, which shows saturation by stable modes. Q_{us} is small (not visible in the plot) and negative, and helps balance Q_u. It should be noted that while Q_{us} equally derives from stable and unstable modes, it vanishes in any calculation that ignores the stable modes. The role of viscous dissipation D is considerably smaller than the dissipation Q_s of stable modes, and dissipation by the zonal modes is negligible. The ETG turbulence in Fig. 3.6 has not actually saturated at the end of the simulation run. While the addition of artificial damping at low k does lead to saturation, the behavior seen in Fig. 3.6 ($Q_u \sim |Q_s| \gg |Q_{us}|, D$) remains unchanged. The damped modes are

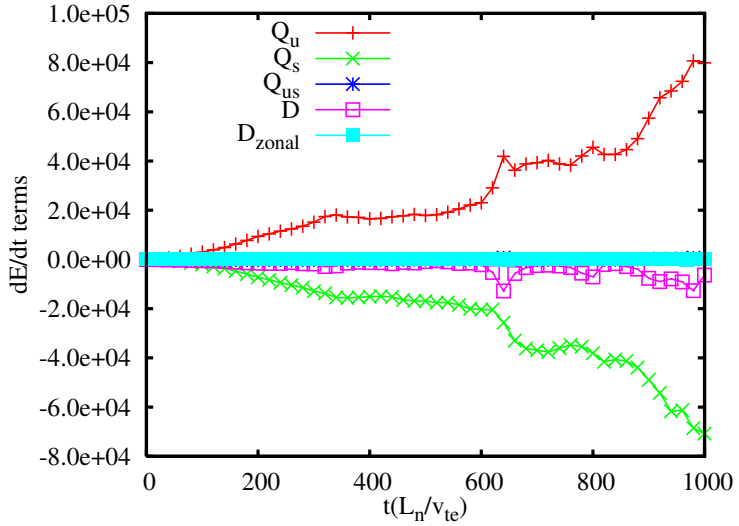

Figure 3.6: Time trace of the terms in Eq. 3.16; Q_u, Q_s, Q_{us}, D and D_{zonal}; in ETG turbulence.

most active in the range of instability. This is seen in the wave number spectrum of heat flux and dissipation. Both Q_{us} and Q_s can be considered as damped mode contributions. It can be seen that the damped modes dissipate energy, $Q_s + Q_{us}$ (Fig. 3.7(b)), at exactly the same place, at low wavenumbers, where unstable modes inject energy Q_u (Fig. 3.7(a)). The dissipation D (Fig. 3.8) is negligible and peaks at high k.

A numerical experiment shows how zonal flows reduce the level of turbulence. A simulation is started in the ETG case. It is allowed to reach a saturated state. At time 400 the equations

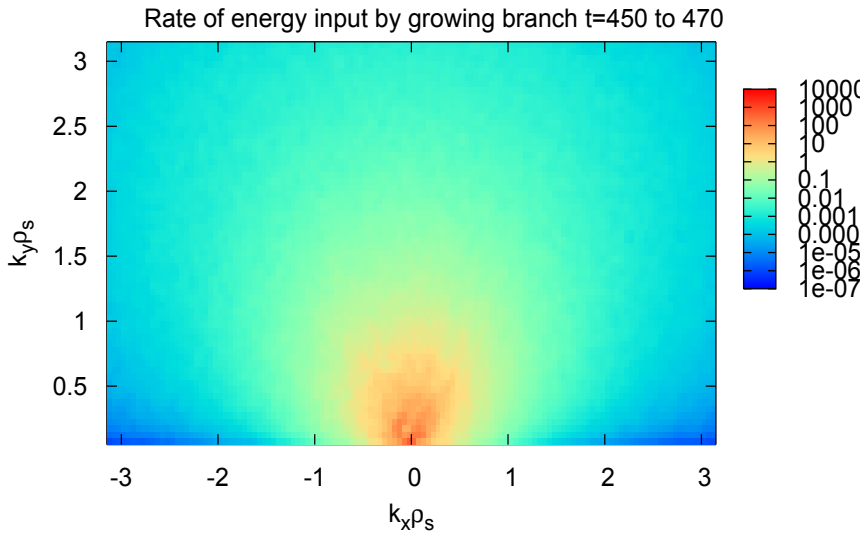

(a)

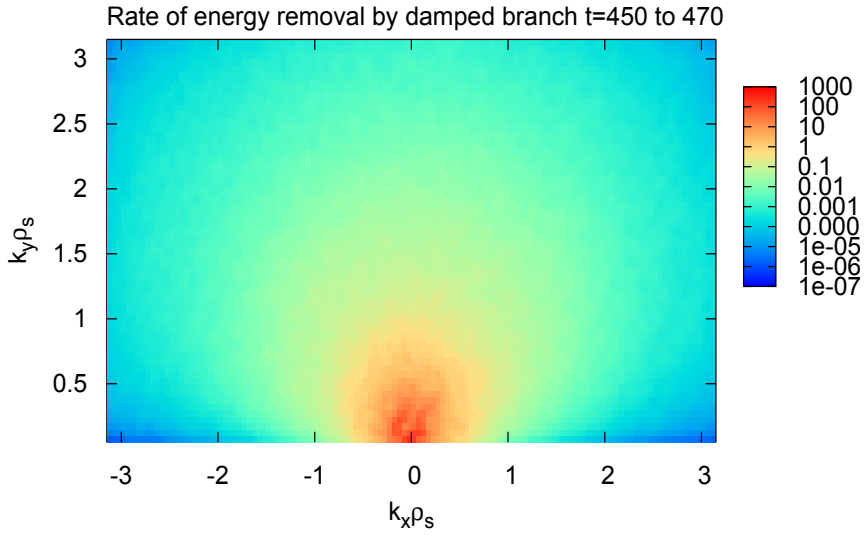

(b)

Figure 3.7: Time averaged k_x-k_y spectrum of the terms in Eq. 3.16 for ETG turbulence. (a) plots the spectrum of energy injection rate by unstable modes, Q_u, while (b) plots the spectrum of energy dissipation by damped modes, $Q_s + Q_{us}$. Only positive k_y values are plotted as the spectrum is symmetric in $\mathbf{k}$.

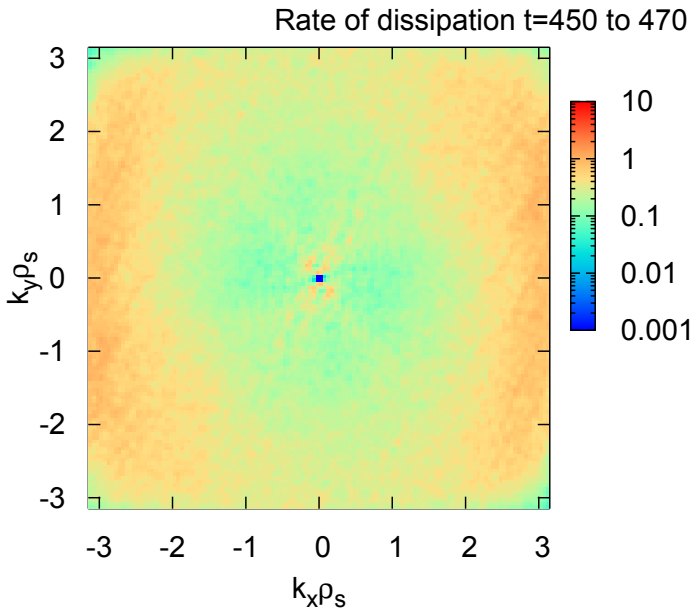

Figure 3.8: Time averaged k_x-k_y spectrum of the dissipation, D (Eq. 3.16), in ETG turbulence.

are switched to the ITG case by changing the parameter δ. In a crude sense, this mimics a transition from a low confinement regime to a high confinement regime induced by turbulence-driven sheared flows [31], [59]. The turbulence level is reduced after $t = 400$. What causes this change in energy? The rate of change of energy, dE/dt, becomes sharply negative after $t = 400$. We see from Eq. 3.16 that dE/dt has a net drive from $Q_u + Q_s + Q_{us}$ and net dissipation $D + D_{zonal}$. Fig. 3.9 shows that as zonal flows are turned on, the viscous dissipation D shows only a slight transient increase and then a decrease. The zonal dissipation D_{zonal} remains small. However, the sum $Q_u + Q_s + Q_{us}$ decreases drastically in magnitude. The sum $Q_u + Q_s + Q_{us}$ is the difference between energy injected by the instability and dissipated by damped modes. This residual must be dissipated by the only other sink, namely, viscous dissipation. Consequently viscous dissipation does not increase (the way it would if there were enhanced energy transfer to small scale) but it decreases to match the reduced residual energy input $Q_u + Q_s + Q_{us}$. The reduced input makes dE/dt negative and brings the energy down. It is also observed that the

level of zonal flows increases. However, the fraction of instability energy deposited into the zonal flow remains very small, and is removed by zonal flow damping, as shown in Fig. 3.10. Fig. 3.10 shows that most of the instability energy is damped by the stable modes in ITG also, with the zonal modes dissipating only a small fraction of it.

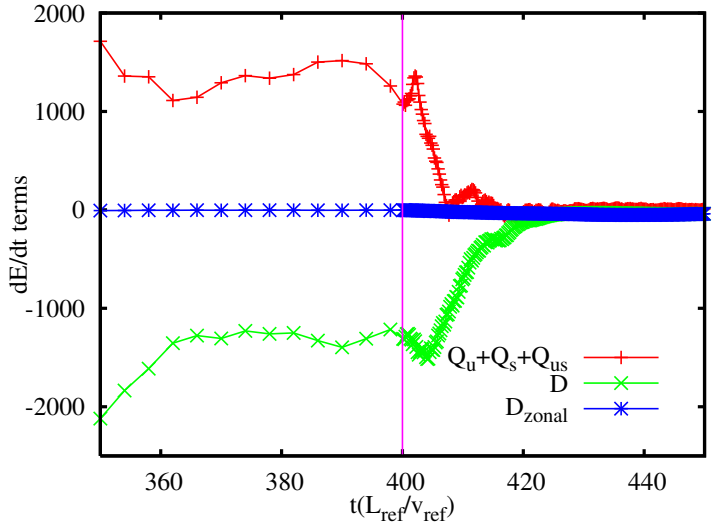

Figure 3.9: Time trace of dE/dt terms in Eq. 3.16. At $t = 400$ the zonal flows are turned on and we see that the high-k dissipation, D, doesn't show any significant increase, rather the heat flux related term, $Q_u + Q_s + Q_{us}$, shows a marked decrease.

3.5 Nonlinear energy transfer diagnostics

To validate the hypothesis that zonal flows enhance energy transfer to stable modes, we analyze the nonlinear energy transfer within the system. Decomposing the pressure and potential fields into the linear eigenmode amplitudes, the energy dependence on the four fields of Eqs. (3.12) - (3.14) is given by

$$E = \sum_{k_y \neq 0} \Big[(1 + k^2 + |R_1|^2)|\beta_1|^2 + (1 + k^2 + |R_2|^2)|\beta_2|^2 + 2(1 + k^2) Re\langle \beta_1^* \beta_2 \rangle + 2 Re\langle R_1^* \beta_1^* R_2 \beta_2 \rangle \Big] + \sum_{k_y = 0} \Big[|p_k|^2 + (\delta + k^2)|\phi_k|^2 \Big]. \tag{3.17}$$

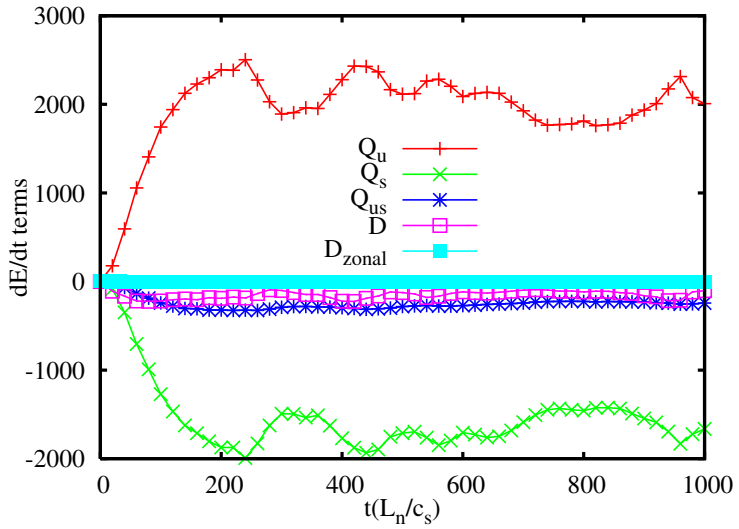

Figure 3.10: Time trace of the terms in Eq. 3.16; Q_u, Q_s, Q_{us}, D and D_{zonal}; in ITG turbulence.

The energy in the unstable modes corresponds to $\sum_{k_y \neq 0}(1 + k^2 + |R_1|^2)|\beta_1|^2$. Eqs. (3.12-3.14) can be recast as energy equations by multiplying by β_l^*, v_z^*, and p_z^*, respectively and adding the complex conjugate equations. Energy transfer channels available to the system are associated with various coupling coefficients. Turbulent energy enters the system through $|\beta_1|^2$ at low k, and energy transfer channels lead from this source to the sinks, the largest of which is $|\beta_2|^2$ at low k. $|\beta_1|^2$ and $|\beta_2|^2$ at high k are also sinks, but energy must cascade through a progression of wavenumbers to reach large k. Energy passes directly from β_1 to β_2, without any intermediate zonal fields, through terms with coefficients C_{112}, C_{121}, C_{122}, C_{211}, C_{212}, and C_{221}. Energy cascades to large k within a single eigenmode through the terms with C_{111} and C_{222}. The terms with C_{1F2}, C_{12F}, C_{2F1}, C_{21F}, C_{F12}, and C_{F21} govern the passage of energy from β_1 to β_2 through the intermediary of the zonal flow. The terms with C_{1P2}, C_{12P}, C_{2P1}, C_{21P}, C_{P12}, and C_{P21} govern the passage of energy from β_1 to β_2 through the zonal pressure. The relative strengths of these channels are governed by the magnitudes of coupling coefficients and by the triplet correlations of the energy equations, as detailed in Sec. 3.7.

Taking a derivative and substituting from Eq. (3.12), the rate of change of energy of the

unstable modes is

$$\frac{\partial}{\partial t}\left[\sum_{k_y\neq 0}(1+k^2+|R_1|^2)|\beta_1|^2\right]=\sum_{k_y\neq 0}2(1+k^2+|R_1|^2)\gamma_1|\beta_1|^2+N_{111}+N_{112}+$$
$$N_{121}+N_{122}+N_{1P1}+N_{1P2}+N_{11P}+N_{12P}+N_{1F1}+N_{1F2}+N_{11F}+N_{12F}. \qquad (3.18)$$

The term $\gamma_1|\beta_1|^2$ is the linear instability energy input rate, where γ_1 is the growth rate of the unstable mode. The terms labelled by N represent the three-wave coupling terms. Their forms are given in the Appendix A. The term N_{111} signifies coupling between the unstable mode $\beta_1(k)$ with two other unstable modes at k' and k''. The terms N_{112} and N_{121} represent coupling of the unstable mode with another unstable and one stable mode. The term N_{122} represents coupling of the unstable mode with two stable modes. The remaining terms, N_{11P}, N_{1P1}, N_{12P}, N_{1P2}, N_{1F1}, N_{11F}, N_{1F2} and N_{12F} are couplings of the unstable mode with a zonal field (zonal pressure or zonal flow) and a second mode, either unstable or stable. These last eight terms can be grouped together as coupling of the unstable mode with a zonal field and either a stable or unstable mode. The four groups of coupling terms just described are plotted in Fig. 3.11, which shows both the ETG and ITG cases. The curve labelled $\gamma_1|\beta_1|^2$ is the linear energy injection rate ($\sum_{k_y\neq 0}2(1+k^2+|R_1|^2)\gamma_1|\beta_1|^2$). It is balanced by the nonlinear energy transfer terms. In the ETG case, all four groups of nonlinear terms play approximately equal roles in saturating the linear instability. In the ITG case the group involving couplings with a zonal field is the most important term for saturation of the instability. This indicates that zonal fields play a prominent role in saturating turbulence in the case of ITG. The zonal fields include both zonal pressure and zonal flow, so it is important to ask what role each field individually plays in saturation. Also, in the couplings with a zonal field, only one mode of the triad is a zonal field, the other mode being either a stable or an unstable nonzonal mode. Hence it is also important to ask about the proportion of energy transferred to the zonal field compared to the energy transferred to the nonzonal mode.

To answer these questions we separate the group involving one zonal field into four subgroups. They are couplings with: 1) zonal pressure and an unstable mode (N_{11P}+N_{1P1}), 2) zonal pressure

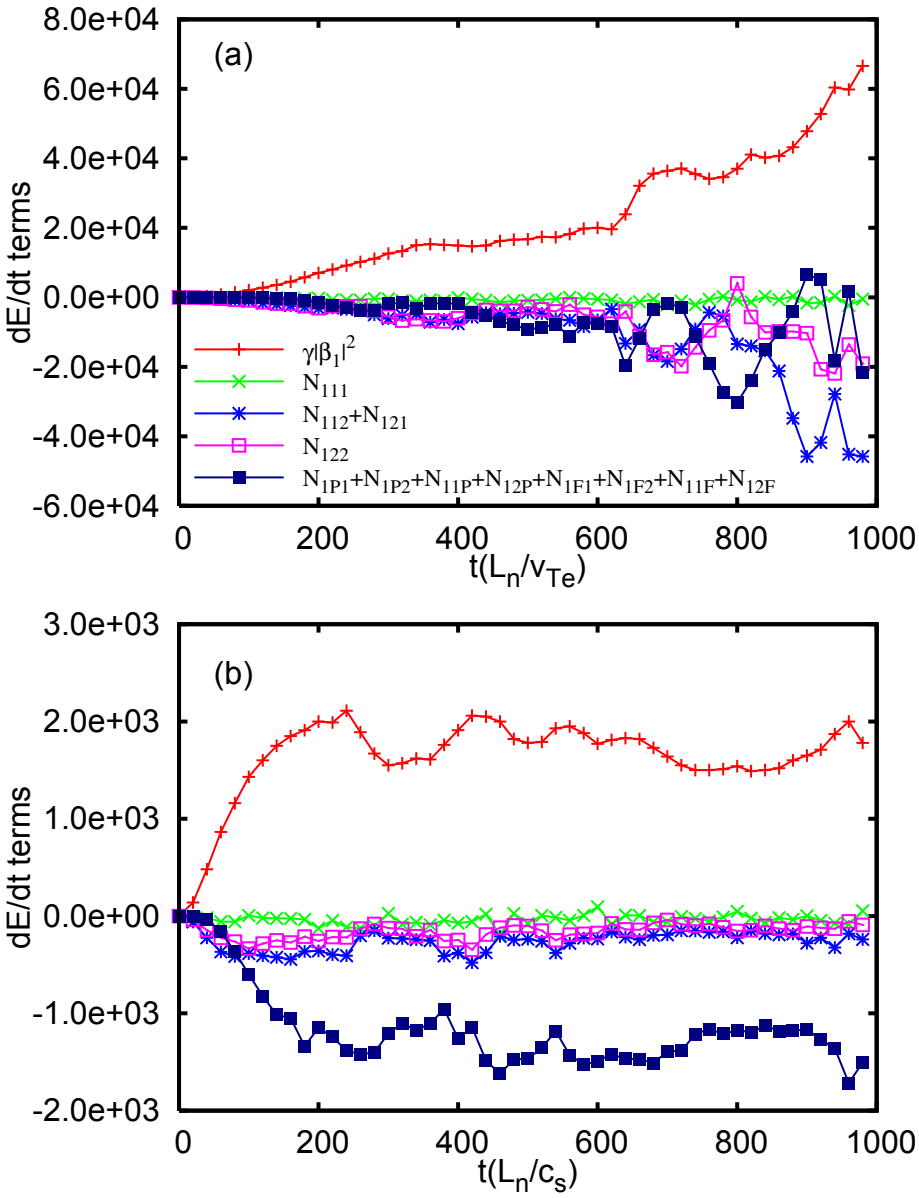

Figure 3.11: The rate of change of the unstable mode energy, $\sum_{k_y \neq 0}(1 + k^2 + |R_1|^2)d|\beta_1|^2/dt$, divided into the various coupling terms of Eq. 3.18, plotted as a function of time. (a) is for ETG case and (b) is for ITG case. The legend is the same for both plots.

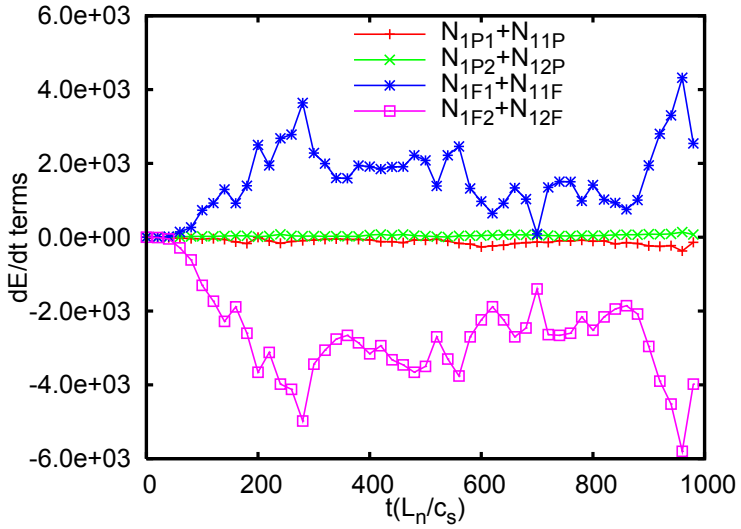

Figure 3.12: The zonal field couplings of the unstable mode energy (terms with either a P or F in their subscripts in Eq. 3.18) in ITG case separated into zonal pressure couplings and zonal flow couplings.

and a stable mode ($N_{12P}+N_{1P2}$), 3) zonal flow and an unstable mode ($N_{11F}+N_{1F1}$) and 4) zonal flow and a stable mode ($N_{1F2}+N_{12F}$). These terms are plotted in Fig. 3.12. This figure is for the ITG case, where the zonal field coupling terms are the most important. Two sets of nonlinear terms dominate. The first is the coupling between the unstable mode at k, a zonal flow and a second unstable mode ($N_{11F}+N_{1F1}$). This term is positive, which means that energy is flowing into unstable modes from this term. Since this energy transfer is summed over all nonzonal wavenumbers, the net transfer of energy between the unstable mode at k and the unstable mode at either k' or k'' should cancel out. Consequently, the energy transfer $N_{11F}+N_{1F1}$ is coming entirely from the zonal flow. For comparison with other transfer rates, we note that $N_{11F}+N_{1F1}$ has a value of approximately 1900 at time $t=400$. The second dominant set of nonlinear terms represents coupling with a zonal flow and a stable mode ($N_{12F}+N_{1F2}$). This set of terms has a value of -3100 at $t=400$, making it larger than $N_{11F}+N_{1F1}$ and negative. This means that this energy is going out of the unstable modes. Some portion of this energy transfer goes into zonal flows. This portion is necessarily larger than $N_{11F}+N_{1F1}$ because, as we will see later, the zonal flow receives net energy from the unstable mode. The energy transfer $N_{11F}+N_{1F1}$

thus recirculates within the unstable mode, through the intermediary of the zonal flow (similar to Ref. [60]). The remainder of the energy transfer, $N_{12F} + N_{1F2}$, from the unstable mode goes into stable modes.

These transfers are depicted schematically in Fig. 3.13(a). The transfer $N_{11F} + N_{1F1}$ is represented by an arrow flowing into the unstable modes from the zonal flow. The portion of $N_{12F} + N_{1F2}$ that goes into zonal flows is represented by $N_{1\to F}$. The portion that flows into the stable modes is represented by $N_{1\to 2}$. $N_{1\to F}$ and $N_{1\to 2}$ are taken as positive quantities. Therefore the portions $N_{1\to F} + N_{1\to 2}$ add up to $-N_{12F} - N_{1F2}$. It is not possible to determine $N_{1\to F}$ and $N_{1\to 2}$ separately from this information alone. To estimate them we need to look at the energy dynamics of the zonal flow. The energy equations for the zonal fields are (for ITG case)

$$\sum_{k_y=0} \frac{\partial}{\partial t}(|p_k|^2) = -\sum_{k_y=0} 2\chi k^4 |p_k|^2 + N_{P11} + N_{P12} + N_{P21} + N_{P22}, \tag{3.19}$$

$$\sum_{k_y=0} \frac{\partial}{\partial t}(k_x^2|\phi_k|^2) = -\sum_{k_y=0} 2\nu k_x^2 |\phi_k|^2 + N_{F11} + N_{F12} + N_{F21} + N_{F22}. \tag{3.20}$$

The terms containing χ and ν represent linear damping of the zonal pressure and flow respectively. The terms labelled N are again the various nonlinear couplings of the zonal fields, which couple only with nonzonal wavenumbers. Following the usual notation, $N_{P(F)1(2)1(2)}$ represents coupling of the zonal pressure (flow) with an unstable (stable) mode at k' and an unstable (stable) mode at $k - k'$. These terms, which are given in the Appendix A, are plotted in Fig. 3.14.

The dynamics of the zonal pressure shows that it receives energy from unstable modes through N_{P11} and saturates by transferring the energy to stable modes through N_{P22}. The linear damping of zonal pressure plays a small role in its energetics. However, the zonal flow dynamics show a strikingly different balance. The zonal flow receives energy equally from unstable modes through N_{F11} and stable modes through $N_{F12} + N_{F21}$ and N_{F22}, with saturation provided by its linear damping. This is schematically shown in Fig. 3.13(b). All the nonlinear terms $N_{F11}, N_{F12}+N_{F21}$ and N_{F22} are shown to be supplying energy to the zonal flow, with only linear damping providing saturation. The energy transfer to zonal flows is also seen to be much smaller then the transfer

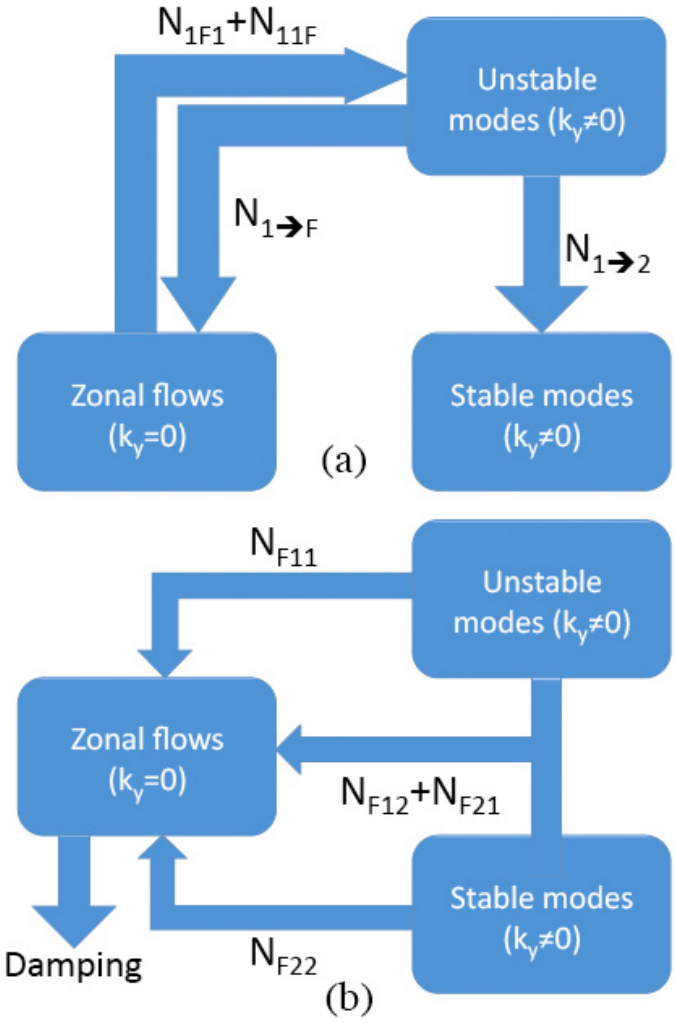

Figure 3.13: A schematic showing the nonlinear energy transfer routes for the unstable mode (a) and the zonal flow (b).

to zonal pressure. The y axis scale of Fig. 3.14(b) can be compared to that of Fig. 3.12. We see that the net transfer into the zonal flow from unstable mode (N_{F11}) is approximately only 2, compared to a value of 1900 for energy transfer from zonal flow to unstable mode ($N_{1F1}+N_{11F}$) at $t = 400$.

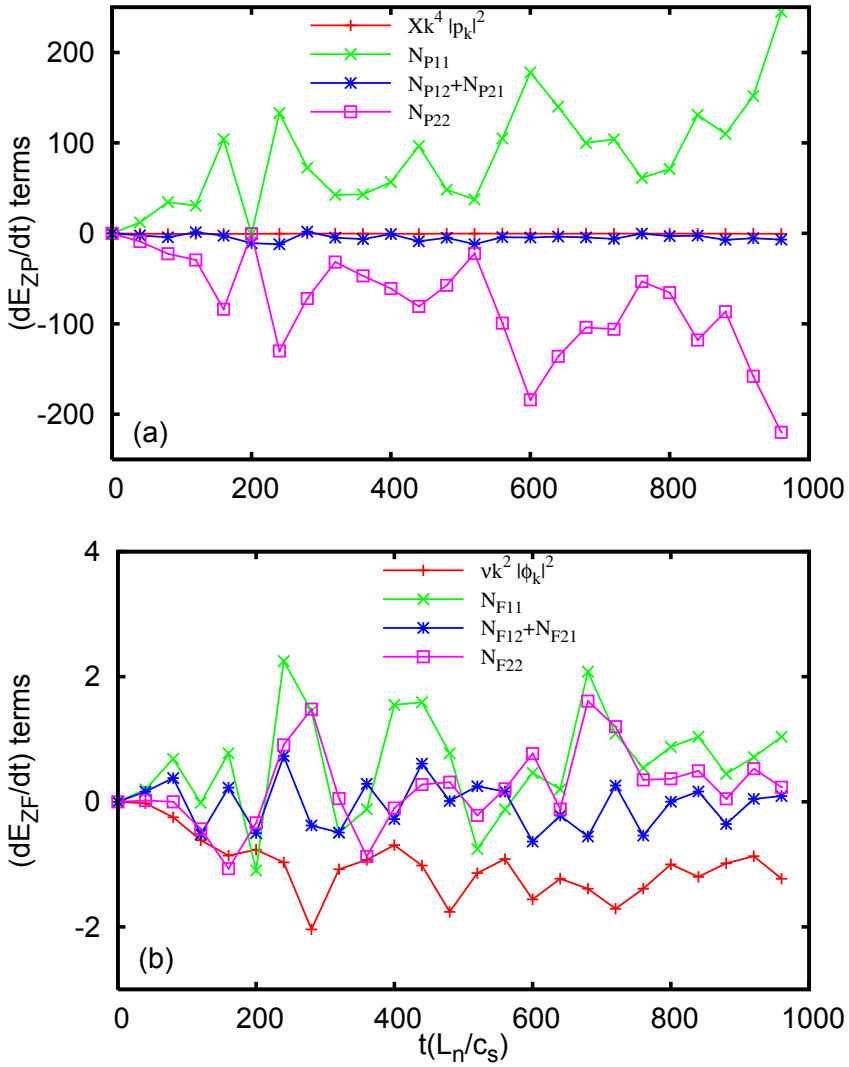

Figure 3.14: The rate of change of energy terms for (a) the zonal pressure (terms in Eq. 3.19) and (b) the zonal flow (terms in Eq. 3.20), for the ITG case.

Looking at Fig. 3.13, we can say that $N_{F11} = N_{1\to F} - (N_{1F1} + N_{11F})$. Since $N_{F11} \ll (N_{1F1}+N_{11F})$ from the above comparison, we can conclude that $N_{1\to F}$ only exceeds $N_{1F1}+N_{11F}$ by a quantity of order unity, which is just 0.1% of $N_{1F1}+N_{11F}$ (which is of order 1000). Given that

$-(N_{12F}+N_{1F2}) = N_{1\to F}+N_{1\to 2}$ and that $N_{1\to F}$ is within 0.1% of $N_{1F1}+N_{11F}$, we can further say that $N_{1\to 2} \approx -(N_{12F}+N_{1F2}+N_{1F1}+N_{11F})$ within a percent. This is shown in Fig. 3.15. This figure shows that N_{111}, $N_{112}+N_{121}$, N_{122}, and $N_{11P}+N_{1P1}+N_{12P}+N_{1P2}$ are small, and that $N_{1F1}+N_{11F}+N_{1F2}+N_{12F}$, which is equal to $N_{1F1}+N_{11F}-|N_{1F2}+N_{12F}| \approx -N_{1\to 2}$, is the only significant net energy transfer term for the unstable mode energetics with a value of -1250 at $t = 400$. Recall that $N_{1\to 2}$ was defined as the energy transferred from the unstable to stable mode via three wave couplings that have a zonal flow as the third term in the interaction triplet. Thus, the net energy transfer dynamics in the equation for $|\beta_1|^2$ is dominated by transfer to the damped eigenmode, with zonal flows acting as a mediator, or a catalyst, of energy transfer from the unstable to stable mode.

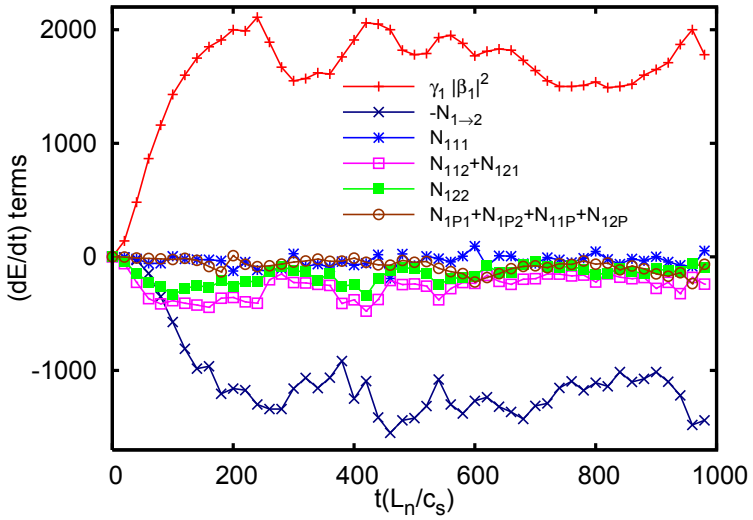

Figure 3.15: The rate of change of energy of the unstable mode in ITG, explicitly showing calculation of the energy transfer from the unstable to stable mode via zonal flows ($N_{1\to 2}$), compared with the other terms in Eq. 3.18.

Another way to show that energy transfer to stable modes via zonal flow is the dominant saturation mechanism is as follows. In a three wave interaction, energy is conserved. Following Eq. (20) of Ref. [61], we get,

$$T_s[k|p,q] + T_s[p|q,k] + T_s[q|k,p] = 0. \tag{3.21}$$

Here, $T_s[k|p,q]$ is the rate of change of energy of Fourier mode k due to the triad interaction with two other Fourier modes p and q. Obviously, some part of this energy transfer goes to mode p and the other goes to q. It can be interpreted that $T_s[p|q,k]$ is the energy transfer to mode p and $T_s[q|k,p]$ is the transfer to mode q. We have tried to apply a similar idea. However, it is more complicated in our case because in addition to Fourier modes, there is also the eigenmode decomposition, which is not orthogonal. Consider all the triads of an unstable mode, a stable mode and a zonal flow. We want to calculate energy transfer from unstable to stable modes, via the zonal flow. These triads obey an energy conservation law:

$$N_{1F2} + N_{12F} + N_{2F1} + N_{21F} + N_{F12} + N_{F21} + N_{m12F} = 0. \tag{3.22}$$

All the terms are defined except N_{m12F}, which arises because of the nonorthogonality of eigenmodes,

$$N_{m12F} = \sum_k \sum_{k'_y=0} 4Re[(1 + k^2 + R_1 R_2^*)(C_{2F2}\beta_1(k)v_z(-k')\beta_2(-k'')) + \tag{3.23}$$

$$(1 + k''^2 + R_1'' R_2''^*)(C_{1F1}\beta_1(k)v_z(-k')\beta_2(-k''))]. \tag{3.24}$$

These terms are plotted in Fig. 3.16. $N_{1F2}+N_{12F}$ is large, negative and represents energy flowing out of the unstable modes. $N_{F12}+N_{F21}$ is tiny and represents the fraction of energy transferred to zonal flows. The term N_{m12F} represents energy transfer to mixed terms. In this simulation it is tiny and negative. $N_{2F1} + N_{21F}$ is large, positive and represents energy transferred to stable modes. The fact that this term balances the energy flowing out of the unstable mode $(N_{1F2} + N_{12F})$, shows that energy transfer to stable modes via zonal flows is the most dominant nonlinear energy transfer channel of the unstable mode.

We have looked at the energy dynamics of the stable modes, and they show a similar and consistent result. The stable modes are also seen to couple primarily with the unstable modes, with the zonal flows acting as a mediator.

The energy transfer rates just described, including the small rates N_{F11} and equivalent differ-

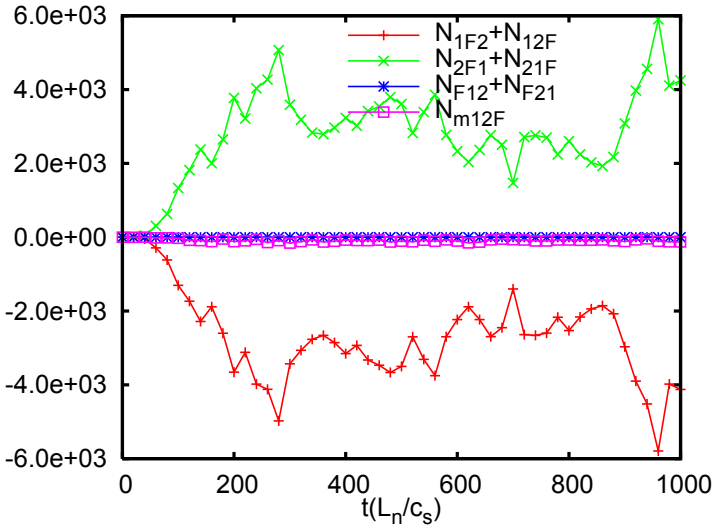

Figure 3.16: We see that all nonlinear energy transfer terms in Eq. 3.22 add up to zero if we include the nonorthogonal cross terms also. This helps in unambiguously identifying the transfer of energy to stable modes via zonal flows ($N_{2F1} + N_{21F}$) as the dominant saturation mechanism.

ences of large rates like $N_{1\to F} - (N_{1F1} + N_{11F})$, are well outside the putative error bars associated with numerical effects that break energy conservation. Observing energy dynamics with growth and damping terms turned off establishes that the rate of non-conservation of energy due to numerical effects is of order of $10^{-7}\%$ of the zonal flow damping. Since zonal flow damping orders the smallest energy transfer processes tracked in this chapter, numerical error does not effect any of the energy transfer rates described above.

We turn now to the question of how zonal flows and stable modes are initially excited. In the linear stage, both zonal flows and stable modes are damped and their amplitudes decrease. At the beginning of the nonlinear stage, both of these are excited by parametric excitation, i.e., by the beating of two unstable modes at different wavenumbers [45]. This stage corresponds to the large overshoot of fluctuation level typically observed in simulations [62], [63]. Once the zonal flow and stable modes reach a finite amplitude, the stable branch is maintained at a finite amplitude by nonlinearly coupling with both the unstable modes and zonal flows. At the same time, the zonal flow is pumped by both the unstable and stable modes. This stage corresponds to the saturated phase of the simulations. Both stages are shown in Fig. 3.17. In this figure

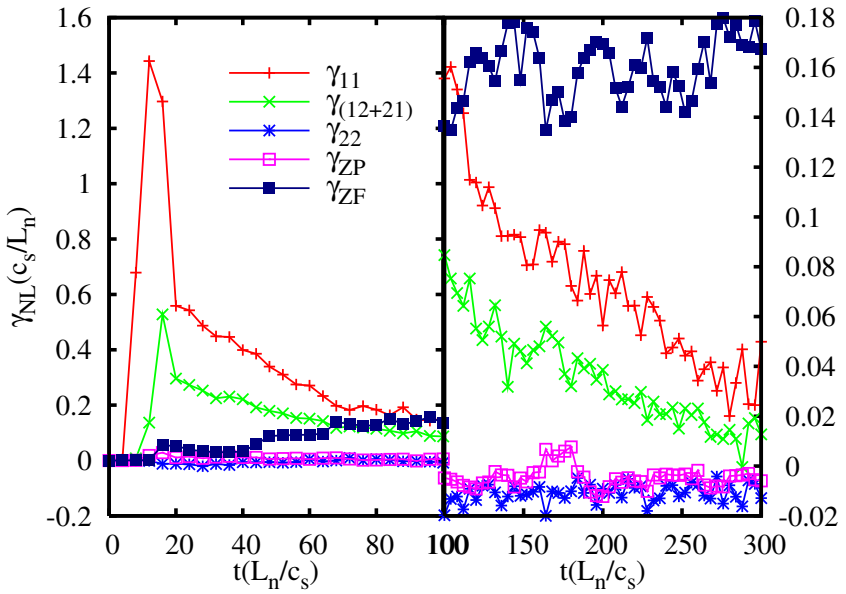

Figure 3.17: The nonlinear growth rate of the stable modes derived from the different nonlinear couplings of the stable mode which are similar to Eq. (3.18). The second panel is a continuation of the first panel with the y axis magnified and x axis shrunk.

the rate of change of energy of the stable mode is divided by the energy of the stable mode, giving a nonlinear growth rate. Just as before, the growth rate is classified into the different coupling terms. For example, γ_{11} is defined as $N_{211}/(\sum_{k_y\neq 0}(1+k^2+|R_2|^2)|\beta_2|^2)$, where N_{211} is the coupling of the stable mode with 2 unstable modes. N_{211} is defined like N_{111} except that the unstable mode at k is replaced by a stable mode. Similarly, $\gamma_{(12+21)}$ represents coupling with one unstable and one stable mode (i.e., $(N_{212}+N_{221})/(\sum_{k_y\neq 0}(1+k^2+|R_2|^2)|\beta_2|^2)$), and γ_{22} represents coupling with two stable modes. $\gamma_{ZP(F)}$ represents coupling with zonal pressure(flow). From $t=0$ up to $t=100L_n/c_s$, the stable mode is seen to be excited by coupling with two unstable modes. After $t=100L_n/c_s$, the coupling with one zonal flow and one unstable mode is seen to dominate. The peak growth rate occurs at $t=12L_n/c_s$. If we look at the energy of the stable mode, it initially decays because it is linearly damped, but then increases due to nonlinear coupling. It's steepest growth occurs at $t=12L_n/c_s$, corresponding to the peak nonlinear growth rate in Fig. 3.17.

3.6 Energy transfer to stable modes within the unstable wavenumber range

The above analysis showing that instability energy is transferred dominantly to the damped mode does not characterize or quantify concomitant energy transfer in wavenumber space. As shown in Fig. 3.10, the ratio of viscous dissipation, which is active at high wavenumber, to dissipation by stable modes summed over the entire wavenumber range, is smaller than 10%. Most of this wavenumber range is unstable because the high k wavenumber range with $\gamma_1 < 0$ is limited for simulation configurations consistent with earlier work [31]. Hence we have looked at how the energy transfer out of a low k wavenumber range compares to the rate of dissipation within that range. The energy spectrum peaks around $k_x\rho_s = 0.0$, $k_y\rho_s = 0.04$, which is greatly shifted from the peak of the linear growth rate around $k_x\rho_s = 0.0$, $k_y\rho_s = 2.0$. The simulation box extends up to $|k_x\rho_s| = |k_y\rho_s| = 3.16$. We calculate the energy transfer within a smaller box, $|k|^2 < 2.0$, $|k'|^2 < 2.0$, $|k''|^2 < 2.0$. This box is less than a quarter of the total simulation box and lies within the wavenumber instability range. The nonlinear energy transfer within this box is shown in Fig. 3.18.

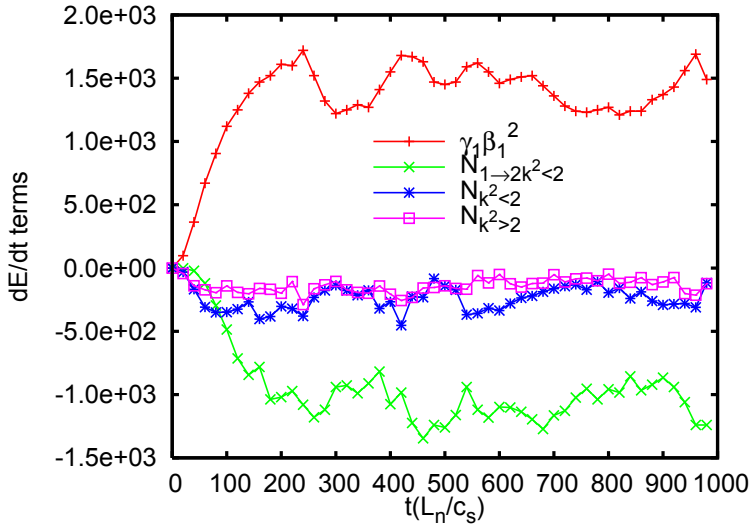

Figure 3.18: Comparison of nonlinear transfer within unstable range with transfer outside it. $N_{1\to 2k^2<2}$ is transfer via zonal flows to stable modes which lie within $|k|^2 < 2$, $N_{k^2>2}$ is transfer to any mode outside of the range $|k|^2 < 2$.

This figure plots 4 quantities which are defined as,

$$\gamma_1\beta_1^2 \equiv \sum_{|k|^2<2} 2\gamma_1 Re[(1+k^2+|R_1|^2)|\beta_1|^2], \tag{3.25}$$

$$N_{1\to 2k^2<2} \equiv \left[N_{1F1}+N_{1F2}+N_{11F}+N_{12F}\right]\Big|_{|k|^2,|k'|^2,|k''|^2<2}, \tag{3.26}$$

$$N_{k^2<2} \equiv \left[\sum_{i,j=1}^{2} N_{1ij}+\sum_{i=1}^{2}(N_{1Pi}+N_{1iP})\right]\Big|_{|k|^2,|k'|^2,|k''|^2<2}, \tag{3.27}$$

$$N_{k^2>2} \equiv \left[\sum_{i,j=1}^{2} N_{1ij}+\sum_{i=1}^{2}(N_{1Pi}+N_{1iP}+N_{1Fi}+N_{1iF})\right]\Big|_{|k|^2<2,\max[|k'|^2,|k''|^2]>2}. \tag{3.28}$$

$\gamma_1\beta_1^2$ is the linear energy input rate summed over modes with $|k|^2<2$. This is balanced by the nonlinear transfer. The dominant term is $N_{1\to 2k^2<2}$. This term represents coupling with stable modes and zonal flow. It is calculated only for modes $|k'|^2<2$ and $|k''|^2<2$. Hence it represents transfer to stable modes only within the box. $N_{k^2<2}$ is sum of all the other coupling terms that do not include a zonal flow, but still lie within the box. $N_{k^2>2}$ is the sum of all nonlinear coupling terms such that $|k'|^2>2$ and/or $|k''|^2>2$. As such it represents energy transferred out of the box. It is very small (less than 20%) compared to the energy transferred to stable modes within the box ($N_{1\to 2k^2<2}$). So even well within the unstable wavenumber range, we get strong coupling of unstable modes with stable mode and zonal flows. This proves that energy is transferred to stable modes which are in the unstable wavenumber range. We expect that the ratio of energy transferred to high k relative to energy dissipated by damped modes at low k can vary from model to model, with the present simulations yielding very low values. However, the general result that ITG saturation and transport in numerical models is essentially independent of the wavenumber resolution much beyond the instability range indicates that energy dissipation by damped modes in the instability range is significant in all cases.

To further probe this result we have used bispectral analysis to look at energy transfer between selected wavenumbers, similar to the study done in Ref. [61]. This is shown in Fig. 3.19 which plots the nonlinear transfer function for eigenmodes at different wavenumbers. The exact

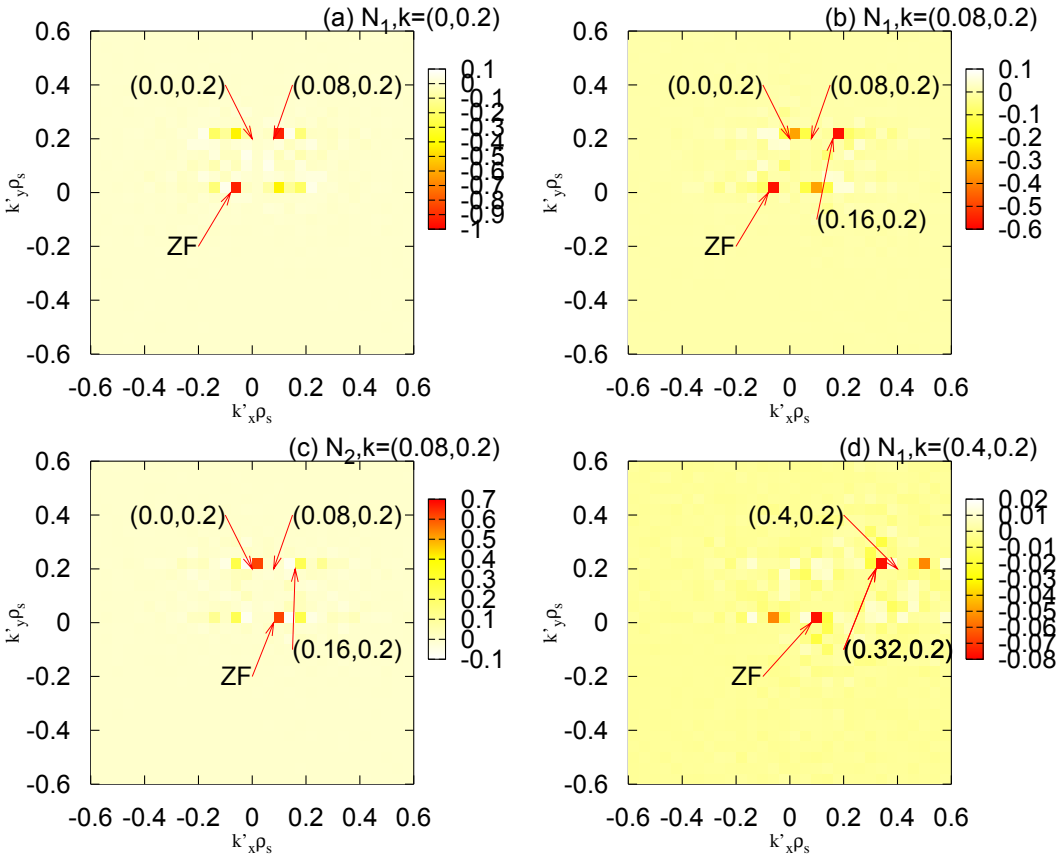

Figure 3.19: The spectrum of nonlinear transfer function for modes at different wavenumbers. See text for more detailed discussion.

quantity plotted in Figs. 3.19(a), (b) and (d) is

$$N_{1k}(k') = \mathcal{A}Re\Big[C_{1mn}\beta_1^*\beta_m'\beta_n''|_{k_y'\neq 0,k_y} + C_{1Pn}\beta_1^* p_z'\beta_n''|_{k_y'=0} + C_{1mP}\beta_1^*\beta_m' p_z''|_{k_y'=k_y} + C_{1Fn}\beta_1^* v_z'\beta_n''|_{k_y'=0} + C_{1mF}\beta_1^*\beta_m' v_z''|_{k_y'=k_y}\Big], \tag{3.29}$$

averaged over the saturated state. The terms in the equation are explained in Appendix A. Effectively, it is the sum of nonlinear energy transfer out of/into the unstable mode at wavenumber k via coupling with modes k' and $k-k'$. The quantity shown in Fig. 3.19(c) is the same except for wherever subscript 1 appears in Eq. 3.29, it is replaced by 2, i.e., the energy transfer out of/into the stable mode at wavenumber k. In Fig. 3.19 different k's are chosen and the nonlinear energy transfer spectrum over k' is plotted. Fig. 3.19(a) is for the unstable mode at $k = (0, 0.2)$. It shows a strong coupling with a zonal flow $k' = (-0.08, 0)$ and as a result, strong energy transfer to $k - k' = (0.08, 0.2)$. In Fig. 3.19(b), we look at the unstable mode at $k = (0.08, 0.2)$. Again it shows strong coupling with the zonal flow at $k' = (-0.08, 0)$ to give energy to $k-k' = (0.16, 0.2)$. It should be noted that the sign of energy transfer to mode $(0, 0.2)$ is still negative, indicating the unstable mode at $(0.08, 0.2)$ gives some energy back to the $(0, 0.2)$ mode. Taking a look at the nonlinear transfer of the stable mode at $k = (0.08, 0.2)$ in Fig. 3.19(c), we see that it receives energy from mode $(0, 0.2)$. This is most of the energy seen in Fig. 3.19(a) going from the unstable mode at $(0, 0.2)$ to mode $(0.08, 0.2)$. Thus the transfer to higher wavenumber is actually transfer to stable modes at higher wavenumber. Fig. 3.19(d) shows nonlinear transfer for a high wavenumber $(0.4, 0.2)$ that is still in the unstable range. The magnitude of nonlinear transfer has reduced by more than a factor 10 compared to Fig. 3.19(a). This is because at every step of energy transfer to higher wavenumber, significant energy is lost to the stable modes.

3.7 Phase matching, coupling coefficients and amplitudes

Now we examine why energy transferred from unstable to stable modes through triads involving a zonal flow as a mediator is the preferred energy transfer channel. Consider the dominant

transfer rate $N_{1F2} + N_{12F}$. From the Appendix A,

$$N_{12F} = \sum_{k_y \neq 0} 2(1 + k^2 + |R_1|^2) Re\left[\left(\frac{1}{R_1 - R_2}\right)\left(\frac{-i}{2}\right) \sum_{k'_y = k_y} k_y \left[R'_2 + \frac{R_2(k''^2 - k'^2)}{(1 + k^2)}\right] \langle \beta_1^* \beta'_2 v''_z \rangle\right] \tag{3.30}$$

where N_{1F2} has the same form with superscripts $''$ and $'$ interchanged. Like all transfer rates, N_{12F} is governed by a triplet correlation of mode amplitudes and a coupling coefficient. The coupling coefficient is $k_y[R'_2 + R_2(k''^2 - k'^2)/(1+k^2)]$. The angle brackets of the triplet correlation $\langle \beta_1^* \beta'_2 v''_z \rangle$ indicate that N_{12F} is part of an equation that was averaged by multiplication with a complex conjugate. The triplet correlation has amplitude and phase information, and the latter in particular contributes critically to the magnitude of N_{12F}. We show that correlations like $\langle \beta_1^* \beta'_2 v''_z \rangle$ and $\langle \beta_1^* \beta'_2 p''_z \rangle$, in which one member is a zonal field and the other members are a stable and unstable mode, have the smallest frequency sum, and hence the longest interaction time of all possible energy transfer triplets. We then show that transfer rates involving a zonal flow (N_{12F}) are larger than transfer rates involving a zonal pressure (N_{12P}) by virtue of the relative magnitudes of amplitudes and coupling coefficients.

3.7.1 Triplet phase

The correlation $\langle \beta_1^* \beta'_2 v''_z \rangle$ is governed by an evolution equation that is derived from Eqs. (3.12)-(3.13). Starting from $d\langle \beta_1^* \beta'_2 v''_z \rangle / dt = \langle \dot{\beta}_1^* \beta'_2 v''_z \rangle + \langle \beta_1^* \dot{\beta}'_2 v''_z \rangle + \langle \beta_1^* \beta'_2 \dot{v}''_z \rangle$ we substitute for $\dot{\beta}_1^*$, $\dot{\beta}'_2$ and $\dot{v}''_z$ from Eqs. (3.12)-(3.13) (transposed to the appropriate wavenumber). The result is

$$\left\{\frac{d}{dt} + i\Big[\omega''_F + \omega'_2 - \omega_1^*\Big]\right\} \langle \beta_1^* v''_z \beta'_2 \rangle = \mathcal{G}, \tag{3.31}$$

where $\omega''_F = \omega_1|_{k'_y = k_y} = -i\nu$ (for the ITG case). The nonlinearity $\mathcal{G}$ is constructed by multiplying the right hand side of the complex conjugate of Eq. 3.12 written for $\dot{\beta}_1^*$ by $\beta'_2 v''_z$ and adding to similar constructs from the right hand sides of Eqs. 3.12, 3.13 for $\dot{\beta}'_2$ and $\dot{v}''_z$ respectively. As such, each term of $\mathcal{G}$ is proportional to quartic correlations. Note that Eq. 3.31 is part of the standard correlation hierarchy in turbulence in which the evolution equation of any correlation

is governed by a nonlinearity comprised of correlations of the next higher order. The equation cannot be solved analytically to reveal its amplitude and phase dependence without some sort of closure. The simulation results, which will be detailed shortly, are well described by closures such as eddy damped quasi normal Markovian (EDQNM) [64]. In EDQNM, part of $\mathcal{G}$ is proportional to $\langle\beta_1^*\beta_2'v_z''\rangle$ and renormalizes the complex triplet frequency to $\hat{\omega}_F''+\hat{\omega}_2'-\hat{\omega}_1^*=\omega_F''+\omega_2'-\omega_1^*+\Delta\omega_F''+\Delta\omega_2'-\Delta\omega_1^*$, where $\Delta\omega_j$ ($j=1$, 2, or F) is a nonlinear (amplitude-dependent) complex frequency. In the rest of $\mathcal{G}$, which we label $\hat{\mathcal{G}}$, the quartic correlations are expressed as products of two quadratic correlations. Applying this, Eq. 3.31 can be formally integrated to yield

$$\langle\beta_1^*\beta_2'v_z''\rangle=\exp\Big\{-i[\hat{\omega}_F''+\hat{\omega}_2'-\hat{\omega}_1^*]t\Big\}\int^t\exp\Big\{i[\hat{\omega}_F''+\hat{\omega}_2'-\hat{\omega}_1^*]t'\Big\}\hat{\mathcal{G}}dt'. \tag{3.32}$$

In the steady state, $\hat{\mathcal{G}}$ varies on a slower time scale than $[\hat{\omega}_F''+\hat{\omega}_2'-\hat{\omega}_1^*]^{-1}$, yielding

$$\langle\beta_1^*\beta_2'v_z''\rangle=\frac{\hat{\mathcal{G}}}{i[\hat{\omega}_F''+\hat{\omega}_2'-\hat{\omega}_1^*]}. \tag{3.33}$$

In this form the frequency mismatch $[\hat{\omega}_F''+\hat{\omega}_2'-\hat{\omega}_1^*]$ is clearly the inverse lifetime of the triplet correlation and $\hat{\mathcal{G}}$ is the component of the correlation that carries the dependencies on coupling coefficients and amplitudes in the form of products of quadratic correlations. For a given $\hat{\mathcal{G}}$, when the lifetime is longer, the correlation and N_{1F2} are larger.

We therefore examine the value of $\hat{\omega}_F''+\hat{\omega}_2'-\hat{\omega}_1^*$, starting first with the linear component $\omega_F''+\omega_2'-\omega_1^*$. In this triad $k-k'$ is a zonal wavenumber, i.e., $k_y'=k_y$. Both k and k' are nonzonal wavenumbers so that $\delta=1$ in ω_1^* and ω_2'. Also, since most of the energy is concentrated in wavenumbers smaller than unity, we can assume that $k^2\leq\nu,\chi\ll1$, and $(\delta+k^2)=1+\mathrm{O}(\nu)$. Then, $\omega_F''=-i\nu$, $\omega_2'=k_y/2-ik_y[(1+\eta)\epsilon]^{1/2}+\mathrm{O}(\nu)$, $\omega_1^*=k_y/2-ik_y[(1+\eta)\epsilon]^{1/2}+\mathrm{O}(\nu)$, and $\omega_F''+\omega_2'-\omega_1^*=\mathrm{O}(\nu)$. If we consider $\langle\beta_1^*\beta_2'p_z''\rangle$ we also have $\omega_P''+\omega_2'-\omega_1^*=\mathrm{O}(\nu)$. However, it is easily verified that any other combination of a zonal frequency and two nonzonal frequencies, or of three nonzonal frequencies yields a frequency mismatch that is order unity instead of order $\nu\ll1$. Note too that if the zonal flow damping rate is order unity, the frequency mismatch also becomes order unity instead of small. Large ν removes the efficiency of energy transfer by

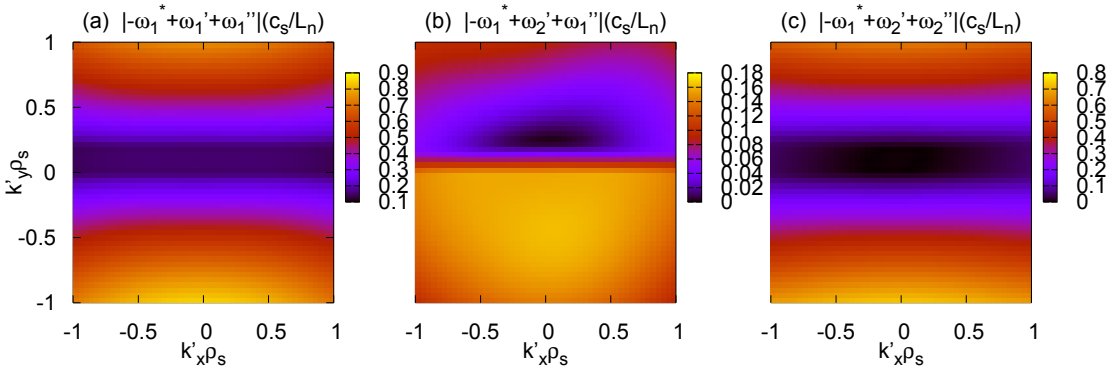

Figure 3.20: The frequency sum using linear frequencies, $|-\omega_i^*(k)+\omega_j(k')+\omega_l(k-k')|$ for $\mathbf{k}=(-0.08,0.2)$, plotted as a function of k'_x and k'_y. In (a) $i=1$, $j=1$, $l=1$, in (b) $i=1$, $j=2$, $l=1$, and in (c) $i=1$, $j=2$, $l=2$.

shortening the interaction time, therefore requiring larger amplitudes to match the instability energy input rate. This mechanism by which zonal flow damping affects turbulence level is a very different effect than the idea that large ν kills the zonal flow and its capacity to suppress turbulence via shear. More work is needed to find out how effective each mechanism is in controlling the level of turbulence.

These analytical predictions can be verified by looking at the frequency mismatch of exact roots of the dispersion relation calculated by the simulation. The wavenumber k is arbitrarily selected as $(-0.08,0.2)$. Then a scan is done over k' to see for which triads $(k,k',k-k')$ the frequency mismatch is minimum. In doing this, several combinations of stable and unstable modes are tested. A triad involves a zonal mode whenever k'_y is either 0.0 or 0.2. First, we look at $|-\omega_1^*+\omega'_1+\omega''_1|$. This is a triad involving three unstable modes. If $k'_y=0.0$ then ω'_1 is taken as $-i\nu$, which is the zonal flow damping. If $k'_y=0.2$ then ω''_1 is taken as $-i\nu$. This is because of Eq. (3.8) which shows that the unstable mode maps to the zonal flow. The scan over k' is shown in Fig. 3.20(a). It shows a minimum value in the regions near k'_y values of 0.0 and 0.2. The exact minimum value is 0.139 at $k'=(1.0,0.0)$, which is a zonal flow. Next, we consider $|-\omega_1^*+\omega'_2+\omega''_1|$. This involves sum of two unstable modes and one stable mode. For $k'_y=0$, $\omega'_2=-i\chi k'^4$, following Eq. (3.9). For $k'_y=k_y$, $\omega''_1=-i\nu$. The scan over k' is shown in

Fig. 3.20(b). Again the minimum lies near $k'_y = 0.2$ which represents coupling to a zonal flow. The exact minimum value of the frequency mismatch is 0.0016 at $k' = (0.04, 0.24)$. This is not a zonal mode coupling but close to it. The frequency mismatch for the mode $k' = (0.0, 0.2)$ is 0.01. We can also combine two stable modes and one unstable mode, $|-\omega_1^* + \omega_2' + \omega_2''|$. If $k'_y = 0$ then $\omega_2' = -i\chi k'^4$. If $k'_y = k_y$ then $\omega_2'' = -i\chi k''^4$. This shows minimum frequency mismatch for a range of k'_y going from 0.0 to 0.2, as displayed in Fig. 3.20(c). The minimum value is 0.0007 at $k' = (-0.2, 0.0)$ and $k' = (0.12, 0.20)$. These observations show that the frequency mismatch is minimum for triads involving a zonal field or modes close to a zonal wavenumber.

The linear frequency mismatch is only part of the correlation time of triplet correlations, except in weak turbulence situations where the nonlinear frequencies are negligible. We now consider the frequency mismatch with the nonlinear frequencies $\Delta\omega_j$. The nonlinear frequencies can be calculated from the closure (see for example Ref. [22]), but we opt here to extract them directly from simulation data as done in Ref. [65]. For each eigenmode for each wavenumber, the frequency spectrum is calculated. A Lorentzian can be fitted to this frequency spectrum. The position of the peak of the Lorentzian gives the real part of $\hat{\omega} = \omega + \Delta\omega$ whereas its width gives the imaginary part. The sign of the imaginary part is chosen depending on whether it is an unstable or stable mode. In this way the nonlinearly broadened frequencies are calculated and used instead of the linear frequencies for calculation of frequency matching.

We again consider the three cases done for the linear eigenfrequencies. For $|-\omega_1^* + \omega_1' + \omega_1'' - \Delta\omega_1^* + \Delta\omega_1' + \Delta\omega_1''|$ a similar scan is done in k' with k again chosen as $(-0.08, 0.2)$. The frequency sum is plotted against k'_y for $k'_x = 0$ in Fig. 3.21(a). The minimum value is 0.083 at $k'_y = 0.12$. However, this is not a triad with a zonal mode. For $|-\omega_1^* + \omega_2' + \omega_1'' - \Delta\omega_1^* + \Delta\omega_2' + \Delta\omega_1''|$ the result is similar to the linear phase calculation. As shown in Fig. 3.21(b), the minimum frequency mismatch occurs again at $k'_y = 0.2$, and its value is 0.029. This is a coupling with a zonal mode (at $k - k'$) and a stable mode (at k'), and it's phase mismatch is less than half of the minimum mismatch for $|-\omega_1^* + \omega_1' + \omega_1'' - \Delta\omega_1^* + \Delta\omega_1' + \Delta\omega_1''|$. This shows that the mismatch is smaller for triads that involve one zonal mode, one unstable and one stable mode, compared to one zonal mode and two unstable modes. For $|-\omega_1^* + \omega_2' + \omega_2'' - \Delta\omega_1^* + \Delta\omega_2' + \Delta\omega_2''|$ the result is shown

in Fig. 3.21(c). Using only linear phases, this quantity showed minimum mismatch for triads involving zonal modes as well as a range of non-zonal triads between $k'_y = 0.0$ and $k'_y = 0.2$. But using the nonlinear phases, we see minimum mismatch only for triads involving zonal modes, i.e., at $k'_y = 0.0$ where the mismatch is 0.003 and at $k'_y = 0.2$ where the mismatch is 0.03.

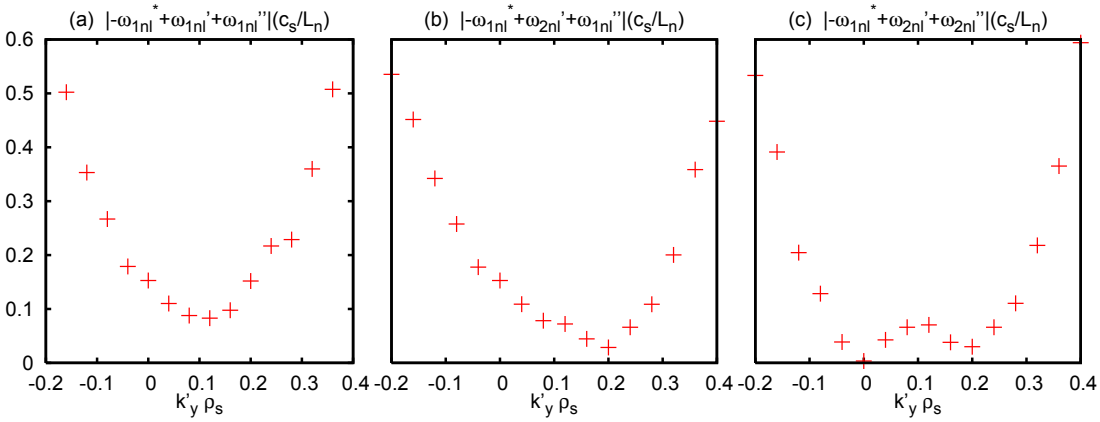

Figure 3.21: The frequency sum using the nonlinear frequencies, $|-\omega_i^*(\mathbf{k})+\omega_j(\mathbf{k}')+\omega_l(\mathbf{k}-\mathbf{k}')-\Delta\omega_i^*(\mathbf{k})+\Delta\omega_j(\mathbf{k}')+\Delta\omega_l(\mathbf{k}-\mathbf{k}')|$ for $\mathbf{k} = (-0.08, 0.2)$, $k'_x = 0$ plotted as a function of k'_y. In (a) $i = 1$, $j = 1$, $l = 1$, in (b) $i = 1$, $j = 2$, $l = 1$, and in (c) $i = 1$, $j = 2$, $l = 2$.

These results show that the frequency mismatch is minimum for triads involving an unstable mode, a stable mode and a zonal mode. Such triads are the dominant nonlinear coupling terms, leading to saturation. Moreover, as stated before, the minimum value of the frequency mismatch scales with ν, the zonal flow damping. This is because the flow damping rate (times i) is the zonal mode frequency in the linear frequency mismatch. This is displayed in Table 3.1, which shows that the frequency mismatch of a triad containing an unstable mode, a stable mode and a zonal flow scales with the zonal flow damping rate. However, we can also consider zonal mode triads in which the pressure damping is used for the zonal mode frequency. The pressure damping is χk^4 so the triads would become $|-\omega_1^* + \omega'_2 - i\chi k^4|$. The same cancellation occurs as explained above and a zonal pressure triad frequency sum can be approximated as χk^4. Since χ is of the order of ν and $k < 1$, the zonal pressure triads would also show a very small value of the frequency sum just like the zonal flow triads, indicating minimum frequency mismatch. As a result, low frequency mismatch does not explain why zonal flow triads are more important than

zonal pressure triads.

Table 3.1: Linear frequency sum for $k = (-0.08, 0.2)$ and $k' = (0.0, 0.2)$ as zonal flow damping, ν, is varied

ν	$\lvert -\omega_1^*(k) + \omega_2(k') + \omega_1(k-k')\rvert$
0.01	0.0104
0.02	0.0203
0.05	0.0503

3.7.2 Coupling coefficients

We examine now the coupling coefficients in the triplet nonlinear terms of the energy equations. We have already identified the coupling coefficient in N_{12F}, prior to discussing in detail its phase. We consider other triplet terms in the evolution equations for the energies $(1+k^2+|R_1|^2)|\beta_1|^2$, $(1+k^2+|R_2|^2)|\beta_2|^2$, $|p_k|^2$, and $(\delta+k^2)|\phi_k|^2$. The coupling coefficient in each triplet term is equal to the product of either $1+k^2+|R_i|^2$ (for non-zonal modes) or unity (for zonal modes) and a corresponding coupling coefficient from the eigenmode evolution equations, Eqs. (3.12) - (3.14). Each coupling coefficient in Eq. (3.12) contains a factor $1/(R_1 - R_2)$. For long wavelengths ($k^2 \ll 1$), $(R_1 - R_2) \approx -2i[(1+\eta)/\epsilon]^{1/2}$, is independent of k. Also, for long wavelengths, the eigenvector magnitudes $|R_1|, |R_2|$ lie within the range of 6 to 7 and they vary weakly with k. Thus the factors $(1+k^2+|R_i|^2)$ are roughly constant. The remaining part of the coupling coefficients is strongly dependent on k, and the power of k indicates magnitude, with smaller powers representing stronger coupling. In analyzing the power, we do not distinguish between k and k', but treat both as comparably smaller than unity. The following wavenumber dependence is found for the coupling coefficients in the evolution equations of the unstable and stable modes, (Eq. 3.12):

$$C_{lmn}(\text{or } N_{lmn}) \sim k^2,$$

$$C_{lFn}(\text{or } N_{lFn}) \sim C_{lmF}(\text{or } N_{lmF}) \sim k, \tag{3.34}$$

$$C_{lPn}(\text{or } N_{lPn}) \sim C_{lmP}(\text{or } N_{lmP}) \sim k^2,$$

where $l, m, n = 1$ or 2. The strongest coupling coefficients are with the zonal flows ($\sim k$). But this holds for both the ETG and ITG cases. The coupling coefficients in the evolution equation of the zonal pressure, (Eq. 3.14), are,

$$C_{Pmn}(\text{or } N_{Pmn}) \sim k^2. \tag{3.35}$$

The coupling coefficients in the evolution equation of the zonal flow, (Eq. 3.13), are,

$$C_{Fmn}(\text{or } N_{Fmn}) \sim \frac{k^5}{\delta + k^2}. \tag{3.36}$$

This shows that the coupling coefficients for the zonal flows are stronger for the ITG case ($\sim k^3$) compared to the ETG case ($\sim k^5$). This is part of the reason why zonal flows are excited to a higher level in the ITG case. However, as explained above (Eq. 3.34) the unstable mode coupling with zonal flows is stronger than its coupling with other modes for both ETG and ITG cases. Hence this alone cannot explain the difference between the two cases. Consequently, we must consider relative amplitude information, which also contributes to the magnitude of the nonlinear transfer.

3.7.3 Amplitude of zonal modes

The strength of a triad also depends on the amplitudes of the three fields in it. We compare the zonal pressure and zonal flow amplitudes in the ETG and ITG cases. The energy level of the zonal flow and zonal pressure averaged over the saturated state are provided in Table. 3.2. The level of zonal pressure is more than zonal flow in both cases. In the ETG case the zonal flow is smaller than zonal pressure by a factor of 15. However, in the ITG case the zonal flow is only 3 times smaller than the zonal pressure. This is possibly due to the fact that the nonlinear coupling coefficients of the zonal flow field are stronger in ITG case compared to ETG case.

The three main points of this section can be summarized as follows. 1) Triplet frequency matching favors triads that include a zonal mode, an unstable mode and a stable mode, in both ETG and ITG. 2) Coupling coefficients in the unstable mode energy evolution equation favor

Table 3.2: Zonal flow and zonal pressure energy levels for ITG and ETG

	ETG	ITG
$\langle p_Z^2 \rangle$	1.17×10^4	5.75×10^2
$\langle v_Z^2 \rangle$	5.60×10^1	6.10×10^1

zonal flow triads over zonal pressure triads, in both ETG and ITG. 3) Amplitude favors zonal pressure triads over zonal flow triads in ETG but gives relatively equal weight-age to both in ITG. These three facts combined together explain why in ITG the saturation happens with a triad involving the unstable mode, a zonal flow and a stable mode, as shown explicitly in section 3.6.

3.8 Discussion

The interaction of zonal flows with ITG turbulence involves damped modes, making the process different from prior descriptions. We showed that zonal flows mediate energy transfer from the unstable mode to a damped mode in the large-scale wavenumber range of the instability. Direct energy transfer to damped modes without zonal-flow mediation is less efficient, and when zonal flows are artificially removed, it requires higher amplitudes to match the energy injection rate of the instability.

After an initial transient phase in which zonal flows and the damped mode are each driven by beating wavenumbers of the unstable mode, the dominant energy transfer is through a 3-wave interaction between the unstable mode, the zonal flow, and the stable mode. Of the net energy transferred from the unstable mode, almost all (more than 99%) ends up in the stable mode, where it is dissipated. The very small amount of energy that ends up in the zonal flow (less than 1%) is balanced by the small zonal flow damping. The triplet interaction of an unstable mode, a zonal flow and a stable mode forms the dominant energy transfer channel through a combination of three factors. Its three-wave nonlinear frequency mismatch is minimum, leading to the largest nonlinear interaction time. It has the largest coupling coefficient. This triplet is also enhanced in ITG relative to ETG by a larger zonal flow amplitude and a smaller zonal pressure amplitude.

This process deviates from the standard picture of zonal flow effects in ITG turbulence in

several ways. Saturation is achieved at low k through the damped mode, which has not been considered in the standard picture. With the damped mode the amount of energy dissipated at high k is not large, nor is the amount of energy transferred to high k. Consequently zonal flow shear, frequently invoked to explain the effect of zonal flows on turbulence, while an active process, is not a significant player in the saturation or energy transfer physics in the simulations described here. The ratio of energy transferred to high k relative to energy dissipated at low k may vary with other models. Zonal-flow drive in the steady state is dominated by the triad of the unstable mode, the zonal flow and the damped mode. Descriptions of zonal flow excitation that do not include damped modes miss the dominant saturation process.

There is considerable evidence that the processes described here for a reduced fluid model also operate in gyrokinetic models of ITG turbulence. The primary difference is that instead of a single damped mode, there are many damped modes [27]. However, it remains true that saturation is caused by damped modes in the same wavenumber range as the instability, that nonlinear transfer to these modes dominates transfer to high k, and that zonal flows participate in the three-wave interactions that take instability energy to the damped modes [66]. The interaction of zonal flows and damped modes in gyrokinetics will be described in detail in the next chapter. One unexpected result from gyrokinetics is that the strongest damped mode excited is a tearing parity mode that makes the magnetic field stochastic and causes magnetic-fluctuation induced electron thermal transport [66], [67]. This mode is excited by the same triad coupling of an unstable mode, a zonal flow, and a stable mode as described in this paper. Hence while mediating a reduction of ion channel transport by lowering the fluctuation level, the zonal flow mediates an *enhancement* of electron channel transport. This is not an optimal situation for confinement. However, the role of zonal flows in mediating energy transfer to damped modes raises the intriguing possibility that it may be possible to externally manipulate the dominant energy transfer through fluctuations other than zonal flows and thereby control to which type of damped mode most of the energy flows. This could then be used to select for a desirable or optimal set of transport properties.

Chapter 4

Subdominant modes in gyrokinetic simulations of zonal flow regulated turbulence

We saw in the previous chapter how zonal flows play the role of an energy transfer catalyst in ITG turbulence. That work was done using a simplified fluid model with a somewhat arbitrary factor of "δ" introduced to mimic the zonal flow instability. Over the last decade, plasma microturbulence is increasingly being simulated by gyrokinetic codes. Gyrokinetic models are more comprehensive than the fluid models and are considered state-of-the-art. They are also more complicated than fluid models. Performing an analysis similar to the previous chapter for a gyrokinetic model presents its own difficulties and challenges but puts it on a stronger footing. It also gives new insight into the interaction of zonal flows and subdominant modes. The present chapter deals with such a study. First we introduce gyrokinetics in Sec. 4.1, followed by a discussion of mode decomposition in gyrokinetics in Sec. 4.2. The energy diagnostics are explained in Sec. 4.3 followed by results of nonlinear energy transfer calculations in Sec. 4.4 which show that the strongest nonlinear interactions involve a zonal flow. In Sec. 4.5 we show that a significant proportion of the energy involved in such interactions is dissipated by stable modes within the

range of small, unstable wavenumbers. In Sec. 4.6 we attempt to make a connection between this new mechanism of zonal flow enhanced energy transfer to stable modes and the conventional mechanism of enhanced energy transfer to dissipative wavenumbers due to zonal flow shear. We then also talk about the frequency matching in gyrokinetics in Sec. 4.7 followed by discussion in Sec. 4.8.

4.1 Gyrokinetics

In all the models studied until now, the plasma has been described as a fluid with certain properties such as flow, density, temperature, etc. These models have been very useful for understanding the underlying physics and obtaining a qualitative picture of the turbulence. These models assume a local thermal equilibrium with a local Maxwellian distribution function. However, a real plasma is very complicated and may not necessarily be in local thermal equilibrium. Fusion plasmas are very hot, their collisionality is very small, and their distribution function can be significantly different from a Maxwellian. Hence, a fluid approach is not rigorously valid and a kinetic approach is required, in which the plasma is described by a single particle distribution function $f_j(\mathbf{x}, \mathbf{v}, t)$ [68], [69]. Here f_j is the distribution function of plasma species j at a position $\mathbf{x}$ moving with velocity $\mathbf{v}$. f_j is normalized to N_j, the total number of particles of species j, i.e., $\int f_j(\mathbf{x}, \mathbf{v}, t)\mathrm{d}\mathbf{x}\mathrm{d}\mathbf{v} = N_j$. It is thought that such a description is sufficient to describe all the important properties of a fusion plasma required for its quantitative prediction.

However, solving for the full distribution function of a plasma in a fusion device is still very difficult even for the largest supercomputers available today. Hence further simplifications are required. Gyrokinetics is one such simplification and it is well suited for studying microturbulent fluctuations in a fusion plasma [70]. In gyrokinetics, use is made of the strong external magnetic field typically present in fusion devices. This field makes the particles circle in a gyro-motion at a fast gyro-frequency. Thus we can assume that,

$$k_\perp \rho_i \sim \mathcal{O}(1), \tag{4.1}$$

$$\rho_* \equiv \frac{\rho_i}{L} \ll 1. \tag{4.2}$$

Here, $k_\perp$ is the typical wavenumber of microturbulent fluctuations perpendicular to the equilibrium magnetic field and ρ_i is the ion gyroradius. The ion gyroradius is considered very small compared to some macroscopic length scale like the gradient length scales, L, and their ratio is defined as the smallness parameter ρ_*. Some other orderings are also utilized in deriving the gyrokinetic equation. For example,

$$\frac{k_\parallel}{k_\perp} \sim \mathcal{O}(\rho_*), \tag{4.3}$$

which signifies that fluctuations have small extent in the perpendicular direction compared to parallel direction (w.r.t. equilibrium magnetic field). Also the frequency of fluctuations (ω) is much smaller then the fast gyromotion frequency of ions (Ω_i),

$$\frac{\omega}{\Omega_i} \sim \mathcal{O}(\rho_*). \tag{4.4}$$

The quantities related to gyromotion, like ρ_i and Ω_i, are calculated taking the particle velocity as their thermal velocity, $v_{T,j} = \sqrt{2T_{0,j}/m_j}$. These approximations are shown pictorially in Fig. 4.1. In addition, the fluctuating quantities are considered small compared to the background,

$$\frac{e\delta\phi}{T_{0,j}} \sim \frac{\delta B}{B_0} \sim \mathcal{O}(\rho_*), \tag{4.5}$$

where, $\delta\phi$ is the perturbed electrostatic potential, $T_{0,j}$ is the background temperature of species j, e is the proton charge, δB is the magnetic field fluctuation, and B_0 is the strong background magnetic field.

The gyrokinetic equation, which averages over the particle gyromotion to remove one degree of freedom, is derived from the Vlasov-Maxwell system of equations. Simple derivations can be found in Refs. [71] and [72]. The Vlasov equation is,

$$\left[\frac{\partial}{\partial t} + \mathbf{v}\cdot\frac{\partial}{\partial \mathbf{x}} + \frac{q_j}{m_j}[\mathbf{E}(\mathbf{x},t) + \mathbf{v}\times\mathbf{B}(\mathbf{x},t)]\cdot\frac{\partial}{\partial \mathbf{v}}\right] f_j(\mathbf{x},\mathbf{v},t) = 0. \tag{4.6}$$

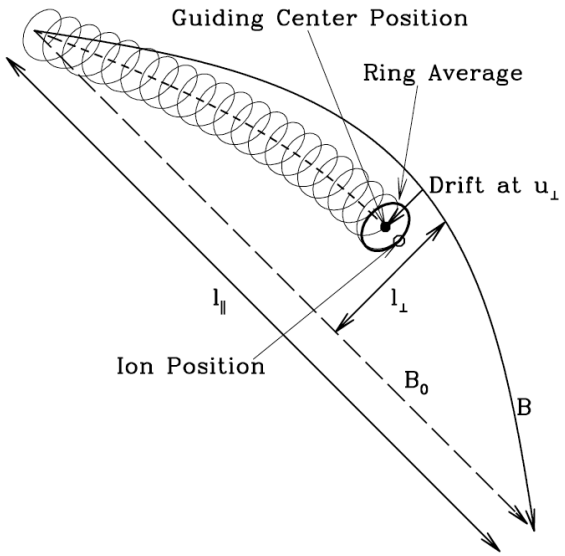

Figure 4.1: Gyro ordering. The parallel scale length, $l_\parallel \sim (1/k_\parallel)$, is much larger than the perpendicular length scale, $l_\perp \sim (1/k_\perp)$, which is comparable to the ion gyro-radius, ρ_i. Also, the frequency of gyromotion, Ω_i, is much faster than the frequency of microturbulent fluctuations, ω. Taken from Ref. [71].

.

The well known Maxwell equations are

$$\nabla \cdot \mathbf{E} = 4\pi \sum_j q_j \int \mathrm{d}\mathbf{v} f_j, \tag{4.7}$$

$$\nabla \cdot \mathbf{B} = 0, \tag{4.8}$$

$$c\nabla \times \mathbf{E} = -\frac{\partial \mathbf{B}}{\partial t}, \tag{4.9}$$

$$c\nabla \times \mathbf{B} = 4\pi \sum_j q_j \int \mathrm{d}\mathbf{v}\mathbf{v} f_j + \frac{\partial \mathbf{E}}{\partial t}. \tag{4.10}$$

Here, $\mathbf{E}(\mathbf{x}, t)$ is the electric field, q_j is charge of species j, $\mathbf{B}(\mathbf{x}, t)$ is the magnetic field and c is the speed of light. These equations are in cgs units. In gyrokinetics the spatial dimension is defined by the guiding center coordinates. The guiding center coordinate ($\mathbf{X}_j$) is the center of

the gyro motion and it is related to the spatial coordinate $\mathbf{x}$ by

$$\mathbf{x} = \mathbf{X}_j - \frac{\mathbf{v} \times \hat{\mathbf{z}}}{\Omega_j}, \tag{4.11}$$

where $\hat{\mathbf{z}}$ is a unit vector pointing along the equilibrium magnetic field and Ω_j is the Larmor frequency of species j. This can be viewed just as a species dependent coordinate transformation from $(\mathbf{x}, \mathbf{v}) \rightarrow (\mathbf{X}_j, \mathbf{v})$.

The gyrokinetic equation is derived by first transforming the Vlasov-Maxwell equations into guiding center coordinates. Then the various quantities are expanded in a perturbation expansion using the small parameters defined in Eqs. 4.2-4.5. Keeping only first order quantities, an averaging is performed over the gyroangle of motion because it is assumed that the gyromotion happens on a timescale much faster than the dynamics we are interested in (Eq. 4.4). The gyro averaging simplifies the equations because it reduces the dimensionality of velocity space from 3 to 2, as the third velocity coordinate is averaged out. In the gyrokinetic model that we use, this reduced velocity space is described by the velocity parallel to the equilibrium magnetic field, $v_\parallel$, and the magnetic moment, $\mu = mv_\perp^2/(2B_0)$, where m is the mass of particle, $v_\perp$ is the magnitude of velocity perpendicular to equilibrium magnetic field which has magnitude B_0. This perturbation expansion and gyro-averaging is applied to the Maxwell equations also. In addition, the perturbation expansion also entails a splitting of the distribution function into a mean and a fluctuating part, $f_j = F_{M,j} + \delta f_j$, where $F_{M,j}$ is the background equilibrium distribution function of species j and δf_j is the perturbed fluctuation. Upon doing this, we get the gyrokinetic Vlasov-Maxwell system of equations. The gyrokinetic Vlasov equation is,

$$\frac{\partial g_j}{\partial t} = \mathcal{L}[g_j] + \mathcal{N}[g_j], \tag{4.12}$$

where g_j is related to δf_j by,

$$g_j = \delta f_j + \frac{2q_j}{m_j v_{Tj}} v_\parallel \bar{A}_\parallel F_{0j}. \tag{4.13}$$

g_j is a function of k_x and k_y, the field line following spatial coordinate z, parallel velocity $v_\parallel$,

magnetic moment μ and time t. The wavenumbers k_x and k_y are Fourier wavenumbers in the plane perpendicular to the equilibrium magnetic field where x is the radial direction and y is the binormal direction. The operator $\mathcal{L}$ represents the linear gyrokinetic operator and $\mathcal{N}$ represents the nonlinear gyrokinetic operator. These are specified in the Appendix B. The gyrokinetic Poisson equation is,

$$\phi = \frac{\sum_j n_{0j}\pi q_j B_0 \int J_0(\lambda_j) g_j dv_\parallel d\mu}{k_\perp^2 \lambda_D^2 + \sum_j \frac{q_j^2}{T_{0j}} n_{0j}(1-\Gamma_0(b_j))}. \tag{4.14}$$

The gyrokinetic Ampere's law is,

$$A_\parallel = \frac{\sum_j \frac{\beta}{2} q_j n_{0j} v_{Tj} \pi B_0 \int dv_\parallel d\mu v_\parallel J_0(\lambda_j) g_j}{k_\perp^2 + \sum_j \frac{\beta q_j^2}{m_j} n_{0j} \pi B_0 \int dv_\parallel d\mu v_\parallel^2 J_0^2(\lambda_j) F_{0j}}. \tag{4.15}$$

All the symbols in Eqs. 4.12-4.15 along with their normalizations are given in Appendix B. Most of this notation is borrowed from Refs. [21], [73].

The simulations in this thesis, unless specified otherwise, are for the Cyclone Base Case (CBC) parameters [46]. CBC defines a set of experimentally relevant parameters. A sample simulation parameters file is shown in Appendix C, which shows the typical parameters used for CBC. It has a safety factor $q = 1.4$, magnetic shear $\hat{s} = 0.8$, local inverse aspect ratio $r/R = 0.18$, mean ion and electron densities $n_i = n_e = 1$ (normalized to some arbitrary n_{ref}), mean ion and electron temperatures $T_i = T_e = 1$ (normalized to some arbitrary T_{ref}), inverse temperature gradient scale length $R/L_T = 6.9$ and inverse density gradient scale length $R/L_n = 2.2$. The plasma β is kept zero, giving only electrostatic fluctuations. Artificial hyper-diffusivity is used in z space and parallel velocity space with coefficients $D_z = 8.0$ and $D_v = 5.0$ [74]. Such high values of hyper-diffusivity help in smoothening out the damped modes (see Sec. 5.3). The perpendicular box size is $(L_x, L_y) = (126\rho_i, 126\rho_i)$ with $k_{x,max}\rho_i = 3.15$ and $k_{y,max}\rho_i = 0.75$, and $|k_{x,min}\rho_i| = |k_{y,min}\rho_i| = 0.05$. The domain of z is $[-\pi, \pi]$ radians, domain of $v_\parallel$ is $[-3v_{T,j}, 3v_{T,j}]$, and domain of μ is $[0, 8T_{0,j}/B_{ref}]$. The resolution in $(k_x, k_y, z, v_\parallel, \mu)$ is $(128, 16, 16, 32, 8)$. The electrons are assumed to be adiabatic, so these are single species simulations.

4.2 Proper orthogonal decomposition

In order to study the damped modes of the fluid models, we decomposed their fields into the linear eigenmodes R_1 and R_2 (Eq. 2.14). We have to do something similar for the gyrokinetic model. The fluid models we studied had only two fields, F_1 and F_2, at each Fourier wavenumber $k_\perp$. However, in gyrokinetic models each wavenumber has an infinite dimensional space in z, $v_\parallel$ and μ. Even after numerical discretization, tens of thousands of modes remain at each wavenumber.

We use the gyrokinetic code GENE to solve the set of gyrokinetic equations [75], [76]. GENE is physically comprehensive, well benchmarked, portable, and highly scalable. We run it in the local flux tube geometry but it can be run in a global geometry also. GENE also has an eigenvalue solver to calculate the linear eigenvalues and eigenvectors of the gyrokinetic linear operator. Linear eigenmodes have been studied earlier in the context of damped modes [25], [27]. However, these modes present significant difficulties in analyzing the energy dynamics of damped modes, hence we do not use them for the energy analysis in this chapter. We will, however, come back to them in the next chapter. In this chapter we utilize proper orthogonal decomposition (POD) modes, also known as singular value decomposition (SVD) [77].

POD is a general decomposition that can be applied to any complex $m \times n$ matrix, M. It decomposes the matrix into three parts,

$$M = U\Sigma V^*, \tag{4.16}$$

where U is an $m \times m$ unitary matrix, Σ is an $m \times n$ diagonal matrix and V^* is an $n \times n$ unitary matrix. The diagonal elements of Σ are called the singular values, which are real and non-negative. The m columns of U are called left eigenvectors while the n columns of V, which is the conjugate transpose of V^*, are the right eigenvectors. Being unitary matrices, the left and right eigenvectors are orthonormal amongst themselves, i.e.,

$$\begin{aligned} UU^* &= I, \\ VV^* &= I. \end{aligned} \tag{4.17}$$

The GENE code solves for the gyrokinetic distribution function $g_{\mathbf{k}}(z, v_{\|}, \mu, t)$ and can output it at regular time steps t_1, t_2, ..., t_n. A particular Fourier wavenumber is selected and its three dimensions $(z, v_{\|}, \mu)$, possibly along with the radially connected k_x modes (see Sec. 5.2.1), are spliced together in one dimension. If there is more than one species then their distribution functions can also be added on to this one dimensional array. However, for simplicity we will be using only one ion species simulations assuming adiabatic electrons for this thesis, unless mentioned otherwise. These one dimensional arrays form the columns of matrix M with the rows designating different time steps. This is shown in Fig. 4.2.

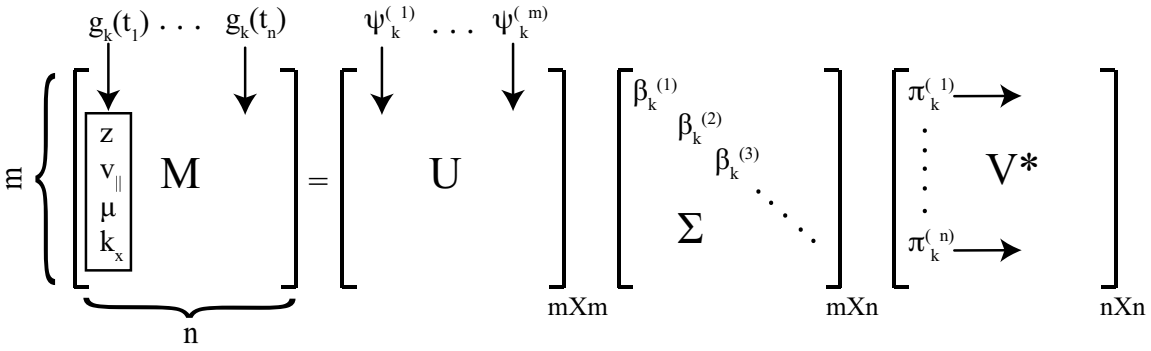

Figure 4.2: The matrix M is an $m \times n$ matrix where $m = N_x \times N_z \times N_{v_{\|}} \times N_{\mu}$ is the number of grid points for each k_y mode and n is the number of time samples. The dimensions z, $v_{\|}$, μ, and connected k_x are spliced along the columns of M and U. Time varies along the rows of M, U, and V^*. Generally, $n < m$ and so we only need to consider the first n POD modes from $\psi_{\mathbf{k}}^{(1)}$ up to $\psi_{\mathbf{k}}^{(n)}$.

Mathematically, the POD of distribution function can be represented as,

$$g_{\mathbf{k}}(z, v_{||}, \mu, t) = \sum_{n=1}^{N} \psi_{\mathbf{k}}^{(n)}(z, v_{||}, \mu) \beta_{\mathbf{k}}^{(n)} \pi_{\mathbf{k}}^{(n)}(t). \tag{4.18}$$

Here N is the number of POD modes in the system, which is equal to the $N_x \times N_z \times N_{v_{\|}} \times N_{\mu}$, where N_x is the number of connected k_x modes (see Appendix B of Ref. [21] or Sec. 5.2.1 for an explanation of k_x connected modes); N_z, $N_{v_{\|}}$ and N_{μ} are the number of grid points in z, $v_{\|}$ and μ dimensions respectively. $\psi_{\mathbf{k}}^{(n)}(z, v_{||}, \mu)$ is the left eigenvector and it is called as the POD mode (columns of U in Fig. 4.2). $\beta_{\mathbf{k}}^{(n)}$ are the singular values (entries of diagonal matrix

Σ in Fig. 4.2), which are real. $\pi_{\mathbf{k}}^{(n)}(t)$ is the right eigenvector and can be thought of as a time dependent coefficient of linear expansion (rows of V^* in Fig. 4.2). Together $\beta_{\mathbf{k}}^{(n)} \times \pi_{\mathbf{k}}^{(n)}(t)$ can be thought as the time dependent amplitude of n^{th} POD mode $\psi_{\mathbf{k}}^{(n)}$. These modes are normalized such that they are orthonormal. The POD modes satisfy the orthonormality condition,

$$\int \frac{\pi B_0 \hat{J}(z) \mathrm{d}z \mathrm{d}v_{||} \mathrm{d}\mu}{F_0} \psi_{\mathbf{k}}^{(m)*} \psi_{\mathbf{k}}^{(n)} = \delta_{m,n}. \tag{4.19}$$

where $\hat{J}(z)$ is a normalized Jacobian of coordinate transformation and $\delta_{m,n}$ is the Kronecker-Delta function. The time traces also satisfy an orthonormality relation,

$$\sum_{l=1}^{N_t} \pi_{\mathbf{k}}^{(n)*}(t_l) \pi_{\mathbf{k}}^{(m)}(t_l) = \delta_{m,n}, \tag{4.20}$$

where the sum is over the time steps from 1 up to N_t.

POD modes are labelled in order of decreasing singular value. POD mode structures are shown in Fig. 5.7 whereas the linear mode structures are shown in Fig. 5.10. The mode structure of the first POD mode is very similar to the structure of first linear eigenmode, which is the unstable ITG mode. The second and higher POD modes are the subdominant modes. The second POD mode shows similarity with the least damped linear eigenmode, as seen in Fig. 3.5 of Ref. [21]. But as we proceed to higher mode number, the similarity between the two starts decreasing and soon they become completely different (again see Figs. 5.7 and 5.10).

4.3 Energetics

The energy-like quantity, for the simple electrostatic gyrokinetic model we are using, is [26], [78],

$$E = \sum_{\mathbf{k}} Re\Big\{ \int dz dv_{\|} d\mu \frac{\hat{J}(z) \pi n_0 T_0 B_0}{F_0} \Big[|g|^2 + \frac{q F_0}{T_0} \chi^* g \Big] \Big\}. \tag{4.21}$$

The subscript j has been suppressed because this expression is written for a single species plasma, but it can be straightforwardly generalized to multiple species by just summing it up over all

the required species. This definition is chosen such that the energy quantity is conserved by the nonlinear terms of the gyrokinetic equation, similar to the fluid models earlier. We substitute the POD (Eq. 4.18) into the energy expression and make use of the orthonormality (Eq. 4.19). We get

$$E = \sum_{\mathbf{k}} Re\Bigg\{ n_0 T_0 \sum_n |\beta^{(n)}\pi^{(n)}|^2 + \int dz dv_\parallel d\mu \hat{J}(z) \pi n_0 B_0 \sum_m \sum_n \chi^{(m)*}\psi^{(n)}\beta^{(m)}\beta^{(n)}\pi^{(m)*}\pi^{(n)} \Bigg\}. \tag{4.22}$$

Here $\chi^{(m)}$ is the generalized potential derived by the Poisson and Ampere's equations from the POD mode $\psi^{(m)}$. For ease of notation we are dropping the subscript $\mathbf{k}$ for all these variables. It is seen that the orthogonality relation applies to the $|g|^2$ part of the energy expression which is the first term on R.H.S. of Eq. 4.22. We call this term the "kinetic energy". The orthogonality relation doesn't apply to the $\chi^* g$ part, the second term in Eq. 4.22, which we choose to call "electromagnetic energy" (although it should be noted that the simulation is electrostatic, so only the electrostatic potential contributes to the electromagnetic energy). The orthogonality of the time traces π can be used to simplify the electromagnetic energy term when we integrate over time. However, we are interested in the time dynamics of the energy quantity and hence choose not to do that. Instead, we compare the magnitudes of the orthogonal and nonorthogonal parts. In Fig. 4.3 we compare the kinetic and electromagnetic energies to find that the electromagnetic energy is negligible in the Cyclone Base Case, which we will be focussing on in this thesis. On a time average, the electromagnetic energy is less than 7% of the total energy.

We also look at each POD mode at a particular wavenumber individually and calculate the percent of electromagnetic energy in them. When Eq. 4.22 is summed over time, then the orthogonality of the time traces π, Eq. 4.20, gets rid of the non-orthogonal terms in the electromagnetic energy. In that case, the energy of the n^{th} POD modes becomes $E_{\mathbf{k}}^{(n)} = E_{KE}^{(n)} + E_{EM}^{(n)}$. The time averaged kinetic energy, $E_{KE}^{(n)}$, and electromagnetic energy, $E_{EM}^{(n)}$, of the n^{th}

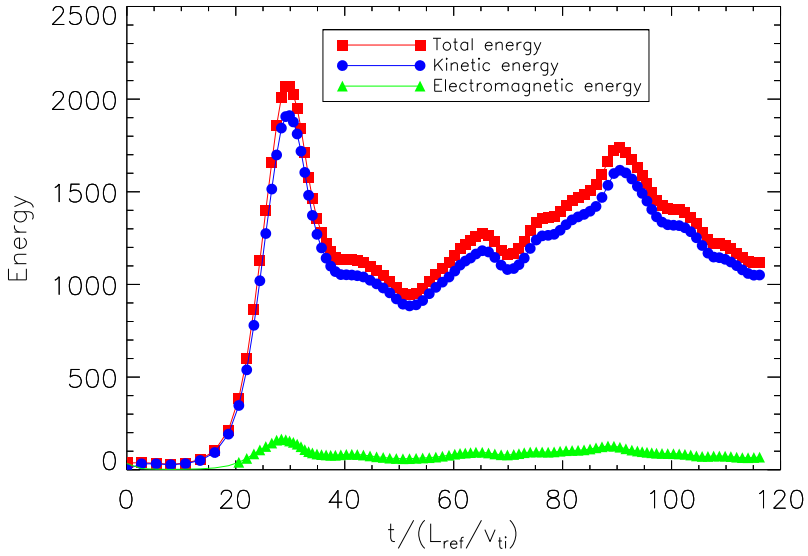

Figure 4.3: Comparison of kinetic energy with electromagnetic energy in CBC (see Eq. 4.22) at $\mathbf{k} = (0, 0.25)$. We see that the nonorthogonal electromagnetic energy contributes very little to the total energy.

POD mode are then given by,

$$E_{KE}^{(n)} = n_0 T_0 |\beta^{(n)}|^2,$$
$$E_{EM}^{(n)} = \mathrm{Re}\left[\int dz dv_\parallel d\mu \hat{J}(z) \pi n_0 B_0 \chi^{(n)*} \psi^{(n)} |\beta^{(n)}|^2\right]. \tag{4.23}$$

In Fig. 4.4 we plot the percentage of the electromagnetic energy in the total energy for first 1000 POD modes at $\mathbf{k} = (0, 0.25)$, which is the most energetic wavenumber in the turbulence spectrum. We see that its contribution is 15% in the first POD mode and then rapidly drops to less than 5% for the subdominant modes. So we can safely ignore it in Eq. 4.22 and define the energy of a POD mode as $|\beta^{(n)}\pi^{(n)}|^2$; n_0 and T_0 are dropped as they are just constants.

Now that we have defined the energy of POD modes, we can derive the energy evolution equation for them. Using the gyrokinetic equation, Eq. 4.12, and the orthogonality properties,

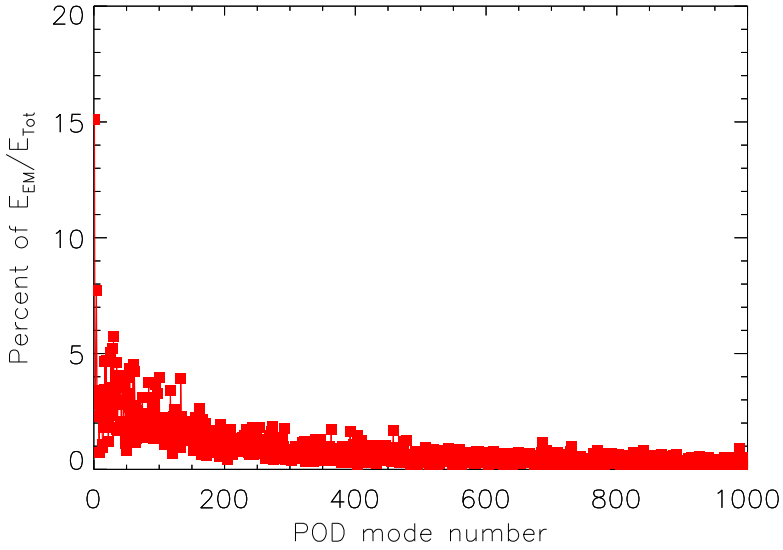

Figure 4.4: Percentage of electromagnetic energy, $E_{EM}^{(n)}$, in total energy, $E_{EM}^{(n)} + E_{KE}^{(n)}$, (see Eq. 4.23) for first 1000 POD modes at $\mathbf{k} = (0, 0.25)$.

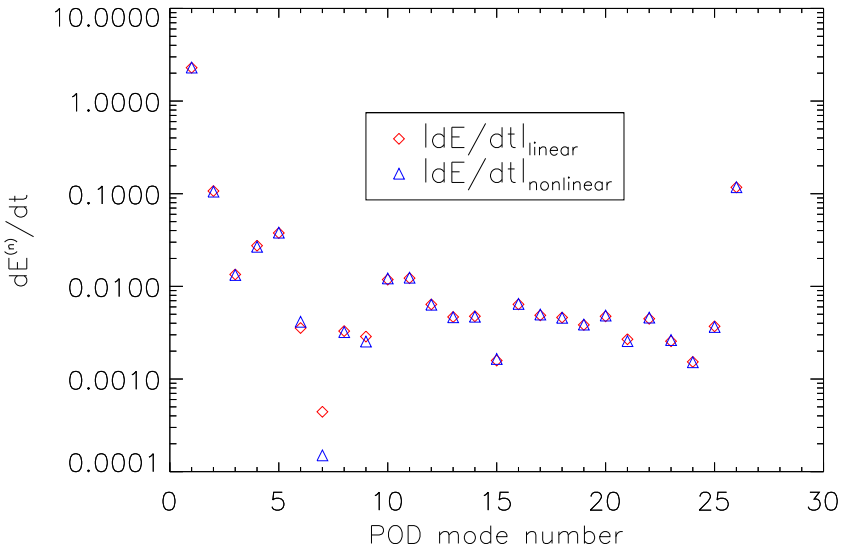

Figure 4.5: The linear and nonlinear terms in Eq. 4.24 are averaged over a saturated state. After making sure they have opposite signs, their absolute value are plotted which almost lie on top of each other, showing good agreement. The last, 26^{th}, point is a sum over POD modes from 26 to 1000.

Eq. 4.19, it is straightforward to show that the energy evolution of m^{th} POD mode is

$$\frac{\partial}{\partial t}\big[|\beta^{(m)}\pi^{(m)}|^2\big] = 2Re\bigg\{\int dz dv_\parallel d\mu \frac{\pi B_0 \hat{J}(z)}{F_0}\psi^{(m)*}\beta^{(m)}\pi^{(m)*}\Big[\mathcal{L}[g]+\mathcal{N}[g]\Big]\bigg\}. \tag{4.24}$$

As expected, there are two contributions to the energy evolution, one from the linear operator, $\mathcal{L}$ and another from the nonlinear operator $\mathcal{N}$. In a saturated state of the plasma turbulence, both these rates are expected to be equal and opposite to each other and cancel out. A time average of these two terms over a saturated state is calculated for the first 25 POD modes at $\mathbf{k} = (0, 0.25)$. After making sure that both are of opposite sign, their absolute values are taken and plotted in Fig. 4.5. We see that they balance each other extremely well, as expected. We further pursue this topic in Sec. 5.2 where we look at the energy balance of higher POD modes and show how this balance can be violated.

The linear term can be further simplified, as shown in Ref. [21] and in Sec. 5.1 of this thesis, to be written as,

$$\begin{aligned}\frac{\partial}{\partial t}\big[|\beta^{(n)}\pi^{(n)}|^2\big]\bigg|_{\text{linear}} =& 2Re\bigg\{\int dz dv_\parallel d\mu \frac{\pi B_0 \hat{J}(z)}{F_0}\psi^{(m)*}\beta^{(m)}\pi^{(m)*}\mathcal{L}[g]\bigg\} \\ =& Q^{(n)} + C^{(n)} + R^{(n)}.\end{aligned} \tag{4.25}$$

It is to be implicitly understood that this is at a particular wavenumber $\mathbf{k}$. $Q^{(n)}$ is the "energy injection" term obtained from the gradient drive term of $\mathcal{L}$ (see Eq. B.4) and $C^{(n)}$ is the "dissipative" term obtained from the $C_j(f_j)$ term of $\mathcal{L}$. The term $R^{(n)}$ is related to curvature and gradient drifts and it comes from all the remaining terms in $\mathcal{L}$. When summed over $\mathbf{k}$, it adds to zero. Hence it does not play a role in the overall dynamics and we ignore it. The time integral (actually, it's just a simple sum over time steps) of heat flux and dissipation, $\langle Q\rangle^{(n)}$ and $\langle C\rangle^{(n)}$ respectively, are calculated as shown by Eq. 5.4. The term $\langle Q\rangle^{(n)} + \langle C\rangle^{(n)}$ is plotted for $\mathbf{k} = (0, 0.25)$, which is the most energetic wavenumber in the turbulent spectrum, from the third POD mode up to the 1000^{th} mode in Fig. 4.6. We see that they all have negative $\langle Q\rangle^{(n)} + \langle C\rangle^{(n)}$, indicating that all these modes are damped. The first two modes are unstable and hence they are

not plotted. Modes 2 and higher are the "subdominant" modes and most of them are damped. After experience with different wave numbers and regimes, we can say that more than 99% of subdominant modes are always damped. The linear rate of change of energy of POD modes is looked at more detail in Sec. 5.1.

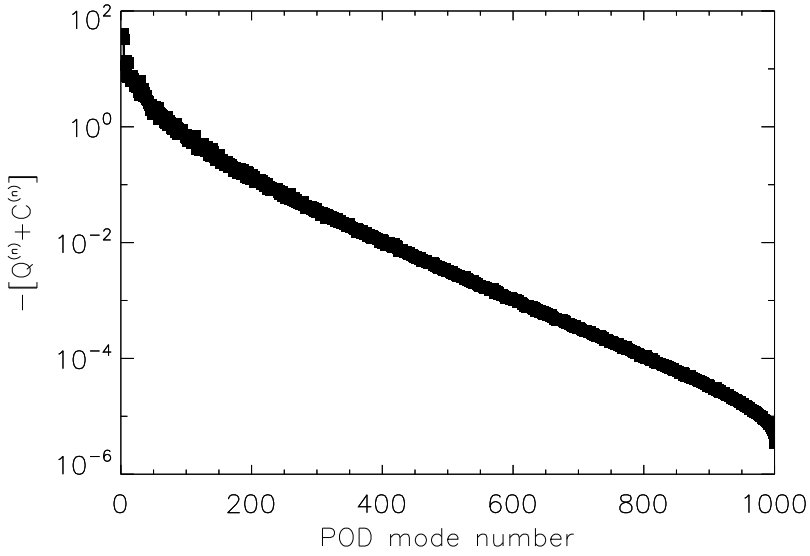

Figure 4.6: The negative of $\langle Q\rangle^{(n)} + \langle C\rangle^{(n)}$ for POD modes 3 up to 1000 at $\mathbf{k} = (0, 0.25)$. All these modes are damped. The first two modes are not plotted because they have positive $\langle Q\rangle^{(n)} + \langle C\rangle^{(n)}$.

4.4 Nonlinear energy transfer

In this section we look at the nonlinear transfer of energy in gyrokinetics, akin to what was done in Sec. 3.5. We have defined the energy of gyrokinetic operator in Eq. 4.21. The rate of change of energy of a Fourier wavenumber $\mathbf{k}$ closely follows Eqs. 4.24 and 4.25, and is given by,

$$\frac{\mathrm{d}E_{\mathbf{k}}}{\mathrm{d}t} = Q_{\mathbf{k}} + C_{\mathbf{k}} + R_{\mathbf{k}} + \left.\frac{\mathrm{d}E_{\mathbf{k}}}{\mathrm{d}t}\right|_{\mathrm{N.L.}}, \tag{4.26}$$

where $Q_{\mathbf{k}}$, $C_{\mathbf{k}}$ and $R_{\mathbf{k}}$ are now for Fourier mode $\mathbf{k}$ rather than for the n^{th} POD mode. This equation is derived in detail in Appendix C of Ref. [21]. The definitions of $Q_{\mathbf{k}}$, $C_{\mathbf{k}}$, and $R_{\mathbf{k}}$ for

our simplified electrostatic case are,

$$Q_{\mathbf{k}} = -2Re\Big\{ \int dz dv_{\parallel} d\mu J(z) \pi n_0 T_0 v_* g^*_{\mathbf{k}} i k_y \chi_{\mathbf{k}} \Big\}, \tag{4.27}$$

$$C_{\mathbf{k}} = 2Re\Big\{ \int dz dv_{\parallel} d\mu J(z) \pi n_0 T_0 v_* \Gamma^*_j C_j(f_j) \Big\}, \tag{4.28}$$

$$R_{\mathbf{k}} = 2Re\Big\{ \int dz dv_{\parallel} d\mu J(z) \frac{\pi B_0 n_0 T_0}{F_0} \Big(g_{\mathbf{k}} + \frac{qF_0}{T_0} \chi_{\mathbf{k}} \Big)^* \Big[- v_{T,j} v_{\parallel} \Gamma_{j,z} - v_d (K_x i k_x + K_y i k_y) \Gamma_j \Big] \Big\}. \tag{4.29}$$

$Q_{\mathbf{k}}$ depends on the temperature gradient and is related to the heat flux which drives the turbulence whereas $C_{\mathbf{k}}$ represents viscous/collisional dissipation. In this work we are using artificial hyper-diffusivity in $C_{\mathbf{k}}$. These two terms are the nonconservative terms, in other words, they are responsible for net energy injection and dissipation from the system. As in Sec. 4.3, $R_{\mathbf{k}}$ is a linear term depending on the gradient and curvature drifts, but it vanishes in the sum over $\mathbf{k}$, so overall it is a conservative term and we choose to ignore it. The nonlinear rate of change of energy is given by,

$$\left.\frac{\mathrm{d}E_{\mathbf{k}}}{\mathrm{d}t}\right|_{\mathrm{N.L.}} = 2Re\Big\{ \int dz dv_{\parallel} d\mu \frac{\pi B_0 n_0 T_0 \hat{J}(z)}{F_0} \Big[g_{\mathbf{k}} + \frac{qF_0}{T_0} \chi_{\mathbf{k}} \Big]^* \times$$
$$\Big[\underbrace{\sum_{\mathbf{k}' | k'_y = 0, k_y} (k'_x k_y - k_x k'_y) \chi(\mathbf{k}') g(\mathbf{k} - \mathbf{k}')}_{\text{zonal coupling}} + \underbrace{\sum_{\mathbf{k}' | k'_y \neq 0, k_y} (k'_x k_y - k_x k'_y) \chi(\mathbf{k}') g(\mathbf{k} - \mathbf{k}')}_{\text{nonzonal coupling}} \Big] \Big\}. \tag{4.30}$$

This is a conservative term because it only transfers energy from one wavenumber to another wavenumber. In other words, when summed over all wavenumbers $\mathbf{k}$, it sums to zero, which can be checked directly. Zonal wavenumbers have $k_y = 0$. We have split the nonlinear coupling term into zonal coupling ($k'_y = 0, k_y$) and nonzonal coupling ($k'_y \neq 0, k_y$). We note that if $k'_y = k_y$, then the third wavenumber in the interaction, $\mathbf{k}'' \equiv \mathbf{k} - \mathbf{k}'$, will be a zonal wavenumber, $k''_y = 0$. These two different coupling components are shown in Fig. 4.7. Also, in GENE there is an option to artificially eliminate zonal flows. This is done by subtracting the flux surface averaged

electrostatic potential from the fluctuating potential at every time step,

$$\phi(k_x, k_y = 0) \rightarrow \phi(k_x, k_y = 0) - \int dz \phi(k_x, k_y = 0) \hat{J}(z) \tag{4.31}$$

In our simple model of electrostatic fluctuations $\bar{\phi}$ is the same as χ. Fig. 4.7 shows the nonlinear

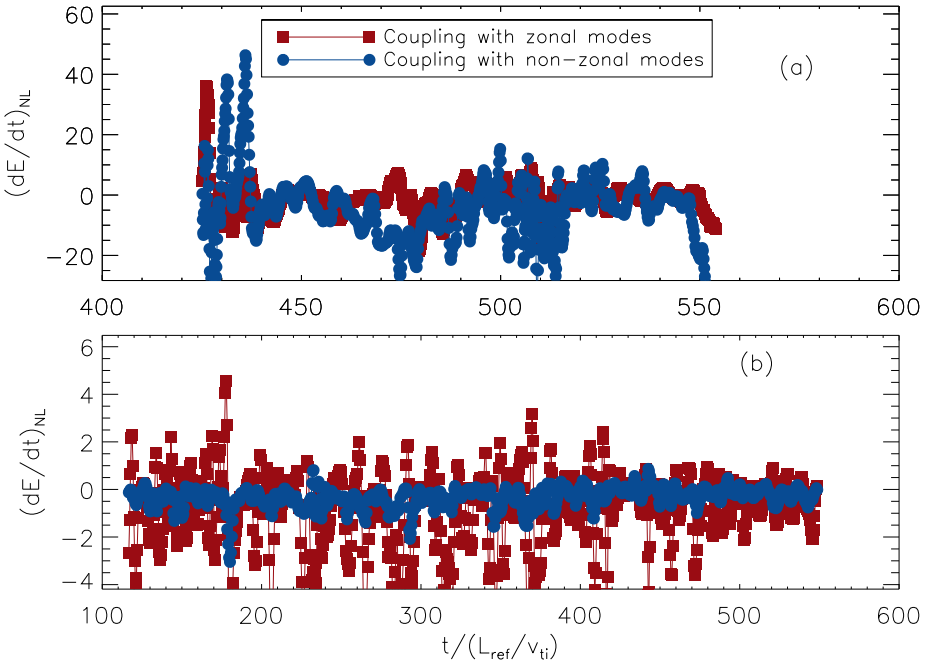

Figure 4.7: Coupling with zonal and nonzonal wavenumbers (Eq. 4.30). (a) When zonal flows are off, we see weak coupling with the zonal modes. (b) When zonal flows are turned on, we see strong coupling with the zonal modes.

couplings for Fourier wavenumber $(0, 0.25)$. In Fig. 4.7(a), zonal flows are artificially suppressed by using the technique outlined above. We see that on time average, the coupling with zonal wavenumbers (-1.3) is small compared to the coupling with non-zonal wavenumbers (-5.1). On the other hand, in Fig. 4.7(b), the zonal potential is allowed to evolve self-consistently; in that case the coupling with zonal wavenumbers is very strong (-0.88) compared to non-zonal coupling (-0.33). We also note that the number of possible combinations of zonal triplets is much smaller than the number of nonzonal triplet combinations, which makes this result even more striking. However, strictly speaking, in considering coupling with zonal modes, we are also including

many modes other than the zonal flow, for example, zonal pressure or density, depending on which moment of the distribution function $g_{\mathbf{k}'}|_{k'_y=0}$ and $g_{\mathbf{k}-\mathbf{k}'}|_{k'_y=k_y}$ we consider. Also, $\bar{\phi}_{k_y=0}$ contains not only zonal flows, which have $k_y = k_{||} = 0$, but also flows that may vary in the field aligned direction, i.e. $k_{||} \neq 0$. However, since the deletion of zonal flows causes such a drastic change in the coupling, it suggests that it is actually the zonal flow component of zonal wavenumbers that is important in the three-wave interactions. This is corroborated in the fluid model of ITG (Sec. 3.5) where the zonal pressure was not important, unlike the zonal flow.

This analysis has been done for a particular Fourier wavenumber. What about POD modes? We derived the energy dynamical equation of a POD mode in Eq. 4.24. In Sec. 4.3 we looked at the nonconservative linear terms in Eq. 4.24. Now we concentrate on the nonlinear term. Throwing away the linear gyrokinetic operator $\mathcal{L}$ in Eq. 4.24, we get the nonlinear rate of change of energy of the n^{th} POD mode,

$$\frac{\partial}{\partial t}\big[|\beta^{(n)}\pi^{(n)}|^2\big]\Big|_{\text{N.L.}} = \sum_{\mathbf{k}'} T^{(n)}_{k,k'} = 2Re\Bigg\{ \int dz dv_{\|} d\mu \frac{\pi B_0 \hat{J}(z)}{F_0} \psi^{(n)*}\beta^{(n)}\pi^{(n)*} \times$$
$$\Big[\underbrace{\sum_{\mathbf{k}'|k'_y=0,k_y} (k'_x k_y - k_x k'_y)\chi(\mathbf{k}')g(\mathbf{k}-\mathbf{k}')}_{\text{zonal coupling}} + \underbrace{\sum_{\mathbf{k}'|k'_y\neq 0,k_y} (k'_x k_y - k_x k'_y)\chi(\mathbf{k}')g(\mathbf{k}-\mathbf{k}')}_{\text{nonzonal coupling}} \Big] \Bigg\}. \quad (4.32)$$

This looks almost like Eq. 4.30, the only difference is that $[g_{\mathbf{k}} + (qF_0/T_0)\chi_{\mathbf{k}}]$ is replaced by $\psi^{(n)}\beta^{(n)}\pi^{(n)}$. That is the general prescription for changing Fourier mode energy expressions into POD mode energy expressions. The symbol $T^{(n)}_{k,k'}$ is just for notational simplicity and represents three-wave interaction between the wave numbers $\mathbf{k}$, $\mathbf{k}'$ and $\mathbf{k}-\mathbf{k}'$, similar to the entropy transfer functions defined in Refs. [61], [79]. Its expression can be read off from the right hand side of Eq. 4.32. Again the nonlinearity is split into coupling with zonal wavenumbers and nonzonal wavenumbers. These terms are plotted in Fig. 4.8. We can see strong coupling with zonal flows for the first POD mode in Fig. 4.8(a). On a time average the coupling with zonal wavenumbers is -1.92 whereas coupling with nonzonal wavenumbers is -0.58. Fig. 4.8(b) is for all the sub-dominant modes summed together. For them also zonal flow coupling is much stronger (0.284) than the nonzonal coupling (-0.0414). It should be pointed out that the number of nonzonal

three-wave couplings greatly exceeds the number of three-wave combinations for zonal mode couplings, so each individual zonal wavenumber triplet will be even stronger than an individual nonzonal triplet. The same exercise was repeated with the zonal flows turned "off" artificially, as indicated in Eq. 4.31. We observed that in this case the zonal mode coupling becomes roughly half of the nonzonal coupling, for both the unstable and subdominant POD modes. Thus, for POD modes also we infer that it is the zonal flow component of zonal wavenumbers which is responsible for the strong coupling.

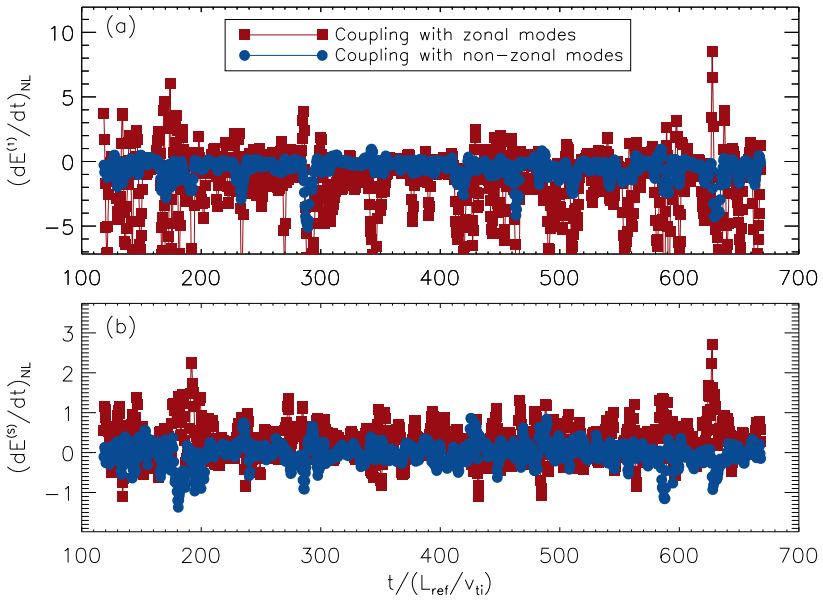

Figure 4.8: Coupling of POD modes with zonal and nonzonal wavenumbers (Eq. 4.32). (a) is for first POD mode at $\mathbf{k} = (0, 0.25)$, and (b) is for subdominant POD modes from 2 up to 1000 summed together at the same wavenumber. The zonal flows have been allowed to evolve self-consistently in these runs.

Next we look at the time-averaged and k'_x-summed spectrum of the nonlinear transfer, $\sum_{k'_x} \langle T^{(n)}_{k,k'} \rangle_t$, in Fig. 4.9. In Fig. 4.9(a) we see that the first POD mode at $\mathbf{k} = (0, 0.25)$ couples primarily with wavenumber $k'_y = 0.25$. This indicates a zonal coupling because the third wavenumber in the triplet interaction is $k_y - k'_y = 0.0$. The sign of the transfer is negative, indicating that energy is being nonlinearly transferred out of the unstable POD mode by this triplet. In Fig. 4.9(b) we see that all the subdominant modes summed together at $\mathbf{k} = (0, 0.25)$

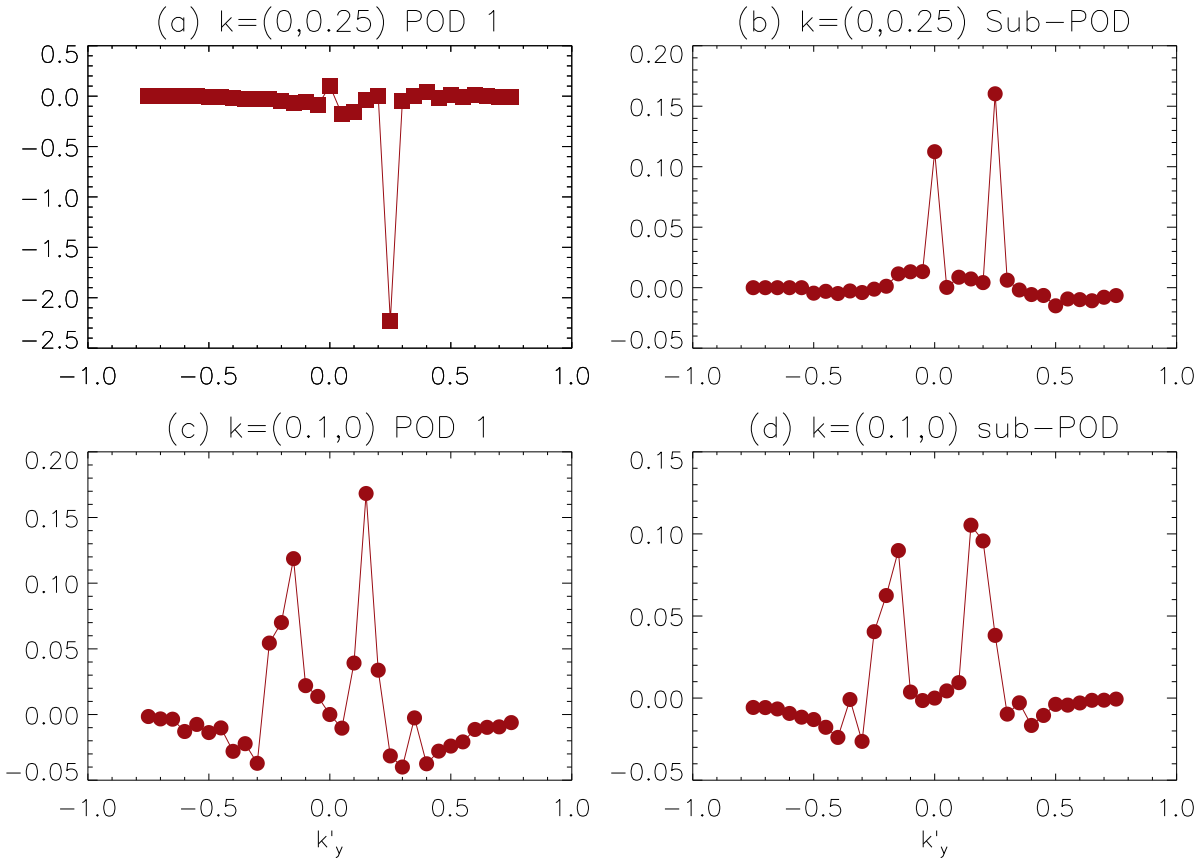

Figure 4.9: The y-axis plots the time averaged and k'_x summed nonlinear transfer spectrum, $\sum_{k'_x}\langle T^{(n)}_{k,k'}\rangle_t$, as a function of k'_y. First 1000 POD modes are considered. (a) is for $n = 1$, $\mathbf{k} = (0, 0.25)$; (b) is for sum over $n = 2, 3, ..., 1000$, $\mathbf{k} = (0, 0.25)$; (c) is for $n = 1$, $\mathbf{k} = (0.1, 0)$ and (d) is for sum over $n = 2, 3, ..., 1000$, $\mathbf{k} = (0.1, 0)$.

show strong zonal couplings, at $k_y' = 0, 0.25$. For these modes the sign is positive, indicating that they receive energy nonlinearly by this triplet interaction. These signs are to be expected since in saturation the unstable mode inputs energy via the linear terms and has to saturate by nonlinear energy transfer out of it, whereas for the subdominant modes the situation is reversed.

This same exercise is repeated at a zonal wavenumber $\mathbf{k} = (0.1, 0)$, which is a wavenumber with one of the highest zonal flow amplitudes. It is illustrated in Fig. 4.9(c) for the first POD mode and in Fig. 4.9(d) for the subdominant modes: the zonal wavenumbers receive energy from all the non-zonal wavenumbers. However, they do not couple with other zonal wavenumbers because of the form of the coupling coefficient. They receive energy nonlinearly and are linearly damped. The peak of the energy transfer to the zonal wavenumber is on the order of 0.1 units. Compare that to the peak of the nonlinear transfer out of the unstable POD mode at $\mathbf{k} = (0, 0.25)$ in Fig. 4.9(a), which is on the order of unity. This indicates that out of the energy coming out of the unstable mode, only a tenth is deposited into the zonal wavenumber. It is true that the unstable POD at $\mathbf{k} = (0, 0.25)$ interacts with many zonal wavenumbers, only one of which is $\mathbf{k} = (0.1, 0)$, and also the zonal wavenumber $\mathbf{k} = (0.1, 0)$ receives energy from many wavenumbers, only one of which is $\mathbf{k} = (0, 0.25)$. However, as these are among the most energetic wavenumbers in the spectrum, we crudely expect one tenth of the energy from the unstable mode to be transferred to zonal wavenumbers, of which zonal flows are a part. This is shown more rigorously in the analysis of Sec. 4.5. As the energy is conserved, nine tenths of this energy should be deposited to the third wavenumber in the three-wave interaction. In this sense, we can say that the zonal flow acts as a mediator of energy transfer because it is an important member of the coupling but not the one that actively dissipates energy. What happens to the energy transferred to the third wavenumber?

4.5 Energy transfer to subdominant modes

In the previous section, we showed that unstable modes strongly couple with zonal flows via three-wave interactions. In this section, we look at where most of the energy in such an interaction

ends up. Due to the large number of such three-wave interactions and also the complexity in performing the POD analysis, it is not possible to analyze each and every interaction in the simulation, as was done for the fluid model (Ch. 3). Instead, we look at specific representative triplets and analyze them individually. We select three wavenumbers $\mathbf{k}$, $\mathbf{k}'$ and $\mathbf{k}'' = \mathbf{k} - \mathbf{k}'$ and break them down into POD modes. It is straightforward to demonstrate energy conservation in a triplet by showing

$$T^{(1)}_{k,k'} + T^{(S)}_{k,k'} + T^{(1)}_{k',k} + T^{(S)}_{k',k} + T^{(1)}_{k-k',k} + T^{(S)}_{k-k',k} = 0. \tag{4.33}$$

Here S denotes all the subdominant modes summed together. $T^{(1,S)}_{k,k'}$ represents the energy transfer of the unstable/subdominant mode at $\mathbf{k}$ due to interaction with $\mathbf{k}'$ and $\mathbf{k}-\mathbf{k}'$. $T^{(1)}_{k',k}+T^{(S)}_{k',k}$ represents the total energy transfer at mode $\mathbf{k}'$ due to interaction with $\mathbf{k}$ and $\mathbf{k}-\mathbf{k}'$. We select $k'_y = 0$ to make this the energy transfer out of/into zonal modes. Similarly $T^{(1)}_{k-k',k} + T^{(S)}_{k-k',k}$ is the energy transfer of mode $\mathbf{k}-\mathbf{k}'$. Looking at these terms individually clearly shows the energy transfer occurring in a triplet.

We start by looking at $\mathbf{k} = (0, 0.25)$, $\mathbf{k}' = (0.1, 0)$ and $\mathbf{k} - \mathbf{k}' = (-0.1, 0.25)$. Its energy transfer terms are shown in block 1 of Fig. 4.10(a). We see that the unstable mode at $\mathbf{k}$ gives out roughly 119 units of energy summed over time, i.e., $T^{(1)}_{k,k'} = -119$. Negative numbers indicate energy flowing out of that mode, as shown by the arrows in the diagram, and positive numbers indicate energy flowing in. By energy conservation, this has to be distributed amongst the other modes of block 1. Some of this goes into the unstable mode at $(-0.1, 0.25)$, $T^{(1)}_{k-k',k} = 66$. Some amount of energy goes into the zonal mode, $T^{(1)}_{k',k}+T^{(S)}_{k',k} = 8$. As was speculated in the discussion of Fig. 4.9(c,d) this is roughly a tenth of the energy input by the instability at $\mathbf{k} = (0, 0.25)$. We see that half of the energy ends up in the subdominant modes. The subdominant modes at $\mathbf{k}$ take 21 units of energy, i.e., $T^{(S)}_{k,k'} = 21$, while the subdominant modes at $\mathbf{k} - \mathbf{k}'$ take up 24 units, i.e., $T^{(S)}_{k-k',k} = 24$. Of the 21 units supplied to subdominant modes at $\mathbf{k}$, 15 goes to the second POD mode at $\mathbf{k}$ which is unstable and 6 units go to the stable subdominant modes. Thus $\mathbf{k}$ injects $119 - 6 = 113$ units of energy into the triplet. Out of this 21% (24 units) is damped

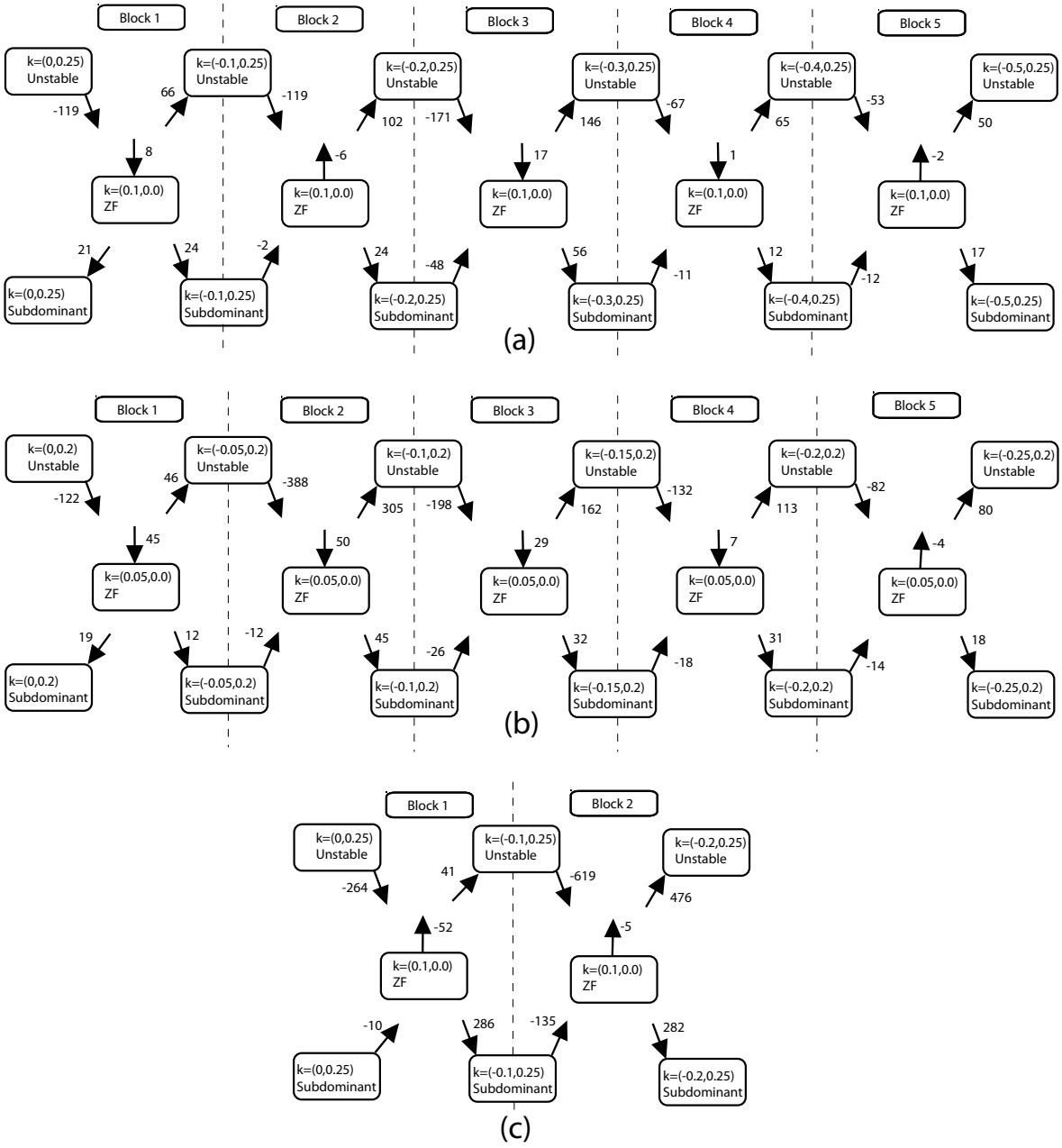

Figure 4.10: Nonlinear energy transfer for a large sample of triplets. See the text for a detailed discussion.

by subdominant modes at $\mathbf{k}-\mathbf{k}'$ because all of them are stable. This analysis is continued in blocks 2, 3, 4 and 5 of Fig. 4.10(a). In block 2, we take $\mathbf{k} = (-0.1, 0.25)$, $\mathbf{k}' = (0.1, 0)$ and $\mathbf{k}-\mathbf{k}' = (-0.2, 0.25)$. The wavenumber $\mathbf{k}$ injects 121 units of energy (119+2). Out of this 24 units (20%) goes into the subdominant modes at $\mathbf{k}-\mathbf{k}'$ and 102 units (84%) goes to the unstable mode. So in this block 20% of energy injected at $\mathbf{k}$ is transferred to subdominant modes at $\mathbf{k}-\mathbf{k}'$. In blocks 2, 3, 4, and 5 all the subdominant modes at nonzonal wavenumbers are damped and hence all energy transferred to them will be dissipated. The reader can verify that the percentages of energy transferred to subdominant modes, and thus dissipated, in blocks 3, 4 and 5 are 26%, 15% and 26% respectively. However, the energy deposited in the unstable mode will not be dissipated and instead will have to be transferred to some other wavenumber until it reaches a dissipative mode. Putting the above percentages together, we see that at the end of block 5, 29% energy remains in the unstable modes and 71% has ended up in stable subdominant modes, all of which will be dissipated.

This calculation was repeated for another set of triplets shown in Fig. 4.10(b). We start with the wavenumber $\mathbf{k} = (0, 0.2)$ and the zonal wavenumber as $\mathbf{k}' = (0.05, 0)$. Just as above, the percentage of energy injected at $\mathbf{k}$ transferred to the subdominant modes at $\mathbf{k}-\mathbf{k}'$ is calculated and comes out to be 12%, 11%, 14%, 21% and 19% in blocks 1, 2, 3, 4 and 5 respectively. Putting these percentages together, by the end of the chain at $\mathbf{k}-\mathbf{k}' = (-0.25, 0.2)$, the subdominant modes have accounted for 57% of the original energy injected. All the subdominant modes in Fig. 4.10(b) are stable which means that all this 57% of energy will be dissipated. Fig. 4.10(c) shows one more case of such a "cascade" of energy. In block 1 we see 104% of energy transferred to subdominant modes and in block 2, 37% is transferred. These numbers show lot more variability then those seen in the two cases above. In this case, low values of hyper-diffusivity coefficients have been used in the simulations, namely, $D_z = 0.25$ and $D_v = 0.2$. In the first two cases we used, $D_z = 8.0$ and $D_v = 5.0$. It is not clear why the hyper-diffusivity affects this energy transfer drastically, whereas the heat fluxes change by just a factor of 1.3, which lies within the standard deviation of the heat flux calculations, for these two different hyper-diffusivities. We take a closer look at this problem in Sec. 5.2.

In every triplet the energy is transferred from a lower magnitude k_x mode to a higher k_x mode. For example, in Fig. 4.10(a) it is from $k_x = 0$ to $k_x = -0.1$ in block 1, from $k_x = -0.1$ to $k_x = -0.2$ in block 2 and so on. This is a forward "cascade" of energy. This indicates that the zonal flow transfers energy from low radial wavenumber to high radial wavenumber, consistent with the shearing mechanism. Is the forward-cascade efficient enough to reach the "conventionally dissipative" high wavenumbers? To answer this question, we looked at the ratio of energy transfer within the range of instability (ROI) to energy transfer outside of this range. The region of instability for the simulation parameters is shown in Fig. 4.11. This region has been calculated using the linear instability analysis. At $k_y = 0.25$ the instability region seems to be bounded at $k_x = 0.2$. Then looking at Fig. 4.10(a) we see that the first two blocks lie within this region. Thus in the ROI about 37% of energy is dissipated by the subdominant modes. For $k_y = 0.2$ the boundary of ROI should be located around $k_x = 0.15$, which would indicate that the first three blocks of Fig. 4.10(b) lie in this region. Putting together their percentages, we get 33% of energy going into the subdominant modes within the ROI. Moreover, even outside of the ROI most of the energy continues to be dissipated by the subdominant modes, even though the dominant mode becomes stable.

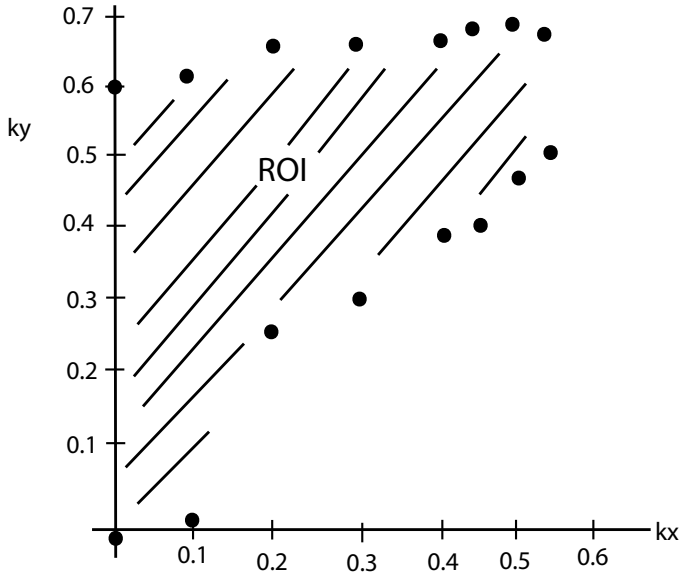

Figure 4.11: The black dots demarcate the boundary of linear instability region in k_x-k_y space for the standard CBC simulations carried out in this thesis.

One more interesting observation is that the nonlinear instability is drastically different from linear instability [22], [80]. In the nonlinear state, we get unstable POD modes up to $k_x = 0.45$ at $k_y = 0.25$, even though linear analysis (Fig. 4.11) would indicate stability at that point. Thus, from the nonlinear stability point of view, the unstable range extends up to $|k_x| = 0.45$ beyond which the stable range starts. This is the wavenumber beyond which there are no more unstable POD modes (at $k_y = 0.25$). Traditionally, the stable range has been assumed to be the "dissipative range". We calculate the ratio of the energy transfer to wavenumbers within the unstable range to the transfer to wavenumbers in stable range for the first POD mode at $\mathbf{k}$, i.e., $\sum_{k'} T^{(1)}_{k,k'}$. This is done for nine wavenumbers between $-0.05 \leq k_x \leq 0.05$ and $0.2 \leq k_y \leq 0.3$. Energy transfer is considered to be within the unstable range if the sum over $\mathbf{k'}$ is restricted to include only $\mathbf{k'}$ values with $|k'_x|, |k'_y|, |k_x - k'_x|, |k_y - k'_y| < 0.5$. Excluding these values from the sum gives the transfer to stable range. The ratio of transfer within unstable range to transfer to stable range is calculated for different combinations of the nine $\mathbf{k}$ wavenumbers and plotted in Fig. 4.12. The different points are for the different combinations. We see that this ratio is converging to around four which indicates that for all the energy transferred to "traditionally dissipative", high-k, stable wavenumbers, there is four times as much energy transferred to the unstable range. So even if the transfer is in the forward direction, subdominant modes at low wavenumber damp a large fraction of energy before it reaches the conventional dissipation region.

The picture that emerges is that the instability injects energy at the scales of the ion gyroradius. It strongly couples with the zonal flows, but they are not responsible for the dissipation by themselves. They help in transferring this energy to the third wavenumber in a triplet interaction where a significant fraction of it goes into the subdominant modes that dissipate this energy. The remaining energy is cascaded to higher radial wavenumbers, but the attrition by damped subdominant modes at each stage of this transfer is enough to sink a large fraction of this energy at lower, unstable wavenumbers. This is a new effect compared to shearing mechanism of zonal flows that leads to energy transfer to stable, larger wavenumbers which have been thought to be the only source of dissipation till now. It shows that coupling to subdominant modes cannot be

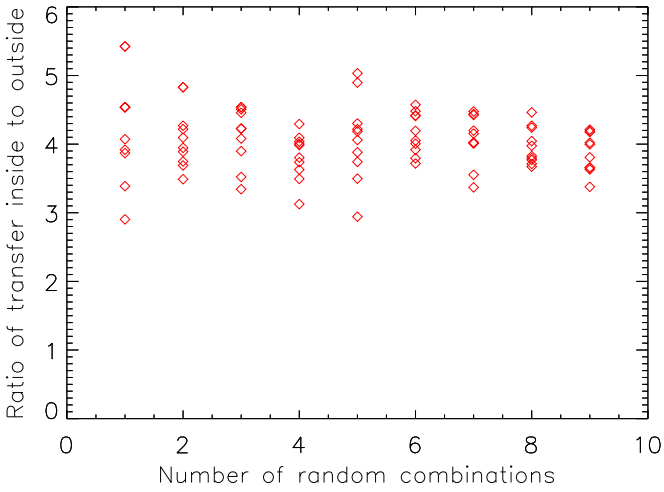

Figure 4.12: Ratio of energy transfer within unstable range to transfer outside of unstable range. On the x-axis we plot the number of combinations taken randomly. For example, a value of 3 on the x-axis indicates that three wave numbers were randomly selected out of the nine and their average was taken. At each such combination 10 ensembles are taken, giving 10 points at each x-axis value.

ignored even in the gyrokinetic models of zonal flow regulated ITG turbulence.

4.6 Shearing and zonal flows

The explanation provided in Sec. 3.6 and Sec. 4.4-4.5 indicates that zonal flows catalyze energy transfer to the subdominant modes, and a significant proportion of it to scales which are unstable. As explained in Secs. 3.7 and 4.7, a key reason for this is related to the frequency matching between zonal flows and subdominant modes, and to the amplitude of zonal flows. It apparently doesn't have anything to do with the shearing effect of zonal flows. However, the zonal flow-drift wave shearing paradigm states that the shearing by zonal flows causes energy transfer from drift waves to large, dissipative wavenumbers and this causes regulation of turbulence [47]. This shearing effect is presumably occurring in our simulations as part of the "forward cascade" of energy in k_x seen in Fig. 4.10. There are some indications in experiments also that this might be taking place [55]. In addition several authors have observed that whenever the shearing rate is above a certain threshold related to the linear growth rate, the turbulence is regulated [81], [82].

So what is regulating the turbulence: the shearing rate of zonal flows or the zonal flow amplitude and its associated frequency matching, leading to enhanced transfer to damped modes? It is difficult to ascertain whether either of these effects is unrelated to turbulence regulation. This is because the zonal flow amplitudes and shearing rates are closely related. To test this out, we run a scan of the ion temperature gradient around the CBC parameters. We look at the zonal flow (ZF) amplitude and shearing rates in Table 4.1. They show the same trend, either increasing or decreasing together. Although this scan has not been verified by resolution studies, the trend is sharp and clear. Thus, it is very difficult to separate the two different effects.

Table 4.1: Temperature gradient scale length (L_{Ti}) scan and comparison of maximum linear growth rates (γ), heat flux (Q), zonal flow amplitude (ϕ_{ZF}), and shearing rate ($\langle\omega_E\rangle$)

L_{ref}/L_{Ti}	$\gamma(v_{Ti}/L_n)$	$Q(W/m^3)$	ϕ_{ZF}	$\langle\omega_E\rangle(v_{Ti}/L_n)$
5.0	0.03	0.049	5	0.07
6.0	0.08	970	10	0.128
6.5	0.1	6630	13	0.257

Furthermore, we look at the behavior of these two quantities during different times in a simulation in Fig. 4.13. In (a) we see that the heat flux continuously increases from $t = 440$ to $t = 455$ during which time the shearing rate is below the average value in (b). Then from $t = 455$ to $t = 470$ the heat flux continuously decreases in (a) and this corresponds to an above average shearing rate in (b). This is similar to the predator-prey oscillations of zonal flow and drift waves [83], [84], indicating that the shearing rate has some correlation with the regulation of heat flux. In (c) and (d) we compare the zonal flow amplitudes at two different zonal wavenumbers; $\mathbf{k} = (0.05, 0.0)$ in (c) and $\mathbf{k} = (0.1, 0.0)$ in (d). We observe that from $t = 440$ to $t = 455$ the amplitude at lower k_x is higher than the amplitude at higher k_x. Then in the later time window when the shearing rate picks up, the amplitude at higher k_x gets a boost up whereas the amplitude at lower k_x decreases further. In fact, during this time window, $\mathbf{k} = (0.05, 0)$ has its lowest amplitude whereas $\mathbf{k} = (0.1, 0)$ is at its peak. Thus, the increase in shearing rate is correlated with the increase of zonal flow amplitude at higher k_x. This is not surprising, because the shearing rate is nothing but $\omega_E \propto \sum_{\mathbf{k}} k_x^2 \phi_k$. Thus the higher k_x

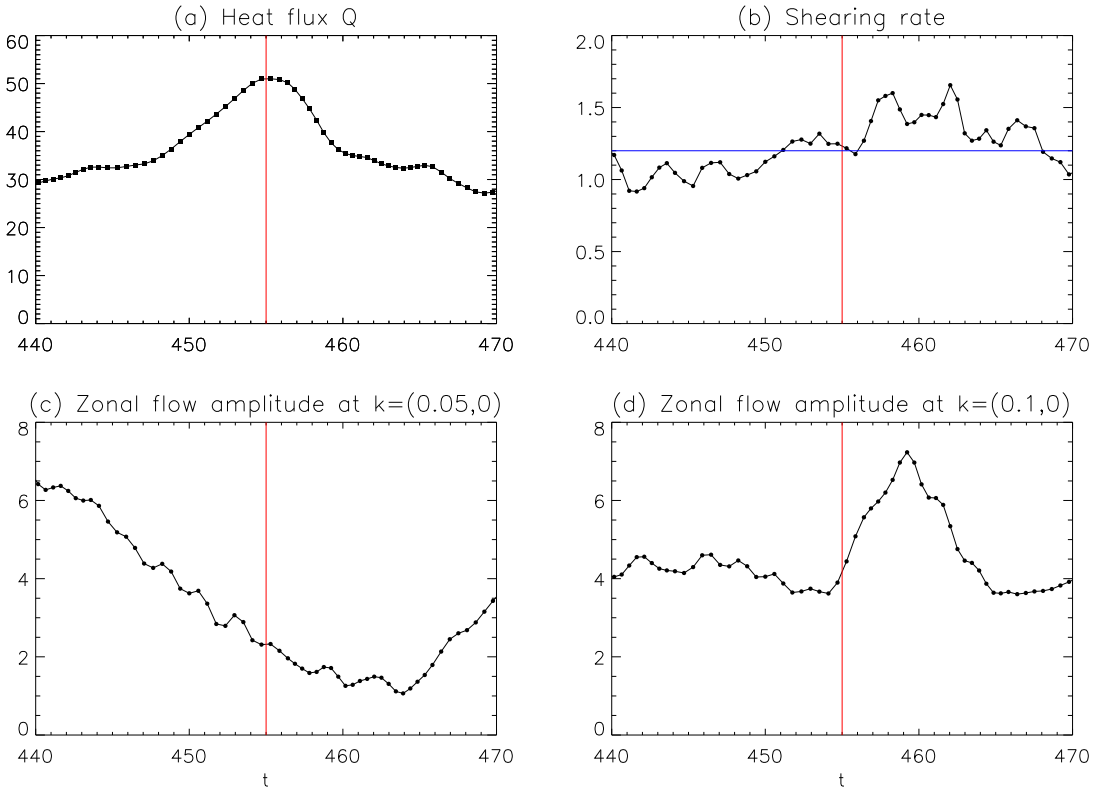

Figure 4.13: Time traces of (a) Heat flux, (b) zonal flow shearing rate, (c) ZF amplitude at $\mathbf{k} = (0.05, 0.0)$ and (d) ZF amplitude at $\mathbf{k} = (0.1, 0.0)$. The red line is at $t = 455$, before which time the heat flux is increasing and after which the heat flux is decreasing. The blue line is at a shearing rate of 1.2 units which is the long time averaged shearing rate of the simulation.

modes have a higher contribution to the shearing rate. This effect is also seen in Ref. [56]. This argument doesn't differentiate between which mechanism is more important but it shows that the shearing mechanism is not uniquely required to explain the regulation of turbulence, as the zonal flow amplitude can also explain it.

4.7 Frequency matching

In Sec. 3.7 we saw the striking property that triplet interactions whose frequency sum is the smallest are the most dominant nonlinear transfer interactions. That was shown using the fluid model of ITG turbulence. We repeat the same calculation with gyrokinetics, although not in its full complexity. First, we calculate the nonlinear frequencies using the time traces of POD modes. The auto correlation of the time traces for the n^{th} POD mode at $\mathbf{k}$ is defined as

$$S_{\mathbf{k}}^{(n)}(\tau) \equiv \frac{1}{T}\int_0^T dt|\beta_{\mathbf{k}}^{(n)}|^2\pi_{\mathbf{k}}^{(n)}(t)\pi_{\mathbf{k}}^{(n)}(t-\tau), \tag{4.34}$$

where β and π are the familiar singular values and time dependent amplitudes, and T is the window of time sampling. Then the frequency spectrum of the n^{th} POD mode is given by,

$$\hat{S}_{\mathbf{k}}^{(n)}(\omega) \equiv \int_0^T d\tau S_{\mathbf{k}}^{(n)}(\tau)e^{i\omega\tau}. \tag{4.35}$$

The power spectrum is just $P(\omega) \equiv |\hat{S}_{\mathbf{k}}^{(n)}(\omega)|^2$, an example of which is plotted in Fig. 4.14. A Lorentzian function of the form $L(\omega) = a_0/[(\omega-\omega_0)^2+\gamma_0^2]$ is also fitted to the power spectrum. The fitting parameters are the amplitude, a_0, the position of peak ω_0, which gives us the real part of the nonlinear frequency, and the half width at half maximum γ_0, which gives us the imaginary part of nonlinear frequency, thus giving $\hat{\omega}_{\mathbf{k}}^{(n)} \equiv \omega_0 + i\gamma_0$ [65]. The sign of γ_0 is chosen as positive for the first POD mode and negative for subdominant modes. A useful relationship in carrying out this analysis is: $\hat{S}_{-\mathbf{k}}^{(n)}(\omega) = \hat{S}_{\mathbf{k}}(-\omega)^*$.

We look at some of the representative triplets in the simulation. We select $\mathbf{k} = (0, 0.2)$, $k_x' = 0.1$, and scan over k_y'. The nonlinear frequencies for all the wavenumbers are determined

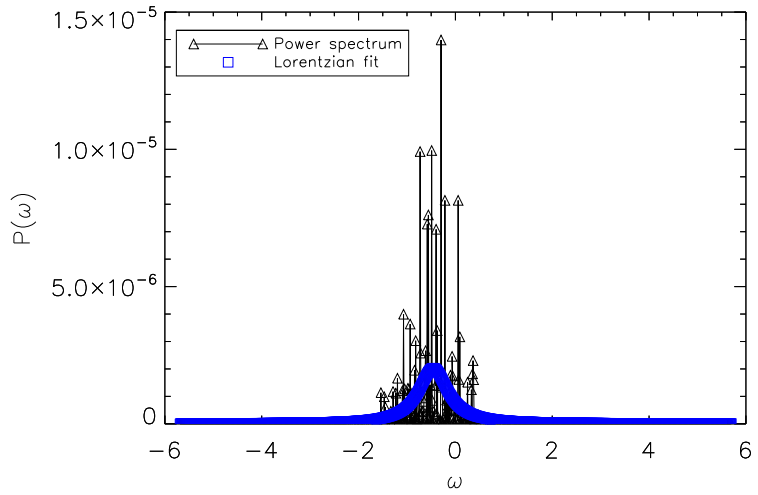

Figure 4.14: The power spectrum for the 5^{th} POD mode at $\mathbf{k} = (0.1, 0.2)$. Also shown is the Lorentzian fit in blue.

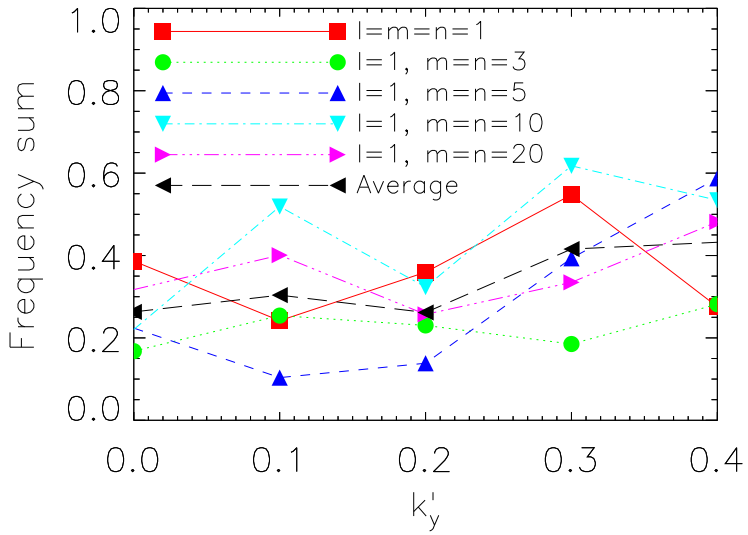

Figure 4.15: Sum of frequency scanned over k'_y i.e. $|\hat{\omega}^{(l)}_{-\mathbf{k}} + \hat{\omega}^{(m)}_{\mathbf{k}'} + \hat{\omega}^{(n)}_{\mathbf{k}-\mathbf{k}'}|$. The wavenumber $\mathbf{k} = (0, 0.2)$ and $k'_x = 0.1$. The combinations of l, m, and n are indicated by the color. The average over 5 POD modes is also plotted.

by fitting a Lorentzian function to the power spectrum, as discussed above. This calculation is done for the first few high amplitude POD modes at all the wavenumbers. The frequency sum $|\hat{\omega}^{(l)}_{-\mathbf{k}} + \hat{\omega}^{(m)}_{\mathbf{k}'} + \hat{\omega}^{(n)}_{\mathbf{k}-\mathbf{k}'}|$ is plotted in Fig. 4.15. The indices l, m and n represent the POD mode number. Five modes are selected, 1^{st}, 3^{rd}, 5^{th}, 10^{th}, and 20^{th} for plotting. Firstly, we see the minimum frequency sum is at $k'_y = 0, 0.1, 0.2$. $k'_y = 0$ is a zonal triplet and so is $k'_y = 0.2$ since $k_y - k'_y = 0$. $k'_y = 0.1$ is very close to a zonal triplet. This shows that triplets with a zonal (or close to zonal) wavenumber have the least frequency sum. As we move away from the zonal triplets, the frequency sum increases (similar to what was seen in Fig. 3.21). Secondly, at $k'_y = 0$ and $k'_y = 0.2$ the triplets with subdominant modes, i.e., $m, n = 3$, 5, 10 or 20, show lower frequency sum than unstable mode triplets with $m, n = 1$. Thus, it is a triplet involving an unstable mode, a zonal mode and a subdominant mode which has the minimum frequency sum. This corroborates the result of the fluid model study which also found that the frequency sum is minimized for the same combination of modes. As discussed in Sec. 3.7 and Ref. [64], the there wave interaction is inversely proportional to this frequency sum $\langle \pi^{(l)}_{-\mathbf{k}} \pi^{(m)}_{\mathbf{k}'} \pi^{(n)}_{\mathbf{k}-\mathbf{k}'} \rangle \propto 1/[|\hat{\omega}^{(l)}_{-\mathbf{k}} + \hat{\omega}^{(m)}_{\mathbf{k}'} + \hat{\omega}^{(n)}_{\mathbf{k}-\mathbf{k}'}|]$. Hence, this combination of modes has the largest correlation time leading to the maximum energy transfer. The reason for dominance of zonal flows should be due to their large amplitude in ITG turbulence, as was the case in the fluid model.

4.8 Discussion

This chapter has dealt with zonal flows in gyrokinetic ITG turbulence. We saw that POD mode decomposition is an extremely useful tool for studying the subdominant modes in gyrokinetics. We were able to decompose the kinetic energy term into orthogonal POD mode contributions and derive their energy dynamical equations. In the next chapter we shall see that POD modes are not optimal for studying the fine scale modes in the turbulence. However, the first few POD modes capture most of the dynamics and energy in the system and in this sense they are very efficient [85]. An inherent drawback of POD is that it fundamentally depends on the nonlinear simulation data. Thus, POD modes change for different simulation runs and different

time samplings.

Overall the results are very similar to the fluid model study. We see that both, Fourier modes and POD modes, show strong three-wave interactions with zonal flows. Zonal flows act as a catalyst of energy transfer from unstable to subdominant POD modes, but themselves dissipate very little energy. This transfer is so efficient that a significant fraction (>30% if we look at linear instability or >50% if we look at nonlinear instability) of the energy injected by the instability is dissipated by damped subdominant modes in the unstable range before reaching the stable wavenumbers. Although these percentages depend on various simulation parameters, they show that zonal flow assisted saturation by damped modes is important in ITG. Even beyond the unstable range, a significant fraction of energy continues to be dissipated by the subdominant modes. These results are important because gyrokinetics is more comprehensive compared to the simple fluid model. While the fluid model mocked up zonal flows by the crude δ parameter, gyrokinetics takes into account the actual nonadiabatic response of electrons to zonal perturbations.

Frequency matching again emerges as one of the most important indicators of dominant three-wave interactions. Triads of an unstable mode, zonal mode and a subdominant mode show minimum frequency mismatch. This principle merits further study as it can prove very handy in dealing with turbulent interactions, especially in gyrokinetics where there are a slew of modes [86]. It can also provide a link with experiments via bispectral analysis [87].

The shearing mechanism of the zonal flow-drift wave shearing paradigm does not seem to be the most important saturation mechanism, compared to the energy transfer to subdominant modes. Nevertheless, it does seem to be active in the energy transfer process and seems intricately linked to the zonal flow amplitude itself. It should be interesting to further tease out the differences between these two mechanisms.

The energy transfer processes in the subdominant mode space seem to be very rich and merit further study. Hence, that is the topic of the next chapter.

Chapter 5

Energy partitioning between damped modes in gyrokinetic turbulence

The previous chapter looked at the dissipation by stable subdominant modes in zonal flow regulated turbulence. It is challenging to analyze the tens of thousands of modes involved in gyrokinetic turbulence. In hydrodynamic turbulence, Kolmogorov's $5/3^{\text{rd}}$ law provides an elegant way of understanding the complexity of turbulence. It expresses the way energy is distributed between Fourier wavenumbers that span a range of scales in the periodic, spatial dimensions. Similarly, in gyrokinetics we have a slew of damped modes that span a range of scales in the non-periodic phase space dimensions (z, $v_{\parallel}$, μ). Is there any quantity or idea that can organize the damped modes in gyrokinetics? In this chapter we calculate the spectra of energy dissipation and amplitude attenuation rates of the damped modes. The aim is to find some regular scaling behavior in these spectra that can provide an organizing principle for the multitude of damped modes. Recently there has been a lot of interest in studying the fine scale structure of modes in gyrokinetics and their intimate connection to dissipation [88], [89]. The damped modes also develop fine scale structure as their damping rate increases, and hence we take a look at their mode structure. In hydrodynamics, the energy transfer is local in k-space, i.e., eddies of some scale exchange energy with eddies of a similar scale. Similarly, in this chapter we also take a look at how energy is exchanged between stable modes with different scales.

5.1 Various dissipation rates of POD modes

One of the most relevant physical quantities related to subdominant modes is their energy dissipation rate. It is their defining property, and determines their role in saturation, hence it is very important. Eq. 4.24 defines the rate of change of energy of POD modes. It contains both the linear ($\mathcal{L}$) and nonlinear terms ($\mathcal{N}$). In Ch. 4 we focused on the nonlinear term, which is a conservative term. For the global energetics we are interested in the linear term that injects or dissipates energy globally. From Eq. 4.25, for the m^{th} POD mode, it is simply given by,

$$\frac{\partial}{\partial t}|\beta^{(m)}\pi^{(m)}|^2\bigg|_{\text{linear}} = 2\text{Re}\bigg\{\int dz dv_\parallel d\mu \frac{\pi B_0 \hat{J}(z)}{F_0}\psi^{(m)*}\beta^{(m)}\pi^{(m)*}\mathcal{L}[g]\bigg\}. \tag{5.1}$$

The linear gyrokinetic operator is made up of three terms, $\mathcal{L} = \mathcal{Q} + \mathcal{C} + \mathcal{R}$ (see Eq. B.4), where $\mathcal{Q}$ is the gradient drive and $\mathcal{C}$ is the dissipative term, either collisional or hyper-diffusive [90]. Operator $\mathcal{R}$ contains the curvature drift, ∇B drift, parallel velocity gradient and finite β terms. The $\mathcal{R}$ term adds up to zero when a sum over the wavenumbers is performed, although it is not zero at individual wavenumbers. However, even though we consider individual wavenumbers, we choose to ignore the $\mathcal{R}$ term because it does not affect the net energy balance and thus, can be considered as a conservative term. This way we define the nonconservative terms as the heat flux ($Q^{(m)}$) and dissipation ($C^{(m)}$) of the m^{th} POD mode (as well as a term $R^{(m)}$ which we do not consider),

$$Q^{(m)} = 2\text{Re}\bigg\{\int dz dv_\parallel d\mu \frac{\pi B_0 \hat{J}(z)}{F_0}\psi^{(m)*}\beta^{(m)}\pi^{(m)*}\mathcal{Q}[g]\bigg\}, \tag{5.2}$$

$$C^{(m)} = 2\text{Re}\bigg\{\int dz dv_\parallel d\mu \frac{\pi B_0 \hat{J}(z)}{F_0}\psi^{(m)*}\beta^{(m)}\pi^{(m)*}\mathcal{C}[g]\bigg\}. \tag{5.3}$$

We can also do a time average of these quantities over the simulation time. For example, this reduces the heat flux to,

$$\begin{aligned}\langle Q\rangle^{(m)} \equiv \sum_t Q^{(m)} &= \sum_t 2\text{Re}\bigg\{\sum_n \int dz dv_\parallel d\mu \frac{\pi B_0 \hat{J}(z)}{F_0}\psi^{(m)*}\beta^{(m)}\pi^{(m)*}\pi^{(n)}\mathcal{Q}[\psi^{(n)}\beta^{(n)}]\bigg\} \\ &= 2\text{Re}\bigg\{\int dz dv_\parallel d\mu \frac{\pi B_0 \hat{J}(z)}{F_0}\psi^{(m)*}\beta^{(m)2}\mathcal{Q}[\psi^{(m)}]\bigg\},\end{aligned} \tag{5.4}$$

where $\langle Q\rangle^{(m)}$ is the time averaged heat flux, $\sum_t$ denotes a sum over the time steps of the simulation and we have used Eq. 4.18 and 4.20. Similarly $\langle C\rangle^{(m)}$ can be defined as the time averaged dissipation. The advantage of this definition is that to calculate these quantities we only need the POD mode structure $\psi^{(m)}$ and singular value $\beta^{(m)}$. Thus we do not need to run a nonlinear simulation again in order to calculate $\pi^{(m)}$. These terms are plotted in Fig. 5.1(a) and (b). We see that both $\langle Q\rangle$ and $\langle C\rangle$ are very large for the first POD mode and rapidly drop close to zero for higher POD modes. $\langle Q\rangle$ has a large and positive value for the first POD mode and then it oscillates around zero for the higher modes. $\langle C\rangle$, being the dissipation, is always negative, shows a very large value for the first mode and then rapidly decays close to zero. Overall, for the higher modes, $\langle C\rangle$ dominates $\langle Q\rangle$ because they all have a negative value for $\langle Q\rangle + \langle C\rangle$. Fig. 5.1(c) plots the absolute value of $\langle Q\rangle + \langle C\rangle$ for POD modes 3 up to 1000, and is the same plot as Fig. 4.6. $\langle Q\rangle + \langle C\rangle$ is positive for the first couple of modes for which $\langle Q\rangle$ is larger than $\langle C\rangle$ but then it stays negative. We see a smooth exponential behavior for a large range of intermediate POD modes.

Next we define the amplitude attenuation rate (AAR), $\mathcal{G}$, so named because it contains one factor of amplitude ($\sim \beta$) less than the energy ($\sim \beta^2$). For the m^{th} POD mode, it is the nonconservative rate of change of energy divided by the singular value,

$$\mathcal{G}^{(m)} \equiv \frac{\langle Q\rangle^{(m)} + \langle C\rangle^{(m)}}{\beta^{(m)}}. \tag{5.5}$$

It is plotted in Fig. 5.1(d). We also plot $\mathcal{G}^{(m)}/\beta^{(m)}$ in Fig. 5.1(e). This can be thought of as a normalized dissipation rate because it does not contain any factor of the singular value β. It shows a linear behavior from the third up to 1000^{th} mode. As the mode number increases, modes develop a fine scale structure in phase space, leading to increased viscous dissipation, which depends on quadratic and quartic powers of gradients in phase space [74]. This quantity can be useful for describing such fine scale structure in gyrokinetic turbulence, but it does not take into account the amplitude information.

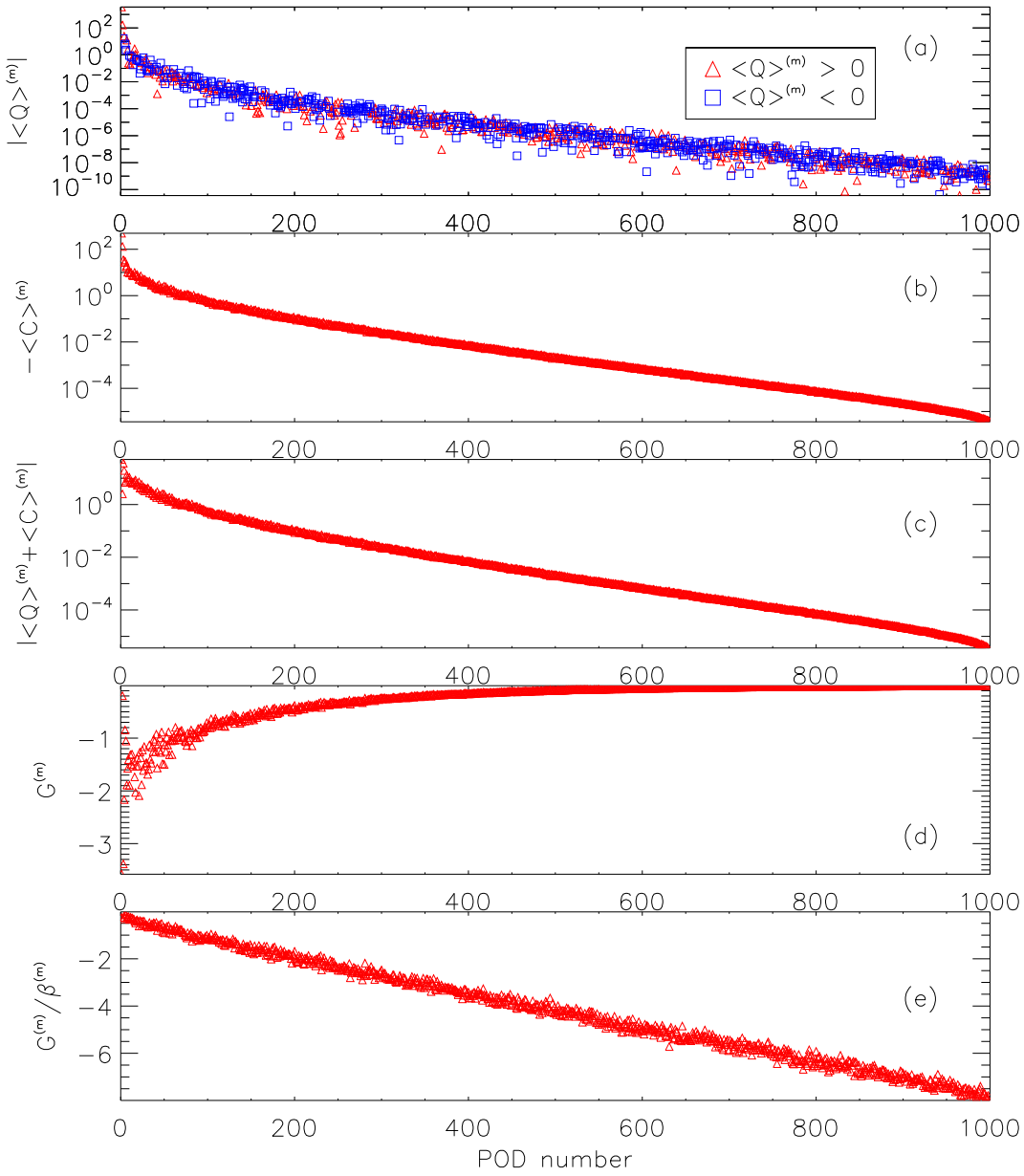

Figure 5.1: (a) plots $|\langle Q\rangle^{(m)}|$ for first 1000 POD modes on a log scale. Since $\langle Q\rangle^{(m)}$ fluctuates between positive and negative values, its sign is indicated by the different markers. (b) shows $-\langle C\rangle^{(m)}$ for first 1000 POD modes; (c), (d) and (e) plot $|\langle Q\rangle^{(m)} + \langle C\rangle^{(m)}|$, $\mathcal{G}^{(m)}$ and $\mathcal{G}^{(m)}/\beta^{(m)}$ respectively for POD modes 3 up to 1000. All these POD modes are calculated for $\mathbf{k} = (0, 0.25)$, however other wave numbers also show similar behavior.

5.2 Amplitude attenuation rate equipartition (AARE)

Several attempts were made in order to understand the partitioning of energy among the subdominant modes in gyrokinetics. This section examines some of the previous efforts in this regard, which showed that the amplitude attenuation rate is equipartitioned between the damped modes. However, before that we look at an important aspect of mode analysis in gyrokinetic simulations, namely k_x connected modes.

5.2.1 Effect of k_x connections

In local simulations, the domain of simulation is a flux tube [91], [92]. In all the analysis done till now, we have used only one (k_x, k_y) Fourier mode for POD decompositions. However, in flux-tube simulations, due to the periodicity in field aligned coordinates, all physical functions have to satisfy the following relation: $|f(k_x, k_y, z = \pi)| = |f(k_x + 2\pi\hat{s}k_y, k_y, z = -\pi)|$ (see Appendix B of Ref. [21], [53]). Practically, this extends the simulation domain along the field line by connecting additional $z = [-\pi, \pi]$ blocks at higher k_x for a given k_y. Typically, one uses five k_x connected modes to get a domain of $z = [-5\pi, 5\pi]$. These connected k_x modes can be spliced together to form the columns of the M matrix for POD as shown in Fig. 4.2. However, when this is implemented, the balance between the linear and nonlinear energy terms for the higher POD modes is disrupted, as shown in Fig. 5.2(b). We see that without connections, in Fig. 5.2(a), which is similar to Fig. 4.5, the linear and nonlinear rates of change of energy for higher POD modes, averaged over saturation, are of equal and opposite strengths. In Fig. 5.2(b) we keep five k_x connected modes and see that the linear and nonlinear rates do not cancel out as accurately. In fact, for certain POD modes they both have the same sign. The cause for this discrepancy is not clear. Due to this reason, it was decided to not keep any connected k_x modes in the POD analysis. It is expected that the mode structures of lower POD modes are not affected significantly by these connections, simply because their amplitude decays rapidly within the $z = [-\pi, \pi]$ domain, so it is okay to ignore them. These connections affect the mode structure of higher POD modes, but these modes contribute a small fraction to the energy and

hence the connections can be ignored. Another important factor in this unresolved issue is the hyper-diffusivity. Unlike all the simulations presented until now, which used relatively high hyper-diffusivity, simulations for Fig. 5.2 had lower hyper-diffusivities, $D_z = 0.25$ and $D_v = 0.2$. Using high hyper-diffusivity coefficients does not lead to an imbalance between the linear and nonlinear rates, at least for the POD numbers shown in Fig. 5.2. Thus, it might be beneficial to redo these calculations taking into account the connected k_x modes with high hyper-diffusivity and/or collisions. In the next section we look at the effect of hyper-diffusivity in greater detail.

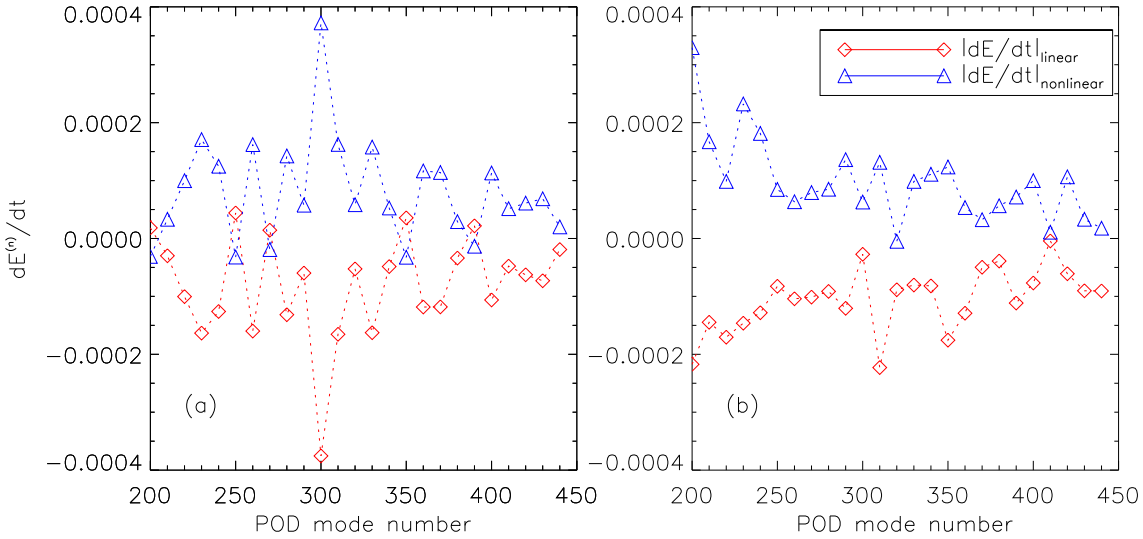

Figure 5.2: Plots of the linear and nonlinear rate of change of energy of POD modes. $dE/dt|_{\text{linear}}$ is given by Eq. 5.1 and $dE/dt|_{\text{nonlinear}}$ is given by Eq. 4.32. These quantities are plotted for the sampling of POD modes 200, 210, 220,..., 440. (a) is without k_x connections while (b) is with five k_x connected modes.

5.2.2 Effect of low hyper-diffusivity

In Sec. 5.1 we calculated various dissipation rates using high hyper-diffusivity values as shown in the parameters file in Appendix C. Studies prior to this thesis have been done using lower values of hyper-diffusivity, $D_z = 0.25$ and $D_v = 0.2$. Those studies show a different behavior of the amplitude attenuation rate, as shown in Fig. 5.3, compared to Fig. 5.1(d). For Fig. 5.3, in addition to low hyper-diffusivity, the time sampling frequency for POD is halved compared to the sampling frequency shown in Appendix C. Also, the POD modes are defined in a slightly different

manner such that their normalization, Eq. 4.19, does not include the background Maxwellian F_0 in the denominator. We see that the AAR ($\mathcal{G}^{(n)}$) attains a flat value after POD mode 200. This is termed as amplitude attenuation rate equipartition (AARE). This can prove to be a very useful quantity as it shows a very simple behavior across all the complicated, higher POD modes. Is this equipartition a universal feature of gyrokinetic turbulence? We see the same behavior at other wavenumbers also. In Fig. 5.4, the AAR is calculated in the same way for two other kinds of turbulence; ETG (Electron temperature gradient turbulence) [93], [94] and TEM (Trapped electron mode turbulence) [81], [95]. These simulations have vastly different parameters from the CBC simulations done till now. However, we see that across all these different kinds of

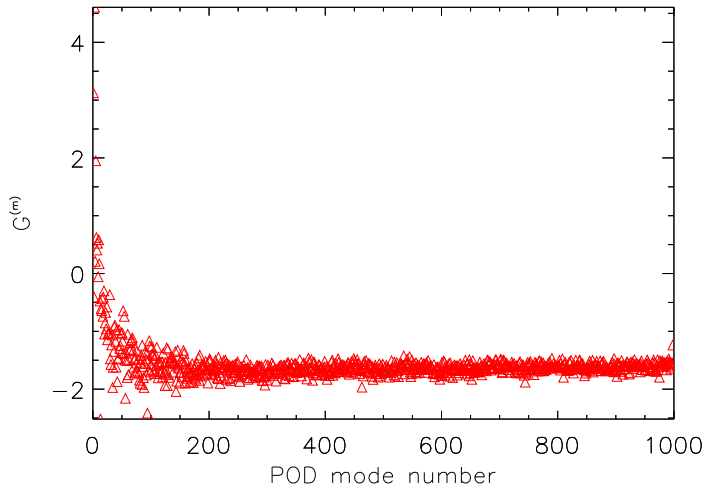

Figure 5.3: A plot of AAR ($\mathcal{G}^{(n)}$) for 1000 POD modes at $\mathbf{k} = (0, 0.25)$ for CBC-ITG turbulence. AAR is calculated for a simulation with lower hyper-diffusivity, lower time sampling frequency and a different normalization of the POD modes. We see equipartition above mode number 200.

turbulence and wavenumbers, we always get equipartition of AAR. There is a sharp drop in the first 50-100 POD modes after which the AAR flattens out. What is the reason for this? If AARE is physically meaningful, then it can be a powerful tool to handle the POD modes. In the next couple of sections we look at some hypotheses for explaining this phenomenon of equipartition of amplitude attenuation rate.

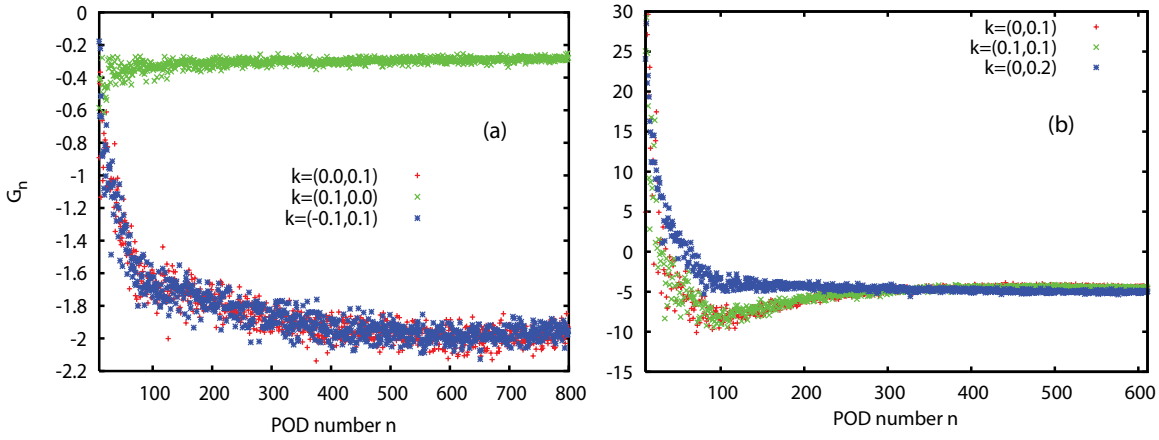

Figure 5.4: Plots of AAR ($\mathcal{G}^{(n)}$) for (a) TEM and (b) ETG turbulence. The simulation parameters can be found in Refs. [93] and [81] for ETG and TEM respectively. The different colors are for different wavenumbers, all of which show equipartition above POD number 300 or so. Resolution in $(k_x, k_y, z, v_\parallel, \mu)$ for TEM and ETG both was (128,16,16,32,8).

5.2.3 Understanding AARE

One way to view the AARE is that for higher POD modes the AAR becomes independent of the mode number n. We turn to the nonlinear couplings in order to explain this mode number independence. Since the amplitude attenuation rate is a linear rate of change, we should expect that in saturation it should be equal and opposite to some three-wave nonlinear term. We can write a heuristic equation for such a balance of the l^{th} POD mode as,

$$\mathcal{G}^{(l)}_{\mathbf{k}} = \sum_{\mathbf{k}'} \sum_{m,n} C_{lmn}(\mathbf{k}', \mathbf{k}'') \beta^{(m)}_{\mathbf{k}'} \beta^{(n)}_{\mathbf{k}''} \int dt \pi^{(l)*}_{\mathbf{k}} \pi^{(m)}_{\mathbf{k}'} \pi^{(n)}_{\mathbf{k}''} \int dz dv_\parallel d\mu \frac{\pi B_0 \hat{J}(z)}{F_0} \psi^{(l)*}_{\mathbf{k}} \chi^{(m)}_{\mathbf{k}'} \psi^{(n)}_{\mathbf{k}''}. \quad (5.6)$$

We keep only $\beta^{(m)}_{\mathbf{k}'} \beta^{(n)}_{\mathbf{k}''}$ on the R.H.S because AAR is divided by $\beta^{(l)}_{\mathbf{k}}$ in its definition (Eq. 5.5). To explain AARE, we should explain why $\mathcal{G}^{(l)}_{\mathbf{k}}$ is independent of not only l, but also m and n. If we are considering ITG turbulence, we know that the dominant coupling is with zonal wavenumbers, i.e., either $k'_y = 0$ or $k''_y = 0$. However, that doesn't tell us what m and n are. Also, we know that AARE is observed not only in ITG but also in TEM and ETG turbulence, where zonal flows are not important. Thus, it does not seem that zonal flows are playing an important role in AARE.

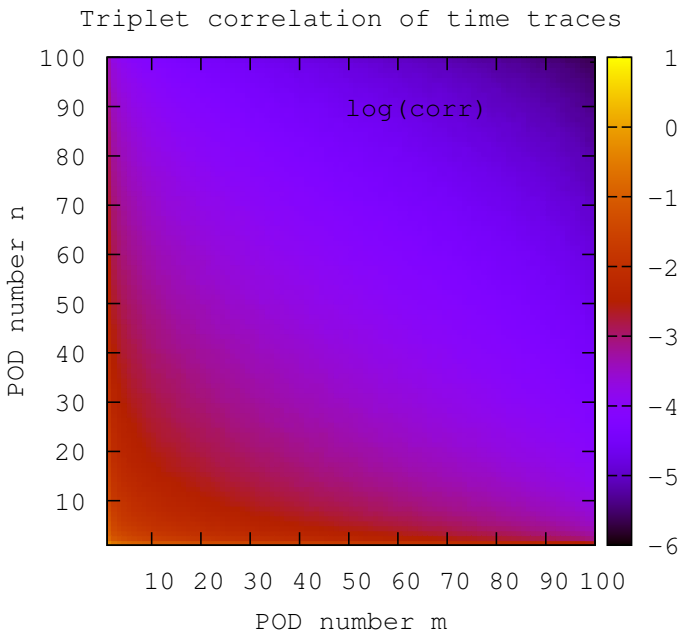

Figure 5.5: A plot of $\log_{10}[\beta^{(m)}_{\mathbf{k}'}\beta^{(n)}_{\mathbf{k}''}\int dt\pi^{(l)*}_{\mathbf{k}}\pi^{(m)}_{\mathbf{k}'}\pi^{(n)}_{\mathbf{k}''}]$ for $l = 500$, $\mathbf{k} = (0.1, -0.25)$, $\mathbf{k}' = (0, -0.25)$ and $\mathbf{k}'' = (0.1, 0)$ as a function of m and n. The plotting grid is coarse grained with a grain size of (10×10) POD modes, thus reducing the range of 1000 POD modes to 100 points.

We can claim that the dominant interactions are with the highest singular value POD modes, i.e., $m = n = 1$. This can be easily verified, as shown in Fig. 5.5. This figure plots the following part of Eq. 5.6: $\beta^{(m)}_{\mathbf{k}'}\beta^{(n)}_{\mathbf{k}''}\int dt\pi^{(l)*}_{\mathbf{k}}\pi^{(m)}_{\mathbf{k}'}\pi^{(n)}_{\mathbf{k}''}$; for $l = 500$, $\mathbf{k} = (0.1, -0.25)$, $\mathbf{k}' = (0, -0.25)$ and $\mathbf{k}'' = (0.1, 0)$ as a function of m (on x-axis) and n (on y-axis). The POD number for $l = 500$ is chosen arbitrarily, but we see the same result for other choices. There are 1000 POD modes but the plotting grid is coarse grained over a box of (10×10) modes, i.e., every (m, n) on the plot is actually a sum of 100 (m, n) combinations in the range $\{10\times(m-1)+1 : 10\times(m), 10\times(n-1)+1 : 10\times(n)\}$. Hence the plot domain is from 1 to 100. The color scale is the logarithm of the triplet correlation quantity and it shows a strong dependence on (m, n). The strongest coupling is with $(m, n) = (1, 1)$, even if the plot is not coarse grained. This implies that we can assume $m = 1$, $n = 1$ in Eq. 5.6 and drop the other terms. This eliminates the m and n dependence of Eq. 5.6. However, the l dependence still remains. To handle that, we take a look at the following terms: $\int dt\pi^{(l)*}_{\mathbf{k}}\pi^{(1)}_{\mathbf{k}'}\pi^{(1)}_{\mathbf{k}''}$ in Fig. 5.6(a) and $\int dzdv_{\parallel}d\mu(\pi B_0\hat{J}(z)/F_0)\psi^{(l)*}_{\mathbf{k}}\chi^{(1)}_{\mathbf{k}'}\psi^{(1)}_{\mathbf{k}''}$ in Fig. 5.6(b). These

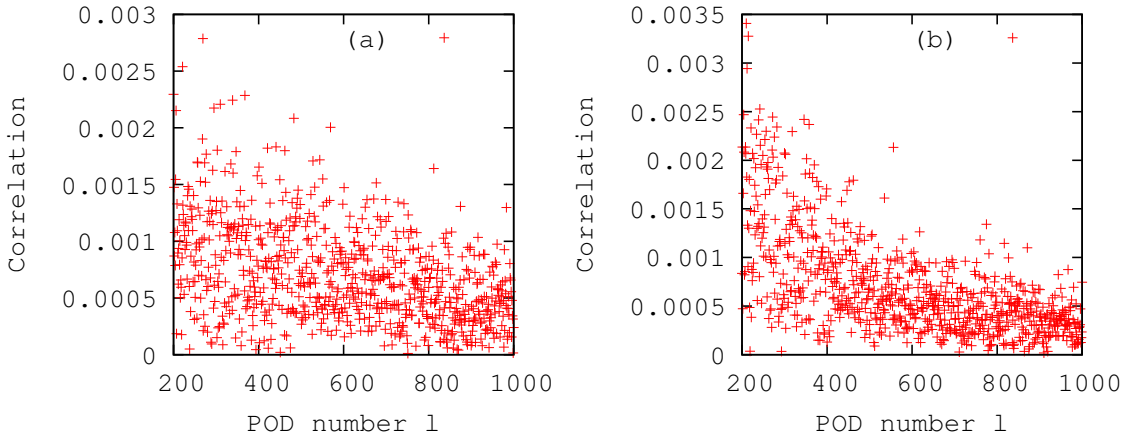

Figure 5.6: (a) shows $\int dt \pi^{(l)*}_{\mathbf{k}} \pi^{(1)}_{\mathbf{k}'} \pi^{(1)}_{\mathbf{k}''}$ and (b) shows $\int dz dv_\parallel d\mu (\pi B_0 \hat{J}(z)/F_0) \psi^{(l)*}_{\mathbf{k}} \chi^{(1)}_{\mathbf{k}'} \psi^{(1)}_{\mathbf{k}''}$ for $\mathbf{k} = (0, 0.25)$, $\mathbf{k}' = (0.1, 0)$ and $\mathbf{k}'' = (-0.1, 0.25)$ as a function of l.

terms are plotted from $l = 200$ up to $l = 1000$, the range in which we observe equipartition. These correlations show a very weak dependence on l although they have a significant scatter around a mean value. This analysis shows that AARE is supported by the underlying mode coupling properties which render the dominant correlations of energy transfer equal for all damped modes, but with considerable statistical scatter.

However, this does not answer everything. We still haven't explained why the triplet correlations in Fig. 5.6 depend very weakly on l. The coupling coefficient in Eq. 5.6, $C_{l11}(\mathbf{k}', \mathbf{k}'')$, still has a l dependence. The form of $C_{l11}(\mathbf{k}', \mathbf{k}'')$ is not known, which is related to another open issue, which is that Eq. 5.6 is a heuristic equation. If it can be derived from first principles, then we can obtain the form of $C_{l11}(\mathbf{k}', \mathbf{k}'')$. We next try to derive Eq. 5.6 from the gyrokinetic equation.

In saturation, the linear rate of energy change of POD modes (Eq. 4.25) should balance the nonlinear rate (Eq. 4.32) when summed over time, i.e.,

$$\langle Q \rangle^{(l)} + \langle C \rangle^{(l)} + \langle R \rangle^{(l)} = -\sum_t 2Re \Bigg\{ \int dz dv_\parallel d\mu \frac{\pi B_0 \hat{J}(z)}{F_0} \psi^{(l)*} \beta^{(l)} \pi^{(l)*} \times \sum_{\mathbf{k}'} (k'_x k_y - k_x k'_y) \chi(\mathbf{k}') g(\mathbf{k} - \mathbf{k}') \Bigg\}. \quad (5.7)$$

Here, Eq. 5.4 and its analogues are used to define the time sum on the L.H.S. Suppose the term $\langle R\rangle^{(l)}$ is negligible and we ignore it. We substitute the POD (Eq. 4.18) for $\chi(\mathbf{k}')$ and $g(\mathbf{k}-\mathbf{k}')$, divide by $\beta^{(l)}$ and convert the sum over time into an integral, assuming that the time step is just a constant Δt (which is approximately correct), to get,

$$\mathcal{G}^{(l)} = -2Re\Bigg\{ \sum_{\mathbf{k}'}\sum_{m,n} \frac{(k'_x k_y - k_x k'_y)}{\Delta t}\beta^{(m)}_{\mathbf{k}'}\beta^{(n)}_{\mathbf{k}''}\int dt \pi^{(l)*}_{\mathbf{k}}\pi^{(m)}_{\mathbf{k}'}\pi^{(n)}_{\mathbf{k}''}\int dz dv_{\parallel} d\mu \frac{\pi B_0 \hat{J}}{F_0}\psi^{(l)*}_{\mathbf{k}}\chi^{(m)}_{\mathbf{k}'}\psi^{(n)}_{\mathbf{k}''}\Bigg\}. \tag{5.8}$$

Here we have used Eq. 5.5 to obtain the L.H.S. Eq. 5.8 looks exactly like Eq. 5.6 and we can identify the nonlinear coupling coefficient as $C_{lmn}(\mathbf{k}',\mathbf{k}'') = (k'_x k_y - k_x k'_y)/\Delta t$. Indeed it turns out to be independent of l, m and n. Can this explain AARE? In deriving Eq. 5.8 we assumed that $\langle R\rangle^{(l)}$ is negligible. Unfortunately, numerical calculations show that $\langle R\rangle^{(l)}$ is comparable to $\langle Q\rangle^{(l)}$ and $\langle C\rangle^{(l)}$. We try to work around this by incorporating $\langle R\rangle^{(l)}$ in the definition of AAR, i.e., $\tilde{\mathcal{G}}^{(l)} \equiv (\langle Q\rangle^{(l)} + \langle C\rangle^{(l)} + \langle R\rangle^{(l)})/\beta^{(l)}$. This quantity, $\tilde{\mathcal{G}}^{(l)}$, will satisfy Eq. 5.8 exactly. Unfortunately, this quantity does not show the nice behavior of equipartition as seen in Fig. 5.3.

Thus, there are many unanswered questions about the AARE. At the same time, there are concerns about noise contamination in the higher POD modes. In fact, in signal processing, POD modes are regularly used to eliminate noise from numerical simulations [96], [97]. The general idea is to decompose the noisy signal into POD and then discard the modes with small singular values. Reconstructing the signal from the remaining modes reduces the noise in the signal. Thus, it is possible that the omnipresent AARE is an artifact of the noise in the POD. Hence, it is necessary to determine if the higher POD modes are physically meaningful or contaminated by noise, which is the topic of the next section.

5.3 Structure and physicality of POD modes

To determine the physicality of POD modes, let us look at their structure in the parallel velocity ($v_{\parallel}$) and parallel spatial (z) coordinates. Fig. 5.7(a) shows the mode structure of select POD modes in the z coordinate, averaged over $v_{\parallel}$ and μ. For this section, there are five k_x connected

modes kept in the domain, so the domain stretches from -5π to 5π, with 2π for each connected mode. For each 2π domain there are 16 grid points, thus giving a total of 80 grid points which are plotted on the abscissa. These are mode structures of the 1^{st}, 10^{th}, 50^{th} and 200^{th} POD modes. The modes are normalized so that their peak matches with the peak of the 1^{st} mode, just for ease of viewing. As was noted in Sec. 5.2.1, the low POD modes (1^{st} and 10^{th}) are not affected by k_x connections as their amplitude drops rapidly outside the central 2π domain. The connections are important for higher POD modes, but their amplitude is very small. We see that the higher POD modes develop fine scale structure. Mode number 200 develops a zig-zag structure between consecutive grid points. This indicates that the mode is not resolved. The structure in parallel velocity, $v_{\|}$, averaged over connected k_x, z and μ is shown in Fig. 5.7(b). In this case there are 32 grid points. Again we see a zig-zag structure developing for higher POD modes but they seem to be better resolved in $v_{\|}$ space.

Physical quantities, which depend on gradients, calculated from unresolved modes cannot be trusted. In the AAR, the dissipation, $\langle C \rangle^{(l)}$, dominates other terms. Both hyper-diffusive dissipation (used here) and collisional dissipation depend on second and higher order gradients in z and $v_{\|}$ [74], [98]. These gradients will not be calculated correctly because the fine scale structure is not resolved. We can expect the dissipation to level out (in other words, equipartition) because the fine scale structure smaller than grid scale, which would have contributed to higher dissipation, is all zeroed out. It should be noted that a mode should be well resolved in both z and $v_{\|}$ for it to be physically meaningful. Even if it is unresolved in only the z coordinate, it is rendered meaningless for physical calculations. We do not look at the resolution in μ as we do not implement dissipation in the μ space. The mode structure has been studied by taking different averaging procedures with different weights. We have also looked at mode structure at particular points in phase space rather than averaging over the remaining phase space coordinates. All these variations do not change the results shown in Fig. 5.7.

We would like to develop a metric to estimate whether a mode is resolved or not. We Fourier transform the mode structure in z and $v_{||}$ space, giving its spectrum in k_z and $k_{v_{\|}}$. These are shown in Fig. 5.8 for the POD modes shown in Fig. 5.7. If the mode is well resolved, then we

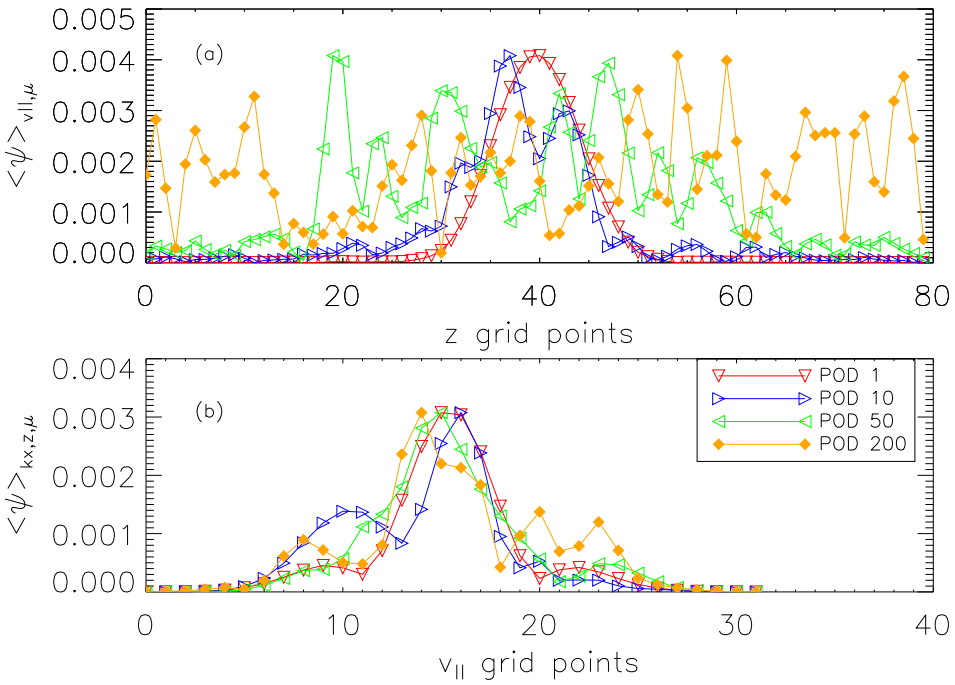

Figure 5.7: (a) POD structure in z space averaged over $v_\parallel$ and μ and taking 5 k_x connected modes. The 80 grid points span a domain of $[-5\pi, 5\pi]$ (b) POD structure in $v_\parallel$ averaged over k_x, z and μ. The 32 grid points span a domain of $[-3v_{Ti}, 3v_{Ti}]$. The legend applies to both plots. Averaging is done with the proper weights, i.e., $\langle\psi\rangle_z = |(\int dz J(z)\psi)/(\int dz J(z))|$ and $\langle\psi\rangle_{v_\parallel,\mu} = |(\int dv_\parallel d\mu\psi)/(\int dv_\parallel d\mu)|$. All POD modes are calculated at $\mathbf{k} = (0, 0.25)$.

expect the Fourier spectrum to fall rapidly at high wavenumbers compared to low wavenumbers. This is the case for POD modes 1, 10 and 50 in k_z space, seen in Fig. 5.8(a). However since mode 200 develops zig-zag structure in z-space we see that its Fourier transform remains relatively flat at higher k_z. The modes appear well resolved in $v_\parallel$ space, which can be seen in Fig. 5.8(b) where the Fourier transform of all the modes drops at higher $k_{v_\parallel}$. Thus, we define the simplest metric

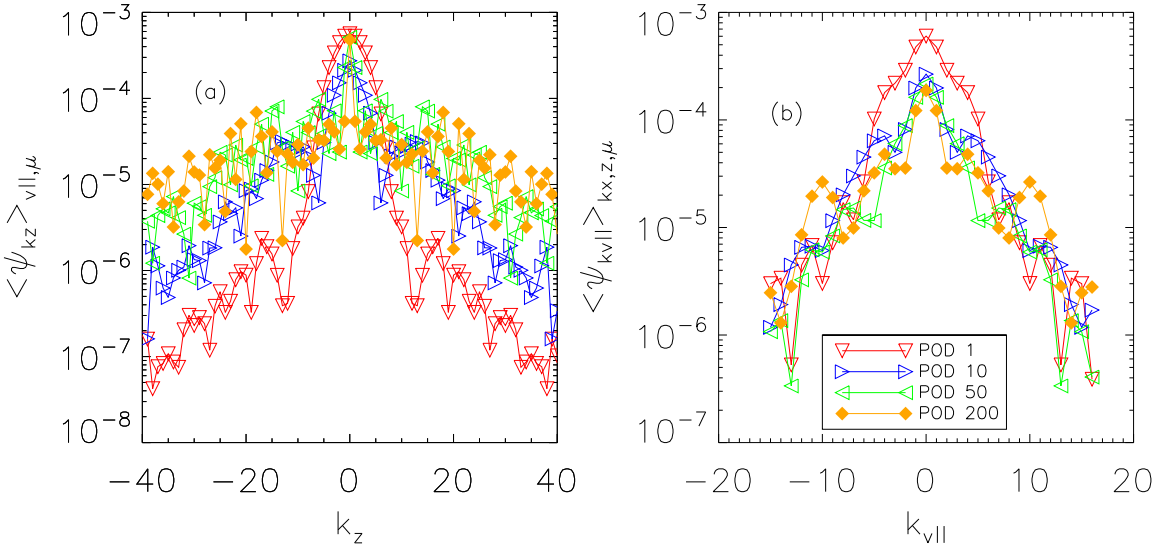

Figure 5.8: Spectrum of POD modes in (a) k_z and (b) $k_{v_\parallel}$. These are Fourier transforms of the POD modes shown in Fig. 5.7. Legend applies to both plots.

as follows. We take the ratio of the average amplitude for the lower half of wavenumbers to the average amplitude for the upper half of wavenumbers. This ratio should be larger than unity for well-resolved modes and should drop to unity for unresolved modes, as the Fourier transform becomes flatter. The central $k_z = k_{v_\parallel} = 0$ spectrum point is ignored in this ratio. This ratio is plotted in Fig. 5.9 where plot (a) is this ratio calculated for the k_z spectrum and (b) is the ratio calculated for the $k_{v_\parallel}$ spectrum. We can see that this ratio falls quickly to unity for the z coordinate and then stays flat at unity. We can estimate that modes above 400 or so are unresolved. The ratio is larger than unity in the $v_\parallel$ coordinate for the first 800 or so modes. However, we can clearly say that out of tens of thousands of POD modes, very few, of the order of 100, are well resolved. This means that we cannot study any broad, generalizable, physical quantity for POD modes beyond the first few hundred.

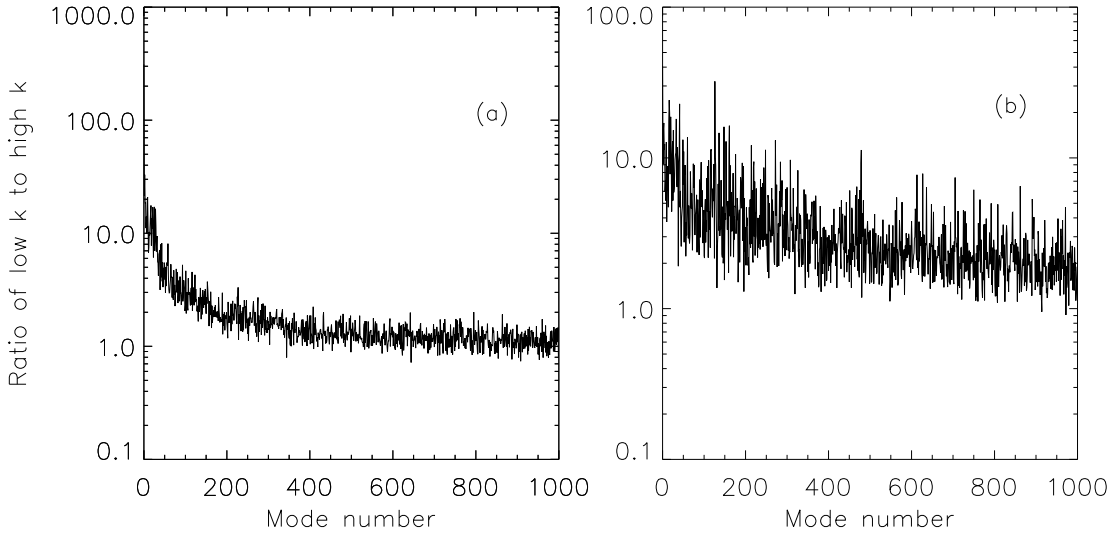

Figure 5.9: Ratio of the average amplitude of POD spectrum in lower half of wavenumbers to the average amplitude in upper half of wavenumbers for (a) k_z spectrum, and (b) $k_{v_\parallel}$ spectrum, plotted for first 1000 POD modes.

AARE is more pronounced when we take lower hyper-diffusivity values (Sec. 5.2.2), for which the POD modes become unresolved at lower mode numbers, around 100. That is precisely where the AARE starts to appear (Fig. 5.3). The above analysis was done using higher hyper-diffusivity, which damps the fine scale fluctuations and hence extends the range of well-resolved POD modes up to 400. There are also indications in resolution studies that the onset of AARE is pushed to higher mode numbers as the resolution is increased. All these results seem to indicate that the AARE is an artifact of the unresolved nature of higher POD modes. However, several questions still remain. Why did we not see AARE in the higher hyper-diffusivity runs? If it is due to the fine scale structure being damped away, then will we see AARE if we extend the simulation run to even higher POD modes? Why does removing the background Maxwellian from the POD normalization (Eq. 4.19) improve the AARE (Sec. 5.2.2)? Why do we need to sample the data at a low frequency to get AARE? More work will be needed to answer these questions. However, since only the first few hundred POD modes are physically meaningful, they are probably not useful in obtaining meaningful spectra. Thus, we decided to take a look at the linear eigenmodes.

5.4 Structure and physicality of linear modes

The linear eigenmodes are eigenvectors of the linear gyrokinetic operator, written in a discretized matrix form. GENE has a full eigenvector solver based on SLEPc, PETSc, and SCALAPACK, which is very useful in this regard [99]. It solves for the left and right eigenvectors of the gyrokinetic operator and their eigenvalues [100]. We denote the n^{th} left eigenvector by $\psi^{(n)}_{l,\mathbf{k}}(z, v_\parallel, \mu)$ and likewise the n^{th} right eigenvector as $\psi^{(n)}_{r,\mathbf{k}}(z, v_\parallel, \mu)$. The left and right eigenvectors are orthonormal to each other under a simple dot product [21]. The orthonormality condition is given by,

$$\sum_{k_x,z,v_\parallel,\mu} \psi^{(m)*}_{l,\mathbf{k}}(z, v_\parallel, \mu)\psi^{(n)}_{r,\mathbf{k}}(z, v_\parallel, \mu) = \delta_{m,n}, \tag{5.9}$$

where the sum denotes a sum over all the grid points of z, $v_\parallel$ and μ and the connected k_x modes. Like the POD modes, here also there is a central $\mathbf{k}$ mode along with connected k_x modes. All the linear mode analyses have been performed with a total of five k_x connections. Similar to Fig. 5.7, Fig. 5.10 shows the structure of the linear modes in z and $v_\parallel$ space, averaged over the other coordinates. Here we have employed the standard average without weights. The numbering of the modes is in order of decreasing growth rate or increasing damping rate. We see that compared with the first POD mode, Fig. 5.7, the first linear mode shares a very similar structure. This mode represents the unstable ITG mode. As the mode number increases, the POD mode structure starts deviating from the linear modes rapidly. For the CBC, only the first linear eigenmode is unstable, rest all modes are damped.

Like the POD modes, even the linear modes develop a fine scale structure. However it appears that the linear modes are better resolved compared to POD (compare mode number 200 in Figs. 5.7 and 5.10). To check this, we again apply the test that was applied on POD modes (Fig. 5.9). We calculate the Fourier spectrum of the linear modes. Then we calculate the ratio of average amplitude in the lower half of the spectrum to the average amplitude in the upper half of the spectrum. This ratio is plotted in Fig. 5.11. We observe that the linear modes are well resolved up to mode number 2000 in both the z and $v_\parallel$ coordinates, after which this ratio flattens out at unity. This is an order of magnitude more well-resolved modes than in the POD.

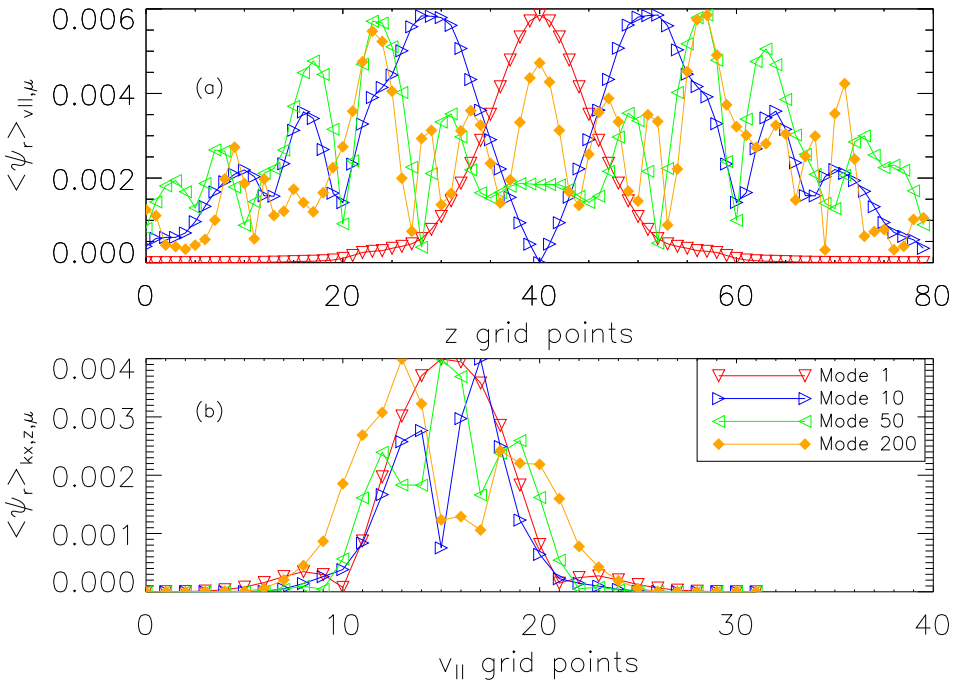

Figure 5.10: Absolute value of linear mode structure in (a) z space averaged over $v_\parallel$ and μ, and (b) $v_\parallel$ space averaged over k_x, z and μ. The modes are normalized so that the peak matches with the peak of Mode 1. The z coordinate has 80 grid points spanning the domain $[-5\pi, 5\pi]$ and $v_\parallel$ has 32 grid points spanning the domain $[-3v_{T,i}, 3v_{T,i}]$.

However, we will see in Sec. 5.6 that the resolved POD and linear modes span a similar range of scales in z and $v_\parallel$, namely, up to the grid scale. In order to get this result we have used higher values of hyper-diffusivity ($D_z = 8.0$ and $D_v = 5.0$) which smoothens out the modes and makes them more physical.

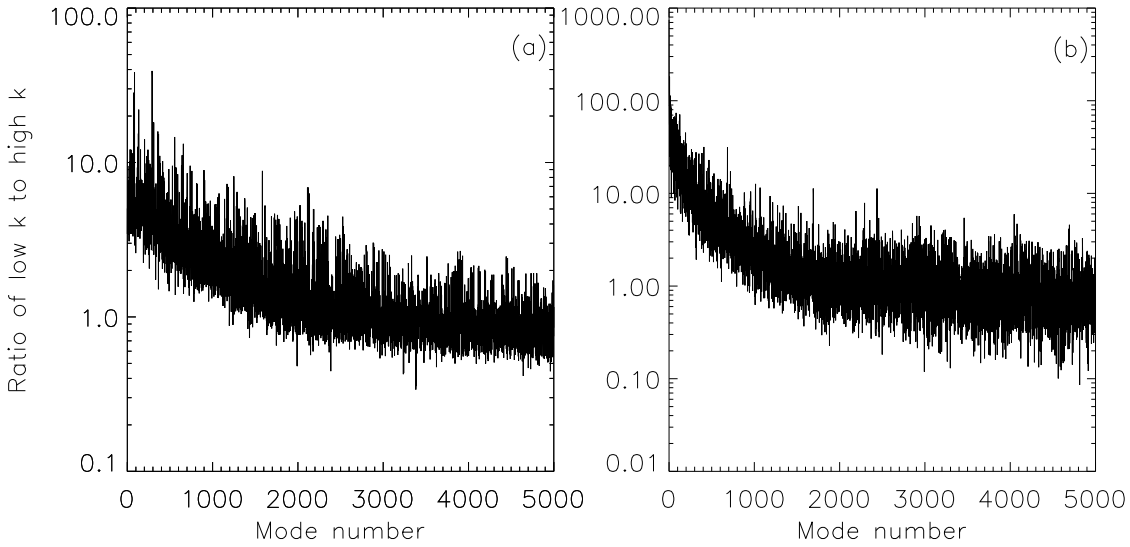

Figure 5.11: Plot of ratio of the average amplitude in lower half of spectrum to the average amplitude in upper half of spectrum for (a) k_z spectrum and (b) $k_{v_\parallel}$ spectrum. The first 5000 linear modes are plotted.

5.5 Amplitude and energy dissipation rate of linear modes

The distribution function can be expressed as a linear combination of the right eigenvectors in the usual way,

$$g_{\mathbf{k}}(z, v_\parallel, \mu, t) = \sum_n \pi^{(n)}_{r,\mathbf{k}}(t)\psi^{(n)}_{r,\mathbf{k}}(z, v_\parallel, \mu). \tag{5.10}$$

Again, for simplicity, we are ignoring the species index, and from now on we will also drop the subscript $\mathbf{k}$. $\pi^{(n)}_r$ is the time dependent amplitude of mode $\psi^{(n)}_r$. In a nonlinear simulation, it is straightforward to extract the amplitudes of the linear modes by taking the dot product of the

distribution function with the left eigenvector,

$$\pi^{(n)}_{r,\mathbf{k}}(t) = \sum_{k_x,z,v_\parallel,\mu} \psi^{(n)*}_{l,\mathbf{k}}(z,v_\parallel,\mu) g_{\mathbf{k}}(z,v_\parallel,\mu,t). \tag{5.11}$$

Here we have used the orthonormality property, Eq. 5.9.

The eigenvalues of these eigenvectors are the linear frequency and growth rates, also calculated by GENE. In CBC, there is one unstable mode, the ITG mode, and the rest are stable, with negative growth rates. In Fig. 5.12 we plot the the growth rates ($\gamma^{(n)}$), real frequencies ($\omega^{(n)}$) and the time averaged amplitudes of these modes over the saturated state of a nonlinear simulation ($\ln[\langle|\pi^{(n)}_r(t)|\rangle_t]$). In (a) we have used a high artificial dissipation with $D_z = 8.0$ and $D_v = 5.0$. In (b) lower values are used, $D_z = 0.25$ and $D_v = 0.2$. The simulations with low hyper-diffusivity show a significant amplitude for the higher, damped modes and the amplitude does not show a decreasing trend with increasing damping rate. With a higher dissipation, there is a larger range of damping rates and also a smooth decreasing trend of the amplitudes. In earlier studies low values of dissipation were used and extremely high amplitude damped modes were observed [21]. It was thought that the non-orthogonality of these modes might be responsible for such high amplitudes, as two "almost parallel" (highly nonorthogonal) modes can have equal and opposite large amplitudes which almost cancel out in the net sum. In fact, POD modes were utilized in order to overcome this issue. It appears that using higher artificial dissipation can alleviate this problem. It should also be remembered that low dissipation makes the higher modes unresolved (Sec. 5.3), which could also have been a contributing factor to the extreme non-orthogonality of such modes earlier.

We can now calculate the amplitude attenuation rate (AAR) for the linear modes, as was done for POD modes. It is simply the time averaged amplitude multiplied by the growth rate, $\langle|\pi^{(n)}_r(t)|\rangle_t \gamma^{(n)}$. The energy dissipation rate (EDR) can also be calculated, which is just the amplitude squared multiplied by growth rate, $\langle|\pi^{(n)}_r(t)|\rangle^2_t \gamma^{(n)}$. These rates are shown in Fig. 5.13. Fig. 5.13(a) and (b) show the AAR and EDR respectively, for the first 10000 linear modes. The first mode is excluded from these plots as it is unstable. There is a lot of scatter but we can see a

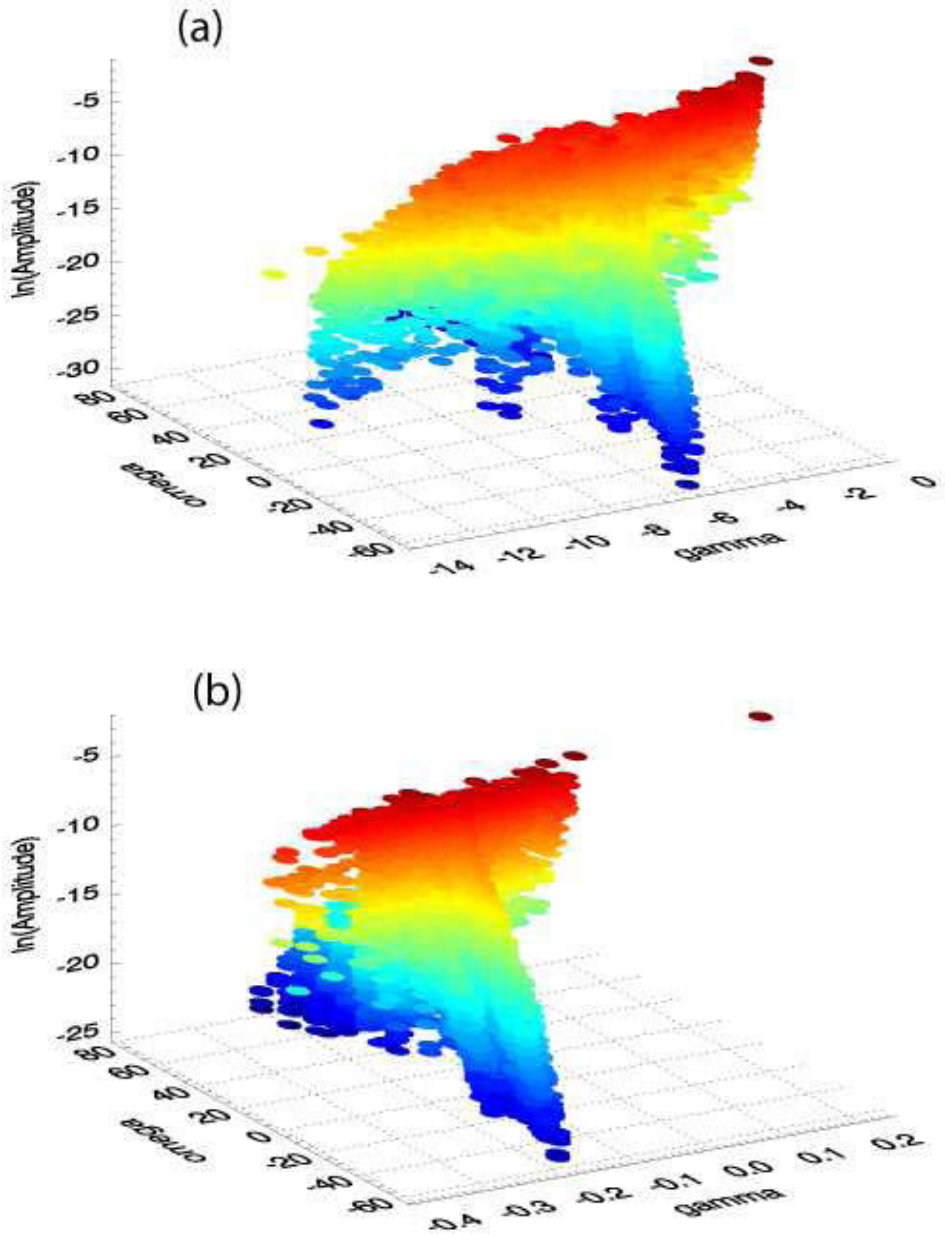

Figure 5.12: Plot of the natural logarithm of time averaged linear mode amplitudes on Z axis (also shown in color), growth rate $\gamma^{(n)}$ on X axis and real frequency $\omega^{(n)}$ on Y axis. Case (a) is using large hyper-diffusivity ($D_z = 8.0$, $D_v = 5.0$) and case (b) is with low hyper-diffusivity ($D_z = 0.25$, $D_v = 0.2$).

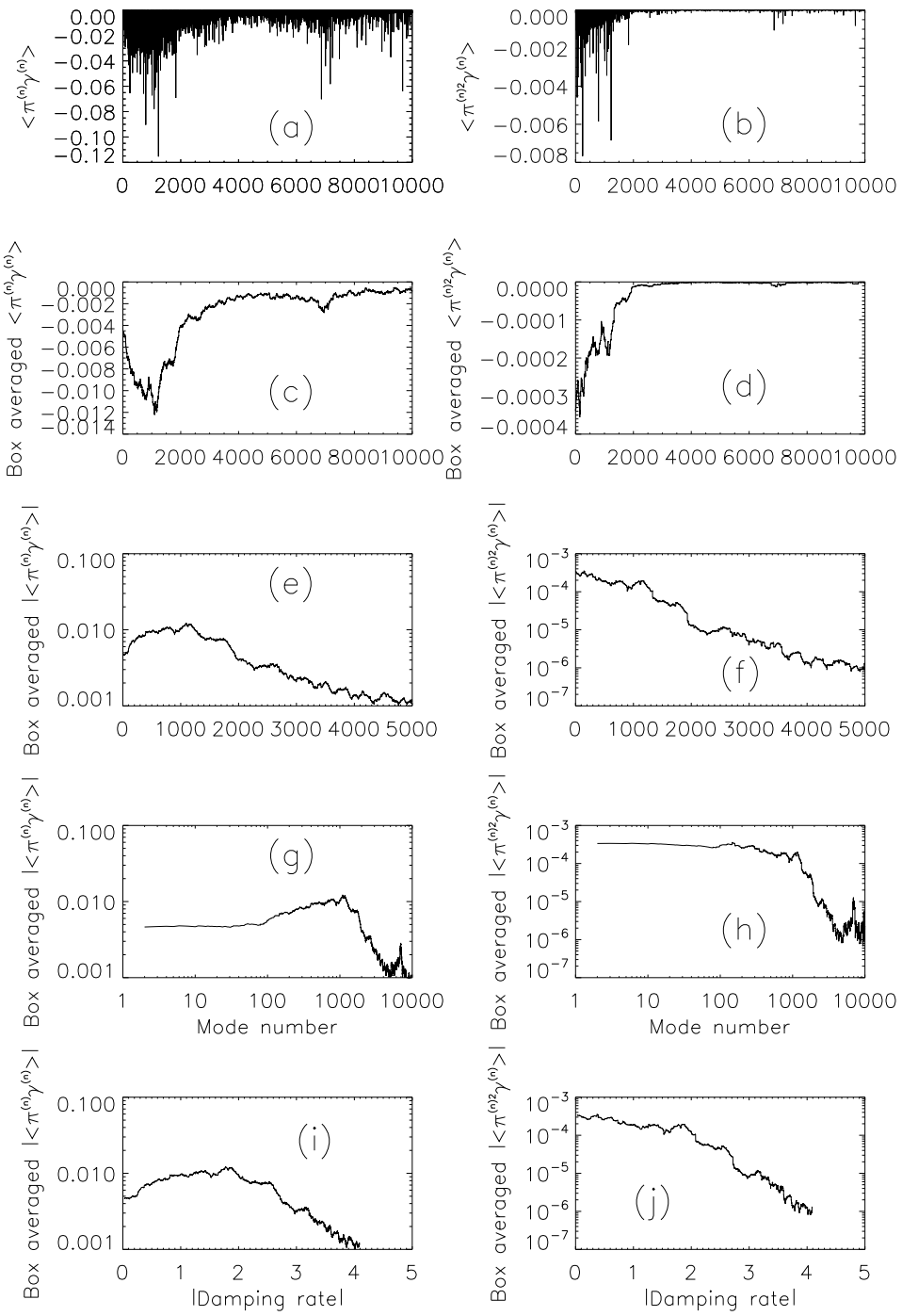

Figure 5.13: Amplitude attenuation rates (on left) and energy dissipation rates (on right) of linear modes, plotted in different ways. See text for a detailed description.

decreasing trend in both for the first 2000 modes. We also know that modes beyond 2000 are not well-resolved (Sec. 5.4). To get rid of the scatter, a box-car averaging procedure is done for the next plots in Fig. 5.13. The ordinate of every point is replaced by the average of the ordinates of the surrounding 200 points (or however many points possible, but less than 200). This smoothens the plots. Fig. 5.13(c) plots the box-averaged AAR and (d) plots the box-averaged EDR. We can now clearly see that these rates flatten after mode 2000. There is some trend up to modes 1000 and a change in behavior from modes 1000 up to 2000. Figs. 5.13(e) and (f) plot the absolute value of AAR and EDR respectively on a log-linear scale, for the first 5000 linear modes. It is plausible that an exponential might fit the EDR spectrum across this range. Figs. 5.13(g) and (h) plot the absolute value of AAR and EDR respectively on a log-log scale, for the first 10000 linear modes. We see three distinct regions in both AAR and EDR. The range from modes 2 up to 100 is relatively flat. The range from 100 to 1000 shows a power law behavior and then the range from modes 1000 up to around 4000 shows a different power law spectrum. This result will have to be verified using more simulations with varying resolutions and parameters to see how robust it is and how these power laws and their break-points change with parameters. However, all these plots are as a function of mode number, which is not a physical quantity. A more physical quantity is the damping rate and eventually we would have to relate the mode number to a damping rate. Figs. 5.13(i) and (j) plot the absolute values of AAR and EDR respectively as a function of the damping rate on a log-linear scale. The range of damping rate corresponds to the first 5000 modes. Again it might be possible to fit two different exponentials to the EDR spectrum.

These spectra are promising and hopefully lead to a better understanding of the damped modes in gyrokinetics. Another useful concept to study in turbulence is the mechanism of energy transfer, which is the topic of the next section.

5.6 Parallel transfer of energy

In gyrokinetics there are thousands of damped modes. In Sec. 5.5 we saw how their energy/amplitude dissipation rates behave. We know that energy is transferred to them by three-wave interactions with unstable modes, and in the case of ITG, with zonal flows. What is the nature of these three-wave interactions? In three dimensional hydrodynamic turbulence it is well known that the energy transfer is local, i.e., the three wavenumbers in the interaction have a similar magnitude. Similarly, energy is transferred from one mode to another in the mode decomposition space. What is the nature of the modes involved in this transfer? We try to answer this question using both POD and linear modes.

5.6.1 Parallel transfer to POD modes

We are interested in tracing how energy flows through the subdominant POD modes. We start with a nonlinear CBC simulation and let it saturate. At one time step in the saturated phase, the amplitude of the first POD mode at wavenumber $\mathbf{k} = (0, 0.25)$ is extracted using the POD orthogonality (Eq. 4.19). This amplitude is multiplied by a factor of 10 and the simulation is allowed to evolve self-consistently. This is akin to injecting some energy into the first POD mode. As the simulation evolves, this energy will get redistributed and eventually dissipated. We observe the energy of the other POD modes at this wavenumber and also at other wavenumbers to see where the excess energy goes. As this energy is transferred to other modes, we expect to see a spike in their energies as well. This is shown in Fig. 5.14. In (a) we see that the first POD mode of $\mathbf{k} = (0, 0.25)$ gets a kick at $t \approx 688$. As time goes on it relaxes back to its original saturated level. We see that at a later time, around $t \approx 694$, the 6^{th} mode energy reaches a peak. This is followed by the 11^{th} mode reaching a peak at $t \approx 695$ and the 26^{th} mode peaking at $t \approx 696$. All the modes are seen to rise at nearly the same time, indicating that energy is transferred simultaneously to all of them. Fig. 5.14(b) plots the same mode energies for the zonal wavenumber $\mathbf{k} = (0.1, 0)$, but we do not see any prominent energy injection peak that stands out. This is probably because, as seen earlier (Fig. 4.9), very little energy is transferred to the zonal

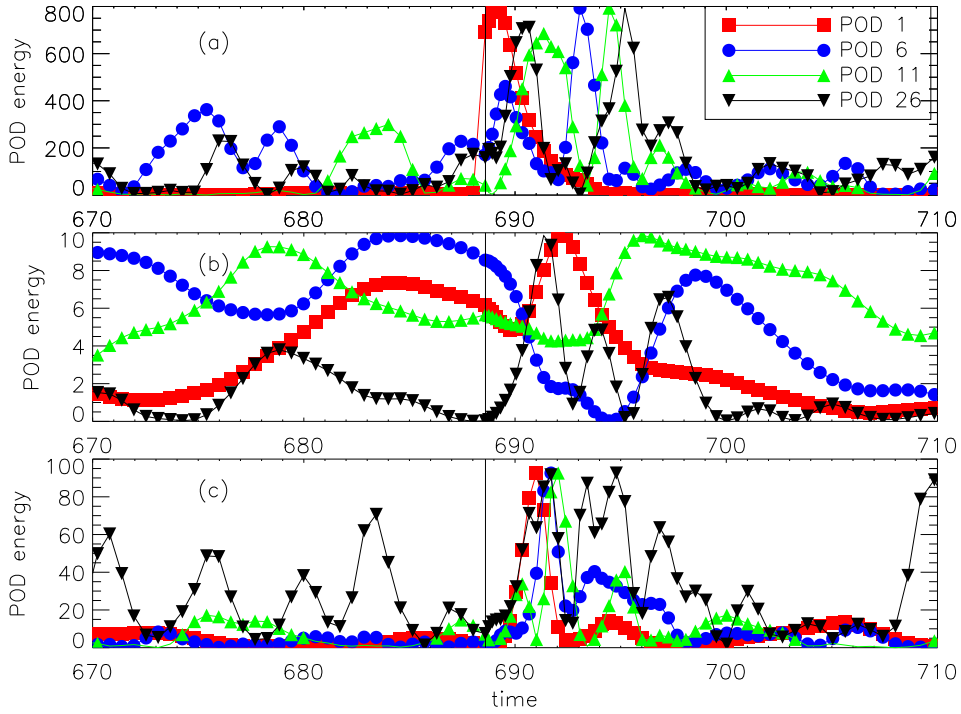

Figure 5.14: Time traces of POD mode energies ($|\beta^{(n)}\pi^{(n)}|^2$) for modes 1, 6, 11 and 26. (a) is for $\mathbf{k} = (0, 0.25)$, (b) is for $\mathbf{k} = (0.1, 0)$ and (c) is for $\mathbf{k} = (-0.1, 0.25)$. The peaks of the subdominant modes have been scaled to match the peak of first POD mode, for better visibility. The vertical line indicates the time at which energy is injected into the first POD mode at $\mathbf{k} = (0, 0.25)$.

modes in such interactions. Finally in (c), we see the mode energies at $\mathbf{k} = (-0.1, 0.25)$, and here also we see that all the POD modes get a spike in their energy at the same time, suggesting energy transfer to all these modes is in parallel.

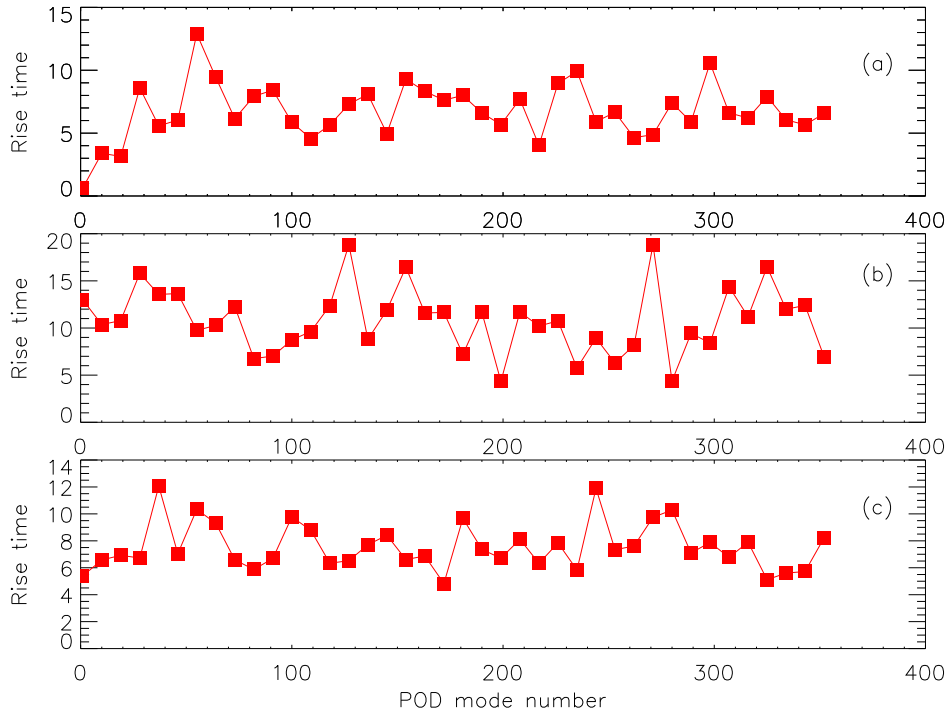

Figure 5.15: Average rise times for a sample of POD modes at three wavenumbers (a) $\mathbf{k} = (0, 0.25)$, (b) $\mathbf{k}' = (0.1, 0)$ and (c) $\mathbf{k}'' = (-0.1, 0.25)$. These are averaged over an ensemble of five simulation runs and plotted for a sample of 40 POD modes: $1, 10, 19, 28, \ldots, 352$.

A cleaner way to look at this is to calculate the rise times of the subdominant POD modes. Rise time is the time it takes from energy injection in the first POD mode to the subdominant mode energy reaching its peak. For example, in Fig. 5.14 the rise time for the 6^{th} POD mode at $\mathbf{k} = (0, 0.25)$ would approximately be $694 - 688 = 6$. This is calculated for a sample of POD modes, over the range of well-resolved modes, at the three standard wavenumbers; $\mathbf{k} = (0, 0.25)$, $\mathbf{k}' = (0.1, 0)$, and $\mathbf{k}'' = (-0.1, 0.25)$. An ensemble average over five ensembles with different initial conditions is taken to smooth out the statistical fluctuations. The results are plotted in Fig. 5.15. We see rise times for $\mathbf{k} = (0, 0.25)$ in plot (a). They do not seem to follow any increasing or decreasing trend, on an average the rise time is same for all the subdominant

modes. In (b) the rise times of the POD modes at $\mathbf{k}' = (0.1, 0)$ are given and they also seem flat. In reality, the zonal modes receive very little energy from the energy injection and do not show a distinctive energy spike. Thus, their rise times correspond to just random fluctuations and hence, their average rise time is higher compared to $\mathbf{k} = (0, 0.25)$. In (c) the rise times for $\mathbf{k}'' = (-0.1, 0.25)$ are given and they show same behavior as $\mathbf{k} = (0, 0.25)$. This analysis shows that energy is transferred to all the POD modes at the same time in a parallel manner.

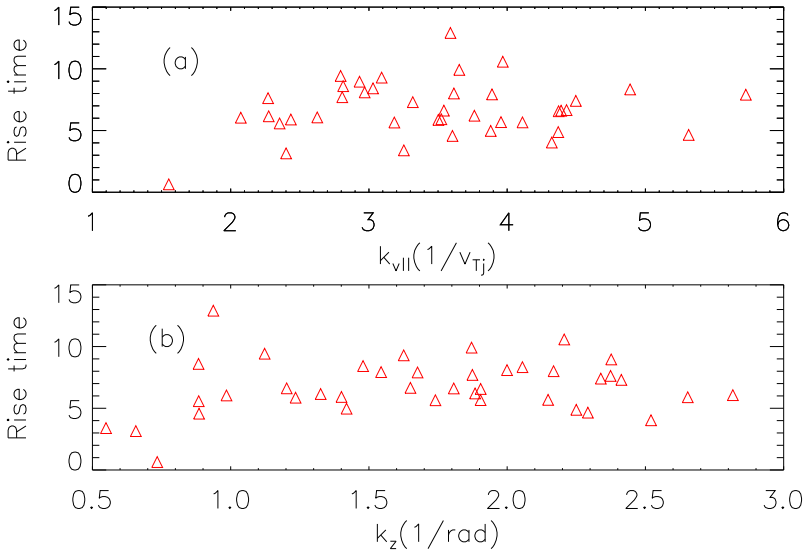

Figure 5.16: Rise times for the 40 POD modes: $1, 10, 19, \ldots, 352$ at $\mathbf{k} = (0, 0.25)$ (same as Fig. 5.15(a)). These are now plotted as a function of average POD wavenumbers $\langle k_{v_\parallel} \rangle^{(n)}$ (in (a)) and $\langle k_z \rangle^{(n)}$ (in (b)).

We can also associate a parallel wavenumber k_z and a parallel velocity wavenumber $k_{v_\parallel}$ with each POD mode. The Fourier transforms of POD modes in z and $v_\parallel$, ψ_{k_z} and $\psi_{k_{v_\parallel}}$ respectively, are already defined in Fig. 5.8. We use them to define an average parallel wavenumber, $\langle k_z \rangle^{(n)}$, for the n^{th} POD mode,

$$\langle k_z \rangle^{(n)} \equiv \sqrt{\frac{\sum_{kz} k_z^2 |\psi_{kz}^{(n)}|^2}{\sum_{kz} |\psi_{kz}^{(n)}|^2}}. \tag{5.12}$$

The average parallel velocity wavenumber, $\langle k_{v_\parallel} \rangle^{(n)}$, is defined in an analogous manner. Fig. 5.15(a) (rise times for POD modes at $\mathbf{k} = (0, 0.25)$) is replotted in Fig. 5.16, with the POD

numbers on the x-axis replaced by their corresponding $\langle k_{v_\parallel} \rangle^{(n)}$ and $\langle k_z \rangle^{(n)}$ in plots (a) and (b) respectively. The data point close to zero rise time is for the first POD mode. Other than that, the rise times are flat over a variation of factor of five in $\langle k_{v_\parallel} \rangle^{(n)}$ and $\langle k_z \rangle^{(n)}$. This shows that parallel transfer occurs over a significant range of scales in the z and $v_\parallel$ coordinates of gyrokinetic phase space. This result will be extended below to linear modes as well (Sec. 5.6.2).

The zonal flow might be playing a role in this behavior. In ITG, zonal flows strongly couple with all the subdominant modes and transfer energy to them simultaneously. It is not a local cascade like hydrodynamic turbulence, but rather a nonlocal cascade in which the zonal flows always participate in the dominant three-wave interaction. Of course, these results will have to be verified with other turbulence simulations as well as higher resolution studies. In the next section we study parallel transfer of energy to linear eigenmodes.

5.6.2 Parallel transfer to linear eigenmodes

We want to find out whether the parallel transfer of energy, seen in POD modes, holds for linear modes also. For that, we perform the same numerical experiment on linear modes. A CBC simulation is allowed to saturate in the nonlinear state. At a particular time step, the amplitude of the unstable linear mode at $\mathbf{k} = (0, 0.25)$ is extracted using the orthogonality condition, Eq. 5.9. This amplitude is then amplified by a factor of 100, akin to injecting energy into this mode. The time traces of the linear mode amplitudes at this wavenumber are observed, and we see spikes in them which are very similar to Fig. 5.14(a). The rise times for these modes are defined and calculated in the same way as was done in Sec. 5.6.1 for POD modes. Also, the average parallel wavenumber, $\langle k_z \rangle^{(n)}$, and average parallel velocity wavenumber, $\langle k_{v_\parallel} \rangle^{(n)}$, of the n^{th} linear mode are calculated just as in Eq. 5.12. The only difference is that instead of the POD mode Fourier transform, $\psi^{(n)}_{kz}$, the Fourier transform of the right eigenvector, $\psi^{(n)}_{r,kz}$, is used as a weight for the average. All this data is used in plotting Fig. 5.17. It plots the rise times for the first 5000 linear modes at $\mathbf{k} = (0, 0.25)$ as a function of their average wavenumbers $\langle k_z \rangle^{(n)}$ and $\langle k_{v_\parallel} \rangle^{(n)}$. The data is ensemble averaged over three simulation runs with different initial conditions. We see a very flat profile of the rise times over a factor of 5 in k_z and almost a

factor of a decade in $k_{v_\parallel}$. This shows that energy is transferred in parallel to linear modes also, spanning a large range of scales in z and $v_\parallel$. There seem to be two different sets of modes, one that receives energy earlier, at $t \approx 0.2$, and another that receives it later, at $t \approx 0.8$. More study will be required to see if this is real or an artifact.

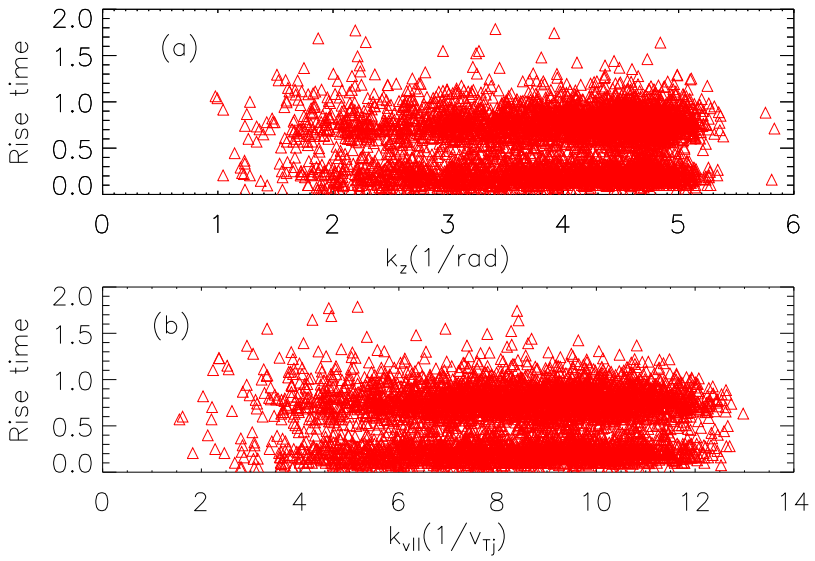

Figure 5.17: Ensemble averaged rise times for the first 5000 linear modes at $\mathbf{k} = (0, 0.25)$, plotted as a function of their average wavenumbers $\langle k_z \rangle^{(n)}$ and $\langle k_{v_\parallel} \rangle^{(n)}$ in (a) and (b) respectively.

5.7 Discussion

This chapter dealt with the energetics of damped modes in gyrokinetic turbulence. We believe that the damping rate is a chief characteristic of such modes, and as such it should play a central role in any theory aiming to describe them. With this goal in mind, we calculated the amplitude and energy damping rates of these modes, using both POD and linear decompositions.

Several problems were encountered when dealing with the higher POD modes. It appears that the POD modes rapidly become unresolved as their mode number increases. This also introduces complications in their energy balance when higher k_x connections are kept. A metric is defined to estimate the physicality of such modes. Hyper-diffusivity seems to be a key factor controlling

the behavior of these modes. Higher hyper-diffusivity extends the number of physical modes, both POD and linear. It also alleviates the problem of nonorthogonality of linear modes. In Ch. 4 higher hyper-diffusivity lead to more consistent results in the calculation of forward energy transfer via zonal flows (Fig. 4.10). There are also indications that the use of a collision operator, and its collisionality, has a big impact on the spectrum of damped modes [101]. The phenomenon of amplitude attenuation rate equipartition (AARE) in high POD modes was observed across all turbulence simulations. Several hypotheses were suggested to explain this observation. It appears that this is an artifact of the unresolved nature of higher POD modes.

The amplitude attenuation rates and energy dissipation rates of linear modes are calculated. Box averaging these spectra helps to smoothen them and reveal their trends. These show promising results in the form of spectra in the range of physical modes that seem to follow power law or exponential behavior. It should be very interesting to explain these spectra analytically. The fact that they follow a regular behavior as a function of damping rate, encourages our belief that the damping rate has to be a central quantity in the description of these modes.

In hydrodynamic turbulence, energy is transferred over the inertial range by means of local interactions amongst wavenumbers that do not differ drastically in magnitude from each other. In gyrokinetic turbulence, it is observed that the damped modes do not interact locally to transfer energy to neighboring modes with similar damping rates. Instead, energy is transferred in parallel to all the damped modes simultaneously. These modes can vary in their scales in z and $v_{\|}$ up to a decade. It is plausible that the zonal flows in ITG are responsible for such non-local interactions, as they are very efficient in energy transfer.

Chapter 6

Conclusions and future directions

Our design has been to present a broad overview of damped modes in plasma microturbulence. Through a comprehensive survey of turbulence models relevant for fusion plasmas, we have shown that damped modes are very important in saturating the energy injected by the unstable modes. While earlier studies had shown this for a few models like the ITG and TEM, this work shows it for a wide variety of models. This is very surprising, because these models have been studied in detail for several decades, with the role of damped modes in them going unnoticed.

Damped modes are important in saturation when their damping rate is comparable to, or less than, the instability growth rate. In such a case, energy dissipation by damped modes peaks in the unstable, small wavenumber range. This is very different from the conventional dissipation that is associated with small scale viscosity. In the fluid models, damped modes dissipate energy at large scales by driving a reversible, negative heat flux back into the equilibrium gradients. While this dissipation is not irreversible, it damps fluctuation amplitudes, affects saturation, and is therefore treated as dissipation in this sense. This results in a drastic reduction of the true heat flux compared to quasilinear estimates. In gyrokinetics, the details of the dissipation mechanism are still not fully understood, although it is the irreversible dissipation, either through hyper-diffusivity or collisions, which seems to dominate the reversible, negative heat flux.

One question that can be asked is: do damped modes affect other kinds of turbulence, and in what way? Homogeneous fluid and astrophysical turbulence is made up of eddies and waves,

are driven by external stirring, and hence do not involve unstable/stable modes. However, inhomogeneous fluid and astrophysical turbulence can have damped modes. One example is the magneto-rotational instability (MRI) in accretion disks [102]. This instability has associated stable modes and the model parameters show that the threshold criterion for excitation of stable modes (P_t) is satisfied in this model. It would be interesting to find out how damped modes affect the transport of angular momentum by the MRI, which is very crucial in accretion disks.

We also looked in detail at the regulation of ITG turbulence by self-consistently generated zonal flows, using a simple fluid model as well as a comprehensive gyrokinetic model. It has been shown that zonal flows help transfer energy from unstable to stable modes via three-wave interactions. The key reasons for the dominance of such interactions are the frequency matching in such triads, the high zonal flow amplitude in ITG, and the nonlinear coupling coefficients. This explanation is very different from the conventional zonal flow-drift wave shearing paradigm [47] which says that shearing due to zonal flows is responsible for enhanced energy transfer to dissipative, large wavenumbers and leads to regulation of turbulence. We do observe a forward transfer of energy consistent with zonal flow shearing, but a significant fraction of this energy is dissipated by damped modes which lie at large wavenumbers that are not traditionally associated with dissipation. Also, we see that the zonal flow amplitude and shearing rates are intimately linked. Thus, it is important to further tease out the effects of shearing versus zonal flow amplitude.

There are several aspects of zonal flows and damped modes that can be further explored. The zonal flow-drift wave shearing paradigm makes several predictions related to predator-prey oscillations, Dimits shift, and zonal flow collisionality [47]. Predator-prey oscillations, in which the zonal flows act as predators and the drift waves as prey, are observed in gyrokinetic and fluid simulations of ITG, as well as in experiments. It would be interesting to see what kind of a behavior damped modes introduce in these oscillations. This can also open up a way to investigate damped mode effects in experiment. Zonal flows are thought to play a key role in the Dimits shift of the ITG instability threshold, by quenching all the turbulence near the threshold. Do damped modes play a role in this? Gyrokinetic simulations can answer this question. Zonal flow collisionality is an important knob to control turbulence level. According

to the view presented in this thesis, this is explained via the dependence of frequency matching on zonal flow collisionality. This can also be verified in gyrokinetic simulations.

An important concept introduced is that of frequency matching, which says that the most dominant three-wave interactions have a minimum frequency sum. How broad is the applicability of this principle? Can it always predict which three-wave interaction will be the most dominant? If yes, this can be a very powerful tool. This can be probed more by running different kinds of simulations, either fluid or gyrokinetic. We have applied this principle using the linear and nonlinear frequencies. It is possible to use the linear frequencies if the nonlinearity is weak, but for strong nonlinearity the nonlinear frequencies can be calculated only from a simulation. It would be very useful to quasilinear techniques if a way can be found to extract the nonlinear frequency directly without running a simulation. Identifying the dominant three-wave interactions can be very helpful in doing a computationally cheaper simulation using only such interactions. It might also be possible to verify this principle in experiment using bi-spectral analysis.

This work has introduced some metrics which can be very handy in analyzing damped modes in turbulence. Firstly, the threshold parameter P_t is very convenient in predicting whether or not one should be worried about damped modes in their model. Secondly, the ratio of low wavenumber to high wavenumber amplitude is very useful in determining the physicality of basis modes. We used two kinds of mode decompositions, POD modes and the linear eigenmodes. Gram-Schmidt orthogonalized modes have also been used to study damped modes before [21]. This raises the question about which modes are suitable for which situations? Is there any preferred mode decomposition for a particular application and, if so, how do we arrive at it? Several new nonlinear energy transfer diagnostics were developed for use in gyrokinetics. Another topic to study is the effect of dissipation mechanisms. Higher hyper-diffusivity seems to be able to alleviate several numerical issues of non-orthogonality and variability faced by the damped modes. What would be the effect of using a realistic collision operator on the behavior of these modes?

The equipartition of amplitude attenuation rate was investigated, but it seems to be an artifact of the unresolved nature of higher POD modes. As the damping rate of modes increases,

they develop fine scale structure in the parallel spatial and velocity space. There are already existing theories describing such a phenomenon [103], [88]. Damped modes (either POD or linear) in high-resolution gyrokinetic simulations can be used to verify/falsify these theories. The amplitude and energy attenuation rates of linear modes show interesting behavior for the well-resolved modes. They show regions of equipartition as well as power law spectra. It would be interesting to develop an analytical theory to explain the observed spectra. The fact that energy is transferred to all the damped modes simultaneously, in parallel, across a large range of scales in phase space, might also play an important role in explaining these spectra. We believe that the damping rate should play a central role in any theory aiming to explain the behavior of damped modes.

Damped modes have turned out to be omnipresent in plasma microturbulence. While they have always been present in numerical simulations, they were never identified as an important entity. Now it is realized that they should always be taken into account when thinking about microturbulence. However, it still remains very important to identify the many effects of damped modes, not only in simulations but also in experiments.

Appendix A

Variables and expressions for the 2-field ITG/ETG model

Expressions relevant for the 2-field fluid ITG/ETG model studied in Ch. 3 are presented in this appendix.

The nonlinear coupling coefficients for Eq. 3.12 are

$$C_{lmn} = \frac{(-1)^{l-1}}{(R_1 - R_2)} \frac{(\mathbf{k}' \times \hat{z} \cdot \mathbf{k})}{2} \left[R'_m - R''_n + \frac{R_{3-l}(k''^2 - k'^2)}{(1+k^2)} \right], \tag{A.1}$$

$$C_{lFn} = \frac{(-1)^{l-1}}{(R_1 - R_2)} \frac{(-ik_y)}{2} \left[R''_n - \frac{R_{3-l}(k''^2 - k'^2)}{(1+k^2)} \right], \tag{A.2}$$

$$C_{lPn} = \frac{(-1)^{l-1}}{(R_1 - R_2)} \frac{(-k'_x k_y)}{2}, \tag{A.3}$$

$$C_{lmF} = \frac{(-1)^{l-1}}{(R_1 - R_2)} \frac{(-ik'_y)}{2} \left[R'_m + \frac{R_{3-l}(k''^2 - k'^2)}{(1+k^2)} \right], \tag{A.4}$$

$$C_{lmP} = \frac{(-1)^{l-1}}{(R_1 - R_2)} \frac{(-k'_y k''_x)}{2}. \tag{A.5}$$

The nonlinear coupling coefficients for the zonal flow equation, Eq. 3.13, are

$$C_{Fmn} = \frac{-i}{2} \frac{k'_y k_x^2 (k''^2 - k'^2)}{(\delta + k_x^2)}. \tag{A.6}$$

The nonlinear coupling coefficients for the zonal pressure equation, Eq. 3.14 are

$$C_{Pmn} = \frac{(k'_y k_x)}{2}(R'_m - R''_n). \tag{A.7}$$

Here $l, m, n = 1$ or 2 and $\mathbf{k}'' = \mathbf{k} - \mathbf{k}'$, $R_{1,2} = R_{1,2}(k)$, $R'_{1,2} = R_{1,2}(k')$ and $R''_{1,2} = R_{1,2}(k'')$. The terms in Eq. 3.16 are

$$Q_u = \sum_{k_y \neq 0} -2k_y(1 + \eta + \epsilon) Im(R_1)|\beta_1|^2, \tag{A.8}$$

$$Q_s = \sum_{k_y \neq 0} -2k_y(1 + \eta + \epsilon) Im(R_2)|\beta_2|^2, \tag{A.9}$$

$$Q_{us} = \sum_{k_y \neq 0} -2k_y(1 + \eta + \epsilon) Im(R_1\beta_1\beta_2^* + R_2\beta_1^*\beta_2), \tag{A.10}$$

$$D = \sum_{k_y \neq 0} -2\chi k^4|p_k|^2 - 2\nu k^2|\phi_k|^2, \tag{A.11}$$

$$D_{zonal} = \sum_{k_y = 0} -2\chi k^4|p_k|^2 - 2\nu k^2|\phi_k|^2. \tag{A.12}$$

The three wave coupling terms in Eq. 3.18 are

$$N_{1mn} = \sum_{k_y \neq 0} \mathcal{A} Re\left[\sum_{k'_y \neq 0, k_y} C_{1mn}\beta_1^*\beta'_m\beta''_n\right], \tag{A.13}$$

$$N_{1Pn} = \sum_{k_y \neq 0} \mathcal{A} Re\left[\sum_{k'_y = 0} C_{1Pn}\beta_1^* p'_z\beta''_n\right], \tag{A.14}$$

$$N_{1mP} = \sum_{k_y \neq 0} \mathcal{A} Re\left[\sum_{k'_y = k_y} C_{1mP}\beta_1^*\beta'_m p''_z\right], \tag{A.15}$$

$$N_{1Fn} = \sum_{k_y \neq 0} \mathcal{A} Re\left[\sum_{k'_y = 0} C_{1Fn}\beta_1^* v'_z\beta''_n\right], \tag{A.16}$$

$$N_{1mF} = \sum_{k_y \neq 0} \mathcal{A} Re\left[\sum_{k'_y = k_y} C_{1mF}\beta_1^*\beta'_m v''_z\right], \tag{A.17}$$

where $\mathcal{A} = 2(1 + k^2 + |R_1|^2)$. The three wave coupling terms in the zonal field energy Eqs. 3.19

and 3.20 are,

$$N_{Pmn} = \sum_{k_y=0} 2Re\left[\sum_{k'_y \neq 0} C_{Pmn} p_z^* \beta'_m \beta''_n\right], \tag{A.18}$$

$$N_{Fmn} = \sum_{k_y=0} 2Re\left[\sum_{k'_y \neq 0} C_{Fmn} v_z^* \beta'_m \beta''_n\right], \tag{A.19}$$

where, in Eqs. (A.13-A.19), $m, n = 1$ or 2.

Appendix B

Notation in Gyrokinetics

Most of the notation is borrowed from Ref. [21]. The normalization of (and definition of some) quantities is

$$
\begin{aligned}
&k_{x,y} \to \frac{k_{x,y}}{\rho_{ref}} && v_{\parallel} \to c_{ref} v_{Tj} v_{\parallel} && \mu \to \frac{T_{ref}}{B_{ref}} T_{0j} \mu \\
&B_0 \to B_{ref} B_0 && t \to \frac{L_{ref}}{c_{ref}} t && m_j \to m_{ref} m_j \\
&T_{0j} \to T_{ref} T_{0j} && n_{0j} \to n_{ref} n_{0j} && q_j \to e q_j \\
&c_{ref} = \sqrt{T_{ref}/m_{ref}} && \rho_{ref} = c_{ref}/\Omega_{ref} && \Omega_j = \frac{q_j B_0}{m_j c} \\
&\Omega_{ref} = \frac{e B_{ref}}{m_{ref} c} && v_{Tj} = \sqrt{2 T_{0,j}/m_j}. &&
\end{aligned}
\tag{B.1}
$$

Here the subscript 'ref' refers to a reference quantity. For example, ρ_{ref} is the reference ion gyro-radius calculated using the reference mass m_{ref}, reference temperature T_{ref} (the mean temperature of the species) and reference magnetic field B_{ref} (the equilibrium magnetic field). j denotes the species index, typically 'i' for ions and 'e' for electrons. The proton charge is e, $n_{0,j}$ is the background number density of species j.

The gyrokinetic equation is expressed as

$$
\frac{\partial g_j}{\partial t} = \mathcal{L}[g_j] + \mathcal{N}[g_j], \tag{B.2}
$$

where g_j is related to the perturbed distribution function f_j through

$$f_j = g_j - \frac{2q_j}{m_j v_{Tj}} v_\parallel \bar{A}_\parallel F_{0j}. \tag{B.3}$$

The linear operator $\mathcal{L}$ is given by

$$\begin{aligned}\mathcal{L}[g_j] = &- v_* F_{0j} i k_y \chi_j + \frac{\beta T_{0j}}{L_p q_j B_0^2} v_\parallel^2 i k_y \Gamma_j - v_{Tj} v_\parallel \Gamma_{jz} \\ &- v_d (K_y i k_y + K_x i k_x) \Gamma_j + \frac{v_{Tj}\mu}{2} \frac{\partial B_0}{\partial z} \frac{\partial f_j}{\partial v_\parallel} + C_j(f_j).\end{aligned} \tag{B.4}$$

The first term on R.H.S. is the gradient drive term, second is the finite β term, third and fourth are the gradient and curvature drift terms, fifth is the parallel gradient term and sixth term represents dissipation due to either collision operator or artificial dissipation. The parallel advection term contains the expression,

$$\Gamma_{jz} = \frac{\partial \Gamma_j}{\partial z} + \mu \partial_z B_0 \frac{q F_{0j}}{T_{0j}} \bar{\phi}. \tag{B.5}$$

The other quantities in Eq. B.4 are,

$$\begin{aligned} F_{0j} = F_0 &= \pi^{-3/2} e^{-(v_\parallel^2 + \mu B_0)}, \\ \chi_j &= \bar{\phi}_j - v_{Tj} v_\parallel \bar{A}_{\parallel j}, \\ \Gamma_j &= g_j + \frac{q_j F_{0j}}{T_{0j}} \chi_j, \\ v_* &= \frac{1}{L_n} + \frac{1}{L_{Tj}} (v_\parallel^2 + \mu B_0 - \frac{3}{2}), \\ v_d &= \frac{T_{0j}}{q_j B_0} (2 v_\parallel^2 + \mu B_0), \\ K_x &= -\sin(z), \\ K_y &= -\cos(z) - \hat{s} z \sin(z), \\ B_0(z) &= \frac{1}{1 + \epsilon_t \cos(z)}. \end{aligned} \tag{B.6}$$

L_p, L_{Tj} and L_n are the equilibrium gradient scale lengths for the pressure, temperature and density respectively (normalized to L_{ref}), v_{Tj} is the thermal velocity for particle species j, $\hat{s}$ is the magnetic shear, and ϵ_t is the local inverse aspect ratio. These expressions assume the $s-\alpha$ model of tokamak geometry which uses circular flux surfaces [104].

The overbar denotes a gyro average which (in a Fourier representation) is accomplished by multiplying by a zeroth-order Bessel function J_0.

$$\bar{\phi} = J_0(\lambda_j)\phi, \tag{B.7}$$

$$\lambda_j = \left(\frac{2B_0\mu}{m_j}\right)^{\frac{1}{2}} \frac{k_\perp}{\Omega_j}, \tag{B.8}$$

$$k_\perp^2 = (k_x + \hat{s}zk_y)^2 + k_y^2. \tag{B.9}$$

The gyrokinetic Poisson equation becomes,

$$\begin{aligned} \phi =& \frac{\sum\limits_j n_{0j}\pi q_j B_0 \int J_0(\lambda_j) g_j dv_\parallel d\mu}{k_\perp^2\lambda_D^2 + \sum\limits_j \frac{q_j^2}{T_{0j}} n_{0j}(1-\Gamma_0(b_j))}, \\ \lambda_D =& \sqrt{\frac{B_{ref}^2}{4\pi c^2 n_{ref} m_{ref}}}. \end{aligned} \tag{B.10}$$

Here λ_D is the Debye length, $\Gamma_0(x) = e^{-x}\hat{I}_0(x)$ ($\hat{I}_0$ is the zeroth order modified Bessel function) and $b_j = \frac{v_{Tj}^2 k_\perp^2}{2\Omega_j^2}$. The gyrokinetic Ampere's law is,

$$A_\parallel = \frac{\sum\limits_j \frac{\beta}{2} q_j n_{0j} v_{Tj} \pi B_0 \int dv_\parallel d\mu v_\parallel J_0(\lambda_j) g_j}{k_\perp^2 + \sum\limits_j \frac{\beta q_j^2}{m_j} n_{0j}\pi B_0 \int dv_\parallel d\mu v_\parallel^2 J_0^2(\lambda_j) F_{0j}}, \tag{B.11}$$

where $\beta = \frac{8\pi n_{ref} T_{ref}}{B_{ref}^2}$. The nonlinear operator is,

$$\mathcal{N}[g_j] = \sum_{\mathbf{k}'_\perp} (k'_x k_y - k_x k'_y)\chi_j(\mathbf{k}'_\perp) g_j(\mathbf{k}_\perp - \mathbf{k}'_\perp). \tag{B.12}$$

Appendix C

Sample GENE parameters file

A sample GENE parameters file for typical simulations shown in this thesis along with an explanation of non-standard parameters used specifically in this work. The standard parameters can be found in GENE documentation.

```
&parallelization
n_procs_s =  1
n_procs_v =  24
n_procs_w =  8
n_procs_x =  1
n_procs_y =  1
n_procs_z =  12
/

&box
n_spec =    1    ! # species
nx0    =  128    ! # radial grid points
nky0   =   16    ! # kys
nz0    =    16    ! # parallel grid pts
nv0    =    32    ! # vpar grid points
nw0    =    8    ! # mu grid points
lx     =  125.628     ! box length in x
kymin =     0.05     ! min ky
lv     =     3.00     ! domain in vpar
lw     =     9.00     ! domain in mu
!adapt_lx = .f.
/
```

```
&in_out
diagdir = './output_directory'
chptdir = './chpt_directory'
write_checkpoint = F
read_checkpoint  = T

istep_mom   =      100
istep_nrg   =      10
istep_energy=     100

!istep_dfout defines the time steps at which to output distribution function
!at selected wavenumbers
!istep_dfout  =     50

!istep_lamp_proj defines the time steps at which to output
!the linear eigenmode amplitudes
!istep_lamp_proj = 50

!istep_nlt defines the time steps at which to output the nonlinear
!energy transfer terms for Fourier or POD modes
!istep_nlt   =     50
/

&general
nonlinear =   T
arakawa_zv =  T !grid for energy conservation
arakawa_cons_bc = T !set #undef hyp_on_h & #undef hyp_over_j in switches.h
calc_dt    = .t.
timelim    =      53000  ! wallclock limit in sec
ntimesteps =      5000  ! total # timesteps
simtimelim =      10000  ! simulation time limit in L_ref/c_ref
hyp_z =   8.0 !hyper-diffusivity coefficient D_z
hyp_v =   5.0 !hyper-diffusivity coefficient D_v

!following block is for calculating the linear eigenmodes, in order for
!this to work, other parameters have to be changed for a linear run
!comp_type='EV' !switch to specify an eigenvalue computation
!which_ev  = 'all_mpl' !solve for all eigenvalues
!n_ev      = 20480 !number of eigenvalues and vectors
!ev_out    = T !output eigenvalues in file eigenvalues.dat
!ev_right  = T !output right eigenvectors in eigenvectors_r.dat
!ev_left   = T  !output left eigenvectors in eigenvectors_l.dat
!ev_n_test = 40960 !twice of n_ev
!vec_out_limit = T!arrange the eigenvectors in order of decreasing growth rate
```

```
/

&extended_diags

!the following block specifies the wavenumbers to output
!if istep_dfout is non-zero
!this is the first step in calculating energy dynamics of POD modes
!in second step, uncomment the SVD_proj block below to perform an SVD analysis
!in third step, uncomment the nlt_pod block below to calculate n.l. transfer
!num_ky_modes = 3 !number of wavenumbers to output
!num_kx_modes = 1 !number of kx connections to keep
!which_ky = 5 0 5 !ky index of output modes
!which_kx_center = 0 2 -2 !central kx index of output modes

!following block performs SVD analysis
!before this, one needs to output the data using istep_dfout
!SVD_proj = T !switch to activate SVD projection routine
!SVD_kx_ind = 0 !kx index of wavenumber at which to do SVD
!SVD_ky_ind = 5 !ky index of wavenumber at which to do SVD
!SVD_nkx0 = 1 !number of connections kept
!SVD_df_n_time = 1000 !total number of time steps in SVD sample
!SVD_start_time = 0.0 !time in sample at which to start SVD
!SVD_df_file_path = './svd_folder' !where to output SVD data
!SVD_sparse_factor = 2 !decrease sampling frequency by this factor
!SVD_f0_flag = F !uncomment to exclude F_0 from SVD normalization

!this indicates the Fourier modes for which to calculate nonlinear transfer
!num_nlt_modes = 1
!kx_nlt_ind = 0
!ky_nlt_ind = 5

!this block calculates energy transfer functions for POD modes, the third
!and final step in the process, and outputs files nlp_ky...dat
!and nlp_info_ky...dat
!nlt_pod = T !switch to activate nonlinear transfer calculation for POD modes
!num_nlt_pod_modes = 3 !number of POD modes to be calculated
!nx0_nlt_pod =  1 !number of connections kept
!num_nlt_modes = 3 !number of wavenumbers to be analyzed
!start_nlt_pod_mode = 10 !the POD mode at which to start analysis
!!num_podmode_skip = 5 !number of POD modes to skip, for example
!in this example, nonlinear transfer will be calculated for PODs 10, 16, 22
!ky_nlt_ind =  5 0  5 !ky index of modes
!kx_nlt_ind =  0 2 -2 !kx index of modes
!SVD_df_file_path = './svd_folder'!directory where SVD_df_ky...files are stored
```

```
!lamp_kick = T !switch to activate energy injection into unstable linear mode
!time_of_kick = 2000 !the time index at which to inject energy
/

&geometry
magn_geometry = 's_alpha' !geometry model
shat     =   0.7960     ! r/q dq/dr
trpeps   =   0.1800     ! r/R_0
major_R  =    1.000     ! R_0 (here = L_ref)
q0       =    1.400     ! safety factor q
/

&species
name   = 'ions'
omn    =    2.220    !L_ref/L_n
omt    =    6.960    !L_ref/L_T
mass   =    1.000    !mass in units of m_ref
temp   =    1.000    !temperature in units of T_ref
dens   =    1.000    !density in units of n_ref
charge =  1          !charge in elementary charge units
/
```

References

[1] I. Eames and J. B. Flor, Phil. Trans. R. Soc. A **369**, 702 (2011).

[2] V. N. Tsytovich, *Theory of Turbulent Plasma* (Consultants Bureau, 1977) pp. 1–4.

[3] A. L. Fetter and J. D. Walecka, *Theoretical Mechanics of Particles and Continua* (Dover Publications, 2003).

[4] A. N. Kolmogorov, Dokl. Akad. Nauk SSSR **30**, 299 (1941).

[5] P. W. Terry, "Concepts in plasma turbulence," University Lecture (2011).

[6] U. Frisch, Proc. R. Soc. Lond. A. **434**, 89 (1991).

[7] H. L. Grant, R. W. Stewart, and A. Moilliet, J. Fluid Mech. **12**, 241 (1962).

[8] R. Herman, *Fusion: The Search for Endless Energy* (Cambridge University Press, 1990).

[9] F. F. Chen, *An Indispensable Truth: How Fusion Power Can Save the Planet* (Springer, 2011).

[10] J. Jacquinot, Nucl. Fusion **50**, 014001 (2010).

[11] L. Artsimovich, Nature **239**, 18 (1972).

[12] D. Meade, Nucl. Fusion **50**, 014004 (2010).

[13] K. Ikeda, Nucl. Fusion **50**, 014002 (2010).

[14] V. P. Smirnov, Nucl. Fusion **50**, 014003 (2010).

[15] J. Wesson, *Tokamaks* (Oxford University Press, 2004).

[16] F. L. Hinton and R. D. Hazeltine, Rev. Mod. Phys. **48**, 239 (1976).

[17] A. J. Wootton, B. A. Carreras, H. Matsumoto, K. McGuire, W. A. Peebles, C. P. Ritz, P. W. Terry, and S. J. Zweben, Phys. Fluids B: Plasma Phys. **2**, 12 (1990).

[18] W. Horton, Rev. Mod. Phys. **71**, 735 (1999).

[19] M. Greenwald, Phys. Plasmas **17**, 058101 (2010).

[20] W. H. Matthaeus, D. C. Montgomery, M. Wan, and S. Servidio, Journal of Turbulence **13**, N37 (2012).

[21] D. R. Hatch, "Mode analyses of gyrokinetic simulations of plasma microturbulence," Ph.D Thesis (2010).

[22] D. A. Baver, P. W. Terry, R. Gatto, and E. Fernandez, Phys. Plasmas **9**, 3318 (2002).

[23] P. W. Terry, D. A. Baver, and S. Gupta, Phys. Plasmas **13**, 022307 (2006).

[24] P. W. Terry, D. A. Baver, and D. R. Hatch, Phys. Plasmas **16**, 122305 (2009).

[25] D. R. Hatch, P. W. Terry, W. M. Nevins, and W. Dorland, Phys. Plasmas **16**, 022311 (2009).

[26] D. R. Hatch, P. W. Terry, F. Jenko, F. Merz, M. J. Pueschel, W. M. Nevins, and E. Wang, Phys. Plasmas **18**, 055706 (2011).

[27] D. R. Hatch, P. W. Terry, F. Jenko, F. Merz, and W. M. Nevins, Phys. Rev. Lett. **106**, 115003 (2011).

[28] J. H. Kim and P. W. Terry, Phys. Plasmas **17**, 112306 (2010).

[29] K. D. Makwana, P. W. Terry, J. H. Kim, and D. R. Hatch, Phys. Plasmas **18**, 012302 (2011).

[30] P. M. Bellan, *Fundamentals of Plasma Physics* (Cambridge University Press, 2008) pp. 41–52.

[31] C. H. Holland, P. H. Diamond, S. Champeaux, E. Kim, O. Gurcan, M. N. Rosenbluth, G. R. Tynan, N. Crocker, W. Nevins, and J. Candy, Nucl. Fusion **43**, 761 (2003).

[32] G. S. Lee and P. H. Diamond, Phys. Fluids **29**, 3291 (1986).

[33] A. Hasegawa and M. Wakatani, Phys. Rev. Lett. **50**, 682 (1983).

[34] G. R. Tynan, C. Holland, J. H. Yu, A. James, D. Nishijima, M. Shimada, and N. Taheri, Plasma Phys. & Controlled Fusion **48**, S51 (2006).

[35] F. Y. Gang, P. H. Diamond, J. A. Krotinger, and A. E. Koniges, Phys. Fluids B: Plasma Phys. **3**, 955 (1991).

[36] A. S. Ware, P. H. Diamond, B. A. Carreras, J. N. Leboeuf, and D. K. Lee, Phys. Fluids B: Plasma Phys. **4**, 102 (1992).

[37] A. S. Ware, P. H. Diamond, H. Biglari, B. A. Carreras, L. A. Charlton, J. N. Leboeuf, and A. J. Wootton, Phys. Fluids B: Plasma Phys. **4**, 877 (1992).

[38] P. W. Terry and W. Horton, Phys. Fluids **25**, 491 (1982).

[39] B. A. Carreras, L. Garcia, and P. H. Diamond, Phys. Fluids **30**, 1388 (1987).

[40] H. Takabe and A. Yamamoto, Phys. Rev. A **44**, 5142 (1991).

[41] A. Das, S. Mahajan, P. Kaw, A. Sen, S. Benkadda, and A. Verga, Phys. Plasmas **4**, 1018 (1997).

[42] A. B. Hassam, Phys. Fluids **23**, 38 (1980).

[43] P. W. Terry and K. W. Smith, Phys. Plasmas **15**, 056502 (2008).

[44] G. G. Craddock and P. W. Terry, Phys. Fluids B: Plasma Phys. **3**, 3286 (1991).

[45] R. Gatto, P. W. Terry, and D. A. Baver, Phys. Plasmas **13**, 022306 (2006).

[46] A. M. Dimits, G. Bateman, M. A. Beer, B. I. Cohen, W. Dorland, G. W. Hammett, C. Kim, J. E. Kinsey, M. Kotschenreuther, A. H. Kritz, L. L. Lao, J. Mandrekas, W. M. Nevins, S. E. Parker, A. J. Redd, D. E. Schumaker, R. Sydora, and J. Weiland, Phys. Plasmas **7**, 969 (2000).

[47] P. H. Diamond, S.-I. Itoh, and T. S. Hahm, Plasma Phys. & Controlled Fusion **47**, R35 (2005).

[48] L. Schmitz, L. Zeng, T. L. Rhodes, J. C. Hillesheim, E. J. Doyle, R. J. Groebner, W. A. Peebles, K. H. Burrell, and G. Wang, Phys. Rev. Lett. **108**, 155002 (2012).

[49] A. Fujisawa, K. Itoh, H. Iguchi, K. Matsuoka, S. Okamura, A. Shimizu, T. Minami, Y. Yoshimura, K. Nagaoka, C. Takahashi, M. Kojima, H. Nakano, S. Ohsima, S. Nishimura, M. Isobe, C. Suzuki, T. Akiyama, K. Ida, K. Toi, S. I. Itoh, and P. H. Diamond, Phys. Rev. Lett. **93**, 165002 (2004).

[50] V. Sokolov, X. Wei, A. K. Sen, and K. Avinash, Plasma Phys. & Controlled Fusion **48**, S111 (2006).

[51] L. Chen, Z. Lin, and R. White, Phys. Plasmas **7**, 3129 (2000).

[52] G. Manfredi, C. M. Roach, and R. O. Dendy, Plasma Phys. & Controlled Fusion **43**, 825 (2001).

[53] G. W. Hammett, M. A. Beer, W. Dorland, S. C. Cowley, and S. A. Smith, Plasma Phys. & Controlled Fusion **35**, 973 (1993).

[54] P. H. Diamond, S. Champeaux, M. Malkov, A. Das, I. Gruzinov, M. N. Rosenbluth, C. Holland, B. Wecht, A. I. Smolyakov, F. L. Hinton, Z. Lin, and T. S. Hahm, Nucl. Fusion **41**, 1067 (2001).

[55] M. Xu, G. R. Tynan, P. H. Diamond, P. Manz, C. Holland, N. Fedorczak, S. C. Thakur, J. H. Yu, K. J. Zhao, J. Q. Dong, J. Cheng, W. Y. Hong, L. W. Yan, Q. W. Yang, X. M.

Song, Y. Huang, L. Z. Cai, W. L. Zhong, Z. B. Shi, X. T. Ding, X. R. Duan, Y. Liu, and HL-2A team, Phys. Rev. Lett. **108**, 245001 (2012).

[56] T. S. Hahm, M. A. Beer, Z. Lin, G. W. Hammett, W. W. Lee, and W. M. Tang, Phys. Plasmas **6**, 922 (1999).

[57] Z. Lin, T. S. Hahm, W. W. Lee, W. M. Tang, and R. B. White, Science **281 (5384)**, 1835 (1998).

[58] P. W. Terry, Phys. Rev. Lett. **93**, 235004 (2004).

[59] R. A. Moyer, G. R. Tynan, C. Holland, and M. J. Burin, Phys. Rev. Lett. **87**, 135001 (2001).

[60] M. K. Verma, Physics Reports **401**, 229 (2004).

[61] M. Nakata, T.-H. Watanabe, and H. Sugama, Phys. Plasmas **19**, 022303 (2012).

[62] T.-H. Watanabe, H. Sugama, and S. Ferrendo-Margalet, Nucl. Fusion **47**, 1383 (2007).

[63] A. M. Dimits, W. M. Nevins, D. E. Schumaker, G. W. Hammett, T. Dannert, F. Jenko, M. J. Pueschel, W. Dorland, S. C. Cowley, J. N. Leboeuf, T. L. Rhodes, J. Candy, and C. Estrada-Mila, Nucl. Fusion **47**, 817 (2007).

[64] M. Lesieur, *Turbulence in Fluids* (Kluwer Academic Publishers, 1990) pp. 161–175.

[65] P. W. Terry and W. Horton, Phys. Fluids **26**, 106 (1983).

[66] D. R. Hatch, M. J. Pueschel, F. Jenko, W. M. Nevins, P. W. Terry, and H. Doerk, Phys. Rev. Lett. **108**, 235002 (2012).

[67] E. Wang, W. M. Nevins, J. Candy, D. Hatch, P. Terry, and W. Guttenfelder, Phys. Plasmas **18**, 056111 (2011).

[68] D. C. Montogmery and D. A. Tidman, *Plasma Kinetic Theory* (McGraw-Hill, 1964).

[69] N. A. Krall and A. W. Trivelpiece, *Principles of Plasma Physics* (McGraw-Hill, 1973).

[70] A. J. Brizard and T. S. Hahm, Rev. Mod. Phys. **79**, 421 (2007).

[71] G. G. Howes, S. C. Cowley, W. Dorland, G. W. Hammett, E. Quataert, and A. A. Schekochihin, ApJ **651**, 590 (2006).

[72] R. D. Hazeltine and J. D. Meiss, *Plasma Confinement* (Addison-Wesley Pub. Co., 1992).

[73] F. Merz, "Gyrokinetic simulation of multimode plasma turbulence," Ph.D. Thesis (2009).

[74] M. J. Pueschel, T. Dannert, and F. Jenko, Comput. Phys. Commun. **181**, 1428 (2010).

[75] F. Jenko, W. Dorland, M. Kotschenreuther, and B. N. Rogers, Phys. Plasmas **7**, 1904 (2000).

[76] For code details see: http://gene.rzg.mpg.de (2013).

[77] G. H. Golub and C. F. Van Loan, *Matrix Computations* (The Johns Hopkins University Press, 1996).

[78] A. Banon Navarro, P. Morel, M. Albrecht-Marc, D. Carati, F. Merz, T. Gorler, and F. Jenko, Phys. Rev. Lett. **106**, 055001 (2011).

[79] B. Friedman, T. A. Carter, M. V. Umansky, D. Schaffner, and B. Dudson, Phys. Plasmas **19**, 102307 (2012).

[80] B. Friedman, T. A. Carter, M. V. Umansky, D. Schaffner, and I. Joseph, Phys. Plasmas **20**, 055704 (2013).

[81] M. J. Pueschel and F. Jenko, Phys. Plasmas **17**, 062307 (2010).

[82] P. Xanthopoulos, F. Merz, T. Gorler, and F. Jenko, Phys. Rev. Lett. **99**, 035002 (2007).

[83] Z. Lin, T. S. Hahm, W. W. Lee, W. M. Tang, and P. H. Diamond, Phys. Rev. Lett. **83**, 3645 (1999).

[84] M. A. Malkov, P. H. Diamond, and M. N. Rosenbluth, Phys. Plasmas **8**, 5073 (2001).

[85] D. R. Hatch, D. del-Castillo-Negrete, and P. W. Terry, Journal of Computational Physics **231**, 4234 (2012).

[86] J.-H. Kim and P. W. Terry, Phys. Plasmas **18**, 092308 (2011).

[87] Ch. P. Ritz, E. J. Powers, and R. D. Bengston, Phys. Fluids B: Plasma Phys. **1**, 153 (1989).

[88] A. A. Schekochihin, S. C. Cowley, W. Dorland, G. W. Hammett, G. G. Howes, G. G. Plunk, E. Quataert, and T. Tatsuno, Plasma Phys. & Controlled Fusion **50**, 124024 (2008).

[89] T. Tatsuno, W. Dorland, A. A. Schekochihin, G. G. Plunk, M. Barnes, S. C. Cowley, and G. G. Howes, Phys. Rev. Lett. **103**, 015003 (2009).

[90] T.-H. Watanabe and H. Sugama, Phys. Plasmas **11**, 1476 (2004).

[91] S. C. Cowley, R. M. Kulsrud, and R. Sudan, Phys. Fluids B: Plasma Phys. **3**, 2767 (1991).

[92] R. E. Waltz, G. D. Kerbel, and J. Milovich, Phys. Plasmas **1**, 2229 (1994).

[93] W. M. Nevins, J. Candy, S. Cowley, T. Dannert, A. Dimits, W. Dorland, C. Estrada-Mila, G. W. Hammett, F. Jenko, M. J. Pueschel, and D. E. Shumaker, Phys. Plasmas **13**, 122306 (2006).

[94] P. N. Guzdar, C. S. Liu, J. Q. Dong, and Y. C. Lee, Phys. Rev. Lett. **57**, 2818 (1986).

[95] F. Ryter, C. Angioni, A. G. Peeters, F. Leuterer, H.-U. Fahrbach, W. Suttrop, and ASDEX Upgrade Team, Phys. Rev. Lett. **95**, 085001 (2005).

[96] D. del-Castillo-Negrete, D. A. Spong, and S. P. Hirshman, Phys. Plasmas **15**, 092308 (2008).

[97] M. Bydder and J. Du, Magnetic Resonance Imaging **24**, 849 (2006).

[98] I. G. Abel, M. Barnes, S. C. Cowley, W. Dorland, and A. A. Schekochihin, Phys. Plasmas **15**, 122509 (2008).

[99] F. Merz, C. Kowitz, E. Romero, J. E. Roman, and F. Jenko, Comput. Phys. Commun. **183**, 922 (2012).

[100] R. A. Horn and C. R. Johnson, *Matrix Analysis* (Cambridge University Press, 2012).

[101] D. R. Hatch, V. Bratanov, and F. Jenko, Bull. Amer. Phys. Soc. **57**, No. 12, GP8.22 (2012).

[102] S. A. Balbus and J. F. Hawley, Rev. Mod. Phys. **70**, 1 (1998).

[103] P. W. Terry and P. H. Diamond, "Impact of clumps on plasma stability and the nature of turbulence in the saturated state," *Statistical Physics and Chaos in Fusion Plasmas*, ed. by W. Horton and L. Reichl, Wiley, N.Y., p. 335 (1984).

[104] R. L. Miller, M. S. Chu, J. M. Greene, Y. R. Lin-Liu, and R. E. Waltz, Phys. Plasmas **5**, 973 (1998).